PhD Dissertations and Master's Theses

11-2021

Acoustic/Gravity Wave Phenomena in Wide-Field Imaging: From Data Analysis to a Modeling Framework for Observability in the Mlt Region and Beyond

Jaime Aguilar Guerrero
aguilaj9@my.erau.edu

ACOUSTIC/GRAVITY WAVE PHENOMENA IN WIDE-FIELD IMAGING:

FROM DATA ANALYSIS TO A MODELING FRAMEWORK FOR

OBSERVABILITY IN THE MLT REGION AND BEYOND

BY

JAIME AGUILAR GUERRERO

A THESIS

SUBMITTED TO THE DEPARTMENT OF PHYSICAL SCIENCES AND THE

COMMITTEE ON GRADUATE STUDIES

IN PARTIAL FULFILLMENT OF THE REQUIREMENTS FOR THE

DEGREE OF

DOCTOR OF PHILOSOPHY IN

ENGINEERING PHYSICS

NOVEMBER 2021

EMBRY-RIDDLE AERONAUTICAL UNIVERSITY

DAYTONA BEACH, FLORIDA

_____ / ___ / _____

Date

ACOUSTIC/GRAVITY WAVE PHENOMENA IN WIDE-FIELD IMAGING: FROM DATA ANALYSIS TO A MODELING FRAMEWORK FOR OBSERVABILITY IN THE MLT REGION AND BEYOND

by

Jaime Aguilar Guerrero

This thesis was prepared under the direction of the candidate's Thesis Committee Chair, Jonathan B. Snively, and has been approved by the Thesis Committee. It was submitted to the College of Arts and Sciences in partial fulfillment of the requirements of the

degree of

DOCTOR OF PHILOSOPHY IN ENGINEERING PHYSICS

THESIS COMMITTEE:

Digitally signed by Jonathan Snively
Date: 2022.02.10 20:18:16 -05'00'

Jonathan B. Snively,
PhD Committee Chair

Digitally signed by Alan Liu
Date: 2022.02.11 07:26:30 -05'00'

Alan Z. Liu, PhD
Committee Member

Digitally signed by Matthew Zettergren
Date: 2022.02.11 10:45:45 -05'00'
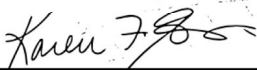
Matthew D. Zettergren, PhD
Committee Member

Digitally signed by Dominique Pautet
Date: 2022.02.11 09:45:30 -07'00'

Pierre-Dominique Pautet,
PhD External Committee Member

Digitally signed by Edwin Mierkiewicz
DN: cn=Edwin Mierkiewicz, o, ou, email=mierkiee@erau.edu, c=US
Date: 2022.02.11 11:50:42 -05'00'

Edwin J. Mierkiewicz, PhD
Graduate Program Chair,
PhD Engineering Physics

Digitally signed by Dr. John Hughes
Date: 2022.02.11 12:01:54 -05'00'

John Hughes, PhD
Department Chair, Physical Sciences

Karen Gaines, PhD
Dean, College of Arts and Sciences

Lon Moeller, JD
Senior V.P. for Academics

Abstract

Acoustic waves, gravity waves, and larger-scale tidal and planetary waves are significant drivers of the atmosphere's dynamics and of the local and global circulation that have direct and indirect impacts on our weather and climate. Their measurements and characterization are fundamental challenges in Aeronomy that require a wide range of instrumentation with distinct operational principles. Most measurements share the common features of integrating optical emissions or effects on radio waves through deep layers of the atmosphere. The geometry of these integrations create line-of-sight effects that must be understood, described, and accounted for to properly present the measured data in traditional georeferenced frames or in thin-layer representations. These effects include intensity enhancements/cancellations, filtering of scales, and apparent phase shifts relative to the underlying wave dynamics. We have designed a simulation framework that uses 2D and 3D input model data to perform these line-of-sight integrations based on ray tracing and geodesic transformations. The primary objective is to characterize these effects, to define quantifiable impacts on measurable parameters, and to create a basis for synthetic data for processes to be revealed in current and future measurements.¶

Contents

List of Tables

List of Figures

zenith and the unwarped images' center coordinates. Positive tilt angles correspond to imagers that are Southeast of the coordinates and negative when Northwest of them. Simulated data: Midwest thunderstorm 2016/07/08 5:15:12 UTC.   133

Figure 4.19. Total spectral power (TSP), total, max and min intensity (photons) of fifty 500×500 km (4×4 km resolution) unwarped images of OH(3,1) IVER centered at (40.83°N, 93.57°W) for two tracks. -axis is uniform tilt angle. TSP frequencies bounded by ±8.26–1 km–1 in both axes. Simulated images from ground-based 512×512 pixel, 180° FOV imagers. Tilt angle is measured between the imager's zenith and the unwarped images' center coordinates. Positive tilt angles correspond to imagers that are Southeast of the coordinates and negative when Northwest of them. Simulated data: Midwest thunderstorm 2016/07/08 5:15:12 UTC.   134

Figure 4.20. 3D visualizations of the OH(3,1) emission layer from an ideal simulation imaged from different locations. The input data are 125 m resolution blocks of 20×10×160 km (, ,) that have been replicated along and to further extend the domain. (top) 3D slices of the wave structure. (bottom) LOS integration at the specified location: the data is displaced by ±200 km along . (left) Oblique LOS leads to scale filtering. (center) Imaging over the zenith provides the most straightforward depiction of the wave. (right) Parallel LOS produces clear enhancements. The intensity units are (photons·cm–3·s–1).   135

Figure 4.21. 1D plot of the structures shown in Figure 4.20. Using a slice of the 3D data, the domain is extended up to 2000 kilometers to further enhance the cancelation effect that happens when the LOS aligns (or not) with the wavefronts. Significant filtering happens for anti-alignment.   136

Figure 4.22. Slices along the SE2NW (–55.7°) track. (top) Cartesian slice of original MAGIC data (ratio 30:1 vertical:horizontal). (bottom 3) ENU slices and positions of the 50 surface imagers and 256 lines-of-sight of three of them.   138

Figure 4.23. Slices along the SW2NE (34.3°) track. (top) Cartesian slice of original MAGIC data (ratio 30:1 vertical:horizontal). (bottom 3) ENU slices and positions of the 50 surface imagers and 256 lines-of-sight of three of them.   139

Figure 4.24. Line-of-sight integrations of a (left) ground- and a (right) satellite-based imager at 400 km height at two different times from the onset of a MAGIC OH(3,1) airglow response due to a tsunami. The results are presented as perturbations to the background mean. Due to the larger coverage of the satellite imager FOV at the airglow height, more wavelengths are observed and available for analysis.   140

Figure 4.26. Simulated images of CO_2 BWT as seen by an imager on board a satellite with parameters: 725 km height, 7.5 km/s orbital velocity, 14.4° azimuth track, 2.67 s time between exposures, 512 cross-track pixels and 48.7° FOV. (left) track shifted by 500

List of Abbreviations and symbols

AGW - Atmospheric Gravity Wave

GW - Gravity Wave

AW - Acoustic Gravity Wave

IAW - Infrasonic Gravity Wave

TID - Traveling Ionospheric Disturbance

ASI - All-Sky Imager

FOV - Field of View

LOS - Line-Of-Sight

VER or ϵ - Volume Emission Rate

IVER - Integrated Volume Emission Rate

FT - Fourier Transform

GCM - General Circulation Model

EPSG - European Petroleum Survey Group

CRS - Coordinate Reference Systems

WGS84 - World Geodetic System of 1984

MAGIC - Model for Acoustic-Gravity wave Interactions and Coupling

GEMINI - Geospace Environment Model for Ion-Neutral Interactions

ENU - East North Up coordinate system

NED - North East Down coordinate system

ECEF - Earth-Center-Earth-Fixed coordinate system¶

Acknowledgements

I thank my family, friends and advisor for the support provided during the preparation of this document, including the long hours spent away while working on the code and visualization. This work is a reflection of the hopes and desires for making meaningful contributions to the Aeronomy and Space Physics scientific community, so that our results can better inform future discoveries and its efforts become a reflection of society at large, of its needs and of its never-ending development.

Chapter 1

Introduction: Aeronomy and Gravity Waves

The Earth's upper atmosphere is host to many dynamical phenomena that are responsible for its structure and circulation. Aeronomy is the study of the upper atmospheric, of its chemical and physical processes. It is multidisciplinary and it is fundamentally based on the observations along the entire atmosphere. The scales of atmospheric phenomena vary greatly and they determine the type of interactions with the background atmosphere. **Figure 1.1** shows the large-scale temperature perturbations up to 500 km height that arise from a convective storm.
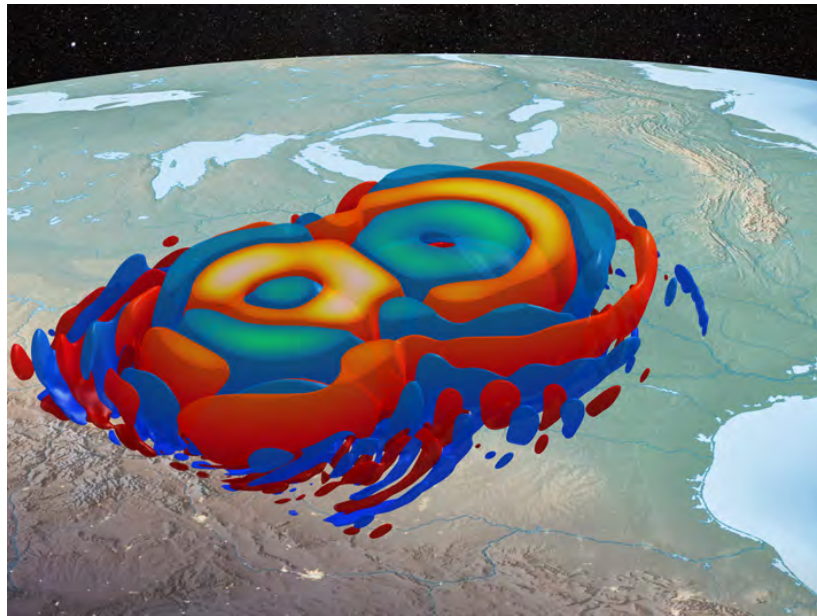
Figure 1.1. 3D modeling of temperature perturbations due to a thunderstorm. The top height is 500 km.

In the mesosphere and lower thermosphere (MLT) region of the atmosphere, at 80-100 km altitude, we find different layered emission due to photochemical reactions of different molecular and atomic species that form the atmosphere; this is the Earth's airglow or nightglow. Studies of atmospheric emissions from ground-based photometry, spectroscopy, or imagery, and in-situ measurements by rocketry have been conducted to determine the heights and emission of these layers (Roach and Meinel 1955, Sharov and Lipaeva 1973, Taylor and Hapgood 1982) that first provided us with clues to the dynamical processes that regulate the upper atmosphere. **Table 1.1** presents the most prominent emissions in the MLT and lower thermosphere region altitude with typical mean heights and full-width-half-maximums. A model of the layers is shown in **Figure 1.2**, where a photograph from the ISS is included for comparison.

Emission line	Emission Wavelength (Å)	Mean Layer Height (km)	FWHM (km)
OH(3,1)	$1500 - 1570$	87	8
Na(^{2}P, ^{2}S)	5890, 5896	90	10
O(^{1}S)	5577	95	8
O$_2$	8655	94	8
O(^{1}D)	6300	230	60

Table 1.1. Some of the most important airglow layer emissions in the MLT region.

In this thesis we are interested in determining the characteristics of distinct wave phenomena through simulations. While it is possible to measure the airglow intensity and the rotational temperature whose relation is a function of wave parameters often described by the Krassovsky parameter (Krassovsky and Shagaev 1977), some intrinsic wave parameters cannot be determined directly from single integrated airlgow measurements, such as vertical wavelength of the wave. These can be described by a

model from distinct airglow layer measurements (i.e. to get phase differences). Nevertheless, vertical wavelength and intrinsic wave characteristics can be derived with sufficient knowledge of the propagation environment, or with multiple measurements sufficient to discern the phase structure of the wave as it evolves over altitude (Swenson, Taylor et al. 1995, Fritts and Alexander 2003, Liu and Swenson 2003, Yue, Vadas et al. 2009, Akiya, Saito et al. 2014, Fritts, Smith et al. 2016, Liu, Xu et al. 2019).
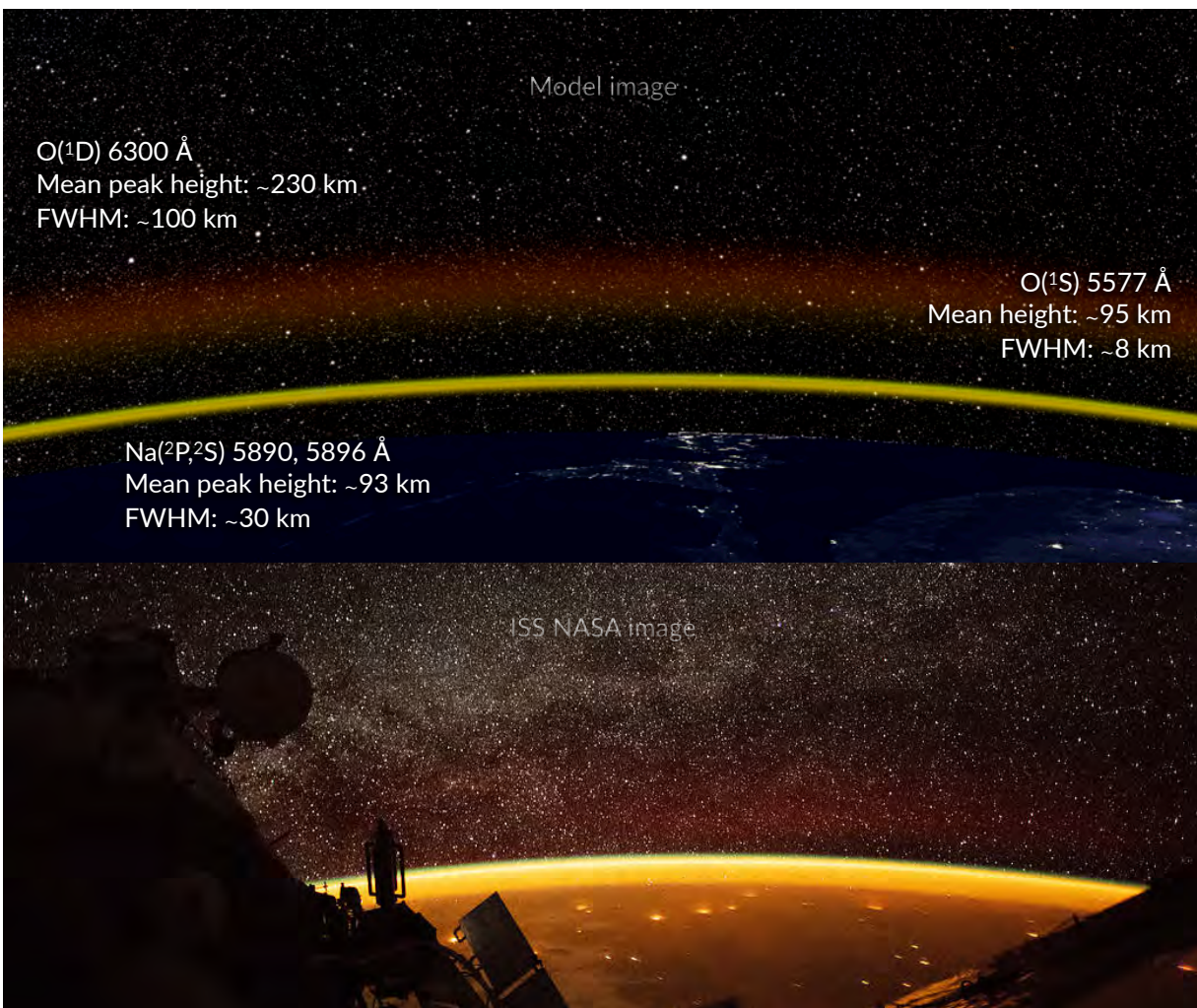
Figure 1.2. (top) Modeled 3D airglow layers. (bottom) Earth's airglow as seen from the ISS at over 250 miles above Australia. *Credit: NASA, https://www.nasa.gov/image-feature/earth-enveloped-in-airglow.*

1.1 Atmospheric Gravity Waves

The stable stratification of Earth's atmosphere allows it to support wave motions that play a fundamental role in modulating its composition and regulating the weather and climate of the near-Earth space environment. Among the most important phenomena are Atmospheric Gravity Waves (AGWs for short) which arise from disturbances to the balance of buoyancy and gravity forces within the atmosphere. It was the early and illuminating work by Hines (1960) that laid the foundation for AGW studies; later works would start developing and testing the theory with observational data and models, such as reviewed on the context on Ionospheric traveling disturbances (TIDs) by Francis (1975) and, more recently, in an extensive review paper by Fritts & Alexander (2003) which outlines the fundamental theory, the description of their sources and propagation, observational capabilities, instabilities, parameterization and their atmospheric impact. More recent studies have endeavored to understand the coupling of all these phenomena throughout the different layers of the atmosphere (Yiğit and Medvedev 2015, and references within). This influence on the overall circulation and structure of the upper atmosphere occurs at different spatial and temporal scales where it is useful to distinguish AGWs based on their frequencies.

The solution to the linearized equations of motion for a compressible atmosphere and the corresponding dispersion relations yield two distinct regimes of AGWs separated by the acoustic cut-off frequency and the Brunt-Väisälä frequency, which define the lowest frequencies of acoustic waves and the highest frequencies of gravity waves. Internal Gravity Waves (or just GWs) have frequencies lower than the Brunt-Väisälä frequency and their horizontal wavelengths extend from a few kilometers to hundreds; the latter low-frequency waves are called inertia-gravity waves and are affected by Earth's rotation. These long-period GWs with larger spatial coverage may also be modulated by the diurnal solar cycle and interact closely with tides and planetary waves

that possess very long timescales and wavelengths. On the higher frequency end of the spectrum exist acoustic waves (AWs), whose frequency is larger than the acoustic-cutoff frequency, and where compressional forces are more significant than the stratification effects of gravity. In the vicinity of either the Brunt-Väisälä or acoustic cut-off frequencies there are also those waves that have no defined vertical group velocity. These waves, also called external gravity waves, are in the evanescent regime which includes those frequencies between Brunt-Väisälä and the acoustic cut-off. See **Figure 1.3** for an overview of all the wave motions supported by the atmosphere including acoustic/ gravity wave phenomena and sound waves.
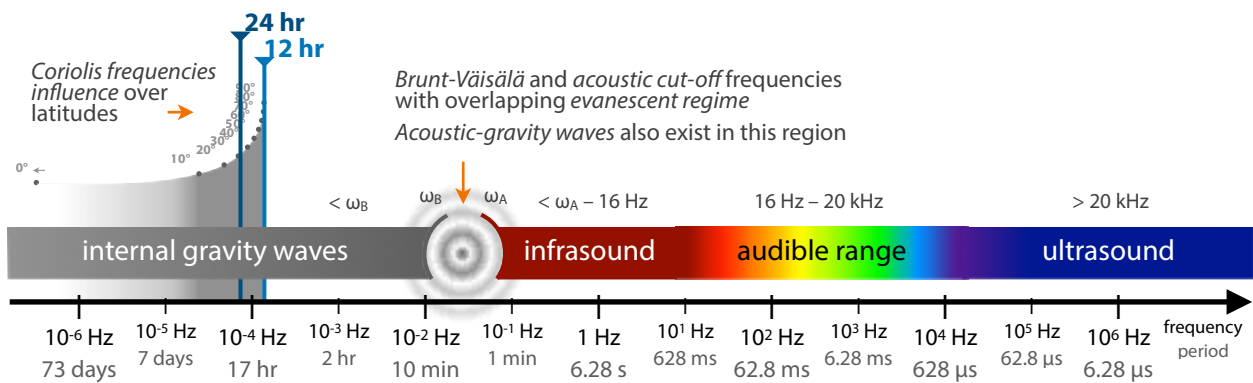
Figure 1.3. Frequency range of wave phenomena supported by the atmosphere. ω_A is the *acoustic cut-off frequency*, ω_B is the *Brunt Väisälä frequency*. Waves with frequencies smaller than ω_B and larger than ω_A are freely propagating. The values of these characteristic frequencies depend on atmospheric conditions and fall in a range highlighted in the graph by the concentric waves; this range of frequencies also represents the possible values for evanescent modes (waves with no vertical group velocity) that exist between ω_B and ω_A and their vicinity. *Acoustic-gravity waves* may also exist in frequencies neighboring ω_B and ω_A. The *Coriolis frequencies* have also been included for reference, along with the corresponding period for 24 hr and 12 hr waves. The period values correspond to 2π/frequency. *Based on a concept from Bittner et al. [2010].*

At a wide range of scales, GWs may have significant impact on all the layers of the atmosphere and are key facilitators of upward momentum and energy exchange. Due to this wide variety of scales, distributions and altitudes, observational studies of GWs and related observables, such as winds and temperatures, require distinct instruments with different scopes, capabilities and, thus, limitations; i.e., lower layers of the atmosphere are reachable by weather stations, balloons, sounding rockets or aircraft equipped with in-situ instruments, while at higher altitudes remote-sensing equipment is needed such as incoherent scatter radars (ISRs) and ground-based or airborne LIDARs, imagers or more sounding rockets. Currently the science derived from these instruments aims to describe and quantify the coupling between the atmospheric layers (Azeem, Yue et al. 2015, Perwitasari, Sakanoi et al. 2015, Fritts, Vosper et al. 2018, Heale, Snively et al. 2019). It is of primary scientific importance to further understand both the sources of GWs and their different atmospheric impacts as they propagate upward. For example, tropospheric forcing by storms and mountains generate waves that have dynamical effects and observable signatures all throughout the upper atmosphere. Acoustic-gravity waves, such as generated by earthquakes, tsunamis and volcanos can also be monitored via the same techniques to derive insight into their source processes (Artru, Ducic et al. 2005, Hickey, Schubert et al. 2009, Makela, Lognonné et al. 2011, Nakashima, Heki et al. 2016) or thunderstorms (Hoffmann and Alexander 2010, Heale, Snively et al. 2019) that generate observable signatures all throughout the atmosphere and up to the thermosphere and can even be traced along Earth's magnetic field lines (Nielsen and Schlegel 1985, Chisham, Lester et al. 2007). As sensing technology, as well as our understanding, have developed over the years we have come to understand the fundamental role of GWs in atmospheric dynamics. **Figure 1.4** shows the increasing trend over the years in atmospheric GW and AW publications; while GWs publications show an increasing steady trend, AWs publications have greatly grown in number since 2015.
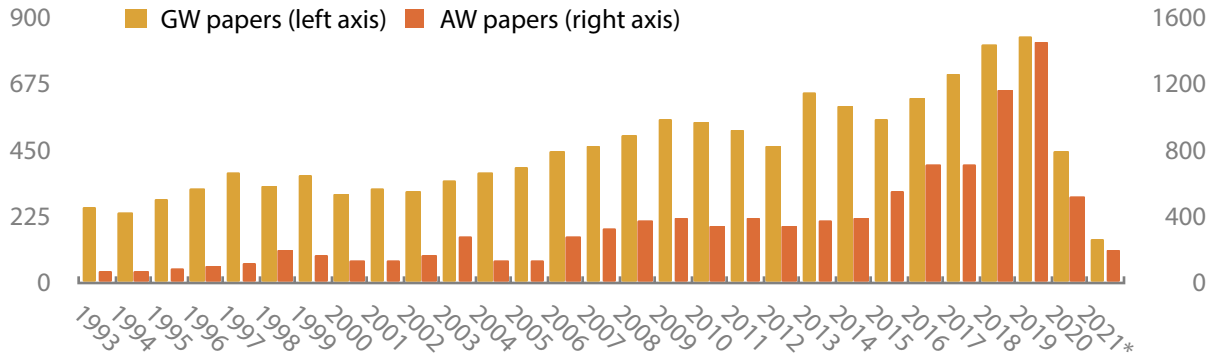
Figure 1.4. GW and AW publication (records) metric from *Web of Science* (all databases) for years 1993 to 2021 (*up to 07/06/2021) for papers containing the search <u>topic</u> "gravity wave* AND atmospher*" and "acoustic wave* AND atmospher*" narrowed to the <u>research fields</u> of: *Meteorology Atmospheric Sciences*, *Physical Sciences Other Topics*, *Remote Sensing* and *Physical Geography. Accessed July 6th, 2021.*

1.2 Remote sensing and imaging

Remote sensing and specifically *imaging* discoveries have had profound impacts for Aeronomy. Technological advances in instrumentation capabilities have enabled us to prove and further develop the underlying theories of the early years. For example, in 2005 the first detection of ionospheric disturbances due to tsunamis used the ideas proposed by Peltier & Hines (1976) to observe small-scale perturbations in GPS data (Artru, Ducic et al. 2005); these first observations would pave the way for scientific applications of GPS sensing of the ionosphere for tsunami diagnostics that may guide future automated detection techniques (Inchin, Snively et al. 2020).

Of particular interest is the mesosphere-low-thermosphere (MLT) region: there are large temperature and wind gradients and they strongly modulate (by refraction, reflection, dissipation, etc.) and generates secondary GWs (Zhou, Holton et al. 2002, Vadas, Fritts et al. 2003, Chun and Kim 2008, Vadas and Becker 2018); this has

important climatological implications. It is also in this region that the Earth's airglow layers' responses to GWs allow for comprehensive optical imaging and subsequent analyses. These dynamic phenomena in the airglow layers are routinely imaged from ground-based and moving platforms such as imagers on aircrafts, including multi-camera configurations, and satellites for nadir (downward) and sub-limb views (Russell III, Mlynczak et al. 1994, Pautet and Moreels 2002, Sakanoi, Akiya et al. 2011, Fritts, Smith et al. 2016); see **Figure 1.5** for a sketch.
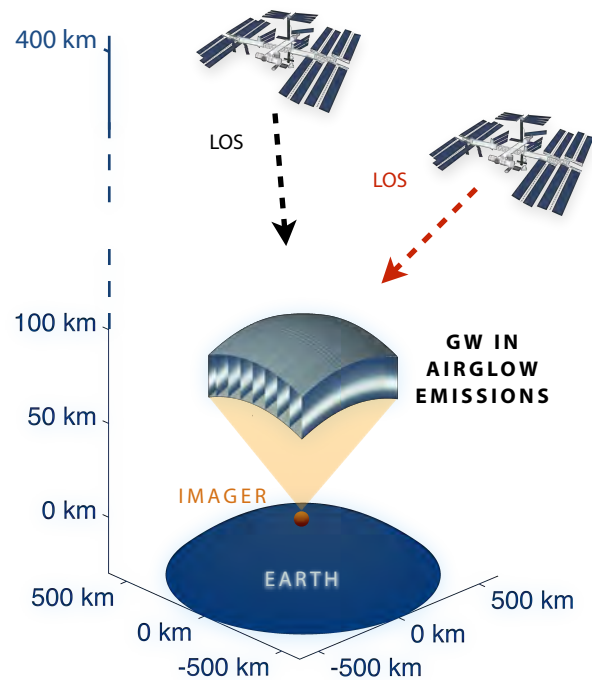
Figure 1.5. Imagers onboard moving platforms may capture different LOS across the airglow layer (viewing wave features from different angles as they pass) that can be chosen to better image features that are sensitive to LOS effects.

Typically, it is the GWs that are observed and studied via the airglow layers, while the AWs have only been predicted to be detectable by OH airglow imagers (Snively 2013, Inchin, Heale et al. 2020). This is due to the AWs characteristic small amplitudes and transient nature, which are on the threshold of current imagers'

sensitivities; they have, however, been identified in sensitive spectrometer data (Pilger, Schmidt et al. 2013). AWs are of particular interest since, while weak at the mesopause region, they can attain large amplitudes in the F region of the atmosphere (150 km and above) where they are observed in the form of traveling ionospheric disturbances (TIDs) (Garcia and Pécseli 2013) and have localized impacts on the thermosphere and ionosphere (Zettergren and Snively 2015 and references therein, Yu and Hickey 2017 and references therein). Similarly, detection and quantification of fast GWs, with phase speeds over 100 m/s, are also of interest as they may readily propagate to the thermosphere and impart significant local body forcing (Vadas and Fritts 2004). Traditional imaging of GWs primarily use the near-zenith (or central) imaging elements of the sensor (i.e., CCD pixels), which correspond to narrow fields-of-view (FOV), where the imaged resolution is highest and LOS enhancement/cancellation effects are minimal; see **Figure 1.7** for a reference on how resolution changes at larger FOV angles.
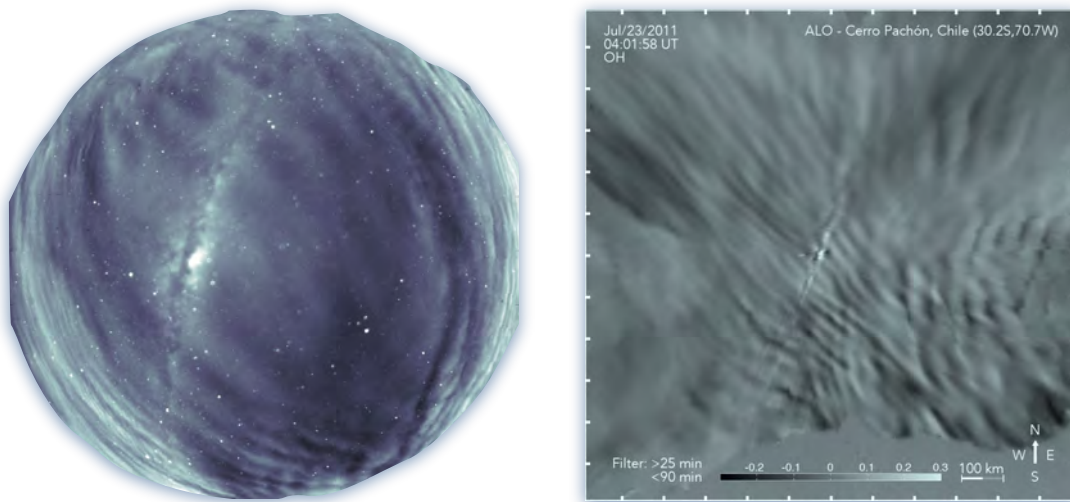
Figure 1.6. Real imager data. The image on the left shows the original OH layer as seen by a real 512×512 imager. On the right, we can see the unwarped-flattened image. A temporal moving average filtering technique is used, which is a process that requires many images at previous/subsequent times; it highlights the time invariant features imaged throughout the night. If the extra temporal data is not available, flat-fielding techniques must be employed.
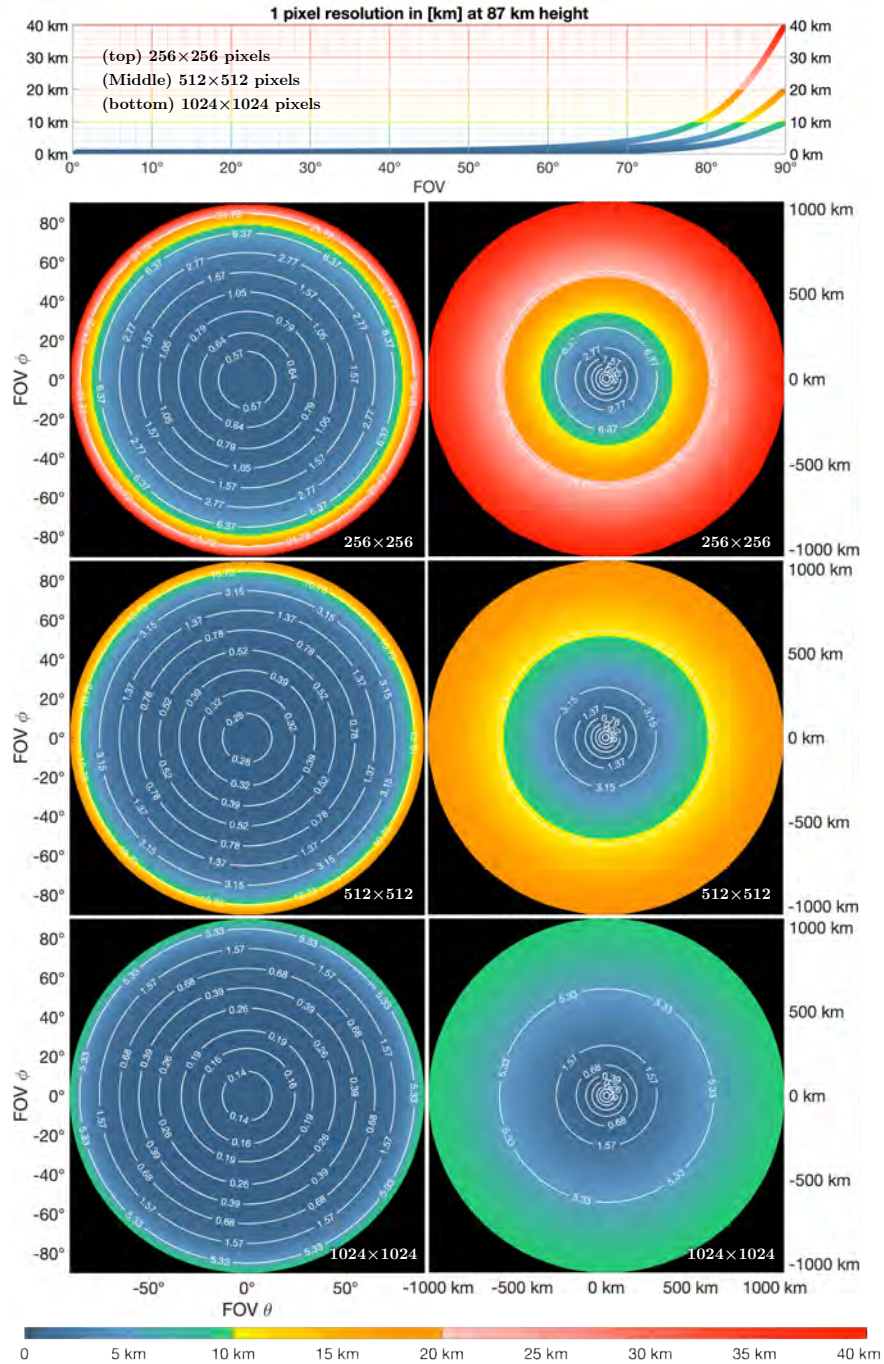
Figure 1.7. Resolution contours of FOV zenith of 3 idealized all-sky imagers at airglow's height of 87 km with fixed color scale. (left) Original imager's coordinates. (right) Unwarped image at airglow height. Each line represents an increment of 10° in FOV, innermost is at 5°. Resolution decreases towards larger FOV angles. Wave features at scales less than the available resolution cannot be resolved (less than twice the available resolution or Nyquist frequency for spectral analyses).

Zenith imaging provides a high resolution image of the flattened[1] volumetric wave structure with increased accuracy for the spectral analysis of the horizontal structure of the wave relative to oblique viewing. There is, however, potential for analyzing the integration through wider FOVs. Airborne and spaceborne imagers have the possibility of traversing over sources and also have the ability to measure at oblique angles (i.e., limb scans). Since faint acoustic waves signatures can become brighter through LOS enhancements when observed obliquely, the capability to image at large FOV angles may improve the chance of detecting them (especially when directly above sources, i.e., Snively (2013)). Recent imaging systems have sufficient spatial and temporal resolution and sensitivity to detect both AWs and fast GWs with short periods (i.e., Pautet, Taylor et al. 2014) and, as mentioned, their observability might depend on LOS enhancements from oblique-viewing. Therefore wide-field and off-zenith imaging may be useful for the study of certain wave phenomena. Successful wide-field imaging depends on the proper characterization of the LOS enhancements so that it may be possible to obtain better estimates for highly slanted GWs such as ground-air coupled surface Rayleigh waves with horizontal slant (Donn and Posmentier 1964) or those observed in the red airglow and TIDs at higher altitudes with large and diminishing vertical wavelengths (Shiokawa 2003, Heale, Snively et al. 2014).

1.2 Off-zenith imaging

Airglow observations made at steep viewing angles lead to scale filtering and intensity enhancement effects. The integration of the emission rates represents loss of information regarding the structure of the airglow layer as it effectively "flattens" it. The

---

[1] This *flattening* is essentially the 2D horizontal structure of the wave since the airglow layer is vertically thin. See Section 2.8 for an expanded discussion.

use of simulated airglow structures enables direct comparisons to the structures present within the emitting layers. **Figures 1.8 & 1.9** show an idealized simulation based on Snively (2013) of a nonlinear wave that has been replicated horizontally to better demonstrate the line-of-sight effects. These have important implications for data interpretation and can effectively blur waves out, reducing their detectability and accurate spectral analyses.
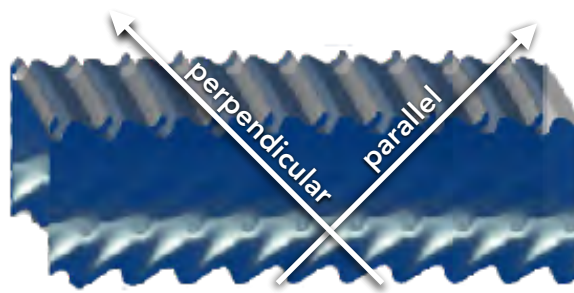
Figure 1.8. A simulated 3D gravity wave packet of OH(3,1) VER, extending infinitely along the airglow layer. The parallel and perpendicular lines-of-sight are shown.

Figure 1.9. Zenith and off-zenith synthetic CCD images. (top) oblique view of the imager where LOS is parallel to the wavefronts and creates intensity enhancements. (middle) Zenith imaging contains little to no LOS effects. (bottom) oblique view of the imager where LOS is perpendicular to the wavefronts with significant filtering of the horizontal wavelength.

1.3 Current Aeronomy Instrumentation

Present research data products from atmospheric optical remote sensing systems include those from (passive) ground-based imagers, photometers, spectrometers and (active) LIDARs (among others) as well as equivalent instruments from space-based platforms. These instruments are commonly used for upper-atmospheric (MLT and ionospheric) measurements of dynamics considered here, significant optical data products exist for lower regions of the atmosphere that may be used synergistically. Particularly, ground-based airglow imagers are found in many research facilities where there is an interest in the local atmospheric dynamics such as mountainous regions or other gravity wave hotspots. Given their relative portability they can be relocated or even be used on airborne missions gaining unique observation geometries and less anthropogenic backscatter interference (Swenson, Taylor et al. 1995, Fritts, Smith et al. 2016). While these kinds of imagers measure brightness from certain wavelengths, it is also possible to combine distinct band or line measurements to obtain rotational temperature from such emissions, as is done by the Advance Mesospheric Temperature Mapper (AMTM) (Pautet, Taylor et al. 2014); see **Figure 1.10**. Temperature measurements are more useful since it factors directly into most of the atmospheric dynamics and their parametrization.

There is also increasing interest in the broad coverage and overlap of imager data. Thus networks such as the Midlatitude Allsky-imaging Network for GeoSpace Observations (MANGO) are beneficial to characterize medium and large-scale wave processes in the upper atmosphere. MANGO consists of a network of nine all-sky imagers spread across the United States (some still to be deployed) imaging the atomic oxygen 630.3 nm airglow; they are able to capture some auroral features and TIDs (Kendall and Bhatt 2017); see **Figure 1.11**.
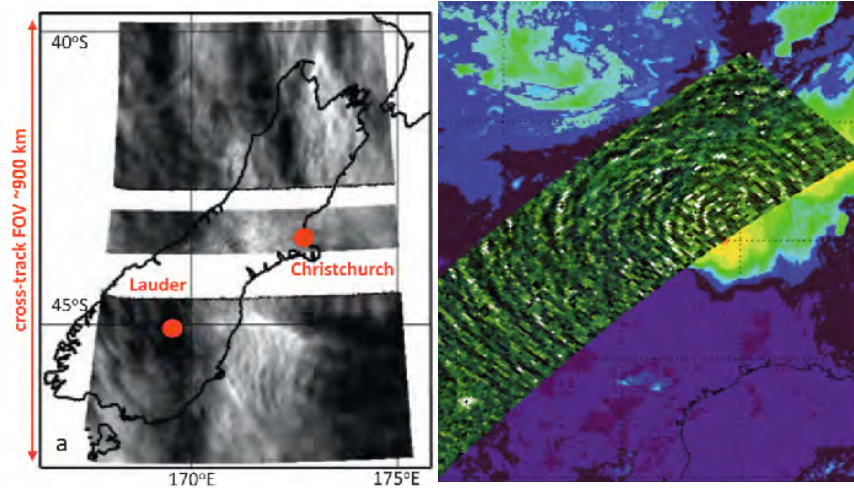
Figure 1.10. (left) OH airglow intensity from AMTM and wing cameras onboard a research aircraft over New Zealand during the DEEPWAVE campaign displaying prominent orographic-generated gravity waves. Taken from [Fritts et al., 2016]. (right) VISI observations of the O_2 762 nm airglow over Oklahoma at a mean layer height of 95 km. Infrared cloud temperature from AIRS is presented to show the location of a super cell that would eventually become a tornado. Taken from [Akiya et al., 2014].
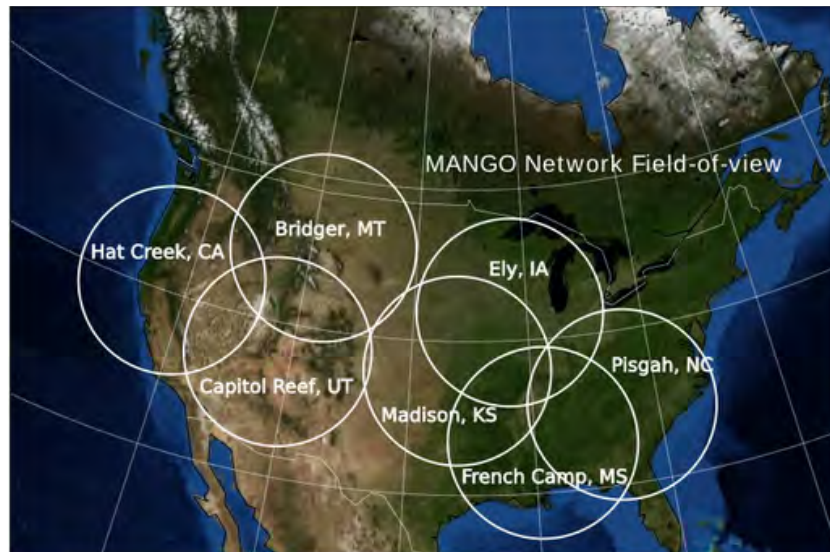
Figure 1.11. MANGO Network coverage of 630 nm airglow imagers over the continental US. The circle represents the extent of the FOV at the mean peak layer height of the 630 nm airglow, around ~230 km. Credit: [MANGOs website at: https://mangonetwork.org].

In addition to being captured by extended ground-based networks, the larger-scale wave phenomena are also covered by imagers on satellites that scan cross-track and are able to image spatially-extended features during their flyovers. One of those instruments is the Visible and near-Infrared Spectral Imager (VISI) onboard the ISS that scans the atomic oxygen emissions at 630 nm, OH at 650 nm and the O_2 at 762 nm (Sakanoi, Akiya et al. 2011); the airglow's mean peak height associated with these emissions are 230 km, 87 km and 95 km, respectively, and the synchronous measurements provide some vertical information of upward-propagating phenomena. Other instruments such as the Atmospheric InfraRed Sounder (AIRS) on the NASA's EOS-Aqua satellite image different wavelengths such IR and CO_2 radiance to provide information about cloud coverage, anthropogenic light and even tropospheric-generated gravity waves (Aumann, Chahine et al. 2003) (see **Figure 1.12**); AIRS has been in operation since 2002 and its mission ends in 2022. While both VISI and AIRS are nadir-facing instruments, limb and sub-limb imaging is also typically performed.
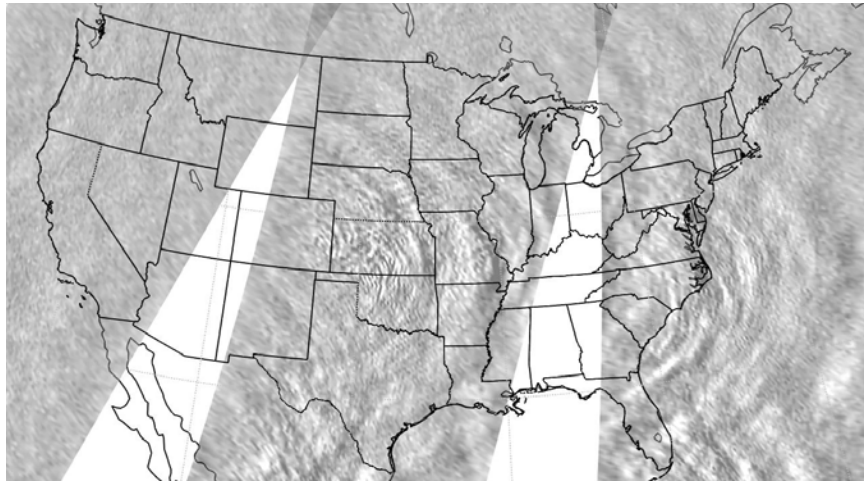
Figure 1.12. AIRS 4.3 µm derived brightness weighted temperature or CO2 radiance with mean peak height of ~37 km for several orbital tracks above the continental US. A super cell convective storm generates gravity waves with large horizontal wavelengths modulated by the westerly winds. Source: [Heale et al., 2019].

The Sounding of the Atmosphere using Broadband Emission Radiometry (SABER) instrument onboard NASA's TIMED satellite provides vertical profiles of volume emission rates for O_2 (1 µm emission line peaking at ~95 km) and two OH bands (1.6 µm and 2.0 µm emission lines peaking at ~87 km) (Russell III, Mlynczak et al. 1994); SABER started operations in 2002 and is still ongoing. Another limb-scanning instrument is the High Resolution Dynamics Limb Sounder onboard NASA's Aura satellite (Gille, Barnett et al. 2003) that uses infrared radiometry to measure radiances with 1 km vertical resolution.

Another method for obtaining vertical profiles and characterize GWs is using GPS occultation to obtain total-electron-content (TEC) profiles. This technique requires a receiver station and satellite to measure the phase delay of the radio waves. There are several positioning and navigation satellite networks in use such as the Global Navigation Satellite System (GNSS) which includes USA's NAVSTAR Global Positioning System (GPS), the GLObal NAvigation Satellite System (GLONASS), ground-based GPS networks as well as satellite radio occultation receivers such as the Constellation Observing System for Meteorology, Ionosphere and Climate (COSMIC/ COSMIC-2) and the Spire commercial satellite constellation. **Figure 1.13** shows a great example of GPS measurements after a tornado for GWs and AWs studies where both GWs and AWs can be clearly seen in the data; from these spatial and temporal plots we can obtain drifts, periods, wavelengths and relative amplitudes[2]. Such observations help us understand the impact of convective sources as the resulting waves propagate up to the thermosphere.

---

[2] It is worth noting that wind data is usually necessary to obtain the intrinsic wave parameters given that strong winds can filter the GWs as it is the most likely case in Figure #10 with the southward GWs disappearing from the data.
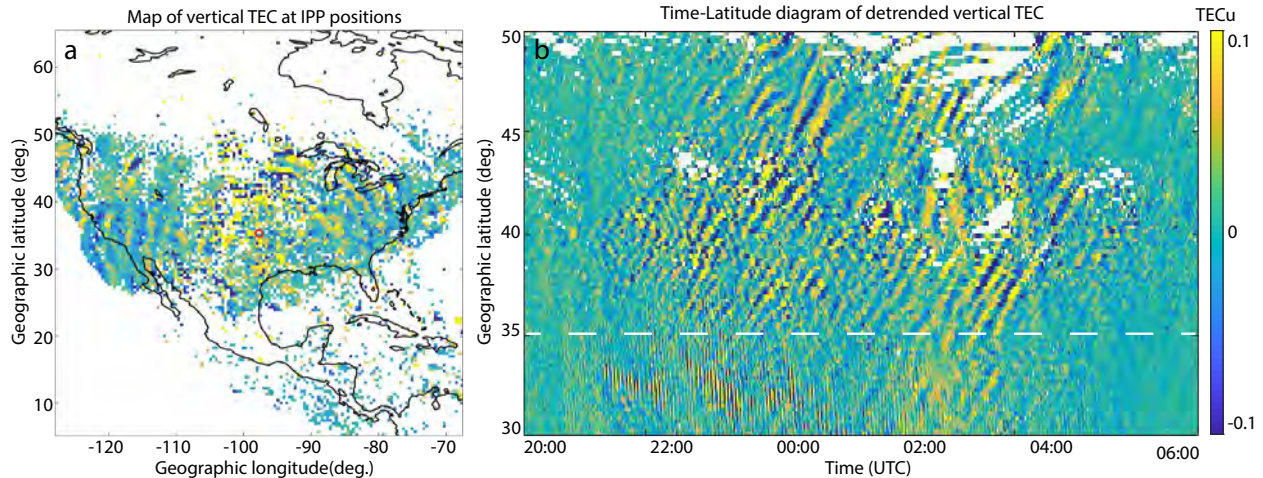
Figure 1.13. GPS measurements of vertical total-electron-content (vTEC) at IPP positions (average height of ~450 km) show both GWs and AWs due to a tornado in Moore, OK. (left) Spatial distribution shows the concentric GWs where the southward wavefronts are filtered most likely due to strong winds. (right) The temporal evolution across a fixed longitude at the location of Moore clearly shows the shorter period AWs with a southward motion following the plasma drift along the magnetic lines. *Source: [Inchin, 2020].*

Two recently-launched remote sensing missions have started to provide high resolution datasets, including imaging, in the ionosphere: *GOLD* and *ICON*. The Ionospheric Connection Explorer, *ICON*, is a NASA and UC Berkeley mission that targets different airglow layers with three different instruments, providing limb, sub-limb and in-situ measurements. For example, The Michelson Interferometer for Global High-resolution Thermospheric Imaging (MIGHTI) instrument observes vertical winds at 5 km resolution (90-170 km) or 30 km resolution (170-300 km) and temperature at 5 km vertical resolution (90-105 km) (Englert, Harlander et al. 2017). The far-ultraviolet (FUV) looks at the 135.6 nm and 157.0 nm atomic oxygen emission during the night while the 135.6 nm at night (Mende, Frey et al. 2017) while the extreme-ultraviolet (EUV) observes the 61.6 nm and 83.4 nm atomic oxygen emissions (Sirk, Korpela et al. 2017). The NASA Global-scale Observations of Limb and Disk (*GOLD*) onboard the

communications satellite SES-14 is designed to work in tandem with *ICON's* FUV instrument since the observed wavelengths overlap (Eastes, McClintock et al. 2017). *GOLD* measures the entire Earth's disk from a geostationary orbit (~35,000 km altitude) while *ICON* will orbit through the thermosphere (~500 km altitude) .

The Atmospheric Waves Experiment (*AWE*) is a pending mission that will situate an instrument on the International Space Station focusing on the MLT-region. It includes a 4-channel infrared imager based on the USU Advance Mesospheric Temperature Mapper (AMTM) that measures the rotational temperature and intensity from the OH(3,1) emission band that has a peak at ~87 km. Being on the ISS places AWE at advantageous position to characterize GWs across a global scale to provide comprehensive insight into the GW spectra, sources, propagation conditions and energy fluxes into upper layers of the atmosphere. It is scheduled to launch in Summer 2023 (Taylor, Eckermann et al. 2018, Taylor, Forbes et al. 2019).

These missions inform the objectives that we hope to achieve with the present research. Our modeling work aims to work with our current observational capabilities, whether we use simulations to explain certain aspects of the data or to understand how and where we should be pointing our instruments in future experiments. Additionally, the conceptualization of new missions always requires modeling capabilities to lay out the expectations for the data products and also develop the necessary tools to analyze such data. Thus, synthetic data from numerical models can play a key role in guiding new observational and data analysis strategies.¶

Chapter 2

Methods: airglow-imager geometry, line-of-sight-ellipsoid intersection and synthetic imagers

The airglow layer and Earth comprise a system that can be geometrically described in different ways. Whether we want to map the airglow layer on a surface, describe it volumetrically or project it according to an instrument's arbitrary point of view, the airglow layer is usually referenced relative to the Earth. The airglow layers can span depths with full-width half maximums (FWHMs) as little as several kilometers to dozens of kilometers and have emission distributions that peak around their *mean airglow layer height*; some of the first airglow studies were in fact trying to determine these heights with the available instrumentation of their time (Roach and Meinel 1955). We now have a good understanding of the density and emission distributions, peak height and variability of the layer, thanks both to modern measurements and simulation studies. However most of our instruments measure the airglow layer as a flat image that results from integrating the emissions through the instruments' lines-of-sight. This combined with the fact that relative depths of the emissions in the layer are small allows us to describe the airglow layer as thin spherical shell at the mean peak height and largely preserve horizontal features. Additionally, the thin-shell representation makes for a simplified geometric description of the airglow layer in reference to the Earth and is commonly used for airglow imaging analyses (Taylor and Hapgood 1982, Coble, Papen et al. 1998). This doesn't mean that this geometry is unable to characterize volumetric representations of the layer given we can consider the thick layer to be represented by a

collection of infinitesimal increments of thin-shells. In fact, for the purpose of simulating integrations along the layer we will do precisely this, where the line-of-sight that cuts through the layer will be divided into differential elements, each intersecting with a thin-shell at the corresponding infinitesimal height increment.

In this chapter we will introduce simple geometric relations that relate a thin-shell representation of the airglow layer to an observer, first on the surface of the Earth, then at any given height and then finally describe an alternative method to map a free-viewing observer. We will next introduce the concept of *imaging sensors* and expand upon the coordinate systems and transformations described previously to obtain mappings to imaging units on a *sensor panel*. Finally, we will describe how to incorporate all of these mappings to create *synthetic images*. Several tables will be included to summarize the formulations for each pair of *forward* and *inverse transformation* as well as a full step-by-step chart for using some of these transformations.

2.1. The airglow-Earth geometry

The most basic description of the airglow layer referenced to the Earth is the airglow-Earth geometry. This is simply the spherical coordinate system where a Cartesian (x, y, z) and a spherical (radius, polar angle, azimuth angle) $(\rho, \theta\, \phi)$ coordinate systems share their origin at the center of the Earth. When the z axis is aligned with the North Pole and the x axes with the prime meridian, then the Cartesian system is also known as the Earth-centered-Earth-fixed or *ECEF coordinates*. Conversely when the azimuth angle is zero at the prime meridian, then the spherical coordinate system can be recast as the *geocentric coordinates* (ϕ', λ, R). When we use an elevation angle that is zero at the equator for geocentric latitude: $\phi' = 90° - \theta$, azimuth becomes longitude

$\lambda = \phi$ and the radius becomes the geocentric distance $R = \rho$. For simplicity we will use the spherical coordinate system for this description. The airglow layer is represented by a spherical thin shell at a height h_0 from the surface of the Earth; the surface is at the radius R_E also called geocentric radius. The arc length of the zenith (polar) angle θ is $\widehat{A}$, whose projections on the x and y planes (also the ϕ plane) are $\widehat{x}$ and $\widehat{y}$ respectively so that $\widehat{A} = \sqrt{\widehat{x}^2 + \widehat{y}^2} = \rho\theta$. A point P on the airglow may then be described by the set of airglow coordinates $P(\widehat{x}, \widehat{y}, h_0)$, the Cartesian coordinates $P(x, y, z)$ or the spherical coordinates $P(\rho, \theta, \phi)$; note that $\rho = R_E + h_0 = \sqrt{x^2 + y^2 + z^2}$. The mapping or transformation equations are done from either of the other two coordinates systems representing the point P to/from the spherical coordinate system. Thus the specific transformations are $P(x, y, z) \longleftrightarrow P(\rho, \theta, \phi)$ and $P(\widehat{x}, \widehat{y}, h_0) \longleftrightarrow P(\rho, \theta, \phi)$; we call left-to-right the f*orward mapping* and right-to-left the *inverse mapping*. It follows that the appropriate mapping equations are the standard spherical coordinate transformations; see **Table 2.1** for reference.

Spherical-coordinate transformation: $P(x,y,z)\longleftrightarrow P(\rho,\theta,\phi)$	
forward mapping given x, y, z	*inverse mapping to x, y, z*
$\rho = \sqrt{x^2 + y^2 + z^2}$ $\theta = \cos^{-1}(z/\rho)$ $\phi = \operatorname{atan2}(y,x)$	$x = \rho\sin\theta\cos\phi$ $y = \rho\sin\theta\sin\phi$ $z = \rho\cos\theta$
Spherical-coordinate transformation: $P(\widehat{x},\widehat{y},z_0)\longleftrightarrow P(\rho,\theta,\phi)$	
forward mapping given $\widehat{x}$, $\widehat{y}$, z_0	*inverse mapping to $\widehat{x}$, $\widehat{y}$, z_0*
$\widehat{A} = \sqrt{\widehat{x}^2 + \widehat{y}^2}$ $\rho = R_E + z_0$ $\theta = \widehat{A}/\rho$ $\phi = \operatorname{atan2}(\widehat{y},\widehat{x})$	$\widehat{A} = \rho\theta$ $x = \overline{A}\cos\phi$ $\widehat{y} = \overline{A}\sin\phi$ $z_0 = \rho - R_E$
Domains and units	
$\rho \in [R_E, \infty)\,\text{km}$ $\quad x,y,z \in [R_E, \infty)\,\text{km}$ $\theta \in [0,\pi]\,\text{rad}$ $\qquad z_0 \in [0,\infty)\,\text{km}$ $\phi \in [0,2\pi]\,\text{rad}$ $\quad \widehat{A},\widehat{x},\widehat{y} \in [0,2\pi(R_E + z_0)]\,\text{km}$	

Table 2.1. The airglow-Earth geometry. Note $z_0 = h_0$.

2.2. The airglow-observer geometry

This geometry shares some nomenclature with the spherical system described above; however, the transformations differ and should not be confused. The (x, y, z) Cartesian system is set with its origin at the position of the observer, $I(O)$, on the surface of the Earth. The airglow is a spherical thin shell at a height h_0 from the surface of the Earth; the surface is at radius R_E. The point P is located within the airglow layer at the Cartesian coordinates $P(x, y, z)$ and can be alternatively be described by either of the following coordinate-pairs: $P(\widehat{A}, h_0)$, $P(\zeta, h_0)$, $P(\zeta, \rho)$ or the coordinate-triplets: $P(\widehat{x}, \widehat{y}, h_0)$, $P(\theta, \phi, h_0)$, $P(\theta, \phi, \rho)$. Refer to **Table 2.2** at the end of this section for a sketch of this geometry. $\widehat{A}$, $\widehat{x}$, $\widehat{y}$ are arc quantities where $A = \sqrt{x^2 + y^2}$ is the projection of $\widehat{A}$ on the $x - y$-plane or ϕ-plane and are related to the Earth-centered spherical polar angle α so that $\widehat{A} = (R_E + h_0)\alpha$; ζ, θ, ϕ are the observer's zenith (polar) angles and are defined in the domains $\zeta \in [0, \pi]$ and $\theta, \phi \in [-\pi, \pi]$; ρ is the distance from $I(O)$ to P (the line-of-sight distance) and $\rho \in [0, \infty)$. The angles θ and ϕ are projections of the zenith angle ζ that represent zenith angles in the z-x and z-y planes respectively; each can form their own 2D airglow-observer coordinate system if, for example, ζ lies on the z-x plane then $\theta = \zeta$ and $\phi = 0$, and vice versa for the z-y plane. Note that this ϕ is not an azimuth angle as in the spherical system. These angles are independently determined and correlate to unique fields-of-view, FOV_θ and FOV_ϕ, which are parameters that determine resolution and maximum angles in an imaging sensor and will be important in following sections. The mapping equations are first determined in 2D for the zenith angle ζ and then expanded to 3D by means of their projections.

Now let us obtain the airglow-observer transformations by using the spherical angle α to state both the law of cosines or the law of sines to obtain:

$$\rho^2 = 2R_E \left(R_E + h_0 \right) \left(1 - \cos \alpha \right) + h_0^2 \tag{2.1}$$

$$\sin \alpha = \frac{\rho}{R_E + h_0} \sin \zeta \tag{2.2}$$

By solving first for α and then obtaining the roots we obtain an expression for the magnitude of the line-of-sight or the zenith angle:

$$\rho = \sqrt{R_E^2 \cos^2 \zeta + 2R_E h_0 + h_0^2} - R_E \cos \zeta \tag{2.3}$$

$$\zeta = \cos^{-1}\left(\frac{h_0\left(2R_E + h_0\right) - \rho^2}{2R_E\rho}\right) \tag{2.4}$$

An alternative method to find an expression for the layer height is by using the Cartesian coordinates that have origin at the center of the Earth: for added clarity, let x_{cart} and z_{cart} represent the Cartesian coordinates of the point in the airglow $P(x_{cart}, 0, z_{cart})$ that lies on the $y-z$-plane, then $h_0 = \sqrt{x_{cart}^2 + y_{cart}^2} - R_E$ where $x_{cart} = \rho \sin \zeta$ and $z_{cart} = \rho \cos \zeta + R_E$, so we have

$$h_0 = \sqrt{\rho^2 + 2R_E\rho \cos \zeta + R_E^2} - R_E \tag{2.5}$$

We can solve for ρ in this expression for h_0 and get the same result for ρ as above. Note that in both results we have kept the positive solutions since the distance ρ is defined to be always positive. Finally by the definition of the radian we can get the arc length quantity as

$$\widehat{A} = \left(R_E + h_0\right) \alpha \tag{2.6}$$

The angle α can be calculated from (2.1) or (2.2) as

$$\alpha = \cos^{-1}\left(1 + \frac{h_0^2 - \rho^2}{2R_E\left(R_E + h_0\right)}\right), \text{ or} \tag{2.7a}$$
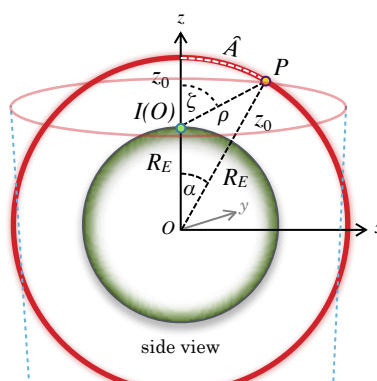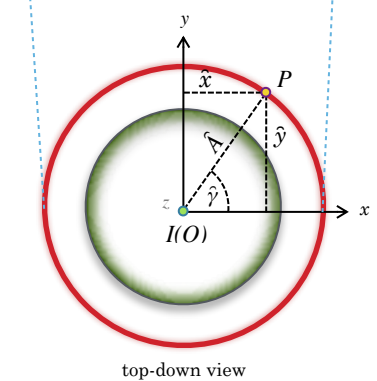
$$\alpha = \sin^{-1}\left(\frac{\rho \sin \zeta}{R_E + h_0}\right) \tag{2.7b}$$

The 3D coordinate mapping links the x and y horizontal dimensions by means of their pythagorean magnitudes: $A = \sqrt{x^2 + y^2}$ and $\zeta = \sqrt{\theta^2 + \phi^2}$. Please note that in this description the zenith angle represent linear distances, in a similar manner to A, but are specified in terms of angles. This is why we can use the pythagorean theorem to recover the azimuth angle between these two specifications. These relations represent two right triangles, one for the arc quantities and one for the zenith angles, where $\gamma = \angle Ax$ and $\gamma' = \angle\zeta\theta$. The important realization is that $\gamma = \gamma'$ so that we can write arc quantities in terms of the zenith angles and vice versa:

$$\begin{aligned} x &= A \cos\gamma = A\theta/\zeta \\ y &= A \sin\gamma = A\phi/\zeta \end{aligned} \tag{2.8}$$

$$\begin{aligned} \theta &= \zeta \cos\gamma' = \zeta x/A \\ \phi &= \zeta \sin\gamma' = \zeta y/A \end{aligned} \tag{2.9}$$

Notice that the cosine and sine quantities will give the necessary sign of either x, y or θ, ϕ, so that $\theta, \phi \in [-\pi, \pi]$ (note that ζ and A will always be positive quantities). The arc quantities can be bound by the assumption that our observer cannot look at zenith angles beyond 90° (over the horizon) so $A, x, y \in [-\pi\left(R_E + h_0\right), \pi\left(R_E + h_0\right)]$.

3D airglow-imager coordinates	**Airglow-imager 3D coordinate transformation:** $$P(\widehat{x},\widehat{y},z_0)\longleftrightarrow P(\theta,\phi,z_0)$$	
 side view	if the system is in $(\widehat{x},\widehat{y},z_0)$ then use: *forward mapping* with inputs: $(\vartheta, \varphi, z_0)$	if the system is in $(\vartheta, \varphi, z_0)$ then use: *inverse mapping* with inputs: $(\widehat{x}, \widehat{y}, z_0)$
	$$\zeta = \sqrt{\theta^2 + \phi^2}$$ $$\rho = \sqrt{R_E^2 \cos^2\zeta + z_0^2 + 2R_E z_0} - R_E\cos\zeta$$ $$\alpha = \cos^{-1}\left(1 + \frac{z_0^2 - \rho^2}{2R_E(R_E + z_0)}\right)^{\dagger}$$ $$\widehat{A} = (R_E + z_0)\alpha$$ $$\widehat{x} = \widehat{A}\theta/\zeta$$ $$\widehat{y} = \widehat{A}\phi/\zeta$$	$$\widehat{A} = \sqrt{\widehat{x}^2 + \widehat{y}^2}$$ $$\alpha = \widehat{A}/(R_E + z_0)$$ $$\rho = \sqrt{2R_E(R_E + z_0)(1 - \cos\alpha) + z_0^2}$$ $$\zeta = \cos^{-1}\left(\frac{z_0(2R_E + z_0) - \rho^2}{2R_E\rho}\right)$$ $$\theta = \zeta\widehat{x}/\widehat{A}$$ $$\phi = \zeta\widehat{y}/\widehat{A}$$
 top-down view	**Airglow-imager 3D coordinate transformation:** $$P(\widehat{x},\widehat{y},z_0)\longleftrightarrow P(\theta,\phi,\rho)$$	
	if the system is in $(\widehat{x},\widehat{y},z_0)$ then use: *forward mapping* with inputs: $(\vartheta, \varphi, \varrho)$	if the system is in $(\vartheta, \varphi, \varrho)$ then use: *inverse mapping* with inputs: $(\widehat{x}, \widehat{y}, z_0)$
	$$\zeta = \sqrt{\theta^2 + \phi^2}$$ $$z_0 = \sqrt{\rho^2 + 2R_E\rho\cos\zeta + R_E^2} - R_E$$ $$\alpha = \cos^{-1}\left(1 + \frac{z_0^2 - \rho^2}{2R_E(R_E + z_0)}\right)^{\dagger}$$ $$\widehat{A} = (R_E + z_0)\alpha$$ $$\widehat{x} = \widehat{A}\theta/\zeta$$ $$\widehat{y} = \widehat{A}\phi/\zeta$$	$$\widehat{A} = \sqrt{\widehat{x}^2 + \widehat{y}^2}$$ $$\alpha = \widehat{A}/(R_E + z_0)$$ $$\rho = \sqrt{2R_E(R_E + z_0)(1 - \cos\alpha) + z_0^2}$$ $$\zeta = \cos^{-1}\left(\frac{z_0(2R_E + z_0) - \rho^2}{2R_E\rho}\right)$$ $$\theta = \zeta\widehat{x}/\widehat{A}$$ $$\phi = \zeta\widehat{y}/\widehat{A}$$
$\dagger$Alternatively use law of sines: $\alpha = \mathrm{sgn}(\zeta)\sin^{-1}(\rho\sin\zeta/(R_E + z_0))$ $\ddagger$Note that an airglow imager can't observe angles larger than $\pm\ \pi/2$.	**Domains and units**	
	$\rho \in [R_E, \infty)\,\mathrm{km}$ $\qquad z_0 \in [0,\infty)\,\mathrm{km}$ $\zeta, \alpha \in [0, \pi]\,\mathrm{rad}^{\ddagger}$ $\qquad \widehat{A}, \widehat{x}, \widehat{y} \in [-\pi(R_E + z_0), \pi(R_E + z_0)]\,\mathrm{km}$ $\theta, \phi \in [-\pi, \pi]\,\mathrm{rad}^{\ddagger}$	

Table 2.2. Airglow-imager geometry sketch and transformations. Note $z_0 = h_0$.

If one considers the problem of finding the geometric relations for an observer that's not on the surface of the Earth, such as an airplane or a satellite, similar relations as those described above can be found. If the observer is at a height h_s above the surface of the Earth then the law of cosines of **Equation 2.1** becomes:

$$\rho^2 = h_s^2 + \left(R_E + h_0\right)^2 - 2h_s\left(R_E + h_0\right)\cos\alpha \tag{2.10}$$

and

$$\alpha = \cos^{-1}\left(\frac{h_s^2 - \rho^2 + \left(R_E + h_0\right)^2}{2h_s\left(R_E + h_0\right)}\right) \tag{2.11}$$

Furthermore, by following a similar reasoning as above we find the remaining equations:

$$h_0 = \sqrt{\rho^2 - 2h_s\rho\cos\zeta + h_s^2} - R_E \tag{2.12}$$

$$\zeta = \cos^{-1}\left(\frac{\rho^2 + h_s^2 - \left(R_E + h_0\right)^2}{2h_s\rho}\right) \tag{2.13}$$

$$\rho = \sqrt{\left(h + R_E\right)^2 - h_s^2\sin^2\zeta} + h_s\cos\zeta \tag{2.14}$$

This expression for ρ reduces to **Equation 2.3** when $h_s \longrightarrow R_E$. This is a more general airglow-observer transformation, suited for an observer at a certain height above the surface of the Earth but whose zenith is still straight up; see **Table 2.3** for reference. If we want to align such zenith to an arbitrary angle, or furthermore, specify the *viewing direction* by specifying an elevation and azimuth angle, as is often the case in satellite communications, then this geometry fails to do so and the required mappings will invariably require more complex vector transformations.

3D airglow-imager coordinates	**Airglow-imager 3D coordinate transformation:** $$P(\widehat{x},\widehat{y},z_0)\longleftrightarrow P(\theta,\phi,z_0)$$	
side view	if the system is in $(\widehat{x},\,\widehat{y},\,z_0)$ then use: *forward mapping* with inputs: $(\vartheta,\,\varphi,\,z_0)$	if the system is in $(\vartheta,\,\varphi,\,z_0)$ then use: *inverse mapping* with inputs: $(\widehat{x},\,\widehat{y},\,z_0)$
	$$\zeta = \sqrt{\theta^2 + \phi^2}$$ $$\rho = \sqrt{R_E^2\cos^2\zeta + z_0^2 + 2R_E z_0} - R_E\cos\zeta$$ $$\alpha = \cos^{-1}\left(1 + \frac{z_0^2 - \rho^2}{2R_E(R_E+z_0)}\right)^{\dagger}$$ $$\widehat{A} = (R_E + z_0)\alpha$$ $$\widehat{x} = \widehat{A}\theta/\zeta$$ $$\widehat{y} = \widehat{A}\phi/\zeta$$	$$\widehat{A} = \sqrt{\widehat{x}^2 + \widehat{y}^2}$$ $$\alpha = \widehat{A}/(R_E + z_0)$$ $$\rho = \sqrt{2R_E(R_E+z_0)(1-\cos\alpha) + z_0^2}$$ $$\zeta = \cos^{-1}\left(\frac{z_0(2R_E+z_0)-\rho^2}{2R_E\rho}\right)$$ $$\theta = \zeta\widehat{x}/\widehat{A}$$ $$\phi = \zeta\widehat{y}/\widehat{A}$$
top-down view	**Airglow-imager 3D coordinate transformation:** $$P(\widehat{x},\widehat{y},z_0)\longleftrightarrow P(\theta,\phi,\rho)$$	
	if the system is in $(\widehat{x},\,\widehat{y},\,z_0)$ then use: *forward mapping* with inputs: $(\vartheta,\,\varphi,\,\varrho)$	if the system is in $(\vartheta,\,\varphi,\,\varrho)$ then use: *inverse mapping* with inputs: $(\widehat{x},\,\widehat{y},\,z_0)$
	$$\zeta = \sqrt{\theta^2 + \phi^2}$$ $$z_0 = \sqrt{\rho^2 + 2R_E\rho\cos\zeta + R_E^2} - R_E$$ $$\alpha = \cos^{-1}\left(1 + \frac{z_0^2 - \rho^2}{2R_E(R_E+z_0)}\right)^{\dagger}$$ $$\widehat{A} = (R_E + z_0)\alpha$$ $$\widehat{x} = \widehat{A}\theta/\zeta$$ $$\widehat{y} = \widehat{A}\phi/\zeta$$	$$\widehat{A} = \sqrt{\widehat{x}^2 + \widehat{y}^2}$$ $$\alpha = \widehat{A}/(R_E + z_0)$$ $$\rho = \sqrt{2R_E(R_E+z_0)(1-\cos\alpha) + z_0^2}$$ $$\zeta = \cos^{-1}\left(\frac{z_0(2R_E+z_0)-\rho^2}{2R_E\rho}\right)$$ $$\theta = \zeta\widehat{x}/\widehat{A}$$ $$\phi = \zeta\widehat{y}/\widehat{A}$$
†Alternatively use law of sines: $$\alpha = \mathrm{sgn}(\zeta)\sin^{-1}(\rho\sin\zeta/(R_E+z_0))$$ ‡Note that an airglow imager can't observe angles larger than $\pm\,\pi/2$.	**Domains and units** $\rho \in [R_E,\infty)\,\mathrm{km}$ $\qquad z_0 \in [0,\infty)\,\mathrm{km}$ $\zeta,\alpha \in [0,\pi]\,\mathrm{rad}^{\ddagger}$ $\theta,\phi \in [-\pi,\pi]\,\mathrm{rad}^{\ddagger}$ $\qquad \widehat{A},\widehat{x},\widehat{y} \in [-\pi(R_E+z_0),\pi(R_E+z_0)]\,\mathrm{km}$	

Table 2.2. General airglow-observer coordinates. This geometry also accounts for the observer height h_s, which can be beneath or above the airglow layer. Note $z_0 = h_0$.

2.3. Limitations of the geometric transformations and the ray-tracing solution

In the last section we mentioned how the airglow-observer geometry can't describe arbitrary points-of-view for an observer at any point in space. The geometry actually works for its 2D configuration, but problems arise when trying to describe the components of the rotated zenith angles in 3D. In other words, we cannot readily use the component approach to separate the dimensions, and instead need to rotate the coordinate system appropriately. Here we will introduce a simplified approach for obtaining a free-viewing observer and, while coordinate rotations will still be necessary when considering a sensor panel later on, for now this approach requires no transformations and thus overcoming the limitations stated above. Additionally, we will find the added benefit of using standard geographic coordinate systems to describe positions and pointing vectors and even represent the Earth as a standard ellipsoid instead of a sphere. These geographic coordinates are in standard use for georeferenced (mapped) data such as geophysical data, areas, positions, satellite tracks, etc., so will also gain the ability to interface naturally with datasets such as the EPSG registry (see **Section 5.2** for more information on this dataset).

Consider now a coordinate system in which we define our geometry as Earth-Centered-Earth-Fixed (ECEF) which in turn is defined as the Cartesian coordinate system where the origin is the center of the Earth, the positive x, y and z axes are towards the Prime Meridian, 90° East and North Pole respectively. The Earth is modeled as an oblate ellipsoid defined by its principal semi-major axis a (equator) and its flattening f, which is a measure of its compression from a sphere into an ellipse; the polar semi-axes b is then obtained from the flattening given its definition $f = (a - b)/a$. The satellite position is denoted by the ECEF Cartesian coordinates x_s, y_s and z_s. The satellite's orientation is defined by the unitary pointing vector whose directions are given in its local tangent plane system namely North-East-Down (NED) or East-North-Up (ENU). These local Cartesian coordinates are relative to the location of the satellite to the surface of an ellipsoid, therefore their origin is determined by their geodetic latitude

ϕ, geodetic longitude λ and ellipsoidal height h; this is the geodetic coordinate system. Alternatively, the satellite's orientation may be given in local azimuth-tilt or azimuth-elevation coordinates where azimuth is the angle on the plane tangent to the ellipsoid and is clockwise from North and tilt/elevation is the angle from the local vertical or from the tangent plane respectively; the local vertical is the line that intersects the satellite's position with the center of the Earth and it can be defined positive when it's radially outward (satellite's zenith) or defined positive when it's radially inward (satellite's nadir). The azimuth-tilt and azimuth-elevation systems are in fact a local spherical coordinate system with unitary spherical radius. The transformation equations we will derive require coordinate mappings between several geographic coordinate systems. The forward mappings we will use are: *geodetic to ECEF*, *ENU/NED to ECEF*, and *local spherical to ENU/NED*. The inverse mappings are *ECEF to geodetic*, *ECEF to ENU/NED*, and *ENU/NED to local spherical*. The particulates such as definitions and equations can be found in **Appendix B**.

Now we will derive the line-of-sight-ellipsoid intersection equations, which are effectively a ray-tracing solution to the free-viewing airglow-observer problem. For a more focused approach the *observer* will be called the *satellite* from now on. We define the line-of-sight as the line segment with magnitude d with origin at the satellite's ECEF position $\vec{s} = x_s\hat{\mathbf{x}} + y_s\hat{\mathbf{y}} + z_s\hat{\mathbf{z}}$ and direction given by its Cartesian pointing vector $\hat{\mathbf{p}} = u\hat{\mathbf{x}} + v\hat{\mathbf{y}} + w\hat{\mathbf{z}}$ where $\|u, v, w\| = 1$; the endpoint of the line is given by $\vec{s} + d\hat{\mathbf{p}}$. The implicit equation of the oblate ellipsoid that represents the Earth and atmospheric layers is $\left(x^2 + y^2\right)a^{-2} + z^2 b^{-2} = 1$. The point where the resulting $\vec{s} + d\hat{\mathbf{p}}$ is at the surface of the ellipsoid is the intersection point and we can substitute its corresponding components in the ellipsoid equation:

$$\frac{\left(x_s + du\right)^2 + \left(y_s + dv\right)^2}{a^2} + \frac{\left(z_s + dw\right)^2}{b^2} = 1 \qquad (2.15)$$

This is a quadratic equation for the unknown scaling parameter d. To cast this into the standard quadratic form $Ad^2 + Bd + C = 0$ we can expand the squares and group factors to obtain:

$$d^2 \left(\frac{u^2 + v^2}{a^2} + \frac{w^2}{b^2} \right) + 2d \left(\frac{x_s u + y_s v}{a^2} + \frac{z_s w}{b^2} \right) + \frac{x_s^2 + y_s^2}{a^2} + \frac{z_s^2}{b^2} - 1 = 0 \quad (2.16)$$

The solution to the quadratic equation is

$$d = \frac{-B \pm \sqrt{B^2 - 4AC}}{2A} = \frac{-B/2 \pm \sqrt{(B/2)^2 - AC}}{A} \quad (2.17)$$

where

$$A = \frac{u^2 + v^2}{a^2} + \frac{w^2}{b^2}, \qquad B/2 = \frac{u x_s + v y_s}{a^2} + \frac{w z_s}{b^2}, \qquad C = \frac{x_s^2 + y_s^2}{a^2} + \frac{z_s^2}{b^2} - 1 \quad (2.18)$$

The discriminant of the quadratic polynomial, $B^2 - 4AC$, determines the type of solution: if the discriminant is positive there are two real solutions which represent 2 intersection points. If the discriminant is negative the solutions are imaginary and there are no intersections. If the discriminant is 0 then the line-of-sight is tangent to the surface of the ellipsoid. Additionally, when the first determinant condition is met, the smaller absolute value solution will be the first intersection. If the satellite is within the ellipsoid (when the geodetic height h_0 is negative) one of the solutions will be positive, that is, aligned with the direction vector, and the other will be opposite. The larger solution is the second intersection and usually means the line-of-sight is going through the Earth and thus should be discarded. However, for limb views both intersections are allowed and careful consideration is required for this case; one possible way to account

for it is to determine allowed elevation angles in the local spherical coordinate system of the satellite; we ignore second intersections in our methods. Refer to **Figure 2.1** for 3D graphs that represent the solution to the line-of-sight-ellipsoid equations.
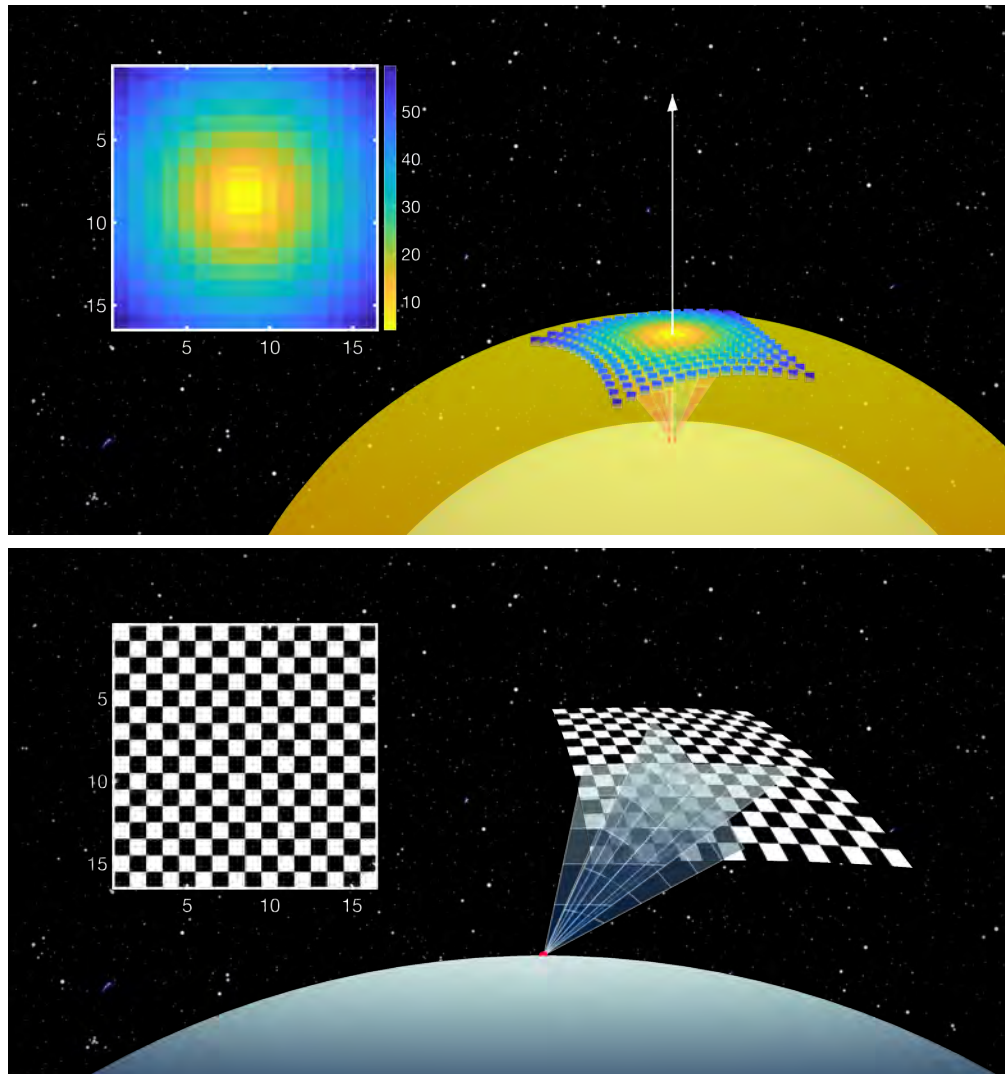
Figure 2.1. Line-of-sight-airglow intersections for imaging elements that are mapped to tilt and azimuth angles. (top) airglow layer in yellow with intersections where the imager is looking straight up; the colors represent tilt angles (zenith is 0°). (bottom) Intersections with imager's zenith aligned at an angle where the imaging elements are represented by a checkerboard pattern.

2.4. Full algorithm for line-of-sight-ellipsoid intersection

The satellite's inputs are its position $\vec{s}$ and its line-of-sight direction determined by local azimuth az and elevation el angles. The oblate ellipsoid's parameters are its semi-major axis a and its semi-minor axis b (obtained from $b = a\left(1 - f\right)$ if the flattening f is given instead). The satellite-ellipsoid intersection can then be obtained by the following steps:

1. Satellite position in ECEF; if satellite position is in geodetic coordinates convert to ECEF.

$$\left(\phi_s, \lambda_s, h_s\right) \xrightarrow{\text{geodetic to ECEF}} \left(x_s, y_s, z_s\right) \tag{2.19}$$

$$\vec{s} = x_s \hat{\mathbf{x}} + y_s \hat{\mathbf{y}} + z_s \hat{\mathbf{z}} \tag{2.20}$$

2. Local spherical system determines the line-of-sight direction; convert from local spherical to local tangent coordinates. Assume local spherical system is on the unitary sphere since only azimuth and elevation are needed to determine direction.

$$\left(az, el, 1\right) \xrightarrow{\text{local spherical to local tangent}} \left(x', y', z'\right) \tag{2.21}$$

3. Rotate local tangent coordinates (ENU or NED represented by x', y' and z') to ECEF and obtain the unitary pointing vector. There is no translation operation in this mapping since only the direction vector $\vec{p} = R\vec{r}_{\text{ENU/NED}} = u'\hat{\mathbf{x}} + v'\hat{\mathbf{y}} + w'\hat{\mathbf{z}}$ is needed. Primes are used to discern between the components of $\vec{p}$ and its

corresponding unitary vector defined as $\hat{\mathbf{p}} = u\hat{\mathbf{x}} + v\hat{\mathbf{y}} + w\hat{\mathbf{z}}$ and calculated as $\hat{\mathbf{p}} = \overrightarrow{p}/\|\overrightarrow{p}\| = \left(u'\hat{\mathbf{x}} + v'\hat{\mathbf{y}} + w'\hat{\mathbf{z}}\right)/\sqrt{u'^2 + v'^2 + w'^2}$.

$$\left(x', y', z'\right) \xrightarrow{\text{local tangent to ECEF direction vector}} \left(u', v', w'\right) \qquad (2.22)$$

$$\left(u', v', w'\right) \xrightarrow{\text{to unitary vector}} \left(u, v, w\right) \qquad (2.23)$$

4. Solve ellipsoid equation with satellite position and unitary pointing vector using **Equations 2.17 & 2.18**.

5. Obtain intersection coordinates (x_i, y_i, z_i) in ECEF using solution to the ellipsoid equation; convert to geodetic coordinates if necessary.

$$x_i = x_s + du, \qquad y_i = y_s + dv, \qquad z_i = z_s + dw \qquad (2.24)$$

$$\left(x_i, y_i, z_i\right) \xrightarrow{\text{ECEF to geodetic}} \left(\phi_i, \lambda_i, h_i\right) \qquad (2.25)$$

The final results yield the location of the intersection point on the airglow in global coordinates. This differs from the airglow-observer geometry approach where previously the final coordinates were relative to the location of the observer itself and expressed in terms of arc quantities or zenith angles. Yet when using an ellipsoid to represent the Earth the location of said observer along the surface is relevant. If, however, local coordinates are required then it fails to perform the appropriate transformations from either ECEF or geodetic coordinates. This is in fact the case for the mapping of the intersection point on an imaging instrument, as we will see in the next section.

2.5. Arc distances and mapping using rhumb lines

We previously defined the *forward mapping* from zenith angles (θ, ρ) to arc lengths and heights $(\widehat{A}, h)$ for airglow-observer coordinates. This transformation is of particular interest because it allows the mapping between two uniform linear orthogonal coordinates, one of zenith angles $(\Delta\theta, \Delta\phi)$, and those in terms of the corresponding arc distances $(\Delta\widehat{x}, \Delta\widehat{y})$[3]. By obtaining this latter grid, one can map data on the airglow from its representation in geodetic coordinates to a linear uniformly-spaced orthogonal grid and therefore perform further linear analyses; more on this in **Section 2.7**. The equations of **Section 2.2** give us this forward mapping for the airglow-observer geometry, which entails using the spherical representation of Earth and the consideration of its limitations detailed in **Section 2.3**. Let us now describe a more general geometric derivation to obtain arc lengths on the surface of any ellipsoid, thus obtaining complimentary transformations to the line-of-sight-ellipsoid intersection equations.

The arc distances of **Section 2.2**, that is the displacements away from the observer on the surface of the sphere, are defined in terms of a constant azimuth or bearing and are in fact distances over *rhumb lines* on the sphere (also called loxodromes) that represents the airglow layer. Whereas *great circles* are the shortest distances between two points on a sphere, a rhumb line maintains the same intersection angle between meridians. By the definition of geodetic coordinates, and as it applies to the transformations mentioned in **Section 2.3** and described in detail in the **Appendix**, the rhumb line is the distance on the surface of the ellipsoid that maintains a constant azimuth angle. It follows that our airglow-observer coordinates are expressed in terms of a constant azimuth angle so that we must interpret arc distances as rhumb lines as opposed to geodesics, which are the equivalent of the sphere's great circles but on an

---

[3] This orthogonality is not preserved in 3D for the coordinates $(\widehat{x}, \widehat{y}, h)$.

ellipsoid. By using rhumb lines we can then create an airglow-observer forward mapping for use with our geographical coordinate systems. The rhumb line equations and their numerical solution have been thoroughly studied in literature and we will only state the general problem here, referring the reader to the formulation of Karney (2021) and references within.

The derivation of the rhumb line equations makes use of auxiliary latitudes, namely the isometric latitude ψ, the rectifying latitude μ and the parametric latitude β. The isometric latitude represents the quantity for which at any point on the surface of an ellipsoid equal increments of ψ and longitude λ represent equal distances d, along meridians and parallels respectively thus shapes are preserved. We can readily understand this concept by drawing deformation indicatrices on a Mercator map (see **Figure 2.2**), which is the map projection that preserves angles (conformal map projection) and where straight lines are precisely rhumb lines. The indicatrices are always circles, and thus shapes are preserved everywhere; on the other hand, scale ratios are not preserved, and the circles get larger at distances further away from the Equator; see **Section 3.1** for more information. While the other auxiliary latitudes are measured in degrees or radians, ψ is not; it is a dimensionless parameter that is valued 0 at the equator and infinity at the poles. It is only useful in the derivation of the rhumb line equation.

The axes on a Mercator map are the isometric latitude ψ on the vertical and the longitude λ on the horizontal; the azimuth angle α[4] is measured clockwise from North. This makes a set of orthogonal coordinates and we can write the azimuth of a rhumb line as:

$$\tan \alpha = \frac{\Delta \lambda}{\Delta \psi} \tag{2.26}$$

---

[4] Not to be confused with the spherical polar angle introduced in Section 2.2 that shares the same notation.
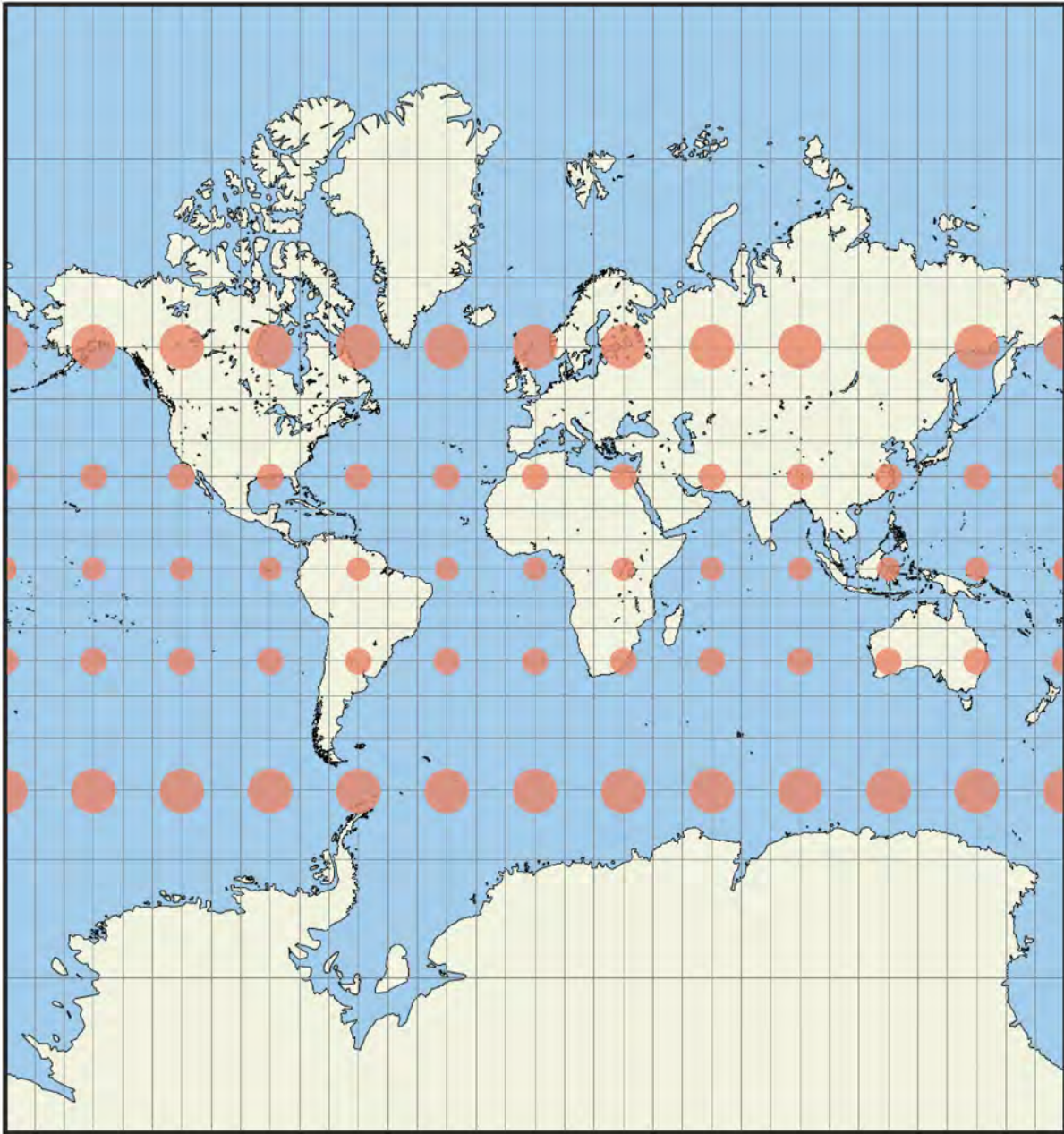
Figure 2.2. The Mercator map projection and its Tissot's indicatrix of deformation (orange circles). This is a conformal map projection that preserves shapes and angles or bearings where straight lines are rhumb lines. This is not an equal-area map therefore landmasses appear distorted far from the Equator.

where the tangent function maps to each quadrant per the definition of atan2(). The isometric latitude is related to the geographic (geodetic) latitude ϕ by:

$$\frac{d\psi}{d\phi} = \frac{\rho}{a \cos \beta} \tag{2.27}$$

where ρ is the meridional radius of curvature, a is the semi-major axis and the parametric latitude β is defined as:

$$\tan \beta = (1 - f) \tan \phi \tag{2.28}$$

where f is the flattening. The distance is obtained by integrating the line segment for the curvilinear coordinates that represent an oblate ellipsoid; this yields

$$\Delta d_{rhumb} = \frac{2M}{\pi} \Delta\mu \sec \Delta\alpha \tag{2.29}$$

where M is the length of a quarter meridian (from the equator to the pole) and the rectifying latitude μ is defined as:

$$\frac{d\mu}{d\phi_G} = \frac{\pi}{2M} \rho \tag{2.30}$$

The rectifying latitude is the meridian distance scaled so that the value at the poles is exactly 90°. It allows for simpler elliptic integrals to solve numerically specifically for distances along parallels. Using the definition of **Equation 2.27** in **2.29** it becomes

$$\Delta d_{rhumb} = \frac{2M}{\pi} \frac{\Delta \mu}{\Delta \psi} \sqrt{\Delta \lambda^2 + \Delta \psi^2} \qquad (2.31)$$

which is indeterminate when $\Delta \phi = 0$ (distances along the meridian). By taking the limits of Δd for $\Delta \psi \to 0$ and $\Delta \mu \to 0$ and then using the definition of both ψ and μ we finally find:

$$\Delta d_{rhumb} = a \cos \beta \, |\Delta \lambda| \qquad (2.32)$$

This equation, along with the definition of β, provides a solution in terms of the geodetic latitude ϕ. However, as mentioned before, when solving for distances along the same latitude an iterative method is used to express β in terms of μ and solving the elliptical integrals that arise, which in turn are a faster and more accurate numerical problem.

Beyond the numerical considerations for dealing with elliptic integrals, we have found the equations for distances over rhumb lines. The forward mapping then consists of transforming from (θ, ρ) or (θ, h) to $(\widehat{A}, h)$ where $\widehat{A} = \Delta d_{rhumb}$. We have described how the line-of-sight ρ intersects with the ellipsoid in the previous section to give the location of the intersection on the surface of the ellipsoid representing the atmospheric layer. These locations are described by any geographic coordinate system. In order to obtain arc distances (distances over rhumb lines) we need to do the appropriate transformations to obtain the intersection point in geodetic coordinates (ϕ, λ) to make use of **Equation 2.32**. Additionally, since the ellipsoidal height h, which is part of the geodetic coordinate system, does not appear in the equations for the rhumb lines, (these are always distances over the *surface* of the ellipsoid) a new ellipsoid with "expanded" semi-major and semi-minor axes by such height is required. This approach allows for the

use of the well-developed methods for solving for the rhumb lines, as opposed to deriving new equations where the ellipsoidal height in the curvilinear coordinates is not zero.

The inverse mapping problem for rhumb lines requires the inversion of the equations above to obtain the auxiliary latitudes in terms of the distance. This requires the integration of **Equation 2.27** to obtain ϕ in terms of ψ. We state the inversion equations here and refer to Karney (2021) for the derivation:

$$\phi = \tan^{-1} \tau \tag{2.33}$$

$$\psi = \sinh^{-1} \tau' \tag{2.34}$$

where $\tau' = \tau \sqrt{1 + \sigma^2} - \sigma \sqrt{1 + \tau^2}$ and $\sigma = \sinh \left(e \tanh^{-1} \left(e\tau / \sqrt{1 + \tau^2} \right) \right)$ where e is the eccentricity (first eccentricity) of the ellipsoid.

An example of computed values of rhumb line parameters are listed in **Table 2.3**.

ϕ	$\Delta\phi$ (1°)	$\Delta\lambda$ (1°)	ψ	μ	β
0°	110,574.3 m	111,319.49 m	0	0	0
15°	110,648.72 m	107,550.49 m	0.2631	14.928°	14.952°
30°	110,852.46 m	96,486.28 m	0.546	29.875°	29.917°
45°	111,131.78 m	78,846.84 m	0.8766	44.856°	44.904°
60°	111,412.27 m	55,800 m	1.3112	59.875°	59.917°
75°	111,618.36 m	28,902.01 m	2.0211	74.928°	74.952°
90°	111,693.95 m	0 m	∞	90.000°	90.000°

Table 2.3. Rhumb line distances over 1° differences along parallels ($\Delta\phi$) and meridians ($\Delta\lambda$) at different latitudes ϕ. These are accurate up to 0.01 meters. The auxiliary latitudes for each geodetic latitude are shown for reference.

2.6. Imager coordinates and the lens function

While the previous relations describe the position of a point on the airglow to a singular observer on the surface of the Earth, we can instead consider an imaging instrument where we correlate different line-of-sight vectors to single imaging units (i.e. pixels). We may then ignore the particulars of the sensor itself, such as physical spacing between imaging units, and simplify the optics system to a single lens function. Let us consider now the airglow-imager geometry using an imaging sensor consisting of a rectangular panel of imaging units, henceforth pixels; we use a rectangular mapping for the location of these pixels in the sensor panel and then use the airglow-observer mapping equations to find the points on the thin airglow layer representation at every height through which each pixel is imaging. We define the span of the panel domain in number of pixels across the x- and y-dimensions (i.e. 512×512 pixels). We assume the spacing between pixels (Δx and Δy) is uniform across the panel. Additionally, each pixel across each dimension has a correspondence to a particular zenith angle, θ for the x-dimension and ϕ for the y-dimension. We assume the center of the sensor panel to be the exact location of the zenith and its edges to be the maximum FOV possible to image. If the all-sky optics system is approximated to be linear, then the distance between each pixel would correspond to uniform $\Delta\theta$ and $\Delta\phi$. In reality, the system does not have a linear profile and $\Delta\theta$, $\Delta\phi$ have a smooth, radially symmetric variation. Therefore a radially symmetric lens function $L(\zeta)$ is used to determine the deviation from linearity.

The lens function is obtained from the lens manufacturer's calibration profile and is usually given as a function of either the zenith angle or the elevation angle and has values within the interval [0,1], so it is normalized. Let's assume we know the exact shape of the calibration profile and let us write it in terms of the zenith angle ζ, this will be our normalized lens function $L_{norm}(\zeta)$. We can now relate the distorted angles to the

ones given by a linear lens by applying the lens function transformations: let ζ_{linear} be the angle that corresponds to a linear lens function and has values in the interval $\zeta_{linear} \in [0°,90°]$, and let L_{norm} be the manufacturer's (non-linear) lens function that is normalized to $90°$ and has values in the interval $\zeta_{norm} \in [0,1]$, then the transformations are

$$\zeta_{warped} = L_{norm}\left(\zeta_{linear}\right) \cdot 90° \quad \longleftrightarrow \quad \zeta_{linear} = L_{norm}^{-1}\left(\zeta_{warped}\big/90°\right) \quad (2.35)$$

The normalized inverse lens function L_{norm}^{-1} transforms back directly to the original zenith angle ζ_{linear}. The normalized lens function L_{norm} is defined for arguments with angle units (degrees or radians depending on the normalization factor's unit) and returns values between $[0,1]$; conversely the normalized inverse lens function L_{norm}^{-1} takes normalized values as inputs, in the interval $[0,1]$, and returns values with angle units. Since the lens function is not defined for angles less than $0°$ or larger than $90°$, we can write a practical lens function that transforms the values in the $[-90°,90°]$ interval and assumes that any value outside this range follows a linear relationship and consequently outputs the same input angle. We can state this as piecewise functions:

$$\zeta_{warped} = \begin{cases} -90° \leq \zeta_{linear} \leq 90 & \text{sgn}\left(\zeta_{linear}\right) L_{norm}\left(|\zeta_{linear}|\right) \cdot 90° \\ \text{otherwise} & \zeta_{linear} \end{cases}$$

$$\zeta_{linear} = \begin{cases} -90° \leq \zeta_{linear} \leq 90 & \text{sgn}\left(\zeta_{warped}\right) L_{norm}^{-1}\left(|\zeta_{warped}|\big/90°\right) \\ \text{otherwise} & \zeta_{warped} \end{cases} \quad (2.36)$$

where we have used the signum function to recover the input angles' signs. We can now conveniently define the lens function to include the $90°$ normalization operations, the signum function and the piecewise definition. This allows for a simple description of the lens function transformations as:

$$\zeta_{warped} = L\left(\zeta_{linear}\right) \quad \longleftrightarrow \quad \zeta_{linear} = L^{-1}\left(\zeta_{warped}\right) \tag{2.37}$$

where we have included all of the expanded definitions and operations from above. The manufacturer's lens function usually takes the shape of a third degree polynomial. If we define (or fit) L_{norm} as such polynomial, then L_{norm}^{-1} should be one of the roots; this is exemplified in **Figure 2.3**. Such a description ensures the reversibility of the transformations (i.e. non-analytical descriptions such as linear fitting or table look up in general would not be reversible); if using numerical polynomial fitting and/or numerical root solving, then the transformations are reversible up to the fit and roundoff error.
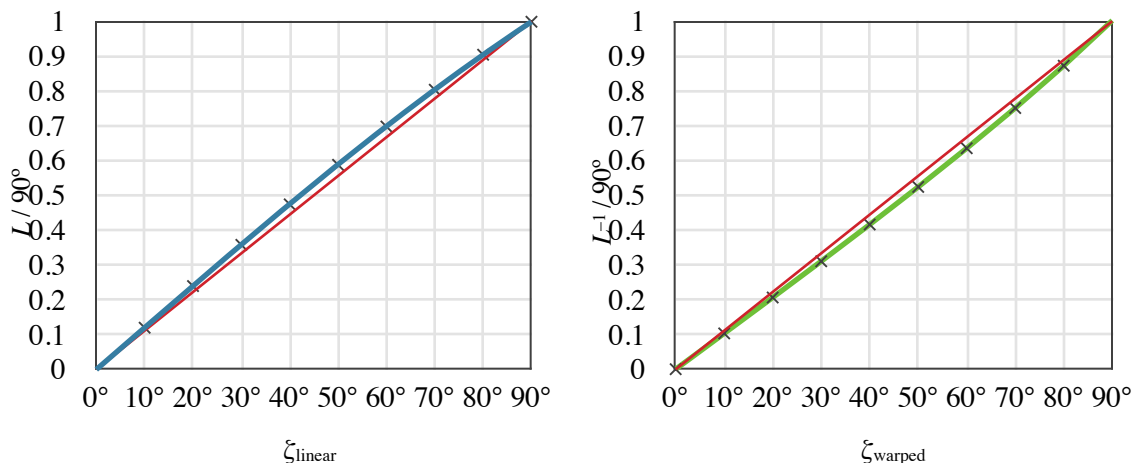
Figure 2.3. (left) Example of a normalized lens function given a linear zenith angle, $L(\zeta_{linear})$; the blue line represents the third-degree polynomial fit. (right) Profile of the corresponding inverse lens function given the warped zenith angle, $L^{-1}(\zeta_{warped}/90°)$; the inverse lens function is a root of the third-degree polynomial fit and the green line only represents the connection between points. The red line represents a linear lens function.

The zenith angles from the linear lens function θ and ϕ can be determined from the Cartesian mesh of the location of pixels within the sensor panel with coordinates

(x_{pix}, y_{pix}); as mentioned before, we consider the pixels to be uniformly spaced and the zenith location to be at the exact center of the panel being the Cartesian mesh in this description. If N_x is the number of pixels in the x-dimension (columns of the mesh) and N_y is the number of pixels in the y-dimension (rows of the mesh) we have:

$$\tilde{x}_{pix} = \left\{ \frac{-N_x + 1 - n_x}{2};\ n_x = 0, 1, 2, 3, ..., 2N_x - 1 \right\}$$
$$\tilde{y}_{pix} = \left\{ \frac{-N_y + 1 - n_y}{2};\ n_y = 0, 1, 2, 3, ..., 2N_y - 1 \right\}$$

(2.38)

$$\tilde{\theta} = \tilde{x}_{pix}\Delta\theta$$
$$\tilde{\phi} = \tilde{y}_{pix}\Delta\phi$$

(2.39)

where $\Delta\theta = FOV_\theta/N_x$, $\Delta\phi = FOV_\phi/N_y$ and $\Delta\theta$, $\Delta\phi$ are the angular spacings or angular resolution in each dimension; we have used tildes (~) to denote discrete arrays. The angular resolutions, along with the respective FOVs, are determined by the optics system. These systems are in practice radially symmetric and thus $\Delta\theta = \Delta\phi$. However different sensor sizes are common and as such the FOV will differ for different numbers of imaging elements. When N_x or N_y are even numbers then $\tilde{x}_{pix}$ and $\tilde{y}_{pix}$ will be $\{..., -2.5, -1.5, -0.5, 0.5, 1.5, 2.5, ...\}$ and when they are odd numbers they will be $\{..., -2, -1, 0, 1, 2, ...\}$; these are always antisymmetric around zero. Note that the resulting angle arrays from **Equation 2.40**, $\tilde{\theta}$ and $\tilde{\phi}$, are always uniform and are antisymmetric around the zenith or 0th angle. By equations (2.40) a sensor panel can be represented by a matrix of column vectors $\tilde{\theta}$ and row vectors $\tilde{\phi}$. The pythagorean magnitude obtained with these angles is the angle $\tilde{\zeta}$ and will be radially symmetric around the center of the panel, so $\tilde{\zeta} = \sqrt{\tilde{\theta}^2 + \tilde{\phi}^2}$; this is the angle that should be warped with the lens function. A sketch of the sensor panel coordinates can be found in **Figure 2.4** and the effect of lens function warping on the pixel locations is visually shown in

Figure 2.5. Collectively these transformations make the *imager or sensor coordinates*, which account for the optics system in a simplified manner and relate points in the atmosphere to pixels or imaging units. The summary of these is presented in **Table 2.4**.
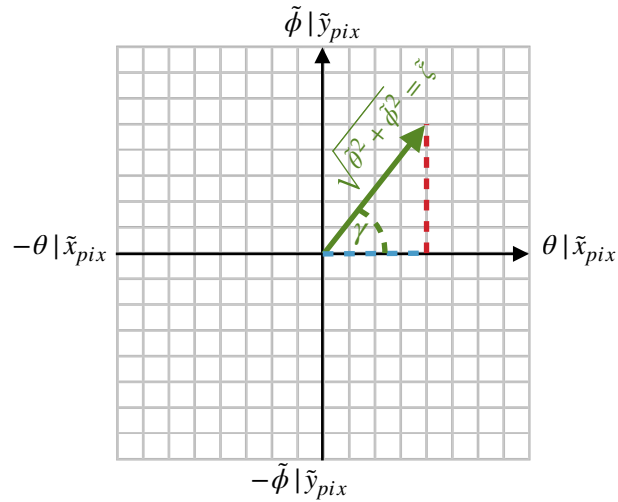
Figure 2.4. Sensor panel coordinates. These are defined for $\tilde{x}_{pix}$ and $\tilde{y}_{pix}$ but are related to the zenith angles by $\tilde{\theta} = \tilde{x}_{pix}\Delta\theta$ and $\tilde{\phi} = \tilde{y}_{pix}\Delta\phi$.
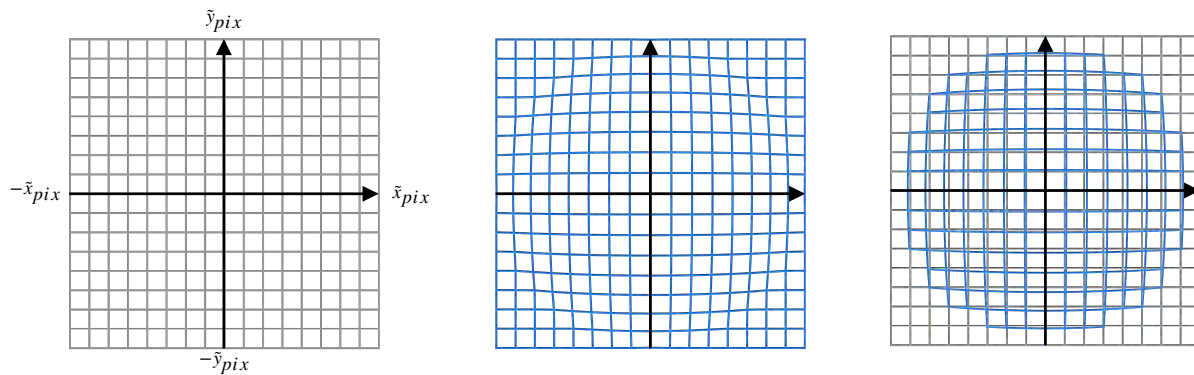
Figure 2.5. (left) Grid representing the location of the pixels (at vertices) in the sensor panel array. (center) Grid representing the warping due to the lens function; the spaces between vertices are not constant within the FOV circle. (right) Overlay of the warped grid and the linear grid; this shows the deviation from linearity more clearly. The panel coordinates are $\tilde{x}_{pix}$ and $\tilde{y}_{pix}$.
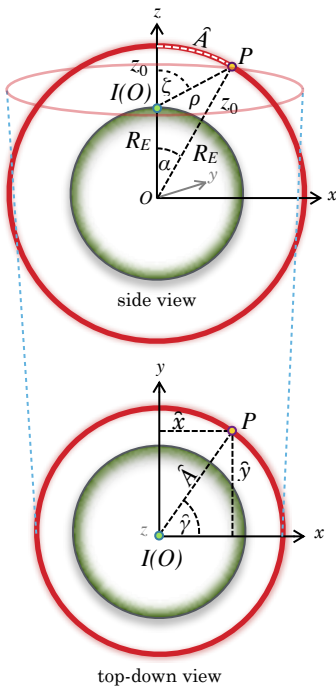
3D airglow-imager coordinates

side view

top-down view

Sensor coordinates

Airglow-imager-CCD 3D coordinate transformation:

$$P(\hat{x},\hat{y},z_0)\longleftrightarrow P(\theta_{\text{linear}}|x_{\text{CCD}},\phi_{\text{linear}}|y_{\text{CCD}},z_0)$$

forward mapping: outputs: $(\hat{x},\hat{y},z_0)$ inputs: $(\theta_{\text{linear}}|x_{\text{CCD}},\phi_{\text{linear}}|y\,_{\text{CCD}},z_0)$	*inverse mapping:* outputs: $(\theta_{\text{linear}},\phi_{\text{linear}},z_0)$ or $(x_{\text{CCD}},y_{\text{CCD}},z_0)$ inputs: $(\hat{x},\hat{y},z_0)$
$\theta_{\text{linear}} = x_{\text{CCD}}(\text{FOV}_\theta/N_x)$ $\phi_{\text{linear}} = y_{\text{CCD}}(\text{FOV}_\phi/N_y)$ $\zeta_{\text{linear}} = \sqrt{\theta_{\text{linear}}^2+\phi_{\text{linear}}^2}$ $\zeta_{\text{warped}} = L(\zeta_{\text{linear}})$ $\rho = \sqrt{R_E^2\cos^2\zeta_{\text{warped}}+z_0^2+2R_E z_0}-R_E\cos\zeta_{\text{warped}}$ $\alpha = \cos^{-1}\left(1+\dfrac{z_0^2-\rho^2}{2R_E(R_E+z_0)}\right)^{\dagger}$ $\hat{A} = (R_E+z_0)\alpha$	$\hat{A} = \sqrt{\hat{x}^2+\hat{y}^2}$ $\alpha = \hat{A}/(R_E+z_0)$ $\rho = \sqrt{2R_E(R_E+z_0)(1-\cos\alpha)+z_0^2}$ $\zeta_{\text{warped}} = \cos^{-1}\left(\dfrac{z_0(2R_E+z_0)-\rho^2}{2R_E\rho}\right)$ $\zeta_{\text{linear}} = L^{-1}(\zeta_{\text{warped}})$ $\theta_{\text{linear}} = \zeta_{\text{linear}}\hat{x}/\hat{A}\quad [x_{\text{CCD}}=\theta_{\text{linear}}(N_x/\text{FOV}_\theta)]^{*}$ $\phi_{\text{linear}} = \zeta_{\text{linear}}\hat{y}/\hat{A}\quad [y_{\text{CCD}}=\phi_{\text{linear}}(N_y/\text{FOV}_\phi)]^{*}$

Airglow-imager-CCD 3D coordinate transformation:

$$P(\hat{x},\hat{y},z_0)\longleftrightarrow P(\theta_{\text{linear}}|x_{\text{CCD}},\phi_{\text{linear}}|y_{\text{CCD}},\rho)$$

forward mapping: outputs: $(\hat{x},\hat{y},z_0)$ inputs: $(\theta_{\text{linear}}|x_{\text{CCD}},\phi_{\text{linear}}|y\,_{\text{CCD}},\rho)$	*inverse mapping:* outputs: $(\theta_{\text{linear}},\phi_{\text{linear}},\rho)$ or $(x_{\text{CCD}},y_{\text{CCD}},\rho)$ inputs: $(\hat{x},\hat{y},z_0)$
$\theta_{\text{linear}} = x_{\text{CCD}}(\text{FOV}_\theta/N_x)$ $\phi_{\text{linear}} = y_{\text{CCD}}(\text{FOV}_\phi/N_y)$ $\zeta_{\text{linear}} = \sqrt{\theta_{\text{linear}}^2+\phi_{\text{linear}}^2}$ $\zeta_{\text{warped}} = L(\zeta_{\text{linear}})$ $z_0 = \sqrt{\rho^2+2R_E\rho\cos\zeta_{\text{warped}}+R_E^2}-R_E$ $\alpha = \cos^{-1}\left(1+\dfrac{z_0^2-\rho^2}{2R_E(R_E+z_0)}\right)^{\dagger}$ $\hat{A} = (R_E+z_0)\alpha$	$\hat{A} = \sqrt{\hat{x}^2+\hat{y}^2}$ $\alpha = \hat{A}/(R_E+z_0)$ $\rho = \sqrt{2R_E(R_E+z_0)(1-\cos\alpha)+z_0^2}$ $\zeta_{\text{warped}} = \cos^{-1}\left(\dfrac{z_0(2R_E+z_0)-\rho^2}{2R_E\rho}\right)$ $\zeta_{\text{linear}} = L^{-1}(\zeta_{\text{warped}})$ $\theta_{\text{linear}} = \zeta_{\text{linear}}\hat{x}/\hat{A}\quad [x_{\text{CCD}}=\theta_{\text{linear}}(N_x/\text{FOV}_\theta)]^{*}$ $\phi_{\text{linear}} = \zeta_{\text{linear}}\hat{y}/\hat{A}\quad [y_{\text{CCD}}=\phi_{\text{linear}}(N_y/\text{FOV}_\phi)]^{*}$

Domains and units

†Alternatively use law of sines:

$$\alpha = \text{sgn}(\zeta_{\text{warped}})\sin^{-1}\left(\rho\sin\zeta_{\text{warped}}/(R_E+z_0)\right)$$

‡Note that an airglow imager can't observe angles larger than ± π/2.

*The values produced for x_{CCD}, y_{CCD} will in general not fall within the allowed values of the $\tilde{x}_{\text{CCD}}$, $\tilde{y}_{\text{CCD}}$ vectors since this is a mapping from a continuous system to a discrete one. In this case the inverse mapping only fits the $\tilde{x}_{\text{CCD}}$, $\tilde{y}_{\text{CCD}}$ vectors when transforming back from the forward mapping.

x_{CCD}, y_{CCD} are always discrete coordinates,
z_0, ρ, θ_{linear}, ϕ_{linear} are in general continuous coordinates

$$\rho \in [R_E,\infty)\,\text{km} \qquad z_0 \in [0,\infty)\,\text{km}$$
$$\alpha \in [-\pi,\pi]\,\text{rad}^{\ddagger} \qquad \hat{A} \in [-\pi(R_E+z_0),\pi(R_E+z_0)]\,\text{km}$$
$$\zeta_{\text{linear/warped}} \in [-\pi,\pi]\,\text{rad}^{\ddagger} \qquad x_{\text{CCD}} \in \tilde{x}_{\text{CCD}} = \{(-N_x+1-n_x)/2;\ n_x=0,1,2,3,...,2N_x-1\}$$
$$\theta_{\text{linear}},\phi_{\text{linear}} \in [-\pi,\pi]\,\text{rad}^{\ddagger} \qquad y_{\text{CCD}} \in \tilde{y}_{\text{CCD}} = \{(-N_y+1-n_y)/2;\ n_y=0,1,2,3,...,2N_y-1\}$$

N_x = total number of pixels in the CCD x-dimension (columns)
N_y = total number of pixels in the CCD y-dimension (columns)
FOV_θ is the zenith field-of-view of the imager in the x-dimension (shouldn't be > 90°)
FOV_ϕ is the zenith field-of-view of the imager in the y-dimension (shouldn't be > 90°)

Table 2.4. 3D airglow-imager-sensor transformations.

2.7. Orthogonal Coordinates, Grids & Interpolation

Typically atmospheric data is given by the geodetic coordinates latitude, longitude and ellipsoidal height, which is an orthogonal coordinate system; however this system is not orthonormal and does not have a linear relationship between its bases which complicates vector operations and linear interpolation in 3D space. The previous is also true for atmospheric data given in airglow-observer coordinates of arc distances and heights or line-of-sight distances, although this is not an orthogonal system. For these reasons and for simplicity coordinate transformations and interpolation in 3D space is usually carried in ECEF coordinates, which is a Cartesian system. However, if we consider arc distances to be the basis for an orthonormal linear system we may represent the curved coordinates as a flat surface and therefore apply 2D linear analyses techniques. This process is called "unwarping" and will invariably distort the data in ways specific to the type of map projection. This is because spheres and ellipsoids are not developable surfaces, that is, they cannot be represented by a flat surface without distortion; see **Section 3.1** for more on this. For the case of atmospheric wave phenomena, spectral analyses in general require an orthonormal basis which are numerically represented by uniform grids. In this section we describe a specific procedure for applying transformations between coordinates based on uniform and nonuniform numerical grids and the numerical implications associated with such grids. The topic of map distortion will be discussed in the following chapter.

We refer to a *grid* as the representation of the Cartesian plane with a discrete numerical matrix, where the *x*-coordinate appears as columns and the *y*-coordinate as rows. Here we will use the terminology *uniform* to describe evenly spaced grids or vectors and *nonuniform* for non-evenly spaced grids or vectors. Uniform coordinates are obtained by making a grid with constant spacing (resolution); each dimension can have

its own different constant spacing so that Δx and Δy may not necessarily be the same. Nonuniform coordinates are usually obtained by applying a transformation or mapping unto a uniform grid since these transformations usually describe a nonlinear relationship between coordinate systems, such as the mappings for airglow-imager coordinates. The source and target coordinates can always be interchanged, forward or inverse mapping applied to them respectively. Which ones of these grids are uniform or nonuniform will depend on which coordinates the uniform grid is created on.

The uniform grids may represent *discrete* coordinate systems, such as the position of pixel units on a sensor panel, or be a numerical representation of a *continuous* coordinate system, such as a height vs horizontal distance matrix with a set spatial resolution. When transforming from a discrete coordinate system to a continuous one the output of the transformation will contain allowed values since the target system is continuous (if it falls within the domain of the continuous coordinates); however, the opposite case will not be necessarily true. When trying to represent the continuous system by a discrete one the desired values may need to be approximated onto the discrete grid; whichever way the fit is done (i.e. rounding, least-squares, interpolation) this will lead to loss of information and may render the transformation irreversible. When the system we want to represent requires these continuous-discrete transformations we may try to find reversible transformations, up to the approximation inherent to the interpolation method. For this purpose we should only interpolate within the continuous system, where all of the discrete values are contained. So, if we want to represent continuous data by a discrete system, we need to first define and transform the uniform discrete grid to the corresponding grid representation of the continuous system. The latter is the nonuniform grid where we want to interpolate the original data onto. After the interpolation we can now transform the newly interpolated data back to the discrete coordinates. In summary we transform the data in original continuous coordinates to a discrete grid (usually nonuniform) that represents those coordinates

then interpolate onto the desired uniform grid. We now see that a transformation from a continuous to a discrete system for the purposes of data representation requires both a forward and inverse mapping and interpolation, as opposed to the discrete to continuous transformation that only requires a forward (or inverse depending on which way you define the transformations) mapping and no interpolation.

2.8. Synthetic images and single line-of-sight instruments

All of the previous sections have been building on the transformations and tools leading to the creation of *synthetic images*, that is, simulated observations for an instrument designed in accordance to the imager coordinates and whose lines-of-sights intersect an atmospheric 3D dataset in accordance to the airglow-observer coordinates. We now define *imaging* as the integration of volumetric data along the line-of-sight of an imaging unit, be it a pixel or a collection of binned pixels. The types of integration are based on the kind of volumetric data. We specifically work with those simulation outputs that are "observables", which are quantities that qualify for remote sensing, i.e. imaging in this case. Photon irradiance and electron density measurements are two of the most common observable quantities we will perform simulations from. Our example dataset includes the observables volume-emission-rates (VER) or ε for airglow emissions and electron densities for total-electron-content (TEC). Additionally, volumetric temperature data is also available, which can be integrated along with the VER to create brightness-weighted-temperatures (BWT) which is an observable that can be obtained from filtered imaging of multiple emission lines (i.e. (Pautet, Taylor et al. 2014)). For these quantities the corresponding integrals are, simply:

Integrated-volume-emission rate (IVER) in units of $cm^{-2} \, s^{-1}$:

$$I\left(\tilde{x}_{pix}, \tilde{y}_{pix}, t\right) = \int_{\rho} \varepsilon\left(\tilde{x}_{pix}, \tilde{y}_{pix}, \rho, t\right) d\rho \qquad (2.40)$$

Brightness-weighted-temperatures (BWT) in units of Kelvin:

$$BWT\left(\tilde{x}_{pix}, \tilde{y}_{pix}, t\right) = \frac{1}{I\left(\tilde{x}_{pix}, \tilde{y}_{pix}, t\right)} \int_{\rho} \varepsilon\left(\tilde{x}_{pix}, \tilde{y}_{pix}, \rho, t\right) T\left(\tilde{x}_{pix}, \tilde{y}_{pix}, \rho, t\right) d\rho \qquad (2.41)$$

Total-electron-content (TEC) in TECU units (1 TECU $= 10^{16}\ m^{-2}$):

$$\text{TEC}\left(\tilde{x}_{pix}, \tilde{y}_{pix}, t\right) = \int_{\rho} n_e\left(\tilde{x}_{pix}, \tilde{y}_{pix}, \rho, t\right) d\rho \qquad (2.42)$$

where ρ is the line-of-sight and the path of integration and x_{pix}, y_{pix} are the pixel coordinates. Each integration yields a synthetic 2D image represented in pixel coordinates. This synthetic image represents the integrated simulated layer which is approximated to be at an *arbitrary fixed mean layer height* at the expected vertical location of the mean peak of the observed emissions or electron densities; this is the *thin layer* or *shell* representation. In reality both the airglow layers and the electron densities are thick layers distributed around these mean peaks at each particular height. For the most typically imaged airglow layers, the mean heights and typical full-width-half-maximums (FWHM) of their intensity distributions are:

- the OH(3,1) airglow band that peaks at ~87 km height with a FWHM of ~8 km,

- The $O_2(b)$ 865.5 nm line that peaks at ~94 km height with a FWHM of ~8 km,

- the $O(^1S)$ 557.7 nm *greenline* that peaks at ~95 km with also a FWHM of ~8 km,

- the sodium D line doublet emissions $Na(^2P, {}^2S)$ 589.0 nm and 589.6 nm that peak at ~90 km with a FWHM of ~10 km, and

- the $O(^1D)$ 630.0 nm *redline* with peak at ~230 km with a FWHM of ~60 km.

Please refer to **Figure 1.3** for a visual representation of each layer's widths. These integrations are done for every imaging unit of sensor panels that have varying sizes. Typical configurations include 1024×1024 pixels binned to 512×512 for better signal-to-noise ratio or newer higher resolution imagers with a 2048×2048 sensor binned to 1024×1024. Our synthetic imagers do not require binning since we currently don't include any type of noise (i.e. ambient, heat, electric) to our simulation. With this consideration we choose our sensor to match the effective pixel size of the imagers we are trying to simulate. However we may consider the integration of several bins of imaging units for the purpose of parallelization, the only requirement is the need for including neighboring lines-of-sights for the linear interpolation. So a single imaging unit requires the lines-of-sights of the neighboring 8 imaging units, making this the smallest parallelization bin possible. See **Figure 2.6** for a schematic.
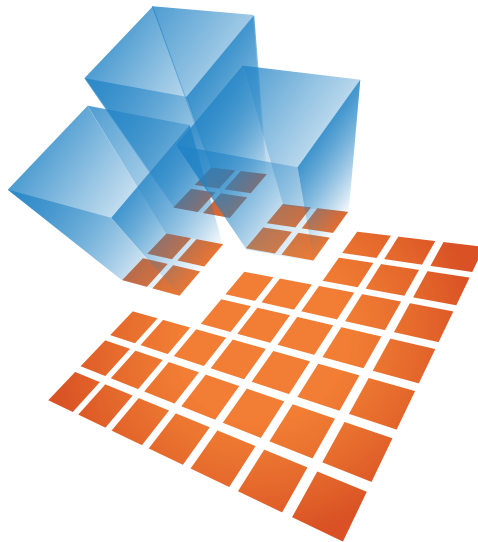
Figure 2.6. Imaging units on a sensor panel. These can be pixels or binned pixels such as a 1024×1024 binned to a 512×512 for increased signal-to-noise ratio. Integration through the line-of-sight requires interpolation between lines-of-sights of neighboring imaging units opening the possibility of parallelization.

There is a balance to interpolation performance that depends on the size of the bin; the larger the bin the faster the computation but also the memory allocation. At some point it may become unfeasible to allocate to memory the entire sensor and looping through the bins (with or without parallelization) will be the only way to perform the interpolation without running out of memory. This is dependent on the interpolant size, which in turn depends on the number of imaging units, the size of the line-of-sight vector ρ and the size of the original data. In fact, in our results sensor sizes of 512×512 with full resolution simulation data require up to tens of GBs of memory, so either we subsample the data or reduce the FOV of the sensor which in turn reduces the amount of data that intersects the lines-of-sight. Still, depending on the gravity wave wavelengths we are trying to study, full resolution might already be unnecessary, where sensor detail is enough to image at least the largest phenomena quantitatively. We can use the airglow-imager geometry to calculate the resolutions at a chosen airglow layer height for a given sensor configuration, we showed this in **Figure 1.5** for the OH layer.

Beyond imaging sensors we may also consider single line-of-sight imaging instruments such as spectrographs or GPS networks. For the latter we can use a thin shell representation of ionospheric electrons so that we may apply the airglow-observer transformations to obtain the intersection of the line-of-sight with the electron density along the F-region (160–800 km). The TEC is then approximated to be at the height of the ionospheric-pierce-point (IPP), which is height of the peak of vertical TEC typically between 250–350 km. The height locations and peaks of these layers are not fixed and fluctuate for different background conditions. While the average heights of the different mesopause airglow layers are more consistent, (they can still vary by several kilometers, see Zhao et al. (2005)), the electrons' distribution may vary greatly, being affected by photoionization, chemistry, the Earth's magnetic field and other electromagnetic factors. Thus the choice of IPP for analysis of TEC fluctuations depends on the nature and altitude of perturbations of the layer.

As a final note for this section it should be noted that background removal is a common procedure, and often a necessary one. The background is essentially the intensity data that is not a perturbation and represents the ambient intensity. The removal process can be accomplished in numerous ways. For simulated data, it is possible to model the background atmosphere, which can be a steady-state solution. This is then integrated with the appropriate line-of-sight mappings to create the background integrated image. Alternatively, the background can be approximated with a polynomial surface, by means of difference images if temporal evolution is available or by applying a time series filter. For the most part, we use the first approach, obtaining background information directly as a simulation output. It should be noted that it is possible to have the background significantly perturbed for large non-linear wave interaction; in this cases other approaches may be better suited, such as designing and applying appropriate bandpass filters.

2.9. Example: Interpolating atmospheric data for all-sky imaging

Here in this section we present detailed steps for a particular set of transformations based on the 3D airglow-imager equations of **Section 2.2**. The input 3D data is given in a discrete uniform rectangular 3D matrix $(\tilde{x}, \tilde{y}, \tilde{h})$ which are the discrete values that represent the continuous nonuniform airglow-observer coordinates $(\widehat{x}, \widehat{y}, h)$; we will use tilde ($\sim$) to denote discrete coordinates. The all-sky imager's sensor coordinates are

$$(\tilde{\theta}_{linear}|\tilde{x}_{pix}, \tilde{\phi}_{linear}|\tilde{y}_{pix}, \rho) \tag{2.43}$$

where the notation "|" reads as "given" and it means the angles $\tilde{\theta}_{linear}$, $\tilde{\phi}_{linear}$ are determined by the choice of $\tilde{x}_{pix}$, $\tilde{y}_{pix}$, by means of **Equation 2.40**; the third coordinate ρ is effectively a pixel's line-of-sight and is a continuous variable chosen arbitrarily within $\rho \in [0,\infty)$. Note that we have a mix of discrete and continuous coordinates for the all-sky imager's coordinates. The goal is to obtain the transformed coordinates $(\tilde{x}_{LOS}, \tilde{y}_{LOS}, \tilde{h}_{LOS})$ which represent points along the line-of-sight (LOS) for each pixel of the sensor. This process is simply the transformation:

$$(\tilde{\theta}_{linear}|\tilde{x}_{pix}, \tilde{\phi}_{linear}|\tilde{y}_{pix}, \tilde{\rho}) \xrightarrow{\text{forward mapping}} (\tilde{x}_{LOS}, \tilde{y}_{LOS}, \tilde{h}_{LOS}) \qquad (2.44)$$

Note that we have to specify a discrete $\tilde{\rho}$ to create a purely discrete representation of the imager coordinates in order to obtain in turn discrete LOS coordinates. A first approach would be to arbitrarily decide what this vector $\tilde{\rho}$ is and construct it with whichever values we want, as long as it is uniform; this will save us the process of doing inverse transformations required to know ρ resolution and minimum/maximum values. Collectively the inverse transformations can provide us with information about the input's data domain and resolutions in the imager's coordinates. While this information can be used to choose design variables for the imager depending on the data, usually the imager's parameters are fixed for real use cases and therefore inverse mappings have limited use. By creating an educated guess for $\tilde{\rho}$, such as using a small $\Delta\rho$ and let it start at 0 and end at a distance that will reach the sought data features (i.e. airglow layer) at every zenith angle we can skip the inverse transformations and go straight into interpolation. We will, however, show the process of obtaining resolution and domain information from these inverse transformations.

To setup our inverse transformations we first need to create the uniform grid of the imager's coordinates $(\tilde{\theta}_{linear}|\tilde{x}_{pix}, \tilde{\phi}_{linear}|\tilde{y}_{pix}, \tilde{\rho})$. The first two coordinates are

determined from the sensor panel characteristics, namely the fields-of-view FOV_θ, FOV_ϕ and number of pixels N_x, N_y, these define the grid $(\tilde{\theta}_{linear}|\tilde{x}_{pix}, \tilde{\phi}_{linear}|\tilde{y}_{pix})$. We now need to discretize the continuous line-of-sight coordinate $\rho \rightarrow \tilde{\rho}$ by choosing a sufficiently small resolution $\Delta\rho$. This is a designer's choice and the minimum value that the system is able to resolve is limited by both the data and sensor resolution. To know these resolution limitations we need to apply the inverse transformations. In either case, it is worth noting that when doing spectral analyses of atmospheric wave data the choice of resolution will always be related to the desired wave parameters by the Sampling Theorem were the Nyquist frequency should function as a threshold for minimum chosen resolutions. We also need to determine the desired domains of $\tilde{\rho}$, and to know the allowed values we need again to apply inverse transformations to obtain what the minimum and maximum values for ρ that are within the airglow-observer coordinates $(\widehat{x}, \widehat{y}, h)$. Conversely, the sensor array doesn't limit the domain values for $\tilde{\rho}$ since $\rho \in [0,\infty)$. Note that the discrete variable $\tilde{\rho}$ does not need to start at 0, especially if there is no data available up to a certain height from the imager. Let us now use the previous considerations to proceed with the creation of the uniform grid and use the inverse mapping equations on the input coordinates $(\tilde{x}, \tilde{y}, \tilde{h})$:

$$(\tilde{x}, \tilde{y}, \tilde{h}) \xrightarrow{\text{inverse mapping}} (\tilde{\theta}_{linear}|\tilde{x}, \tilde{\phi}_{linear}|\tilde{y}, \tilde{\rho}) \qquad (2.45)$$

We could ignore the outputs $(\tilde{\theta}_{linear}|\tilde{x}, \tilde{\phi}_{linear}|\tilde{y})$ since they are not a representation of the discrete grid we are trying to create, they represent the data in nonuniform imager coordinates. However, they provide the effective domain size for the pixel vectors and could be used to crop the $(\tilde{\theta}_{linear}|\tilde{x}_{pix}, \tilde{\phi}_{linear}|\tilde{y}_{pix})$ grid if, for example, the data doesn't span the entire FOV of the imager. This inverse mapping yielded the corresponding values for $\tilde{\rho}$ that are contained within the input data. The minimum available resolution can then be calculated by $\Delta\tilde{\rho}_{min} = \min(\nabla\tilde{\rho})$ where $\nabla\tilde{\rho}$ is the gradient of the matrix $\{\tilde{\rho}\}$

that contains the local $\Delta\tilde{\rho}$ for all points in the grid. We can now construct the $\tilde{\rho}$ vector as $\tilde{\rho} = \{\tilde{\rho}_{min}, \ldots, \tilde{\rho}_{min} + n\Delta\tilde{\rho}, \ldots, \tilde{\rho}_{max}; n = 1,2,3,\ldots\}$ where the minimum and maximum values are taken from all elements of $\tilde{\rho}$. Finally we can now have a purely discrete uniform representation of the all-sky imager coordinates as

$$(\tilde{\theta}_{linear}|\tilde{x}_{pix}, \tilde{\phi}_{linear}|\tilde{y}_{pix}, \tilde{\rho}) \tag{2.46}$$

which is what we originally set out to find to be able to apply the transformation in (2.42) and obtain $(\tilde{x}_{LOS}, \tilde{y}_{LOS}, \tilde{h}_{LOS})$. We now have the necessary coordinates for interpolation of the input data. This interpolation is from nonuniform to uniform grids, which requires a scattered data interpolant of choice. Finally, to create synthetic images all that is required is the integration along the line-of-sight coordinate ρ. For such integration the resulting coordinates of the imaged data are $(\tilde{\theta}_{linear}|\tilde{x}_{pix}, \tilde{\phi}_{linear}|\tilde{y}_{pix})$ and this is the image we have been looking for. We can now do some post-processing that is helpful in extracting perturbations from the background. A concise summary of this entire procedure is presented in **Table 2.5**. Note that for clarity a new notation for uniform and nonuniform vectors is introduced and the transformation equations have been broken into steps and grouped together by colors.

Airglow in ENU coordinates

Airglow in airglow-imager coordinates

Integrated Image

Background removed

Unwarped
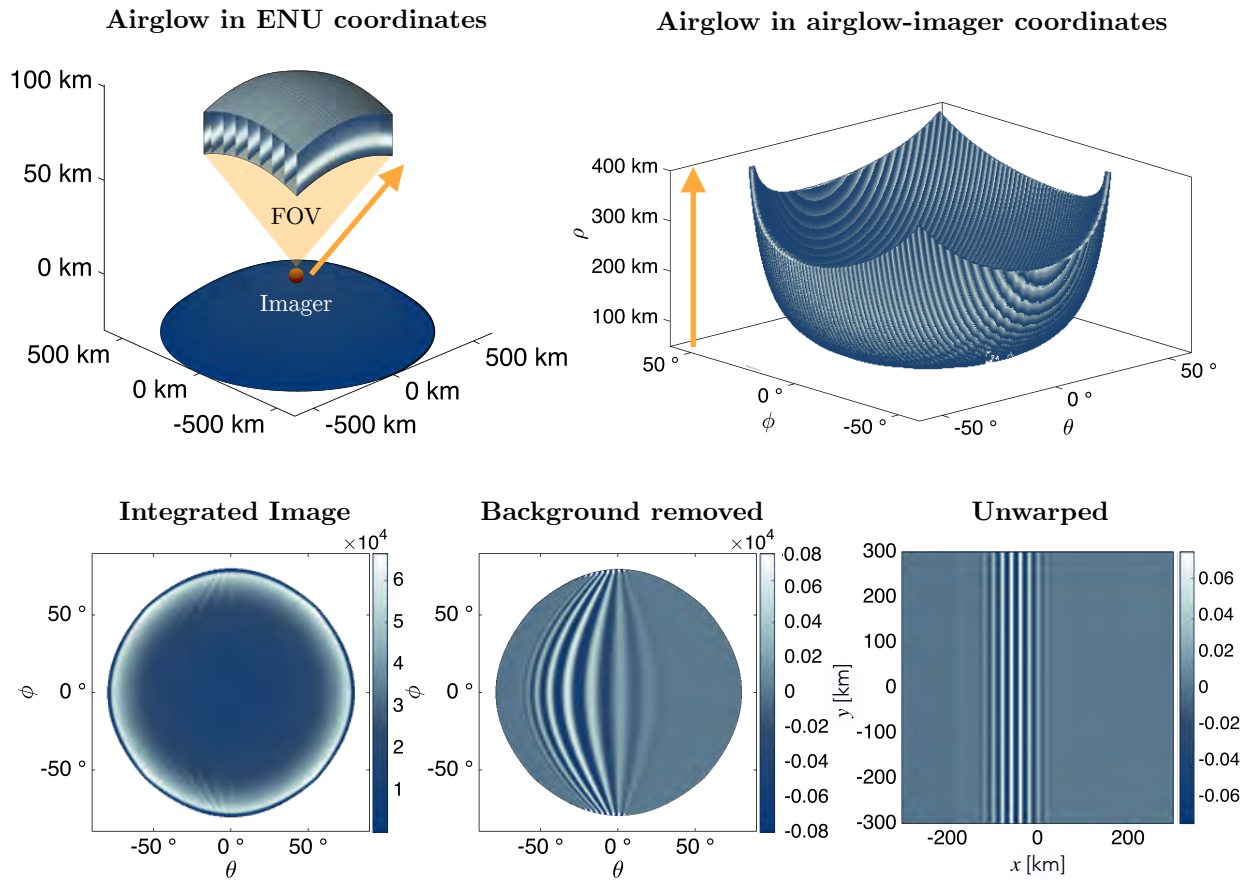
Figure 2.7. Interpolation of airglow coordinates. (a) 3D sketch of the imager-airglow system in ENU coordinates. (b) The airglow emission data in airglow-imager coordinates. In both panels the arrow represents the integration (imaging) path. (c) The resulting synthetic IVER image. (d) IVER image with the background removed. (e) Unwarped image in uniform kilometer grid.

WORKFLOW FOR INTERPOLATING DATA IN ATMOSPHERIC COORDINATES AT AIRGLOW-IMAGER'S COORDINATES

for clarity: • stands for uniform, ∗ stands for nonuniform quantities

System originally given in $(\widehat{x}_\bullet, \widehat{y}_\bullet, h_\bullet)$, use: forward mapping with inputs: $(\theta_\bullet, \phi_\bullet, \rho_\bullet)$; but first determine domain sizes by using inverse mapping.						

1		Input 3D coordinates	$(\widehat{x}_\bullet, \widehat{y}_\bullet, h_\bullet)$	6	a	Transform the uniform grid	$\zeta_{\mathrm{u}\bullet} = \sqrt{\theta_\bullet^2 + \phi_\bullet^2}$
2	a	3D → 2D (magnitude)	$\sqrt{\widehat{x}_\bullet^2 + \widehat{y}_\bullet^2} = \widehat{A}_\bullet$		b	Forward lens function	$\zeta_{\mathrm{w}\bullet} = L(\zeta_{\mathrm{u}\bullet})$
	b	2D inverse mapping equations	$\alpha_\bullet = \widehat{A}_\bullet / (R_E + h_\bullet)$ $\rho_* = \sqrt{S^2 + (R_E + h_\bullet)^2 - 2S(R_E + h_\bullet)\cos\alpha}$ $\zeta_{\mathrm{w}*} = \cos^{-1}\left(\dfrac{S^2 + \rho_*^2 - (R_E + h_\bullet)^2}{2S\rho_*}\right)$		c	2D forward mapping equations	$h_{\mathrm{LOS}*} = \sqrt{\rho_\bullet^2 - 2S\rho_\bullet \cos\zeta_{\mathrm{w}\bullet} + S^2} - R_E$ $\alpha_* = \cos^{-1}\left(\dfrac{S^2 - \rho_\bullet^2 + (R_E + h_*)^2}{2S(R_E + h_*)}\right)$ $\widehat{A}_* = (R_E + h_*)\alpha_*$
	c	Inverse lens function	$\zeta_{\mathrm{u}*} = L^{-1}(\zeta_{\mathrm{w}*})$		d	2D → 3D (components)	$\widehat{x}_{\mathrm{LOS}*} = \widehat{A}_* \, \theta_\bullet / \zeta_{\mathrm{u}\bullet}$ $\widehat{y}_{\mathrm{LOS}*} = \widehat{A}_* \, \phi_\bullet / \zeta_{\mathrm{u}\bullet}$
	d	2D → 3D (components)	$\theta_* = \zeta_{\mathrm{u}*} \, \widehat{x}_\bullet / \widehat{A}_\bullet$ $\phi_* = \zeta_{\mathrm{u}*} \, \widehat{y}_\bullet / \widehat{A}_\bullet$	7		Output	$(\widehat{x}_{\mathrm{LOS}*}, \widehat{y}_{\mathrm{LOS}*}, h_{\mathrm{LOS}*})$
3		Determine domain sizes	$\rho_\bullet \in [\min\rho_*, \max\rho_*]$ $\theta_\bullet \in [\min\theta_*, \max\theta_*]$ $\phi_\bullet \in [\min\phi_*, \max\phi_*]$	8		Interpolate data in original uniform coordinates $(\widehat{x}_\bullet, \widehat{y}_\bullet, h_\bullet)$ onto the new nonuniform coordinates $(\widehat{x}_{\mathrm{LOS}*}, \widehat{y}_{\mathrm{LOS}*}, h_{\mathrm{LOS}*})$	
4	a	Angles from pixel location	$\theta_\bullet = x_{\mathrm{CCD}} \, \mathrm{FOV}_\theta / M$ $\phi_\bullet = y_{\mathrm{CCD}} \, \mathrm{FOV}_\phi / N$				
	b	Crop if necessary	$(\min\theta_* \le \theta_\bullet \le \max\theta_*)$ $(\min\phi_* \le \phi_\bullet \le \max\phi_*)$				
5		Create new ρ vector	$\Delta\rho = \min(\Delta\widehat{x}_\bullet, \Delta\widehat{y}_\bullet, \Delta h)$ $\rho_\bullet = [\min\rho_* : \Delta\rho : \max\rho_*]^{\ddagger}$				

†Alternatively use law of sines: $\alpha = \mathrm{sgn}(\zeta_{\mathrm{warped}})\sin^{-1}(\rho\sin\zeta_{\mathrm{warped}} / (R_E + z_0))$

‡The colon notation implies:

$\rho_\bullet = \{\rho_{*\min}, \ldots, \rho_{*\min} + n\Delta\rho, \ldots, \rho_{*\max}; \; n = 1,2,3,\ldots\}$

Table 2.5. Workflow for interpolating data in atmospheric coordinates at airglow-imager's coordinates. Different sections have been highlighted in varying colors. Steps 2 and 6 correspond to the inverse and forward mapping respectively of the airglow-image coordinates.¶

Chapter 3

Methods: 3D Data Visualization

3D rendering has been increasingly explored in the context of atmospheric data in the forms of visualization of sparse meteorological data, 3D printing, or virtual and augmented reality experiences. NASA's Scientific Visualization Studio website has many relevant examples of this with notable visualizations by Shirah (2018, 2021), Kekesi (2020) and Kekesi & Perkins (2010), the latter included in **Figure 3.1**.
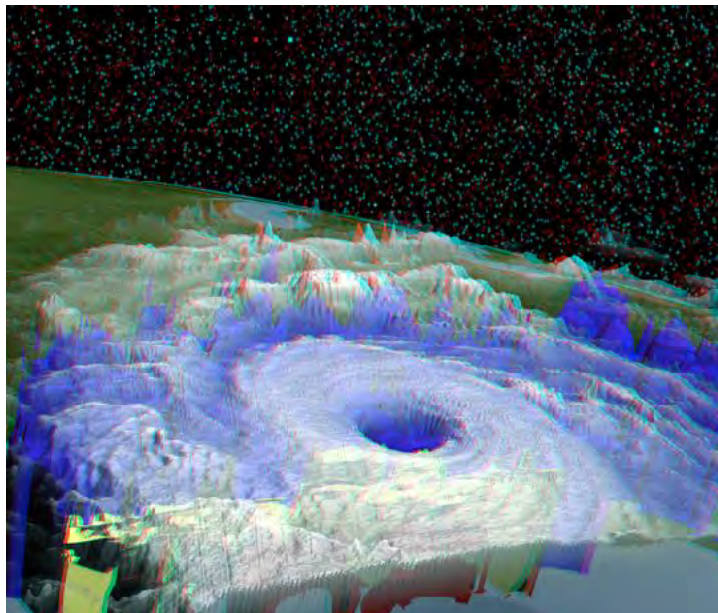
Figure 3.1. Stereoscopic visualization of hurricane Katrina on August 28, 2005. Composition includes cloud cover data from TMMR's Visible and Infrared Scanner (VIRS) and GOES and rain from TRMM's Tropical Microwave Imager (TMI). [Credit: Kekesi & Perkins, 2010].

So when we think about data visualization two approaches come to mind: visualizations that suit our mathematical analyses and visualizations that better represent the morphology of the data. One fundamental concept in terms of representing data in space is data projection, which is representing 3D data in a 2D plane. This process requires choosing which spatial coordinates to project our data onto and these may or may not be appropriate for either mathematical or morphological analyses. Therefore it is of great importance to fully understand the types of projections suited for conveying the results of our research. In general, our data analysis techniques are computationally more efficient in 2D space. Additionally, considering large datasets can be built in 4D data grids to include time evolution, 2D projections or slicing still represents the most viable method for determining parameters even in fundamentally three-dimensional phenomena (i.e. non-linear interactions). Part of this research focuses on developing better 3D visualization tools in an effort to recognize the viability for volumetric data interpretation.

Our 2D and 3D modeled data comes from two physics-based models and their coupling. First is the compressible atmospheric dynamics model "MAGIC" (Snively, Pasko et al. 2010), the Model for Acoustic-Gravity wave Interactions and Coupling which simulates quantities including winds, temperature and emission rates for atmospheric dynamics following inputs from physically constrained or idealized sources. Secondly we use the self-consistent multi-fluid ionosphere model "GEMINI" (Zettergren and Semeter 2012), the Geospace Environment Model for Ion-Neutral Interactions, and its coupling with MAGIC to obtain TEC and also volume emission rates of oxygen 630 nm airglow. The MAGIC-GEMINI coupling is one way, where the mesospheric and thermospheric results of MAGIC are taken as inputs for GEMINI to obtain modeled data representing physical responses throughout the ionosphere. In this chapter we will present visualization tools and coordinate transformations appropriate for atmospheric gravity waves and atmospheric disturbances in the context of our modeled data. These

simulated results have helped and shaped the methods developed here for visualization techniques and therefore are optimized for them. The techniques used in this research include *isosurfaces* for large-scale perturbations, a *morphology enhancement technique* developed for use with thin layers and synthetic images, and *point clouds* to visualize dense data sets such as electron density or high-resolution wave breaking. For the development of this Chapter we will use two data sets, the first one is modeled after convective thunderstorm cell from MAGIC featured in Heale et al. (2019) and the second one is from a tsunamigenic OH airglow response modeled in MAGIC featured in Inchin et al. (2020) with additional results for coupling with GEMINI.

3.1. 2D and 3D visualization techniques

3.1.1. Slices

The gateway to understanding the need for volumetric 3D visualization is through the use of slices, which has been in use since 3D simulations were first created. 2D plots of simulated data can be obtained directly from 2D outputs or as slices and integrations from 3D data. This is the most commonplace data visualization format and is necessary to perform spectral analysis on wave phenomena: i.e., obtain horizontal or vertical wavelengths in longitude vs latitude or height vs longitude plots respectively. 2D plots allow us to clearly distinguish dynamic wave features in volumetric data and thus are a primary analysis tool for interpretation of AGWs. 2D plots portray data in limited (albeit accessible) ways that may or may not be fully representative of the 3D dynamics they are depicting. Thus, the choice of where and how to slice the data will determine the morphology of the plot and understanding the projection it represents is necessary for a correct interpretation. A collection of slices like these can be built into 3D space in an effort to visualize volumetric data; see **Figure 3.1** for an example. By using

appropriately selected slices we can describe characteristics from the simulated data such as model domains and features along more familiar coordinate projections. How successful this is depends on the choice of coordinates as well as the number of slices, viewing angle and choice of colormap scales. **Figure 3.2** provides an example of the same 3D data, sliced at the same heights but with different projections and aspect ratios. The plots on the right are the original MAGIC coordinates and the plots on the left side have been mapped along the curvature of the Earth in the ENU local coordinate system. While each slice clearly represents "flat" horizontal features at the selected heights, they fail to show the morphology along the z axes. Additionally, it may prove useful to reduce the number of slices shown and adjust viewing angles accordingly to reduce occlusion and maximize viewing area. As a general remark, MAGIC and GEMINI have good slice visualization in their native coordinate systems: MAGIC in Cartesian and GEMINI in its diapole coordinates that are aligned to Earth's magnetic field lines; interpolations may be required to define slices obliquely.
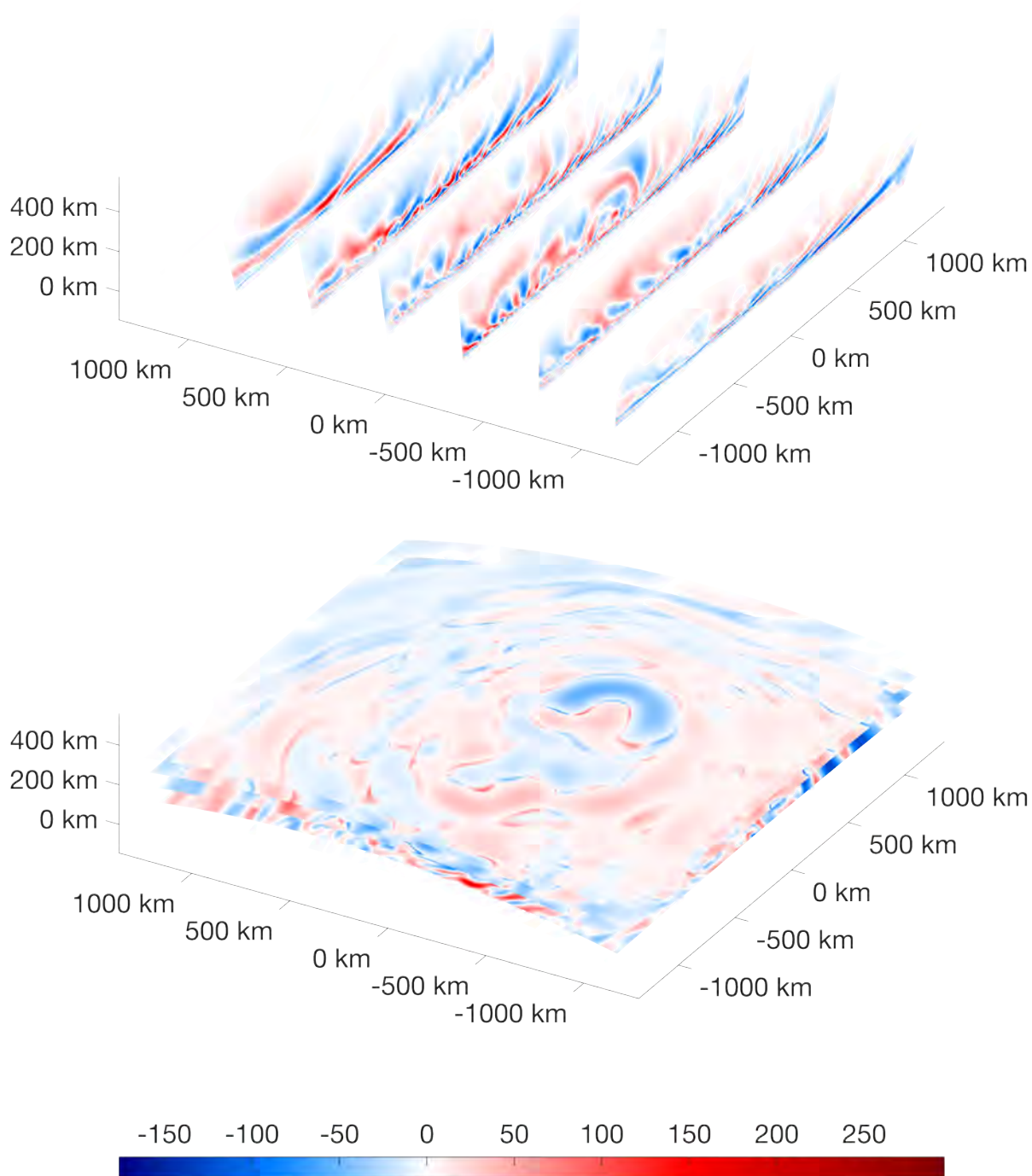
Figure 3.1. Slices at regular intervals for visualization of a 3D MAGIC volumetric data. (Top) latitudinal slices; (bottom) height slices. Transparency has been applied up to a certain threshold. The limitations of stacking slices for visualizing 3D data, as the overlap doesn't allow for a clear morphologic appreciation.
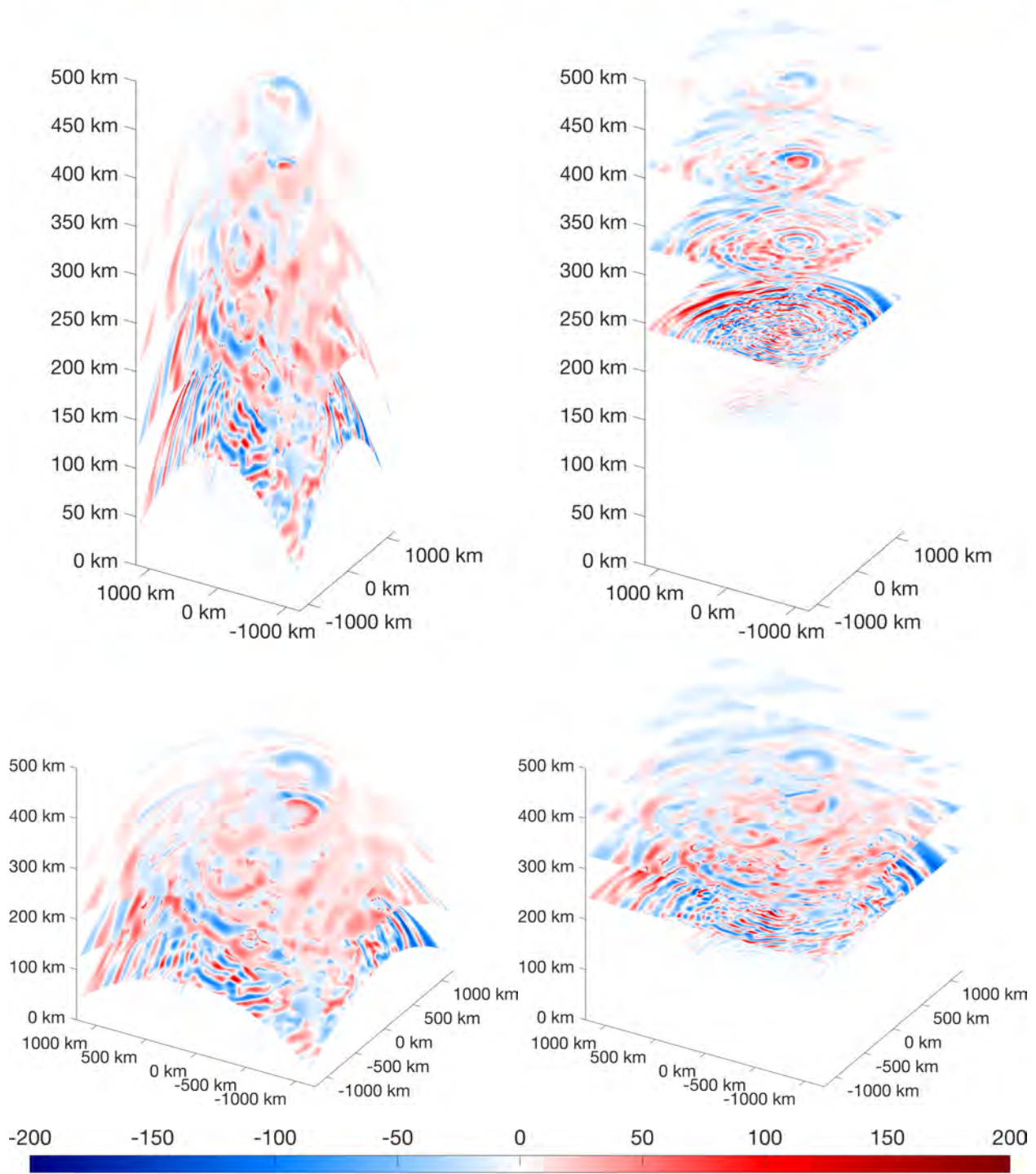
Figure 3.2. Comparison of slices at regular intervals for visualization of a 3D MAGIC volumetric data for different height ratios. (left) Data follows the curvature of the Earth. (right) Data in its original Cartesian coordinates. (top) Height ratios of z vs x, y of 1:14. (bottom) Height ratios of z vs x, y of 1:5.

In a different use case, **Figure 3.3** shows an example on how to use slices to describe model domains, coordinate projections and interfacing and coupling of models. This graphic is a visual tool that assists in the understanding of boundary conditions, the size of each domain and necessary interpolations to feed one model's output into another. In this case a full 3D visualization, as the ones discussed in the following sections, may in fact obfuscate the desired connections, reducing their accessibility and utility.
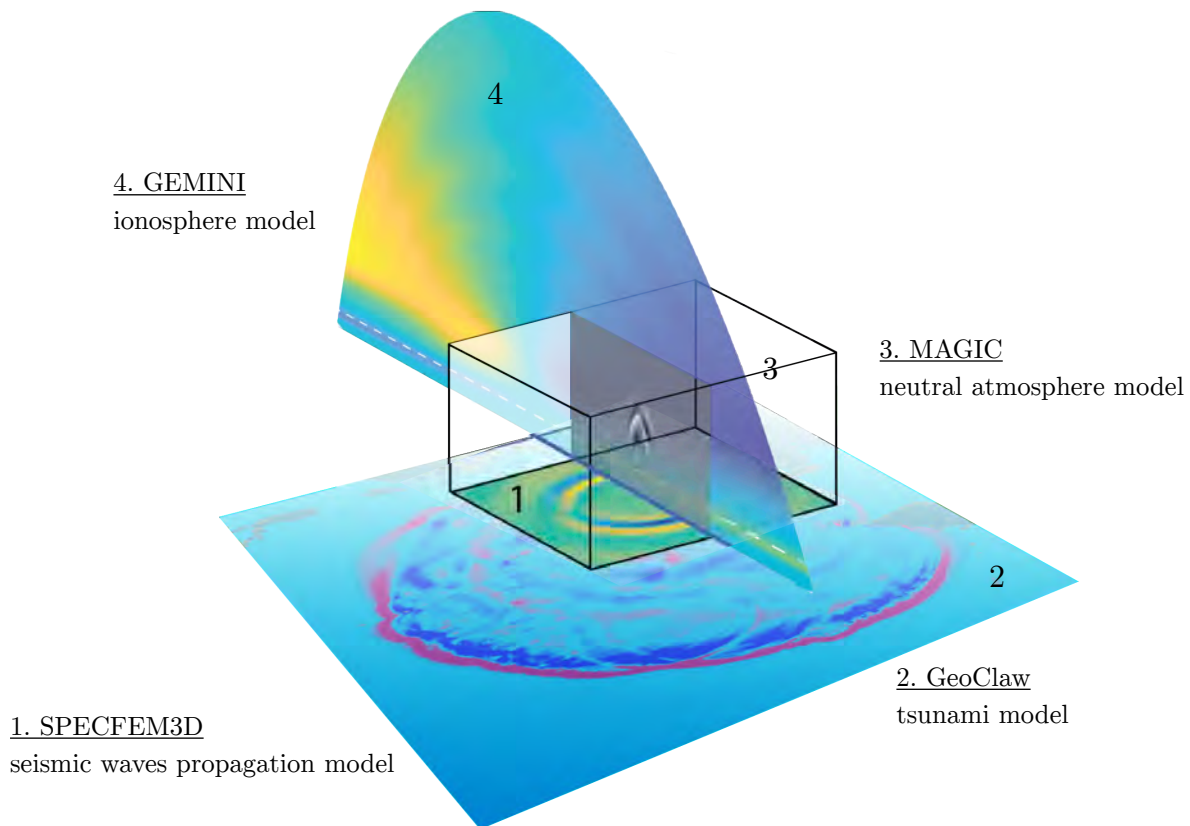
Figure 3.3. Good example of use of slices: describing the coupling between models, domains and boundaries. Shown models are: GEMINI (Zettergren and Semeter 2012), MAGIC (Snively 2013), SPECFEM3D (Komatitsch and Tromp 2002) and GeoClaw (Berger, George et al. 2011). Courtesy: Pavel Inchin (2020).

Let us discuss another example of why 2D plots may meaningfully simplify data that is inherently a 3D quantity. **Figure 3.4** shows wind measurements from a radiosonde and and empirical model, given in cylindrical coordinates. A 3D stem plot of these quantities has been created, however the relationship between values is better understood in terms of their projections on the familiar planes: zonal, meridional and horizontal. 2D plots of the projections are enough for a general understanding of the wind. There may yet be value for the 3D stem plot and that is in the context of the other 3D visualizations techniques discussed later in this chapter. Ultimately the use of 2D plots is a purposeful decision that depends on the features being analyzed.
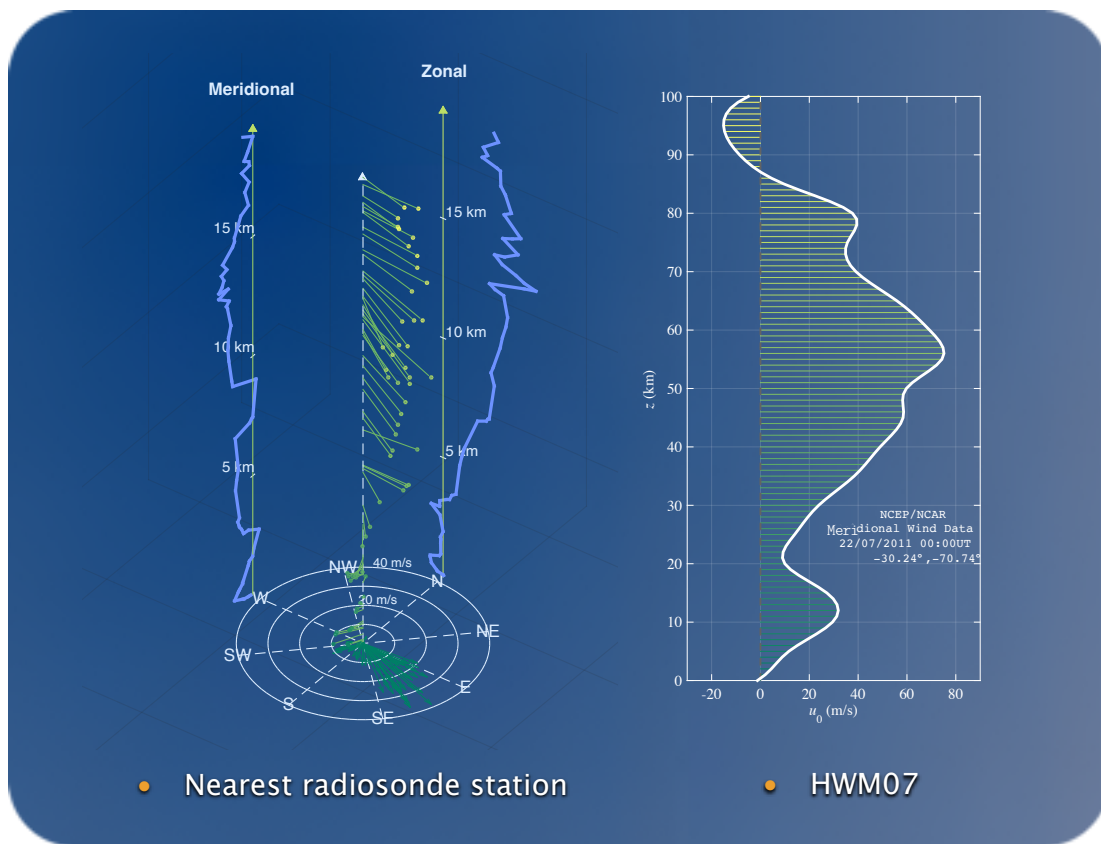
Figure 3.4. 3D wind stem plot with projection on the meridional, zonal and horizontal planes. Data is from a radiosonde (SCSN Santo Domingo station from University of Wyoming's Department of Atmospheric Science Upper Air Soundings) and modeled wind from HWM07 empirical model (Drob, Emmert et al. 2008).

When it comes to visualize wave data it is useful to do so in terms of perturbations, which means *subtracting* the background. While this is not a trivial process for real imaged data, when working with simulated data often the background is readily available for subtraction. This background could come from simulation of the steady state solution at the given time, or it can be obtained as a spatial or temporal mean; alternatively filtering techniques for signal analysis can be used to obtain perturbations as well. These latter processes more closely resemble the techniques used to obtain perturbations from real data. We define *absolute perturbations* simply as the subtraction of background from the simulated data and *relative perturbations* as those also divided by background (shown as a fraction or percentage). Absolute perturbations are given in the data's units and are useful when comparing to calibrated measurements. They also provide a visualization of the morphology in the most significant orders of magnitude. An example is provided in **Figure 3.5** using MAGIC results for a thunderstorm in the US midwest (Heale, Snively et al. 2019). The morphology of the data can be significantly different when using relative perturbations, revealing fluctuations that may be locally significant relative to their background. **Figure 3.6** shows a comparison between absolute and relative percentage perturbations for a GEMINI simulation of the O(^{1}D) airglow emission perturbations due to a tsunami (Inchin 2020). Relative perturbations can help understand the propagation of perturbations across the entire domain, however they can also bring out numerical artifacts, such as those due to computational precision or boundary effects. For this reason it is important to have a firm understanding of the computational characteristics of the simulation to properly interpret these relative perturbation plots. However, they may prove useful to study the local perturbations, that is, those with similar orders of magnitude or neighboring perturbations that can be grouped by any relevant atmospheric quantity, such as height or density. In the case of **Figure 3.6**, the only

significant observable morphology is the one shown for the absolute perturbation. Nevertheless, by using a relative perturbation plot we can trace perturbations all along the magnetic field lines, where they will eventually excite its opposite hemisphere counterpart, enough to be measurable; this may not provide any insight into the physical process but it serves as a diagnosis tool for the model and can reveal noise and artifacts where fluctuations are large relative to the ambient emission intensity.
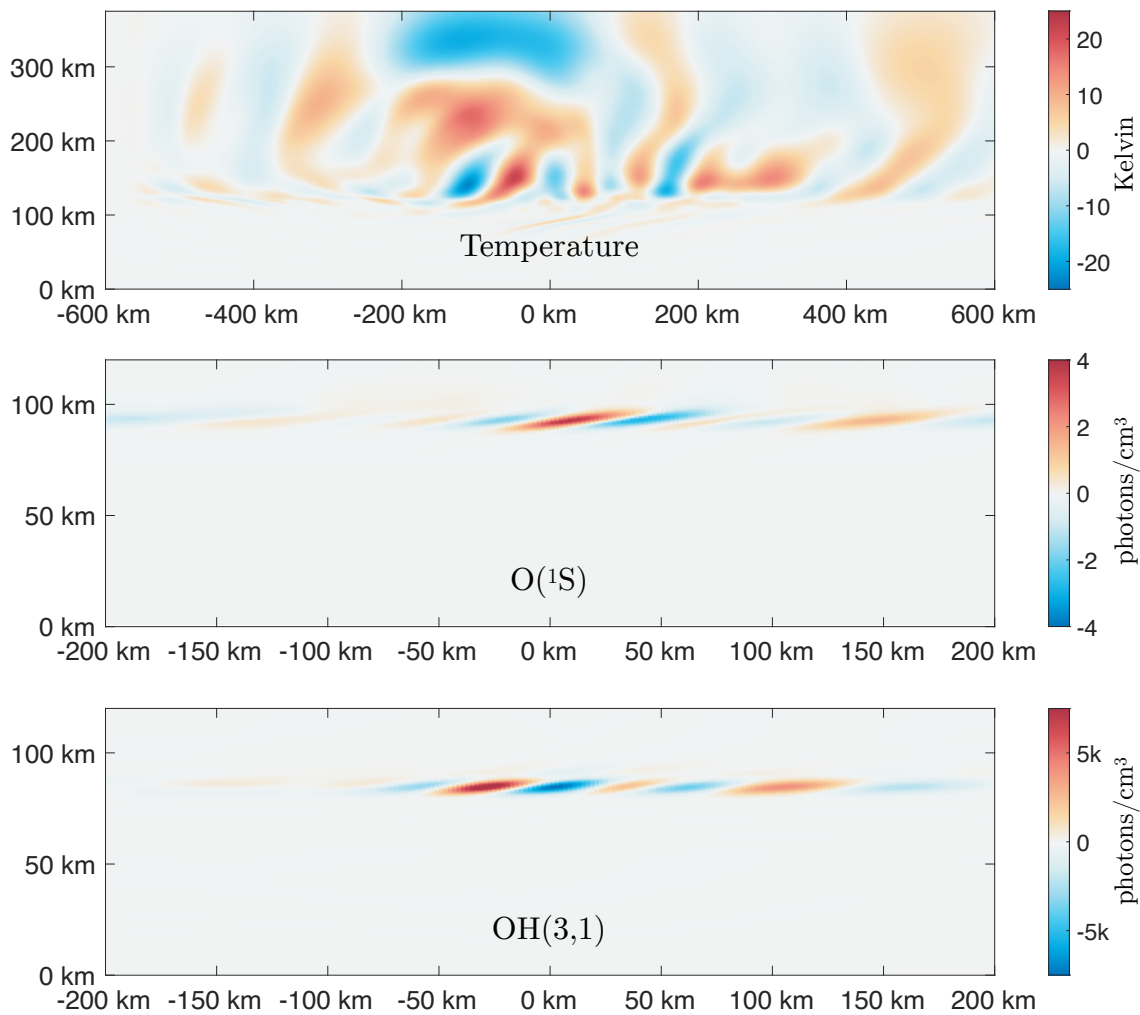
Figure 3.5. Absolute perturbation plots of MAGIC temperature, OH(3,1) and O(^{1}S) emissions due to a simulated thunderstorm. Data is sliced at middle position which is centered at latitude (42°).
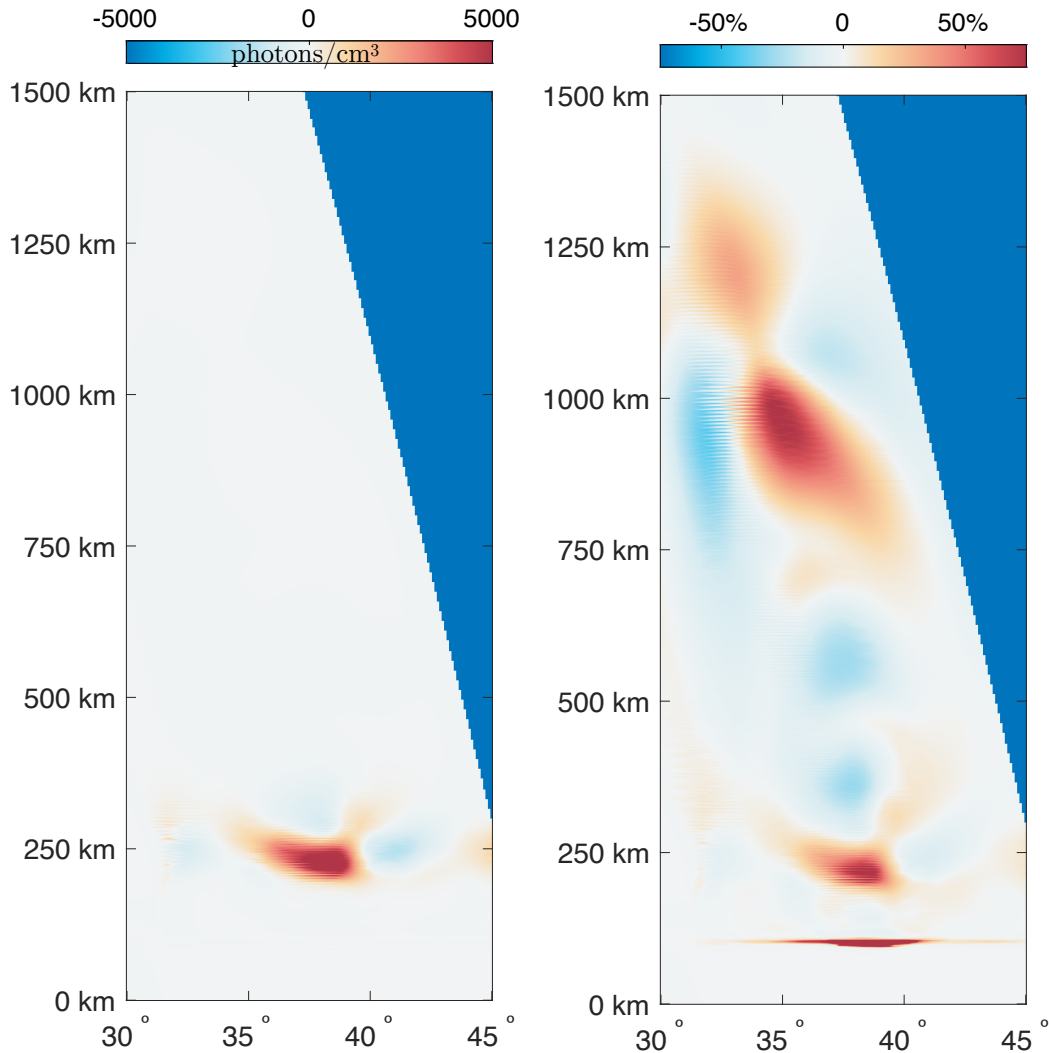
Figure 3.6. GEMINI O(^{1}D) airglow emissions perturbation plots due to a tsunami, projected onto geodetic coordinates and sliced at middle longitude (142°). (left) absolute perturbations; (right) relative percentage perturbations.

If we want to represent morphology in volumetric 3D data in a more significant way we have to circumvent some of the challenges associated with it. The main one being the fact that we interact with media through projections on a plane, so that we may print, publish and easily distribute it. We currently do possess several technologies for visualizing data in true 3D environments such virtual or augmented reality (AR/VR)

and 3D printing. Beyond these, however, there will always be data occlusion that has to be considered. The following sections present several techniques for meaningfully representing 3D volumetric data that is relevant to atmospheric wave phenomena at different scales.

3.1.2. Point clouds

A collection of rendered objects in 3D space where each object is at the location of a data point represents a point cloud. These "particles" are usually spheres or squares and are usually color coded to represent some meaningful quantity, such as the data point value itself, some type of gradient or textures. Point clouds are particularly useful when it is possible to track individual elements such as in a simulation of dynamical system of particles. This technique is used commonly for visualizing mass densities fluids such as liquids, gas, smoke, clouds or even plasma in magnetohydrodynamics (Macklin and Müller 2013, Lehmann, Federrath et al. 2016); relevant uses for AGW phenomena is in the study of turbulence (Fritts, Wang et al. 2017). Here we present a volumetric visualization of an acoustic wave seen in airglow emissions in **Figure 3.7**. This representation characterizes well the density distribution of the particles, volume emission rates in this case, and can provide insight into the sampling of data according to morphologic features, such as whether large 3D-spatial gradients have enough resolution. **Figure 3.8** provides a comparison of point cloud sparsity and its impact on its visualization; it can be argued that for more complex features a lesser number of particles may provide a clearer view. It is important to mention that in a movie format there is a natural expectation from the viewer that each particle is persistent and tracked across frames. This is not the case for our point clouds which are not simulations of position dynamics, but rather fixed grid points whose values may or may not be represented in the point cloud.
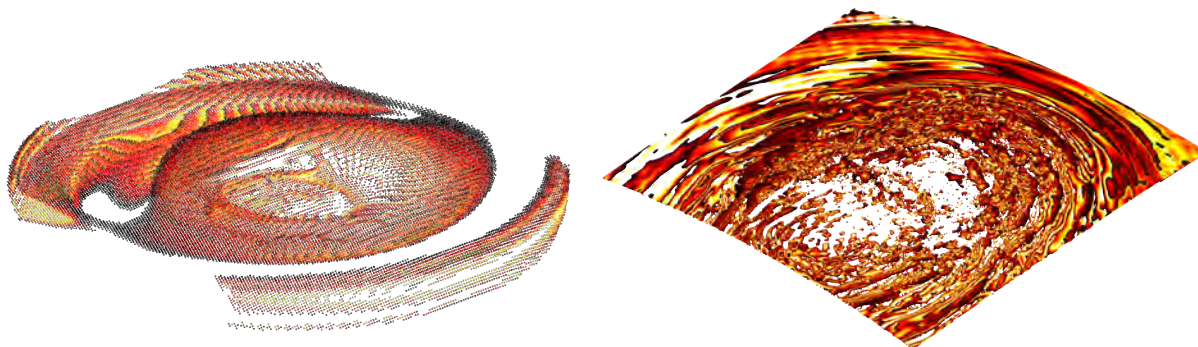
Figure 3.7. *Point clouds* of AGWs: (left) acoustic wave in O(^{1}D) 630.0 nm emission line due to a tsunami; (right) gravity wave in OH(3,1) emission band due to a thunderstorm. The same colormap has been used, however the point cloud on the right is much denser than the left one. Transparency has been linearly mapped to data values.
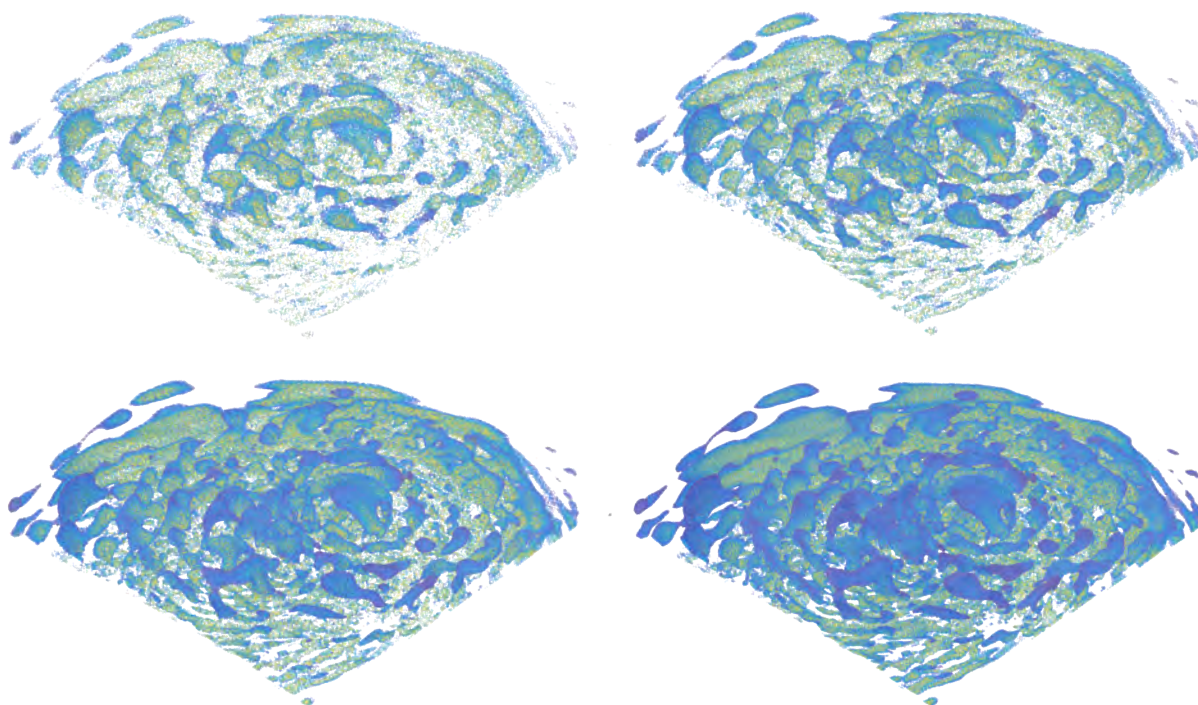
Figure 3.8. *Point clouds* of AGWs in temperature distribution at different particle densities: from top to bottom and left to right: 1:40, 1:20, 1:10, 1:5. Particle sizes are the same. Transparency has been linearly mapped to data values.

3.1.3. Isosurfaces

An isosurface is the 3D rendering of surfaces that connect data points with the same value, the isovalue, or the interpolation of them that yields such value. Its algorithm ensures that the nearest neighbors are chosen to conform to a smooth surface without overlapping. For large-scale/spatially-widespread features (such as highly-linear AGWs) isosurfaces provide a clear morphological view and when presented in movie format may provide excellent visualization of wave dynamics. The selection of isovalue is a design choice that will determine the amount of detail and shapes represented; it can be seen in **Figures 3.9** and **3.10** that a smaller isovalue captures the model's noise floor and domain extents while the large isovalue better represents observable perturbations.
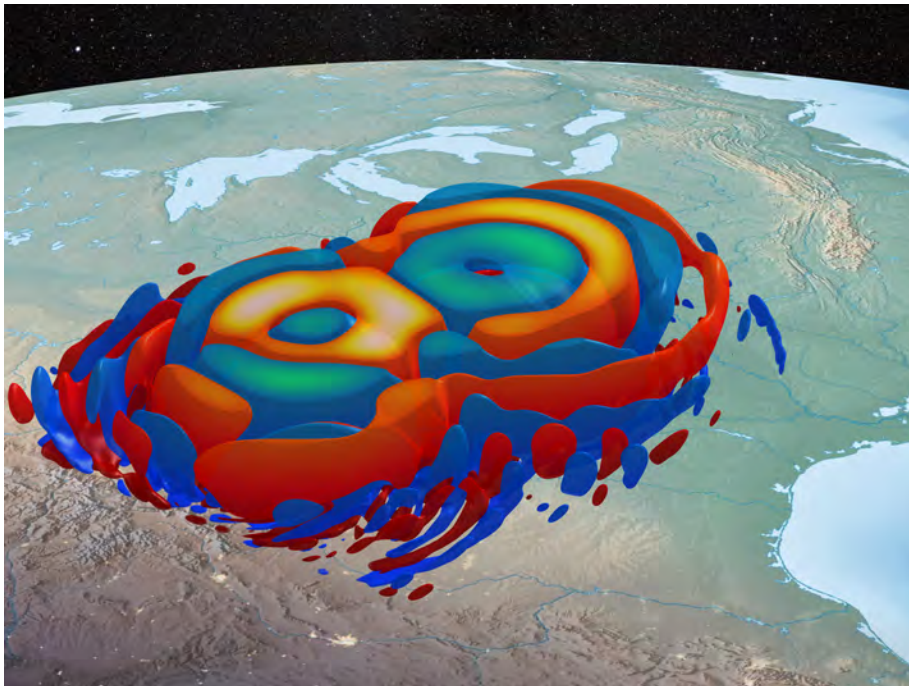
Figure 3.9. *Isosurfaces* of positive and negative MAGIC temperature perturbations for an isovalue of $\pm 2K$ due to a thunderstorm over the Midwest. Top height is 250 km.
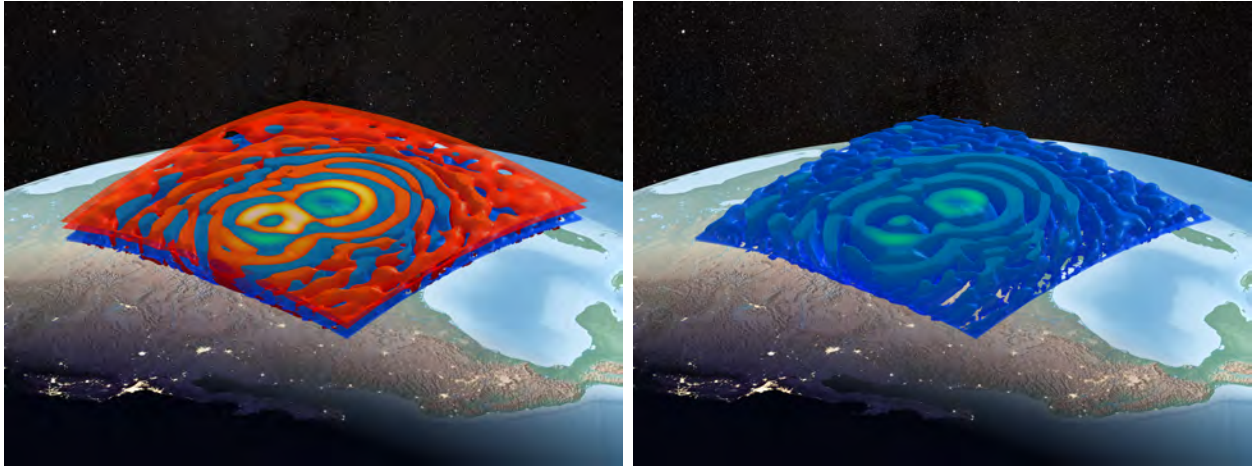
Figure 3.10. *Isosurfaces* of positive and negative (left) and only negative (right) MAGIC temperature perturbations for an isovalue of ± 0.1K due to a thunderstorm over the Midwest.

One of the challenges that isosurfaces seek to alleviate is the comparison between vertical and horizontal features, especially when horizontal wavelengths are much larger than vertical ones. One technique we can apply is *vertical stretching*, that is, the stretching of vertical scales so they appear comparable to the horizontal ones. This is another designer's choice and the end result will vary between uses. **Figures 3.11** and **3.12** show this for two MAGIC different simulations; **Figure 3.13** shows this for a GEMINI simulation. These examples show a clear vertical structure that appears "flatter" in the original scales. We can conclude then that having so much vertical extension appearing so flat means that the waves are highly slanted and line-of-sight imaging will have a significant impact on the imaged horizontal structure. In fact, overlapping projected images with isosurfaces in 3D space provides a direct comparison on the impact of such slants as well as the assumed layer height; we will show this later in **Chapter 4**. See Wright, Hindley et al. (2017, 2021) for more examples on vertical stretching of isosurfaces and a discussion of vertical wave parameters.
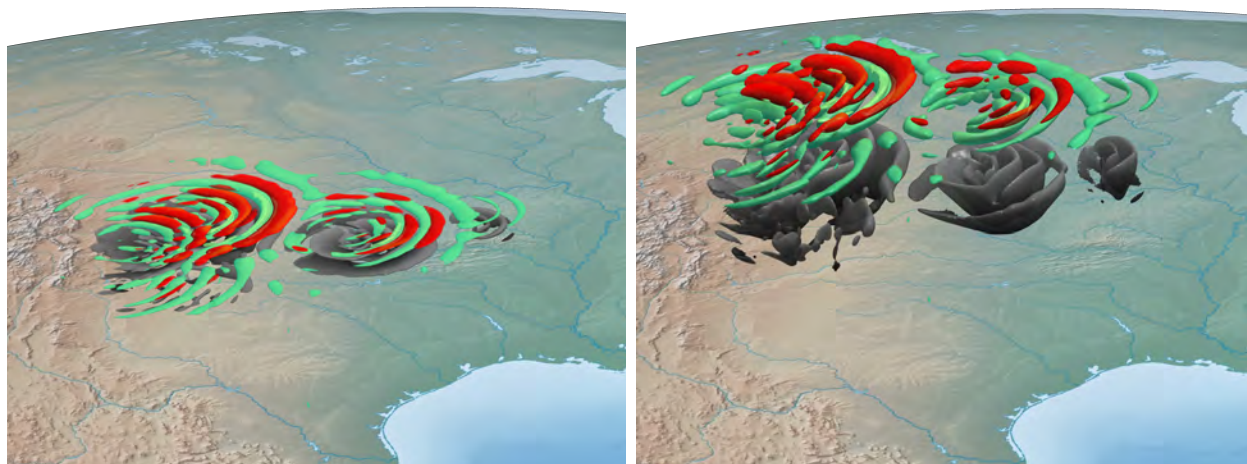
Figure 3.11. *Isosurfaces* of positive perturbations of MAGIC CO_2 radiances in gray, OH VER in green and OI VER in red due to a thunderstorm over the Midwest. (left) True scale. (right) Stretched in the vertical direction to better show vertical structure. Simulated date: 2016/07/08 12:51:30 UTC.
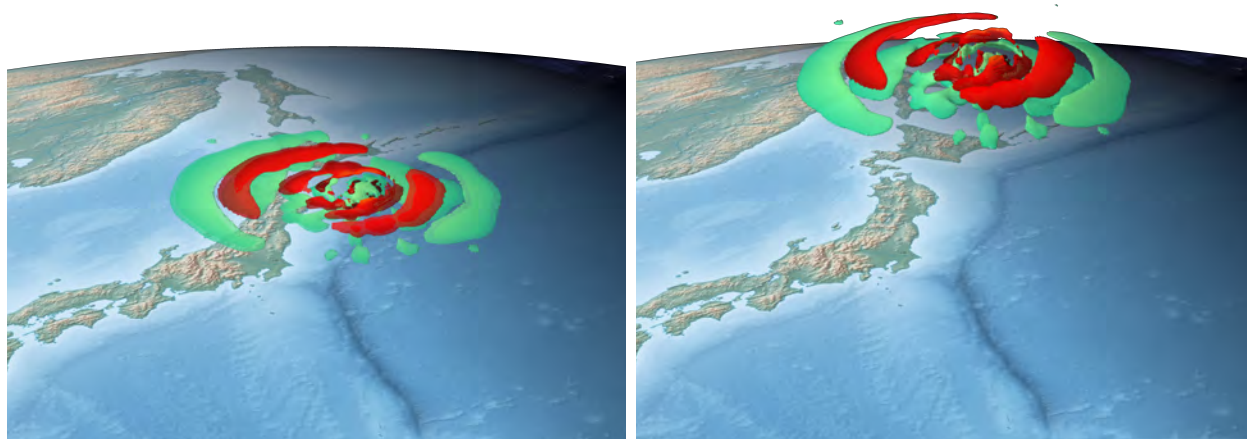
Figure 3.12. *Isosurfaces* of positive perturbations of MAGIC OH VER in green and OI VER in red due to a tsunami. (left) True scale. (right) Stretched in the vertical direction to better show vertical structure. Simulated date: 2016/07/08 12:51:30 UTC.
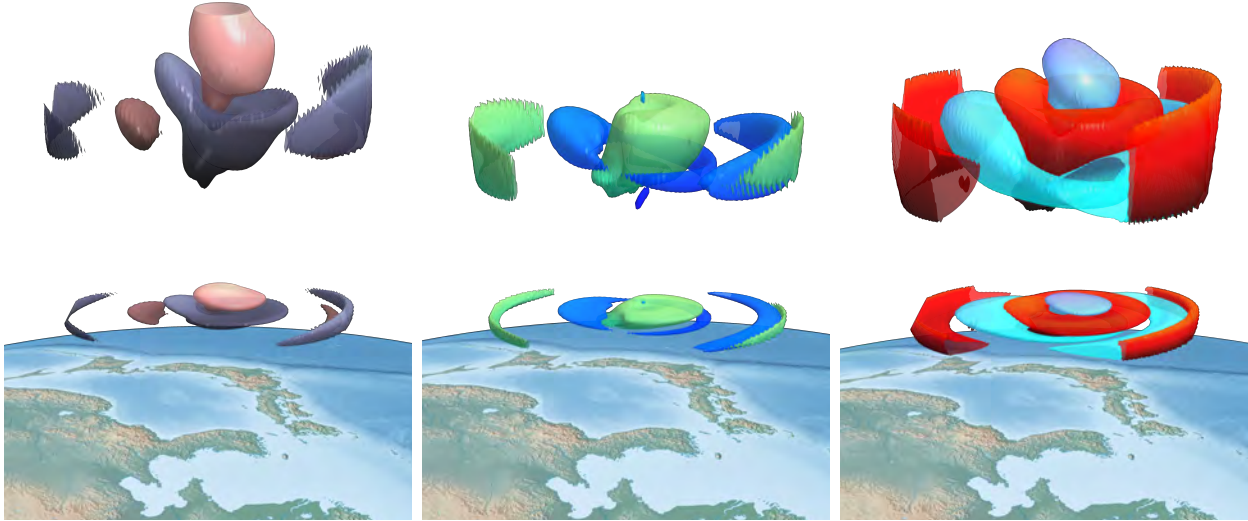
Figure 3.13. *Isosurfaces* of positive and negative perturbations for GEMINI due to a tsunami: electron density in pink (+) and gray (−), O(^{1}S) in green (+) and blue (−), O(^{1}D) VER in red (+) and light blue (−). An overlay of vertically stretched out isosurfaces at the top of each plot is included for comparison. There is very pronounced slant in the morphology of the wavefronts. Simulated date: 2011/03/11 14:46:23 LT.

Isosurfaces should be calculated from perturbation quantities and they can vary greatly in shape whether using absolute or relative perturbations. As discussed before for the case of slices, absolute perturbations will more appropriately show features within a given order of magnitude while relative perturbations will feature smaller detail throughout the entire domain. This is particularly useful when analyzing purely the propagation of information throughout the domain, such as in GEMINI simulations where relative perturbations can trace the impact all across to opposite magnetic hemisphere. Additionally we can better observe linearity and nonlinearity development across the vertical domain. While the significance of relative perturbations may be more technical than physical we may yet study the local influence throughout the atmospheric layers which could be relevant for in-situ measurements if such a study were desired. We show some interesting results from GEMINI when using relative perturbations in

Figure 3.14: the left and center plots show two different isovalues at the same simulation time. The smaller isovalue connects more surfaces and encapsulates the larger perturbations. Compare these plots to those of **Figure 3.13**; the perturbation plots are better at tracing the acoustic signatures propagation. Finally we demonstrate the effect of varying isovalues to trace perturbations along the entire magnetic field line in **Figure 3.15**.
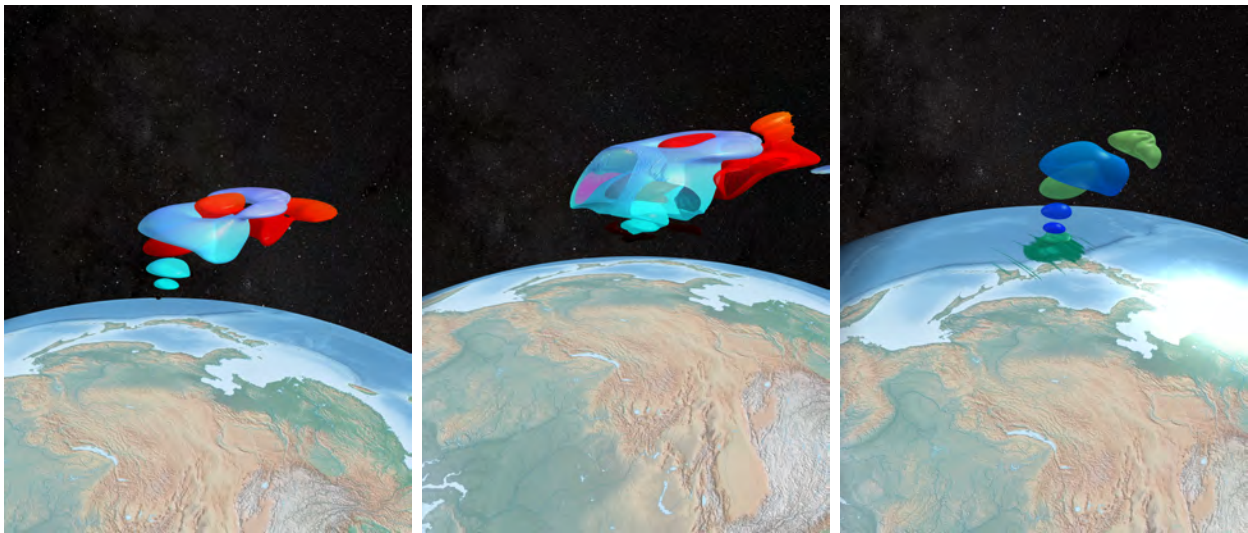
Figure 3.14. *Isosurfaces* of relative perturbations isovalue of GEMINI O(^{1}D) VER (left and center) and OI 557.7 nm VER (right). Isovalues at 200% (left) 80% (center) and 20% (right) The large isovalue brings out significant wave structures even at high altitudes.
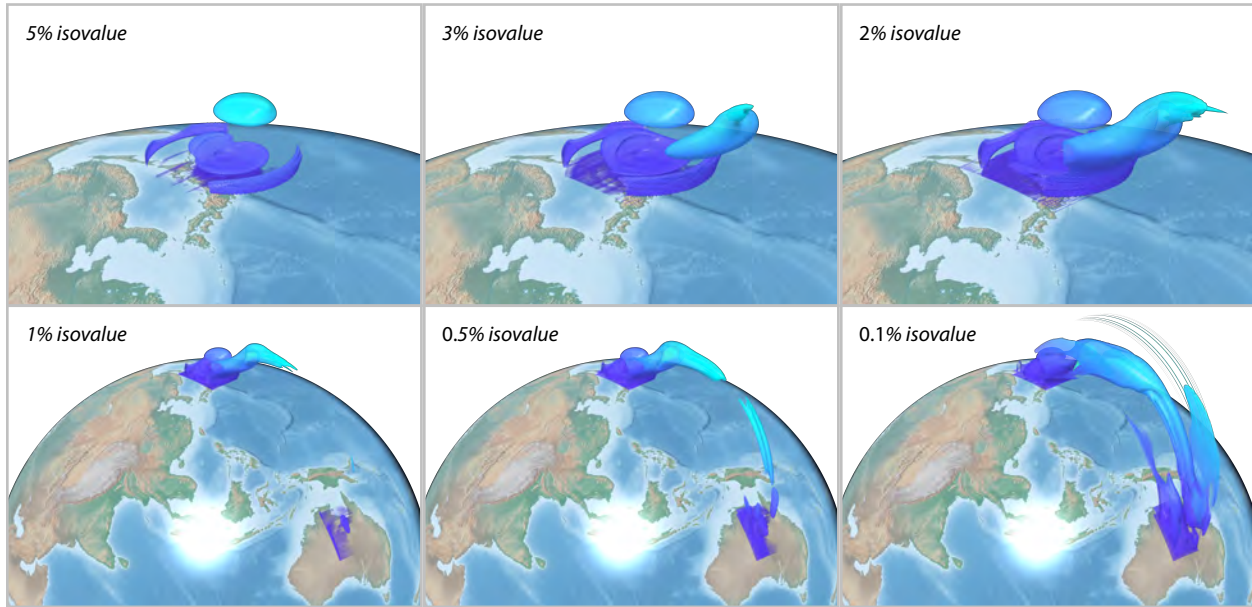
Figure 3.15. Comparison of different isovalues for *isosurfaces* of electron density along GEMINI's domain. The electric field perturbations are instantaneously propagated along the magnetic field lines under GEMINI's electrostatic approximation. Simulated date: 2011/03/11 14:46:23 LT.

3.1.4. Morphology enhancement

This technique has been developed to enhance topology for thin layers, represented by 2D plots, such as those obtained with real imager data. This consists in extruding 2D data by an amount equivalent to each pixel's magnitude and proportional to an arbitrary constant. By giving 3D topology to the data, we can better compare flat images to 3D volumetric structures such as isosurfaces or point clouds. We will use CO_2 and OH VER data on the thunderstorm over the Midwest to explain this technique. We have **Figure 3.16** with a schematic of the morphology enhancement creation process: the 3D surface is a composition of *caps*, which are slices chosen at the edges of the data where the top cap is used to protrude itself by an arbitrary stretch factor. The end result is an artificial volume that gives a 3D perspective to interpret intensity values.

Just as we saw in our discussion of isosurfaces, stretching vertical scales may greatly improve the visualization as exemplified in **Figure 3.17** with a comparison of height vs horizontal ratios, or, it may create a distorted visualization that may instead be harder to interpret. Particular to this technique is the choice of caps, mainly the choice of the top height; **Figure 3.18** presents an example where we choose different top caps through the upper part of the thin airglow layer. Lastly we show **Figure 3.19** and **Figure 3.20** where we include the whole globe and optional transparencies for the surfaces. Since this technique is derived from the use of slices some of the considerations mentioned before still apply. Namely for large spatial scales occlusion is still a concern when stacking layers and certain projections might still be better suited for this technique. However most 3D visualization use the concept of world coordinates, which is a fixed Cartesian system that represents 3D space. This concept we will be further developed on in the following section.
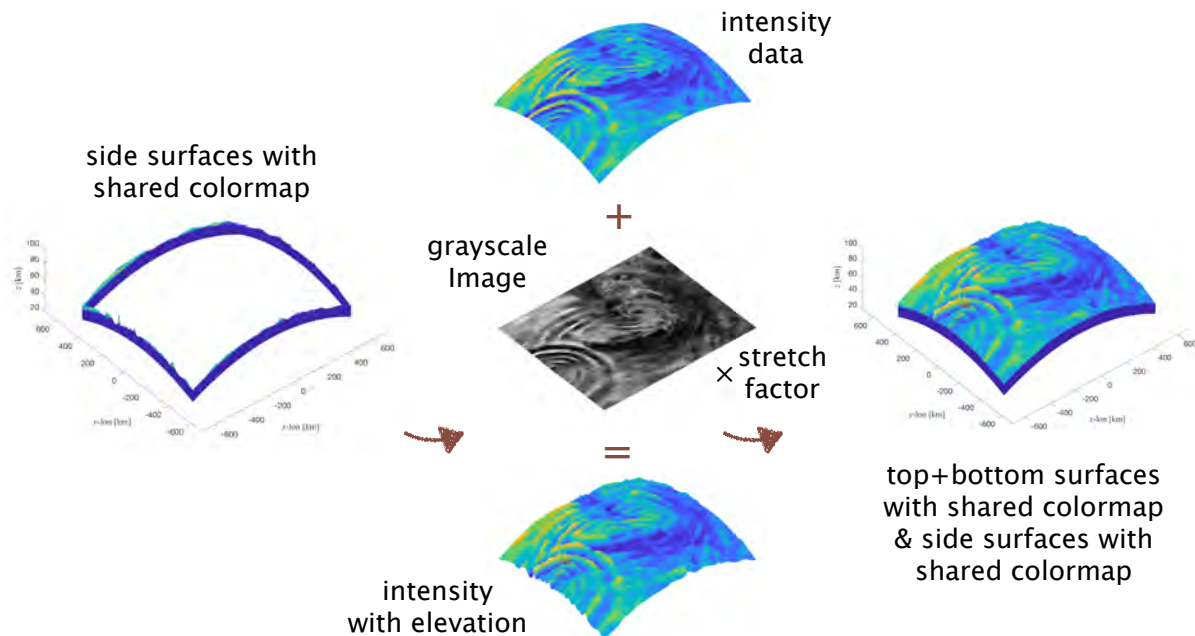
Figure 3.16. Schematic of the creation of a *morphology enhancement visualization.* Side surfaces are slices plotted in 3D space, intensity data of the top slice is stretched by an arbitrary stretch factor.
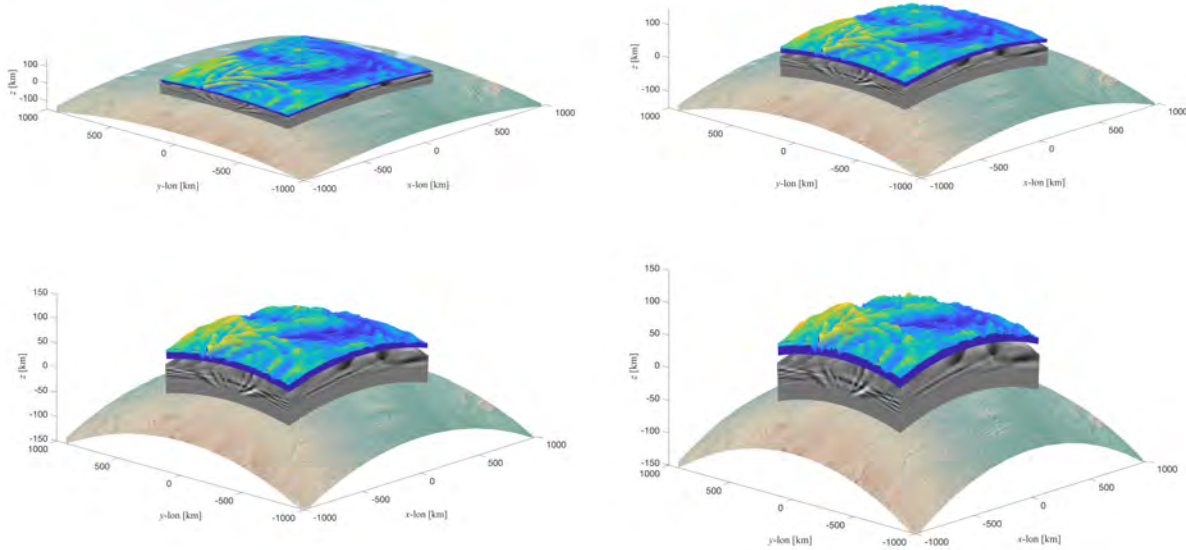
Figure 3.17. Comparison of different z vs x, y ratios for a *morphology enhancement visualization.* From left to right and top to bottom: 1:1, 2:1, 3:1, 4:1.
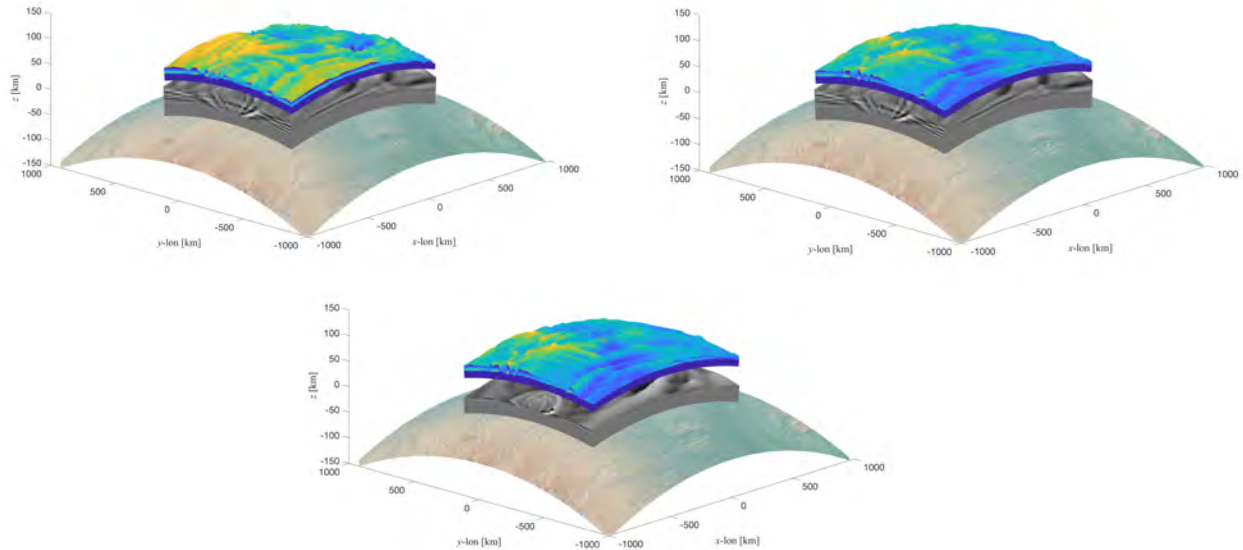
Figure 3.18. Comparison of different top surface choice for a *morphology enhancement visualization.* From left to right and top to bottom: CO_2 @ 60 km & OH @ 90 km, CO_2 @ 60 km & OH @ 95 km, CO_2 @ 35 km & OH @ 95 km.
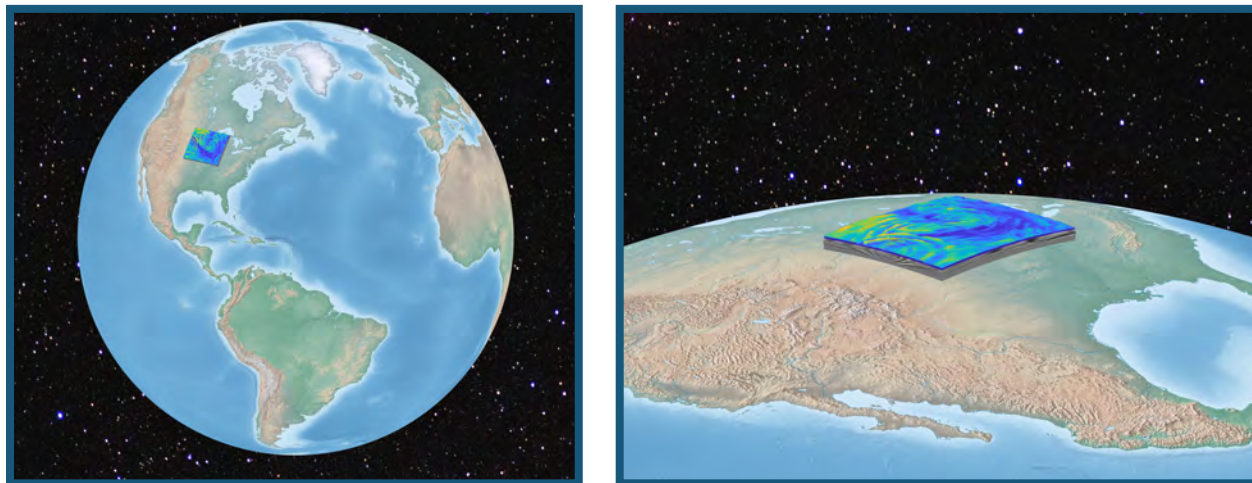
Figure 3.19. *Morphology enhancement surfaces* mapped to the globe with a true 1:1 z vs x, y ratio.
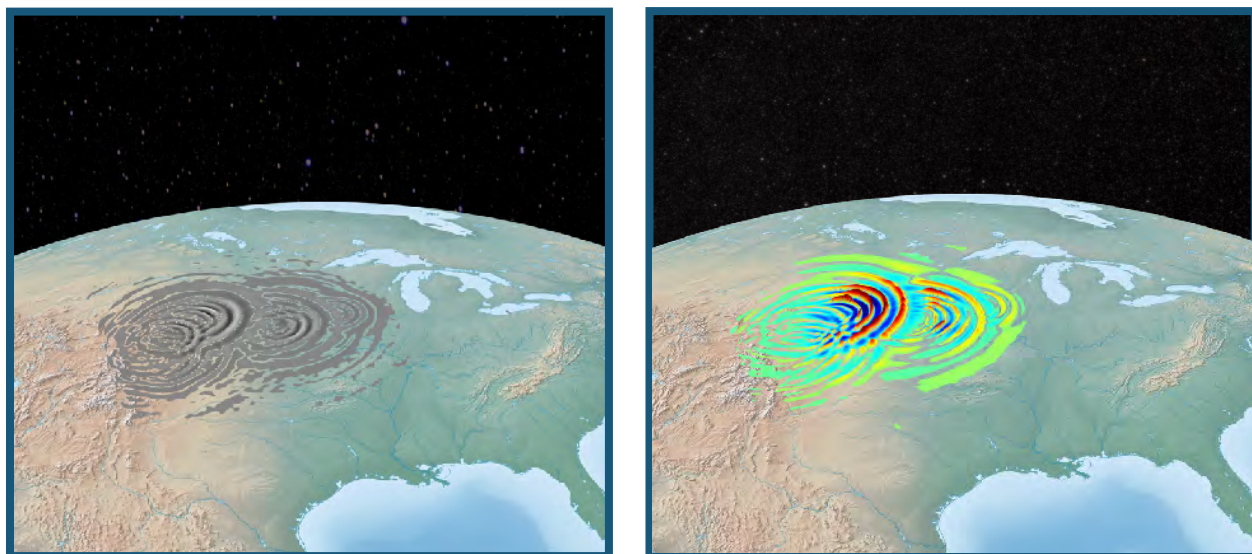
Figure 3.20. *Morphology enhancement surfaces* with included transparency linearly mapped to the lower values up to a certain opacity threshold. (Left) CO_2 BWT (right) OH(3,1).

As a final remark for this technique, it must be acknowledged that the choice of *intensity* layer that maps out the height that creates the topography may or should be in fact different than the intensity itself. In other words, any relevant sliced data can be suited for creating the height displacement including estimates of actual displacements. This opens the opportunity to represent different physical quantities, such as vertical gradients or the Krassovsky parameters that relate intensity and temperature perturbations and may better characterize the morphological and dynamical features (Ghodpage, Taori et al. 2015 and references therein). This is left as a thought for future work.

3.2. Camera projections

We will briefly discuss the 2 possible ways of viewing 3D space defined by the *world coordinates* that describe it. In computer graphics 3D objects positions are described by the Cartesian system that makes up the world coordinates, in this space both the 3D objects and the *camera* exist. The relationship between the objects and the camera is given by the *camera coordinates* and this can be a complex set of linear transforms depending on the complexity of the *camera system* (such as optics and particulates of the camera calibration). The most basic camera properties are its position in the world coordinates, its field-of-view that determines the target plane, its up-vector that determines the viewfinder orientation and finally the type of *camera projection*. The 2 projections we will use are *orthographic camera projection* and *perspective camera projection*:

- *Orthographic camera projection* preserves the size of objects and it's the default view in MATLAB. This projection images objects within a box.
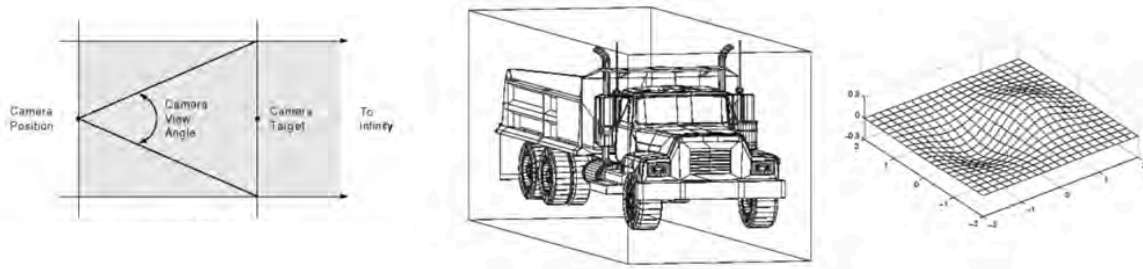
Figure 3.21. Orthographic camera projection. *Source: MATLAB documentation.*

- *Perspective camera projection* causes foreshortening with distances, similar to how an observer would see objects in 3D space. This projections images objects within a cone.
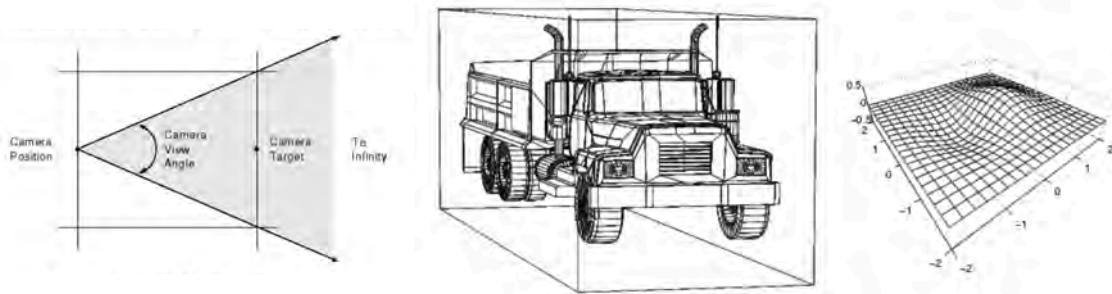
Figure 3.22. Perspective camera projection. *Source: MATLAB documentation.*

We will generally use an orthographic camera projection for interpreting volumetric data, due to its characteristic of preserving scales. In fact, when not specified, all volumetric renderings are assumed to be an orthographic camera projection. On the other hand perspective camera projection is useful when simulation points-of-view for an arbitrary observer. This is a concept akin to the equations we derived back in Chapter 2 relating an observer to points on the airglow layer; by rendering objects in 3D space and using a perspective camera projection we can readily simulate the field-of-view in terms of the 3D visualization of our choice. Here are some examples of this: as a baseline we have **Figure 3.23** with orthographic camera projections, then we have **Figure 3.24**

that shows the perspective view from a satellite with a track right through the heart of the storm, **Figure 3.25** shows the perspective view from a ground observer and finally using the Tohoku simulation data is **Figure 3.26** that presents a comparison of simulated perspective views from ground-based imagers looking at airglow layer.
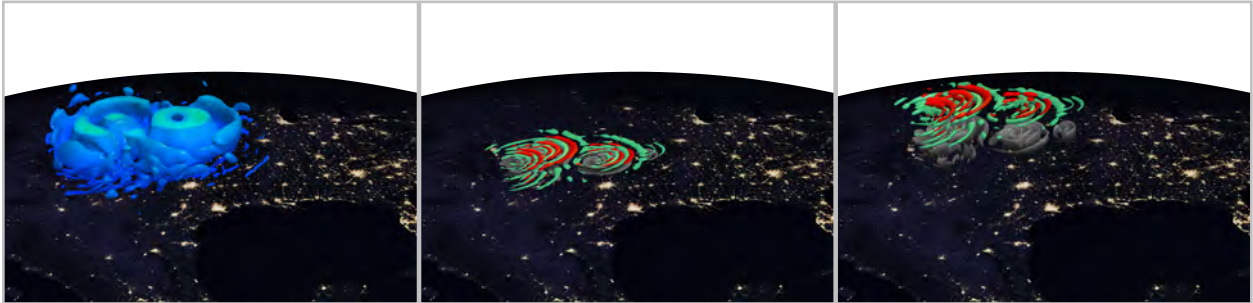
Figure 3.23. *Orthographic camera projections* of positive perturbations for: (left) temperature in blue, (center) CO_2 radiances in gray + OH VER in green + OI VER in red (right) same as center but stretched in the vertical direction to better show vertical structure. The big cities seen in the center are Houston, TX on the coast and Dallas-Fort Worth, TX. Simulated date: 2016/07/08 12:51:30 UTC.
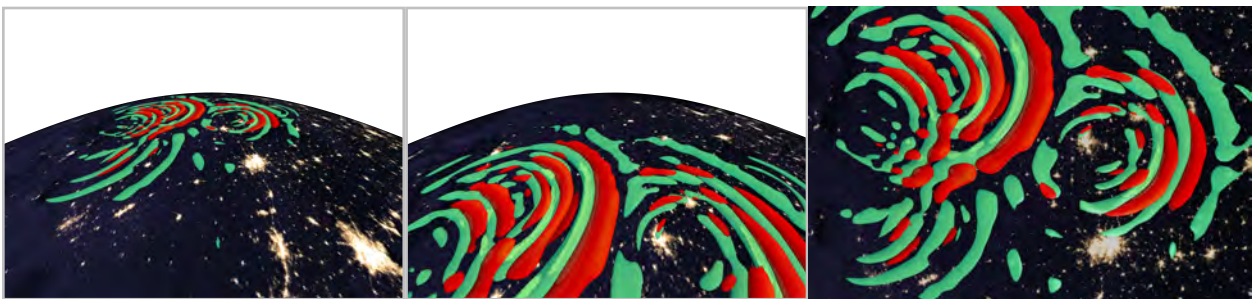
Figure 3.24. *Perspective camera projections* of positive perturbations for: OH VER in green + OI VER in red. The camera is at an altitude of ∼400 km with a track at ∼11° North. The different images are different positions along its track, (left) approximately above the city of San Angelo, TX and (center) New Cordell, OK. The (right) image is an observation straight down (towards nadir). The big cities seen here are Dallas-Fort Worth, TX and Oklahoma City, OK. Simulated date: 2016/07/08 12:51:30 UTC.
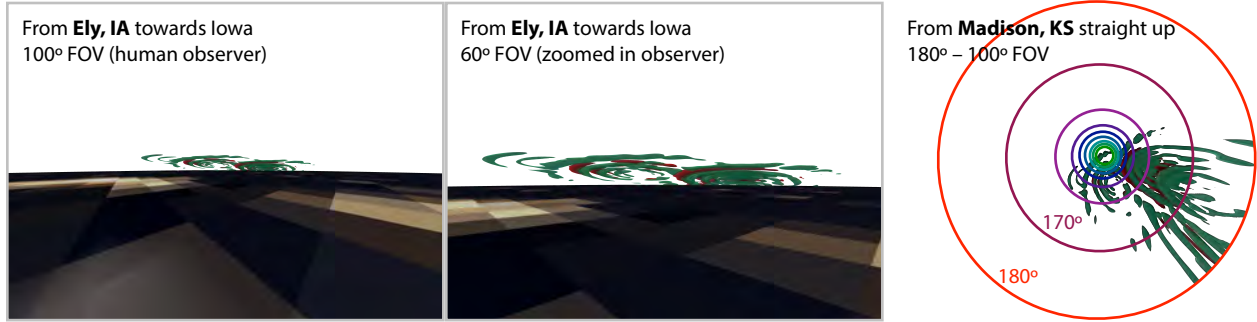
Figure 3.25. *Perspective camera projections* of positive perturbations for: OH VER in green + OI VER in red. The camera represents a human observer on Ely, IA looking towards the center of the storm in Iowa. (left) The average FOV of 100° is a good approximation of what the human eye would see (focused vision) if the airglow was bright enough. (center) A zoomed in view at 60° FOV. (right) An observer (or imager) on Madison, KS looking straight up: while an all-sky imager would be able to capture the entire 180º FOV, a human or standard camera would see closer to 100° FOV of the sky, in this case, the smallest circle plotted. Simulated date: 2016/07/08 12:51:30 UTC.

Perspective camera projection is useful for simulating different instruments FOV in the 3D environment. We can readily create visualizations that clearly show the data and instruments, relation in 3D space and relative to the globe, such as to create fly-over imagery for satellites and evaluate perspective distortions even before synthesizing imagery from simulated data.

OH(3,1) MAGIC O(^{1}S) MAGIC O(^{1}S) GEMINI O(^{1}D) GEMINI
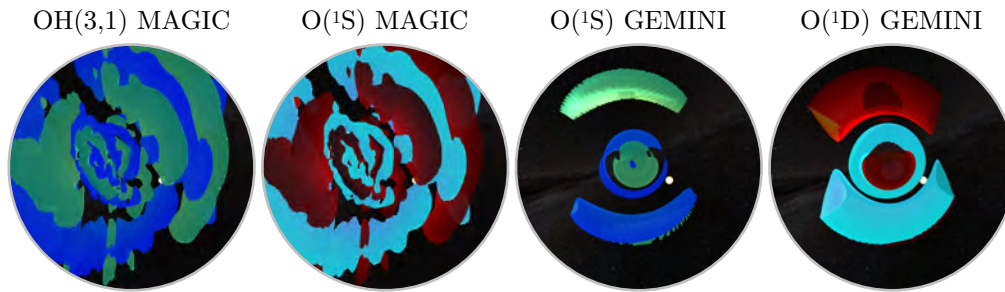
Figure 3.26. *Perspective camera projections* of positive and negative perturbations of OH(3,1) and O(^{1}S) from MAGIC and O(^{1}S) 557.7 nm and O(^{1}D) 630.0 nm from GEMINI. The observer is on the coast of Japan looking straight up (towards zenith) with a FOV of 160°. We have included stars (celestial sphere) and the position of the Sun; the latter can be seen close to zenith, which means that a CCD imager would be completely saturated in the daylight. (Note that we only consider *nightglow* imaging). Simulated date: 2011/03/11 16:21:22 LT for MAGIC and 14:46:23 LT for GEMINI; sunset was at 5:32 pm that day.

3.3. Map projections

So far, we have described the tools we developed for 3D visualization. These exist in the 3D space that is always defined as a 3D Cartesian system, the world coordinates. The great advantage of doing so is that data does not need to be projected and can be presented in true scale. This applies as well to the globe itself. The Earth, being approximately an oblate ellipsoid of revolution, is not a *developable* surface, meaning it cannot be represented without distortion as a continuous flat surface. The 3D globe representation is in fact the only one that preserves distances, directions, shapes and areas. But this being a true 3D object means that physically presenting data may be limited to cases where a 3D "globe" spherical projector may be used, which may or may

not be suited to the information we are trying to visualize, such as small regional detail or several layers of information that also extend in spherical radii above the surface. Using a 3D computer renderer is a much more fruitful and practical case and it is commonplace for familiar mapping software such as Google Earth or Systems Tool Kit (STK); in this case it is effortless to layer projected data that is shape- and area-preserving with great precision thanks to the current satellite mapmaking capabilities. This is an example of a *perspective map projection* and it's the one most people are familiar with; a photograph from space, aerial photography or a zoom-in on Google Earth are all perspective projections. This concept is not unlike the *perspective camera projection* we discussed previously. Conversely, if we place the observer at infinity then we achieve the *orthographic map projection,* a concept akin to the *orthographic camera projection.* These projections are also *azimuthal map projections*, which means all directions from the center point are straight lines and are accurate. See **Figure 3.27** for an overview of how the perspective map projection changes with the position of the viewer.
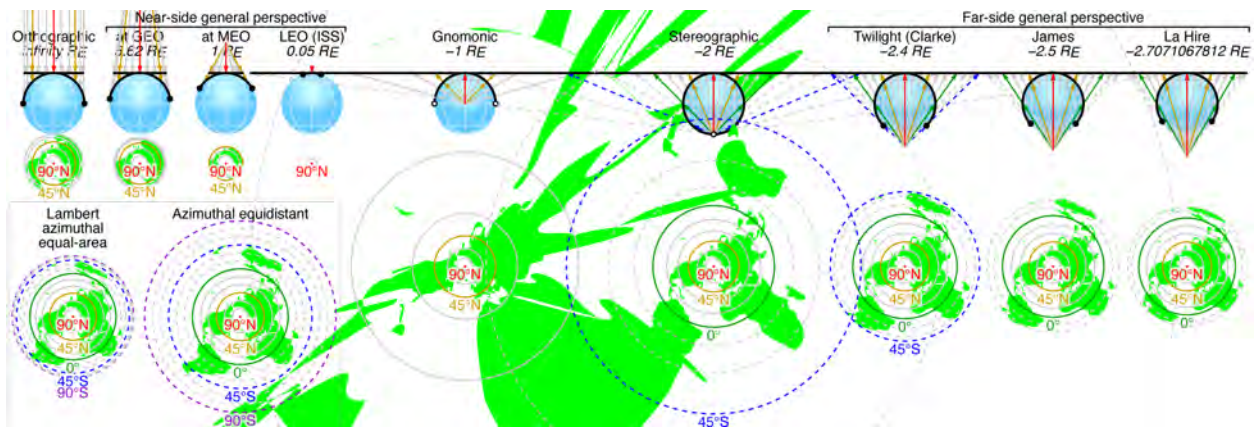
Figure 3.27. Overview of perspective map projections. *Source: Wikipedia, by Cmglee - Own work, CC BY-SA 3.0, https://commons.wikimedia.org/w/index.php? curid=38583511.*

We can in fact create a perspective map projection by rendering the globe in 3D and placing the camera at a vantage point using the perspective camera projection. There are two implications for this: firstly, it requires a 3D rendering environment and plotting onto the globe, and secondly, there is no precise mapping between the data and the pixels show on screen. This approach is necessary when doing perspective projections on 3D volumetric visualizations, as we saw in **Section 3.2.** However, each map projection has a geometric definition that relates pixels in a 2D image to exact locations on the map. If we recall from **Chapter 2**, synthetic images are described by their pixel coordinates $(\tilde{x}, \tilde{y})$ and are related to geodetic positions on the atmospheric layers, therefore we can choose to project them onto any suitable map projection. This process of mapping the integrated data in $\tilde{x}$ and $\tilde{y}$ pixel coordinates to the globe in latitude and longitude coordinates is called *unwarping*. The choice of map projection depends on the properties that matter the most for the unwarped data. The three most important properties of map projections are:

- *Conformal* which preserves angles locally (i.e. 90° angles between parallels and meridians) which in turn means shapes will be accurate.

- *Equal-area* which accurately portrays areas in relation to others everywhere on the map.

- *Equidistant* which accurately portrays distances between one or more points on the map depending on the type of projection.

Efforts to satisfy these properties have lead to the creation of dozens of map projections throughout history, including many arbitrary projections to suit the cartographer's need. In general, the type of projection to use will depend on two things: the shape and size of the area (i.e. is it a long-stretching, small or large area?) and the property that is more relevant to the data (i.e. equal-area for densities or conformal for shape comparison). This brings us to the particular needs of AGWs captured in images, whether synthetic or real data. By and large the most important property is the accurate measurement of

86

distance, therefore an *equidistant* projection will be most suited. That being said, equal-area projections are useful for certain parametrization of AGWs in global circulation models, such as comparing regional hot-spots across the globe or mapping momentum fluxes. **Figure 3.28** shows two types of momentum flux plots, the ones from a high-resolution model by Wedi, Polichtchouk et al. (2020) that are using equal-area maps and the ones from observational data by Zhou, Scaife et al. (2013) which are lower resolution satellite measurements and projected onto an equirectangular map. Regional hot-spots can be directly compared across the globe in the equal-area map, so we can accurately compare the area of a hotspot in the equatorial region to that of those at higher latitudes. The same cannot be done for the equidistant map, where areas are distorted and enlarged towards the poles. Even so, equirectangular maps, or *cylindrical* in general, are far more common for global studies, and the lack of general discussion on map projections suggests there is no purposeful advantageous use of map projections properties. Perhaps this is also due to the properties of the equirectangular map being *orthonormal* which means parallels and meridians have equal spacing and cross at a right angles. This orthonormality allows for the description of map and data in terms of *zonal* and *meridional* directions in uniform angle units; however, it is important to understand that distortion will always increase towards the poles. While the map coordinates themselves are orthonormal, the data projected onto them is not at true scale and is affected by the distortion. This distortion will play an important factor in any spectral analysis of data that has been projected, thus decompositions in native coordinate systems may be preferred.
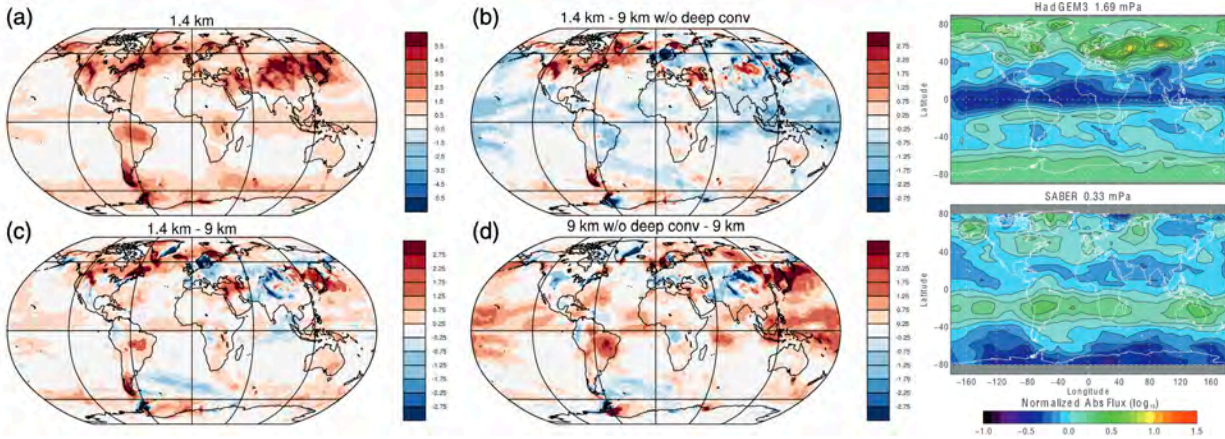
Figure 3.28. Literature comparison: global map projections for momentum fluxes. (Left) zonal-mean absolute gravity wave momentum flux [mPa] on an equal-area map projection (Wedi, Polichtchouk et al. 2020). (right) Model and satellite-derived absolute gravity wave momentum fluxes on an equirectangular map projection (Zhou, Scaife et al. 2013).

In **Figure 3.29** we have taken a plot directly from Sassi, Richter et al. (2010) in the equirectangular map projection and reprojected it onto an equal-area projection, the Galls-Peters projection. This is a plot of frontogenesis thresholds across the globe for WACCM, a global circulation model, that are used for gravity wave parametrization. This plot features a lot of regional hotspots in the high-latitudes, where distortions are the greatest. For comparison examine the two large features across the Bering Strait how their areas are more comparable in the equal area map. A useful tool for visually representing these distortions are the Tissot's indicatrices of deformation. These are connected to the metric of each map coordinate, in other words, it is directly related to the measure of distances at each coordinate. By obtaining these distances for a small value, such as 0.1°, an ellipse can be created and then drawn at a larger scale where its axes and rotation demonstrate the deformation as deviations from circles; see Goldberg and Gott (2006) for an expansion on this topic, including extra deformation parameters. **Figure 3.30** shows the corresponding deformation indicatrices for the projections in the

preceding figure. It is very evident that both of these projections have high distortions near the edges, a trait shared by all cylindrical projections.
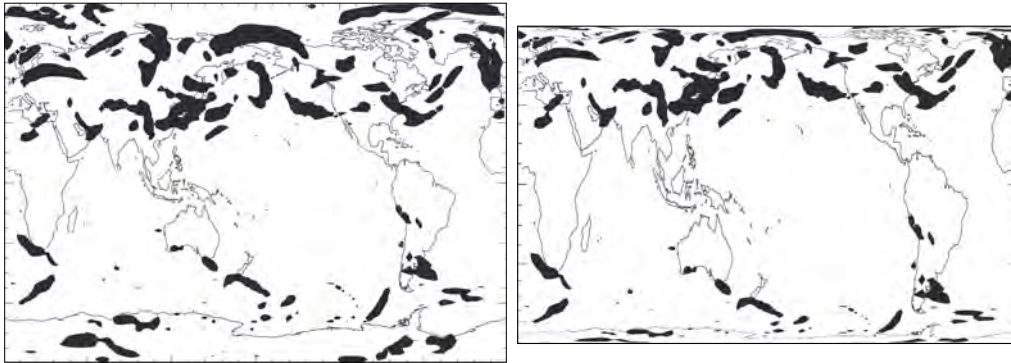
Figure 3.29. A comparison between an equirectangular map projection and an equal-area map projection with data. (left) is a gravity wave frontogenesis threshold plot for a global circulation model, WACCM, in an equirectangular map projection (detail from Richter, Sassi et al. 2010). (right) Same plot but reprojected onto the Gall-Peters equal-area projection, a map projection that greatly distorts shapes but accurately portrays sizes across the globe.
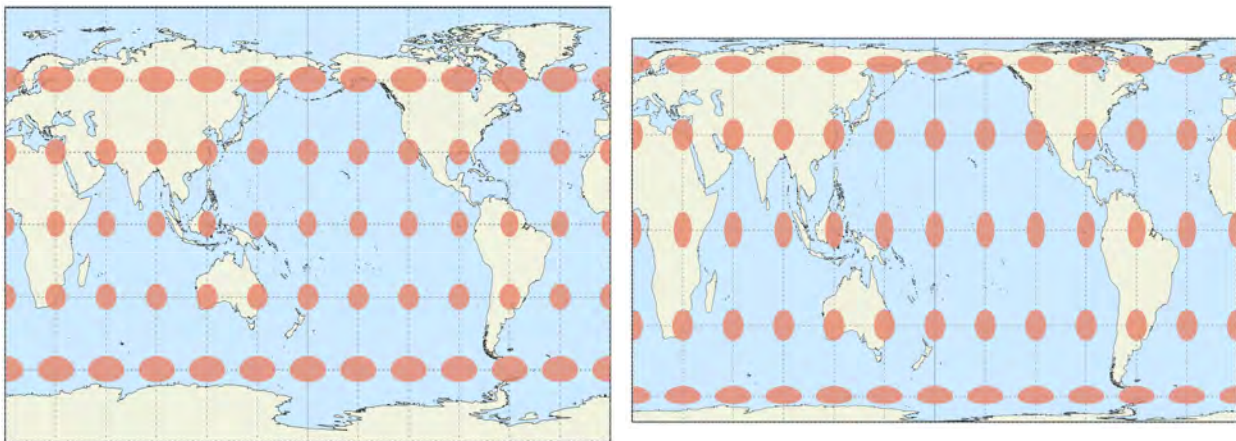
Figure 3.30. A comparison between an equirectangular map projection and an equal-area map projection with their Tissot's indicatrices of deformation: (left) equirectangular (also equidistant cylindrical or, in this case plate carré) that has been shortened on the horizontal axis and (right) the Gall-Peters equal-area.

For most equator-centered maps the high latitudes will show large distortions. For this reason it is commonplace to use *azimuthal projections* for polar regions. As before, a choice must be made for the most appropriate azimuthal projection; we've already shown examples of these in **Figure 3.27**. Using the same frontogenesis example as before, we now project the data onto an equidistant, equal-area and conformal azimuthal projections in **Figure 3.31** and their corresponding Tissot's indicatrices in **Figure 3.32**. We can see near the North Pole the deformation is minimal for all three projections. The equidistant plot has the property that all the distances from the center point are great circles (or geodesics for ellipsoids) and are correct. The equal-area projection benefits are minimal here since most of the frontogenesis features are close to the center. Equal-area maps are most relevant for whole world comparisons, so studies focusing only on regional AGWs may not benefit from them, where conformal and equidistant options more useful.

Figure 3.31. A comparison between azimuthal map projections with data: (left) azimuthal equidistant, (center) Lambert azimuthal equal-area and (right) stereographic which is conformal. Adapted from,Richter, Sassi et al. (2010)**.**
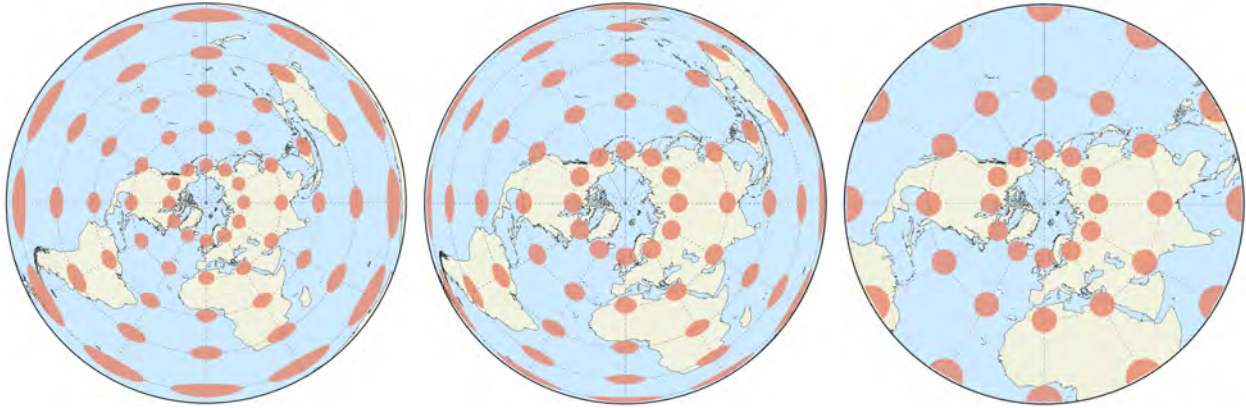
Figure 3.32. A comparison between azimuthal map projections and their Tissot's indicatrices of deformation: (left) azimuthal equidistant, (center) Lambert azimuthal equal-area and (right) stereographic which is conformal**.**

3.3.1. Projecting imaging data

The previous consideration will inform what types of map projections are most useful and relevant to AGWs scales for MAGIC/GEMINI results. A good candidate relevant for all-sky imager data is the Mercator map projection that was discussed in **Section 2.5**, a conformal map projection that is useful in the definition of rhumb lines for calculating distances on the surface of an ellipsoid. As we saw before, the lines-of-sights for imagers have constant azimuth angles which therefore implies the use of rhumb lines is accurate. Therefore using the Mercator projection seems like the natural choice, and it has two positive characteristics: E-W and N-S cardinals are aligned with the x and y axis respectively and secondly all straight lines correspond to arc-lengths. The major concern is the fact that the spacing of the coordinates is not uniform, a requisite for spectral analysis. Another possibility is to use a map projection that works naturally with the airglow-imager geometry. Recalling again **Section 2.5** which talks about calculating arc distances for mapping the airglow from an origin point (imager's location), then two possibilities arise: mapping with rhumb lines as we just discussed, or

mapping with great circles or geodesics. The former gives rise to the *loximuthal projection*, a pseudocylindrical projection, and the latter is a fundamental property in any azimuthal projection, which we have already discussed. There is an additional relevant projection, the *gnomonic projection*, where great circles are all straight lines; this projection only exists for a spherical representation of the Earth. We can examine the associated distortions at mid-latitudes for both the loximuthal and gnomonic projections in **Figure 3.33**. As expected, the loximuthal projection has rhumb lines aligned with parallels and meridians but it shows greater distortions between parallels. In contrast, the gnomonic projection has great circles as straight lines and shows little deformation within the chosen region. It should be mentioned that for points around the equator most projections will be excellent choices for preserving all of the properties. To satisfactorily decide upon a choice of projection we still need to fundamentally understand what we are trying to plot; this has been the recurring factor throughout this discussion. AGWs and related phenomena are modulated by winds and the Coriolis force which have a zonal dependency related to the Earth's rotation. As such, there is no significance in describing AGWs in terms of great circles or geodesics; it is more meaningful to have them aligned with the parallels. If this becomes our design parameter then any cylindrical or pseudocylindrical projection with low regional distortion will accurately represent meridional features of the AGWs and reasonably characterize spectral analyses.
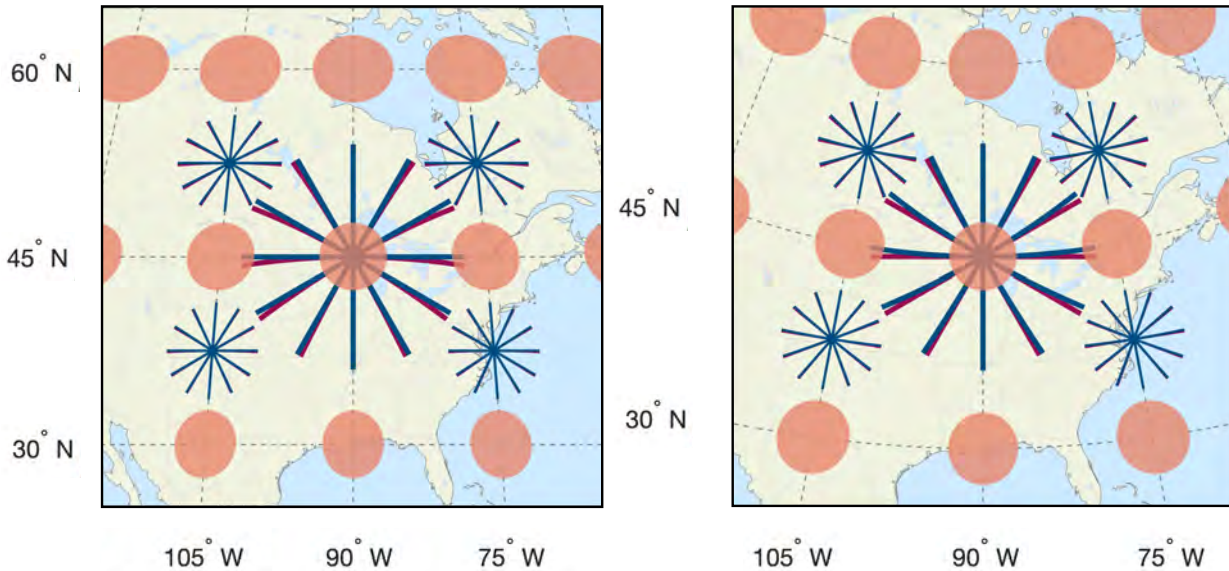
Figure 3.33. A comparison between the loximuthal map projection (left) and the gnomonic map projection (right) with their Tissot's indicatrices of deformation, centered at (40°N, 90°W). Plotted lines are distances of 1000 km from the center point: rhumb lines (blue lines) and great circles (red lines).

In an effort to better understand the merits of cylindrical map projections in comparison to the loximuthal projection, **Figure 3.34** shows contours of 3 distortion parameters in percentage: parallel, meridian and area. These distortions have a direct impact on the characteristics of any feature that might be present in our data. We can see that overall the loximuthal projection has the lowest distortion values, except for area. If conserving equal-area within the map borders is not a concern then loximuthal will be the choice with lowest overall distortion. However, loximuthal is not a true cylindrical map projection and has all types of distortions. The angle deviation error introduced by it is effectively analog to using an azimuthal or conic projection in terms of obtaining meridional/zonal components; now we've come full-circle to choosing again between these projections. It should be evident at this point that using non-equal-area cylindrical projections will yield accurate equidistant meridional scales, but obtaining the equivalent for parallel scales is not possible in any of these map projections.
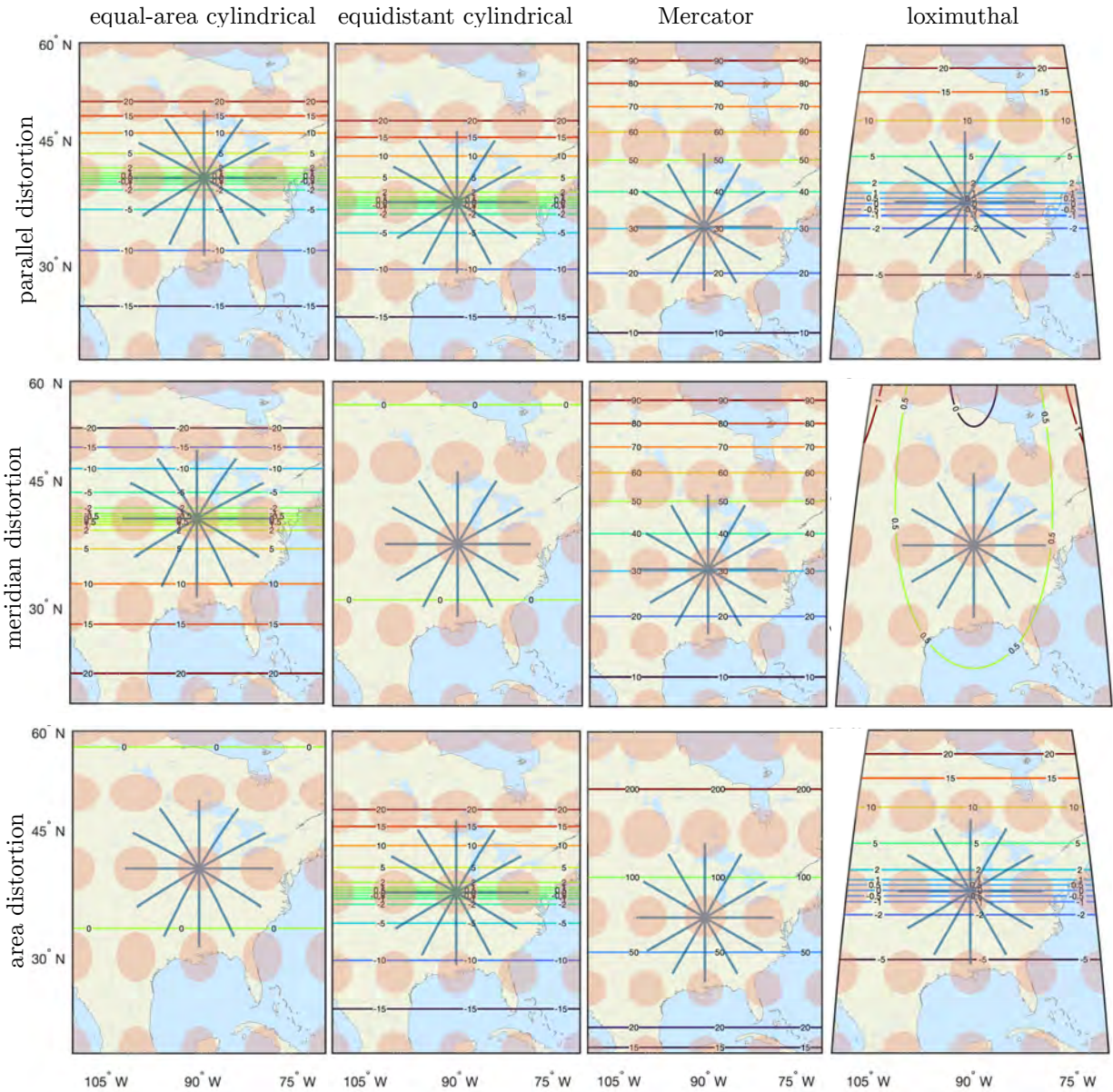
Figure 3.34. A comparison of cylindrical and the loximuthal projection and their distortions around mid-latitudes. Contour plots represent the percentage of distortion for the measure shown on the left. Tissot's indicatrices of deformation are also plotted at 10° latitude/longitude intervals. The blue lines are rhumb lines with a length of 1000 km. The loximuthal projection is the only one that has angle distortions, implied by the shape of the bounds of the plot which are the [110°W, 70°W] meridians. All projections, except for Mercator, have their standard parallels set at the latitude of the center of the data (40°N); for Mercator the standard parallel is set at the equator by definition.
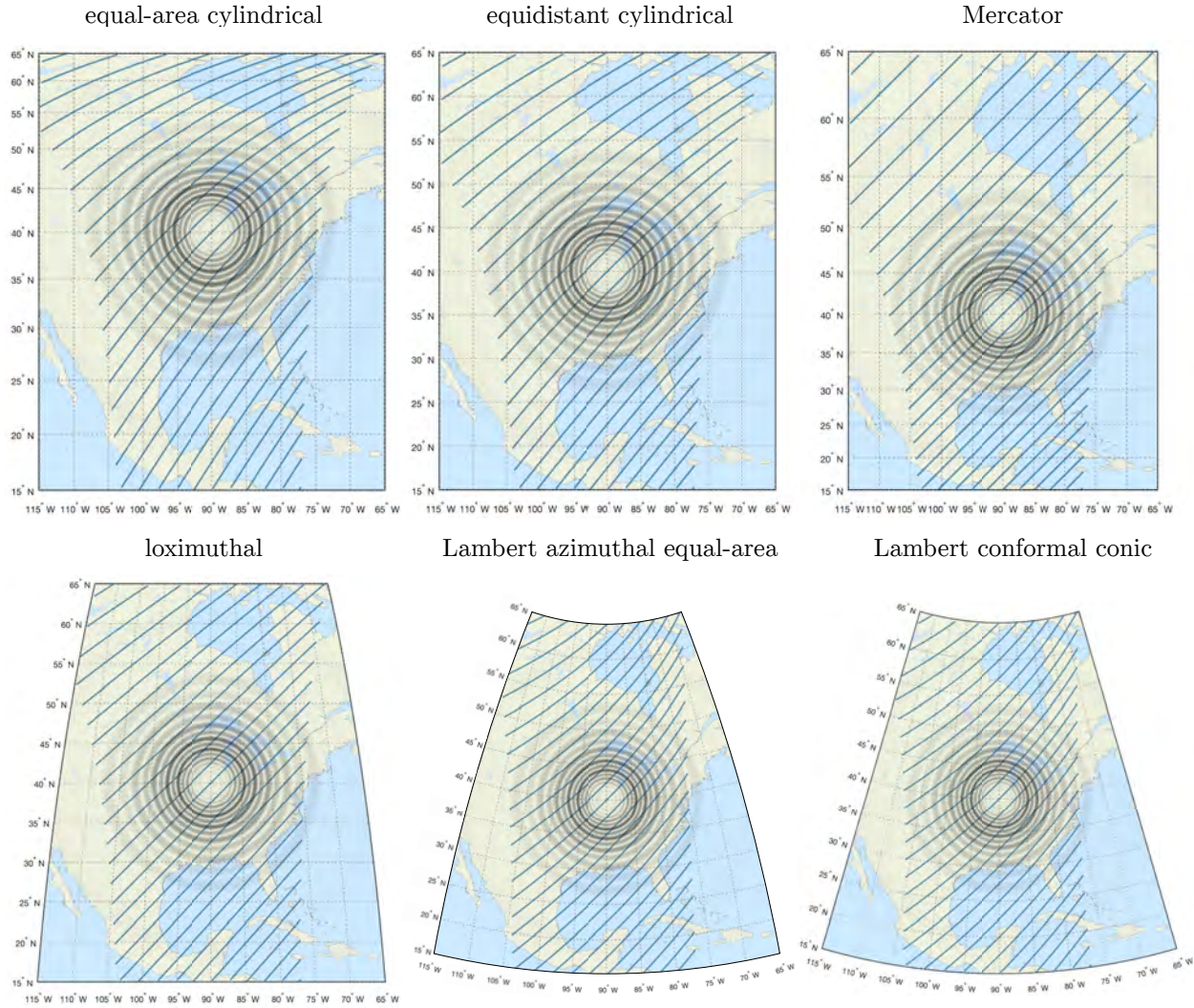
Figure 3.35. A comparison of map distortions for mock wavefronts with 45°-from-North orientation on different map projections around mid-latitudes. A MAGIC ideal concentric simulation is also plotted at (40°N, 90°W).

We can draw two conclusions from the previous discussion: azimuthal and conic projections are great at preserving shapes and scales even at comparable large distances from center; secondly, cylindrical projections align parallels and meridians but contain significant distortions at medium distances from center. Refer to **Figure 3.35** for a comparison using mock wavefronts to show distortion along the meridians. However cylindrical projections may better be suited for spectral analyses. This is in line with our

opening statement where we referred to two types of visualizations, those suited for mathematical analyses and those visualizations that preserve morphology or shape. In case of the Earth, if our mathematical analyses where done in spherical or even ellipsoidal coordinates, then the need for map projections is unnecessary and we could do those separately from the shape-preserving visualizations. For wave analyses, it is clear, we have to find a compromise, and the loximuthal projection is in fact a compromise map projection that is valuable for wave analyses near the center of the projection.

3.3.2. The loximuthal projection

We have discussed the loximuthal projection in the previous section and it was implied back in **Section 2.5** when obtaining the equations for distances over loxodromes or rhumb lines. This is a pseudo-cylindrical compromise projection that may suit wave analysis of atmospheric data, since it preserves East-West alignment and angle distortions are small around the center coordinate. As expected, this map projection is constructed by calculating the shortest[5] rhumb lines from a center point. **Figure 3.36** shows the wold map as projected in loximuthal coordinates. In contrast to other cylindrical projections, there is only a standard parallel to set, which is also the center of the coordinates. Different choice of standard parallel changes the shape and distribution of the graticule, as shown in **Figure 3.37**. Therefore, this projection is only useful for wave analyzes for a region around the choice of center coordinates. We can also see the angle and scale distortions follow the same deformation, making it easier to account for these in analyses, either as compensation in the found parameters or straight as an inherent error. This is the projection we have chosen for *unwarping* MAGIC data that is originally in Cartesian coordinates, and re-interpret it as ellipsoidal shells.

---

[5] The shortest rhumb line is the one that ends at the 180° meridian from the center coordinate. Otherwise this projection would allow for infinite extension through infinite rhumb lines.
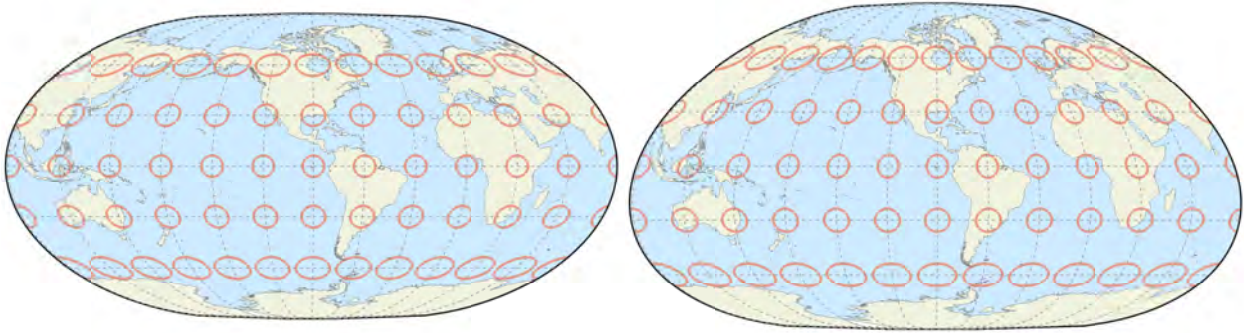
Figure 3.36. The loximuthal projection and its Tissot indicatrices of deformation, centered at 90°W. (left) Standard parallel is the equator. (right) the standard parallel is set at 40°N.
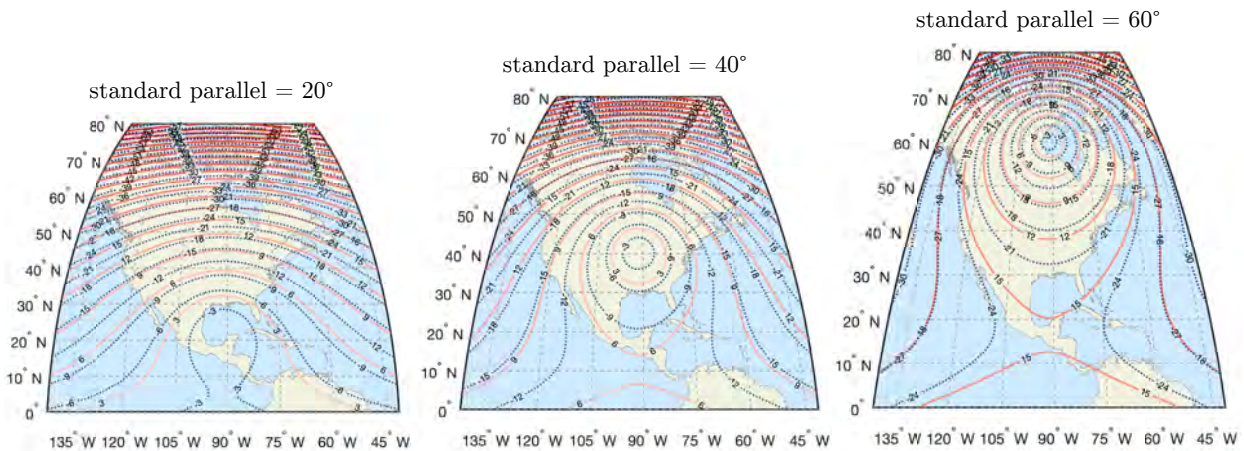
Figure 3.37. Loximuthal map projection with different standard parallels and aligned at 90°W longitude. Blue contours are maximum/minimum scale deformation and red contours are right-angle deviation. The shape of the map itself changes with different choice of standard parallel.

3.3.3. Projecting the MAGIC Cartesian grid

Local simulations with the MAGIC model are based on 3D Cartesian coordinates which means that there will always be inherent errors when mapping into geodetic

coordinates. MAGIC model inputs (such as background winds) are usually aligned East-West for the *x*-coordinate and South-North for the *y*-coordinate. For this reason the loximuthal projection becomes a viable option for mapping MAGIC results. We explore the effect of using different map projections to unwarp MAGIC in **Figures 3.38** and **3.39**. Note that while the unwarping projections are different, all of the plots are projected onto a loximuthal projection. We additionally show in these the effects of choosing different center coordinates for each projection.
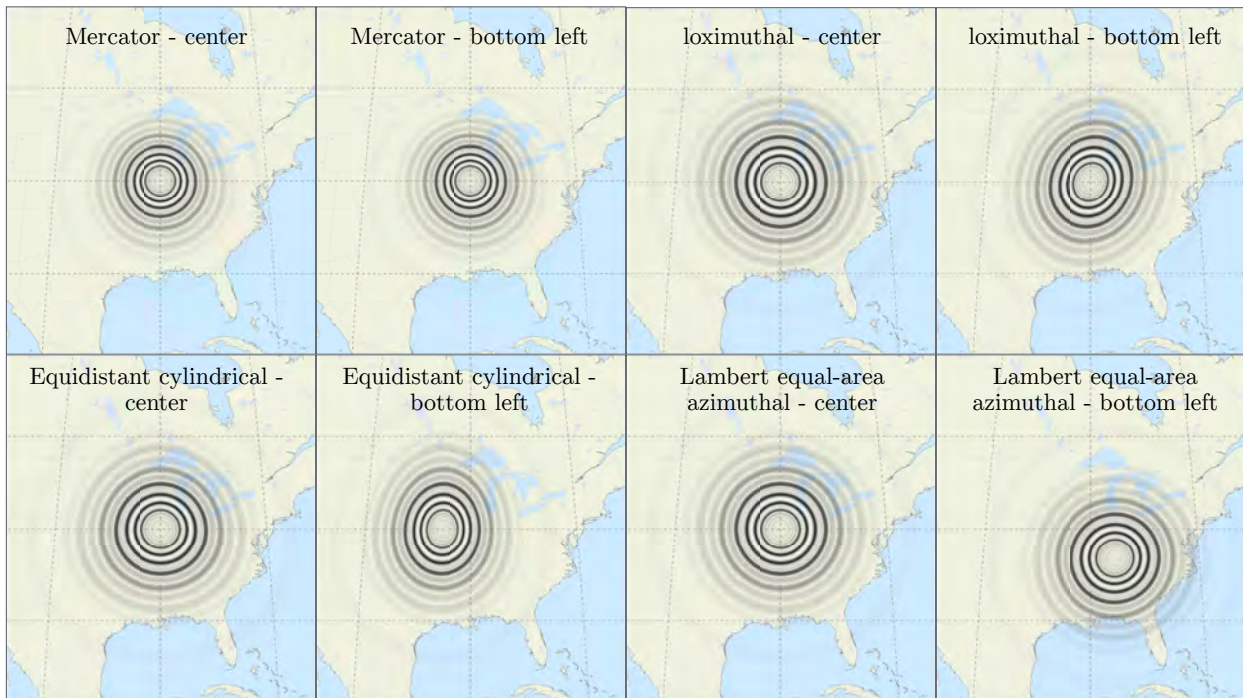
Figure 3.38. A comparison of different unwarping projections for MAGIC data. An ideal concentric simulation is used. Two center coordinates have been used for each projection: the middle coordinates and the bottom left of the MAGIC domain.
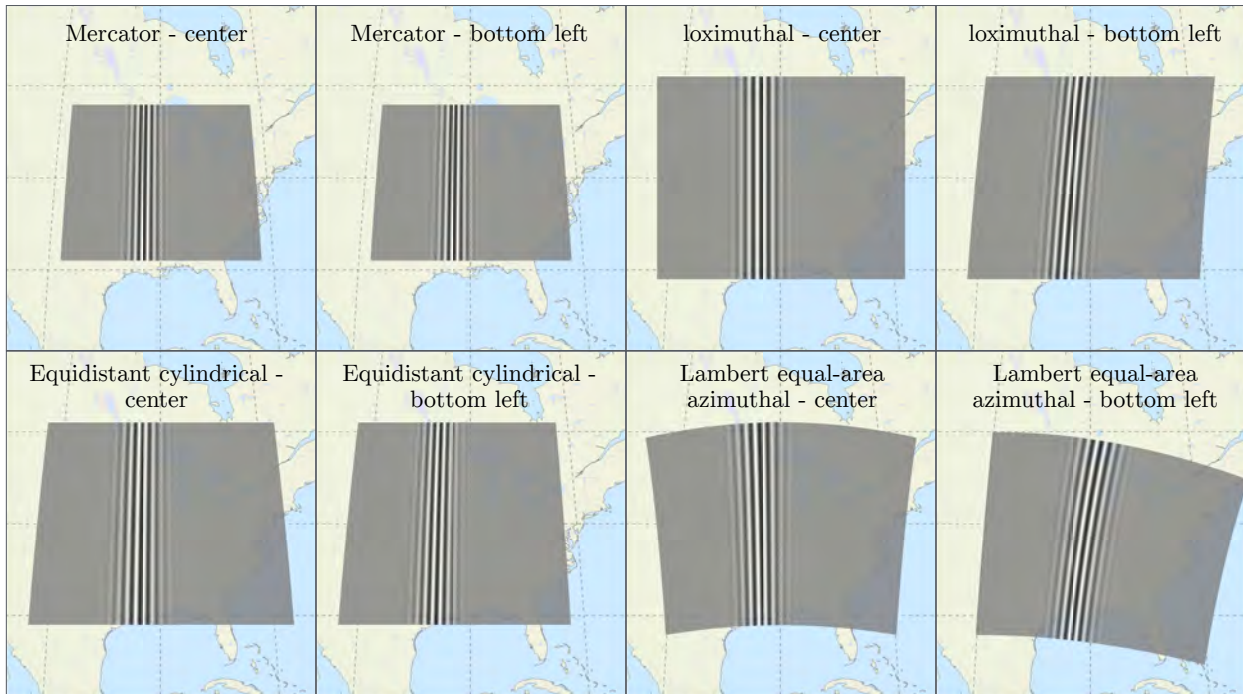
Figure 3.39. A comparison of different unwarping projections for MAGIC data. An ideal linear simulation is used. Two center coordinates have been used for each projection: the middle coordinates and the bottom left of the MAGIC domain.

It is evident from these plots that the mapped results can vary greatly in shape and position depending of not only the type of projection, but also the place of the center coordinates. The Mercator projection, for example, makes all the scales be smaller everywhere, introducing a base error everywhere. Note that the loximuthal-center projection appears undistorted; this happens when the unwarping projection is the same as the map plotting projection. With this reasoning, it is worth unwarping and plotting MAGIC data in the same projection to avoid compound errors. Another example is shown in **Figure 3.40**, where a temperature perturbation slice at 250 km height is shown with angle and scale deformation contours. We include further deformations in **Figure 3.41**. These deformations are calculated by MATLAB by perturbing locally the map projection and measuring the deviations from true distances.
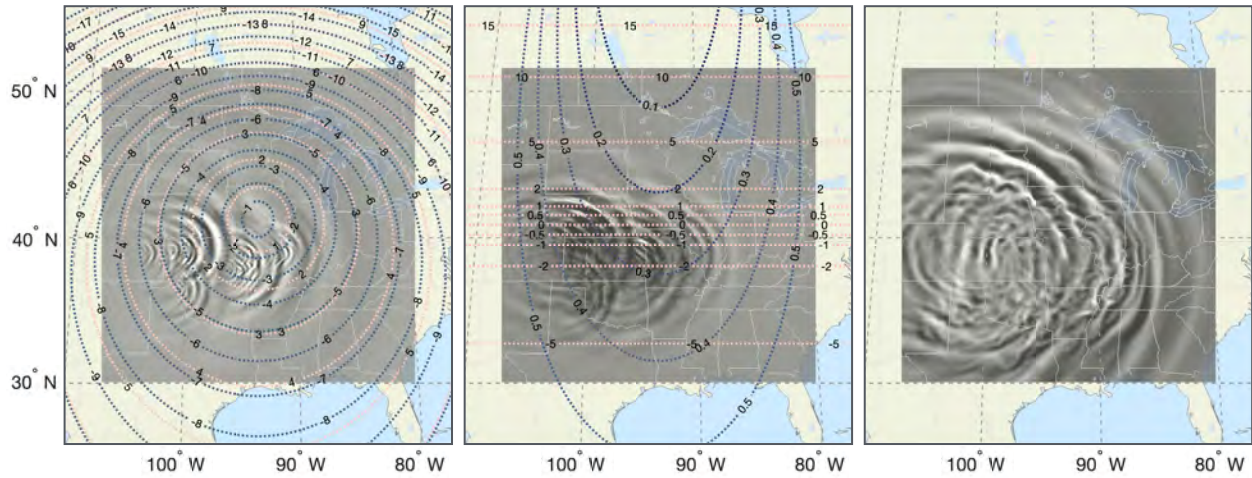
Figure 3.40. Three MAGIC simulation outputs, unwarped as a loximuthal projection and plotted onto a loximuthal map projection. (left) CO_2 vertical BWT perturbations with right-angle deviation contours shown in pink and maximum-to-minimum deformation ratios shown in blue. (center) OH(3,1) vertical IVER perturbations with parallel scaling contours shown in pink and meridian scaling shown in blue. (right) Temperature perturbations at 250 km height. Simulated data: Midwest thunderstorm 2016/07/08 5:15:12 UTC.
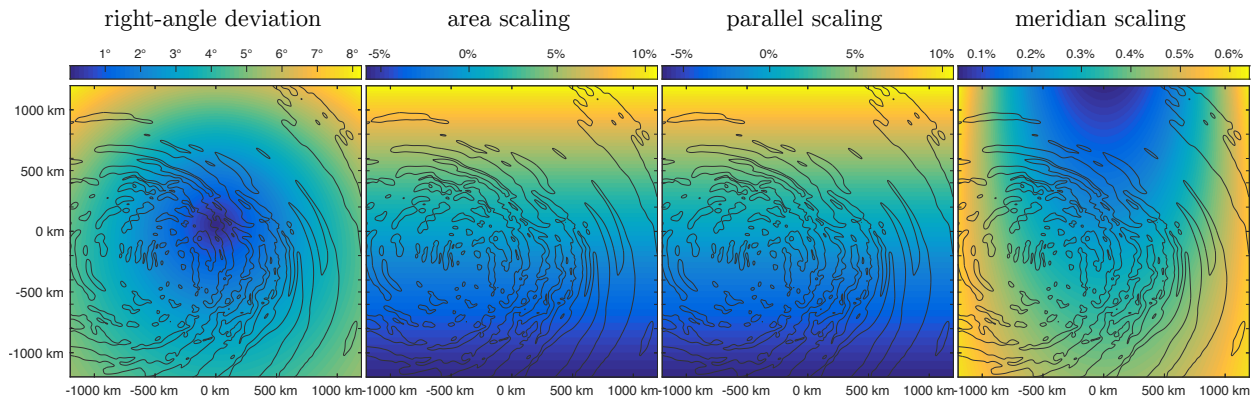
Figure 3.41. Distortions of the loximuthal unwarping of a MAGIC Cartesian grid centered at coordinates (40.82°N, 93.57°W). Low level contours of the MAGIC temperature perturbation data are shown for reference. Simulated data: Midwest thunderstorm 2016/07/08 5:15:12 UTC.

Since the meridional deformations are very small and this projection is always aligned with the East-West, the accuracy of zonal (East-West) measurements is very good. Furthermore, meridional (South-North) measurement errors can be calculated as shown in **Figure 3.41** for all the MAGIC domain. This error can then be properly propagated with spectral analysis confidence intervals to show a better estimate of the obtained wave parameters.

3.4. Example: combining all the visualization tools

In this section we will provide an overview of different cases for simultaneously utilizing different visualization tools for MAGIC and GEMINI simulation results. The first and foremost information that should be conveyed is the overall structure, or morphology, of the phenomena being studied; this includes a sense of its scale, domain and a clear perception of what type of wave structure it is. An example of this is shown in **Figure 3.42**, where a timestamp of MAGIC temperatures are shown for large scales in the 3D isosurface plot; along with it there are the more familiar slices that can provide a direct comparison with similar studies. If appropriate, grids, colorbars, labels and dates can be added to clearly quantify the scales. The 3D isosurface often helps validate the domain and dynamics of the simulation with a quick glance, while the slices convey the information of the magnitude of the perturbations, as well as the components of the wave parameters. This is a good start of a comprehensive analysis, but it is focused at the particular scales picked by the choice of isosurface.
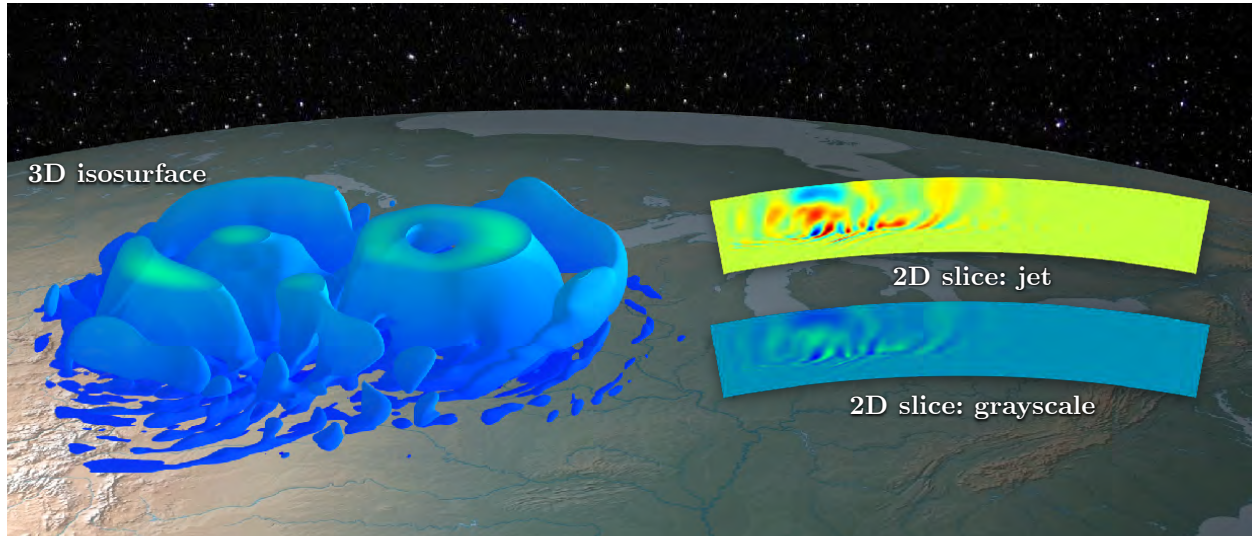
Figure 3.42. (background) Volumetric visualization (isosurface) of positive temperature perturbations of 3D modeled data above the US midwest. The simulation source is a large group of convective thunderstorms. (foreground) 2D slice through the middle latitude of the same 3D data shown in 2 distinct colormaps. (top) Jet colormap is a community standard for temperature. (bottom) A grayscale-based colormap may better represent positive and negative perturbations.

We present in **Figures 3.43 - 3.47** showcases of camera projections in combination with synthetic imaging and map projections. **Figure 3.43** shows isosurfaces of OH airglow perturbations that are both plotted on the exact same 3D space; green are the positive perturbations while blue are the negative ones. The left image is shown with an *orthographic camera projection* from a high altitude while the right circular image is a *perspective camera projection* where the camera is at the same location as the imager of **Figure 3.44**, looking straight up, aligned to North and with a 160° FOV. Compare the 3D perspective view to the simulated image in **Figure 3.44**. The data comes from a tsunamigenic OH airglow response modeled in MAGIC featured in Inchin et al. (2020). **Figure 3.44** left is a 3D sketch of the LOS intersections of a ground-based imager (at the location of the red dot) with the airglow layer (yellow shell) where the parula colors correspond to individual pixels and their corresponding FOV angles with the 0° at

zenith (center). The 2D unwarped image is the simulated observation in an *orthographic map projection*. The data comes from a tsunamigenic OH airglow response modeled in MAGIC featured in Inchin et al. (2020).
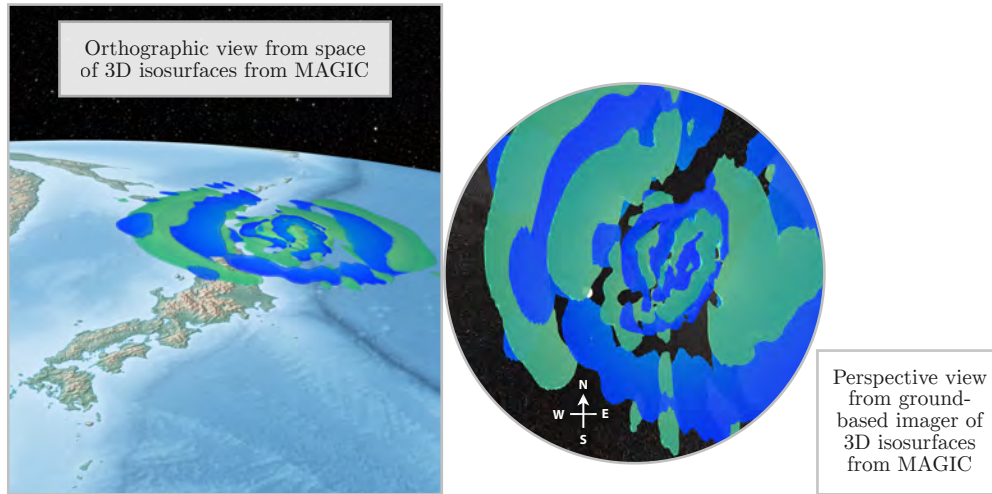
Figure 3.43. Isosurfaces of OH airglow perturbations due to a tsunami off the coast of Japan. Green are positive perturbations while blue are negative ones. (Left) Orthographic camera projection from a high altitude. (right) Perspective camera projection from a ground-based imager (same location of **Figure 3.44**). Note that at the time of the simulation the Sun is close to zenith and would have saturated a real CCD imager. Data provided from Inchin, Snively et al. (2020).
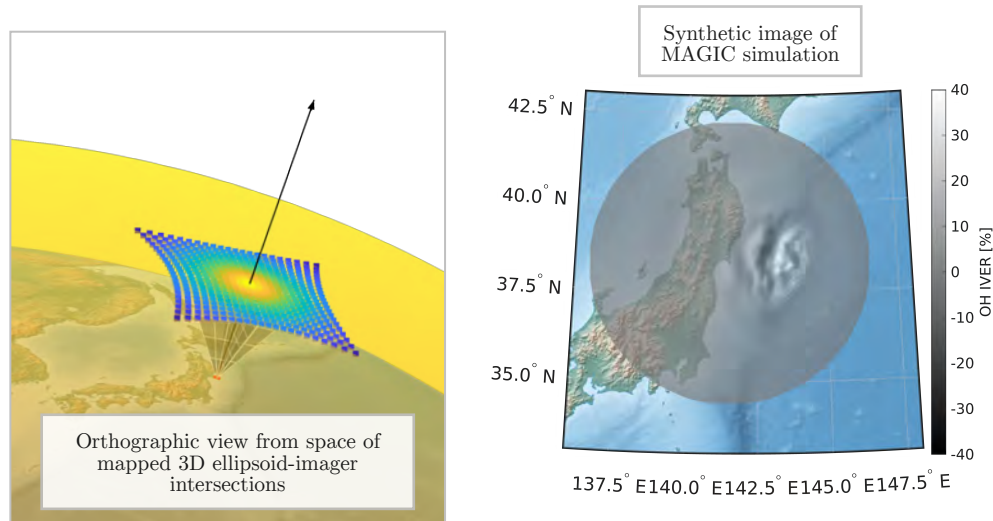
Figure 3.44. Synthetic imaging off the coast of Japan. (left) 512×512 pixels and 160⁰ FOV synthetic image of a modeled OH airglow tsunamigenic response unwrapped onto an orthographic projection. (right) Visualization of the CCD pixel intersections at the airglow layer. A similar version appears on Inchin, Snively et al. (2020).

Now we use another simulation along with synthetic images this time from an imaging instrument onboard a satellite. **Figure 3.45** are images of CO_2 BWT both plotted on the same 3D space; they represent positive perturbations. The left image is shown with an *orthographic camera projection* from a high altitude while the right image is a *perspective camera projection* where the camera is onboard a satellite looking straight down with a 48.95⁰ FOV. Compare the 3D perspective view to the simulated satellite image in **Figure 3.46** with approximated AQUA satellite values (Aumann, Chahine et al. 2003). The data comes from modeled CO_2 BWT disturbances due to a convective thunderstorm from MAGIC featured in Heale et al. (2019). For **Figure 3.46** the background image is a 3D sketch of the satellite position (red dot) and attitude sphere (with pitch, yaw and roll guides) along with imager sensor checkerboard projections on the airglow layer (yellow shell). The 2D unwarped images are the simulated satellite observations along the track in *orthographic map projections*. The

data comes from modeled CO_2 BWT disturbances due to a convective thunderstorm from MAGIC featured in Heale et al. (2019).
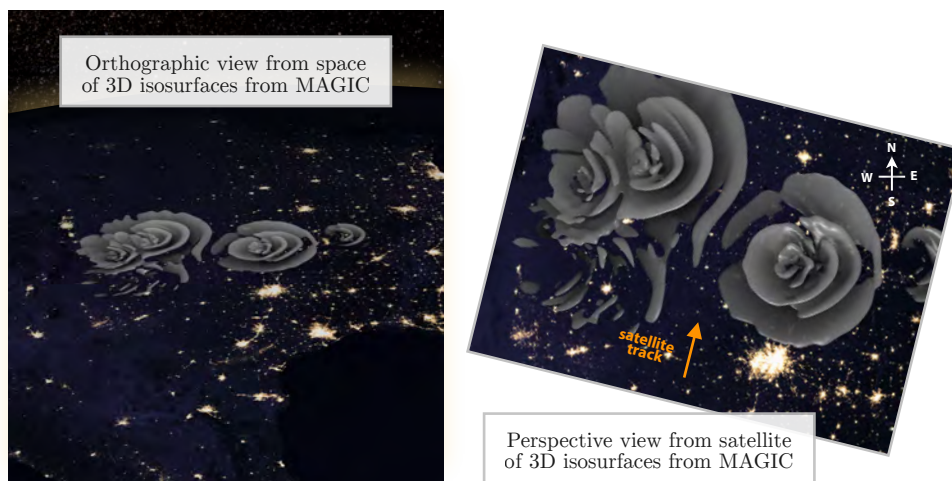
Figure 3.45. Isosurfaces of CO_2 BWT positive perturbations due to a convective thunderstorm over the midwest. (left) Orthographic camera projection from a high altitude. (right) Perspective camera projection from an imager onboard a satellite with a 48.95° FOV. Data from [Heale et al., 2019].
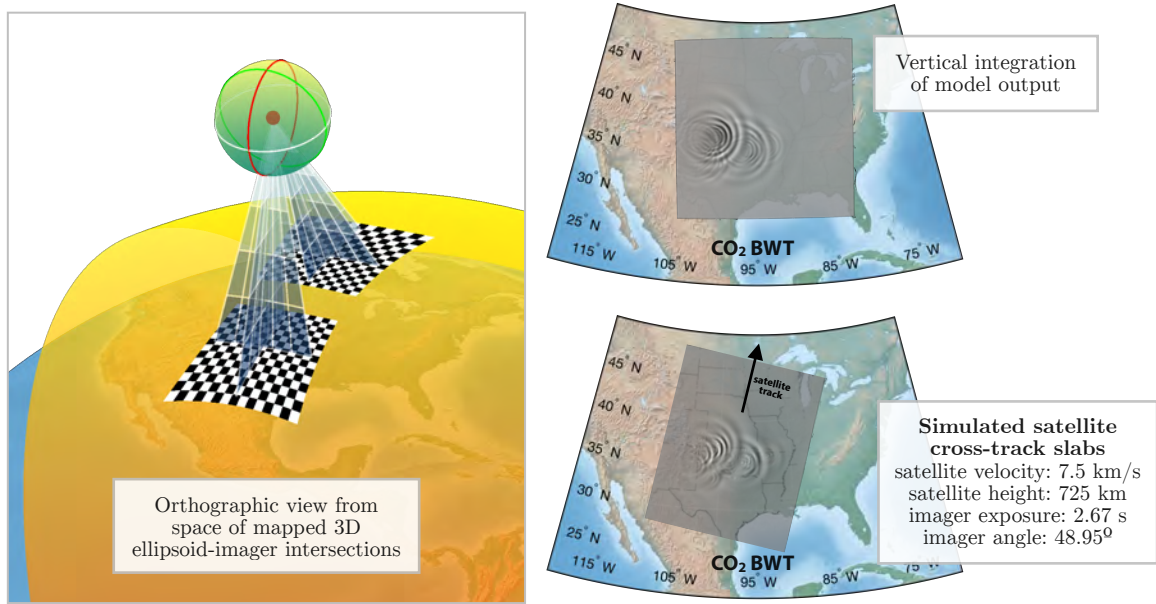
Figure 3.46. Synthetic imaging from a satellite along-track. (left) Visualization of forward and backward facing CCD imagers with checkerboard pattern. (right top) Vertical integration of model output of CO2 BWT. (right bottom) Simulated satellite observation of nadir cross-track slabs using approximated AIRS satellite track values.

We finally show **Figure 3.47** with 3D outputs from GEMINI of electron density plotted using point clouds; the red dot and arrows represent a single GPS receiver station with two different LOS. In this example we can see that while both 3D models are using an *orthographic camera projection*, one is plotted onto a 3D globe and the other onto a 2D *plate carrée map projection*.
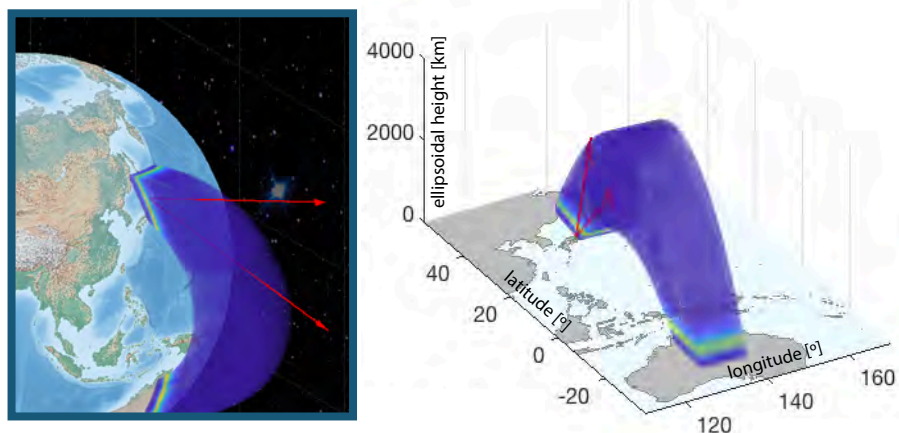
Figure 3.47. 3D Point clouds representing the same electron density on the GEMINI domain (along magnetic lines). The arrows are two lines-of-sight for a GPS receiver. (left) Plot on a globe, (right) plot on a plate carrée (equirectangular) projection. Both (left) and (right) 3D models are plotted with an orthographic camera projection.

Chapter 4

Results: line-of-sight effects and characterization

In the previous chapters, a foundational framework was laid for a systematic study of line-of-sight effects. Its main advantage being the scope of the coordinate transformations, which allow for freely placing instruments and data with accurate geometry and mapping. While a main effort of this thesis was spent in constructing bespoke tools needed for reconstruction of synthetic observables and quantitative mapping of 3D data, in this chapter we will pursue a case study to systematically characterize line-of-sight effects for a specific simulation. In doing so, we further establish the capabilities of the analysis code while also assessing observability effects on spectral analysis of unwarped imagery data. It was briefly mentioned in **Chapter 1** the implications of off-zenith imaging; it leads to intensity modulations and scale filtering effects due to the oblique alignment or anti-alignment with wavefronts through a volumetric atmospheric layer. In this chapter we will further expand upon this concept by presenting results from a series of tests for imagers at different positions from zenith to extreme viewing angles. A power spectrum analysis will be used as the main gauge for characterization of scale filtering, while total intensity will be used to assess enhancements or cancelations.

4.1. Case in study

As with the previous chapters, we will use data from the study case by Heale, Snively et al. (2019) due to its multilayered simulation of small-to-medium scale gravity waves over a large spatial extent for which we can apply our synthetic imagers and characterize line-of-sight effects. This simulation study models a large Mesoscale Convective System (MCS) in the Midwestern US on July 8th, 2016 that took place between 0 UTC and 6 UTC (7 pm to 1 am CDT local time). These types of deep convection systems are an important source of gravity waves that influence atmospheric circulation and reach altitudes up to the thermosphere (Holton, Haynes et al. 1995, Song, Chun et al. 2003). The simulation is first run on MAGIC with data inputs at the troposphere from the Next Generation Radar (NEXRAD) for thunderstorm reflectivity and Digital Precipitation Rate (DPR). Ambient winds are taken from MERRA-2 for 0 km to 60 km and HWM08 for 60 km to 500 km, using the technique of Stephan and Alexander (2015). Neutral densities and temperatures are calculated from NRLMSISE-00. The resolution of MAGIC grid is $4 \times 4 \times 1$ km ($x \times y \times z$), temporal cadence of 60 s and centered around coordinates (40.83°N, 93.57°W) with a total domain extension of $2400 \times 2400 \times 500$ km. MAGIC simulation results are then coupled with GEMINI to model the propagation through the ionosphere and thermosphere; GEMINI results will be addressed at the end of this chapter. For this particular study, we will focus on a single time step at 5:15:15 UT or at 341 frames into the simulation. At this time the sources are still actively generating gravity waves, and there has been significant interaction with the background atmosphere since the onset of the thunderstorm and start of the simulation. This allows for this particular time step to feature both smaller scales from instabilities and substantially linear large-scale waves. These can be seen in the 3D render of OH(3,1) isosurfaces of 10,000 photons/cm³ perturbations shown in **Figure 4.1**. Smaller perturbations of 340 photons/cm3 are

shown in **Figure 4.2** where the entire simulation domain can be appreciated. Note that both figures present the layer stretched by a factor of ten in order to enhance the vertical structure for better appreciation. The OH(3,1) airglow layer is thin in relation to the horizontal scales, where the layer thickness has a FWHM of approximately 8 km and the horizontal scales of several hundred kilometers. Furthermore, the vertical structure of the wavefronts within the airglow layer is at times very small, as is the depth of the layer itself; this has important implications for imaging at moderate FOV angles and leads to significant filtering of scales at larger FOV angles as discussed further down. For vertical scale comparison the CO_2 BWT 3D render is shown in **Figure 4.3** with a tenfold stretch as well. The vertical scales seen in the CO_2 BWT are much larger; while the underlying waves have larger vertical scales than those seen in the OH(3,1) layer, the CO_2 layer is also simply deeper than the OH layer. While this is expected for convectively generated waves, insight of the gravity waves' vertical progression is not contained in single-layer mesospheric airglow observations unless viewed obliquely by multiple instruments for tomographic reconstruction (Hart, Doyle et al. 2012). The true scale of waves throughout the entire vertical domain can be directly assessed from the temperature isosurfaces, as shown in **Figure 4.4**. The obvious downside is that temperature over altitude is typically not an observable, and must be weighted over the depth of another quantity being measured, which is a feature inherent to the "flattening" of volumetric data when imaged. This clearly shows the biggest limitation for single-layer (or single-wavelength) imaging: the impossibility to measure three-dimensional structure without multiple oblique perspectives. However, models and visualization tools can fill the gaps and describe the evolution of the gravity waves both spatially and temporally and, specifically, how they relate to our measured data.

The largest feature present in the simulation is the appearance of 3 main concentric sources of gravity waves that correspond to the three large convective cells seen in the NEXRAD data (not shown here). These concentric wavefronts will be the

testbed for our scale-filtering characterization. They retain both large-scale features as well as high frequency components, discernible within the same image. The largest wavefronts are seen propagating Northeast in semi concentric circles. With the assurance from the 3D renderings we know that they have very small vertical scales and we can expect imagers that view parallel to these Northeastward-propagating fronts will be enhanced. Moreover, because of the selfsame shallow depth, we expect the filtering of scales will be severe for imagers looking across the wavefronts.
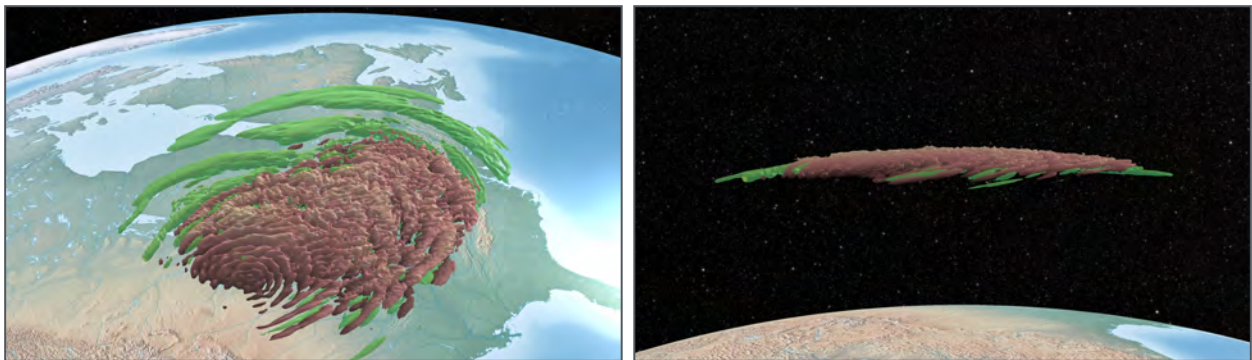
Figure 4.1. 3D renders of OH(3,1) isosurfaces of $\pm 10,000$ photons/cm³ perturbations of the simulation data in two different views. Positive perturbation are shown in green colormap and negative in pink. The height axis has been stretched by 10 times (scale of 10:1 vertical vs horizontal). Simulated data: Midwest thunderstorm 2016/07/08 5:15:12 UTC.
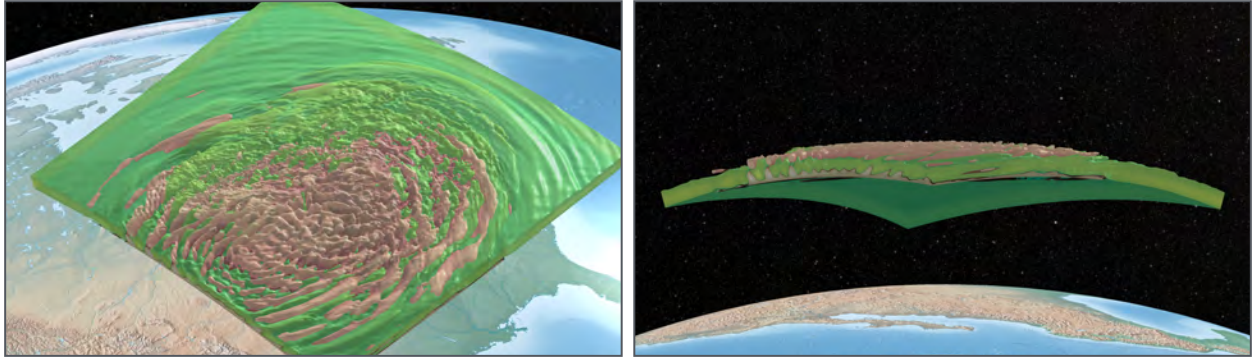
Figure 4.2. 3D renders of OH(3,1) isosurfaces of ± 340 photons/cm³ perturbations of the simulation data in two different views. Positive perturbation are shown in green colormap and negative in pink. The height axis has been stretched by 10 times (scale of 10:1 vertical vs horizontal). Simulated data: Midwest thunderstorm 2016/07/08 5:15:12 UTC.
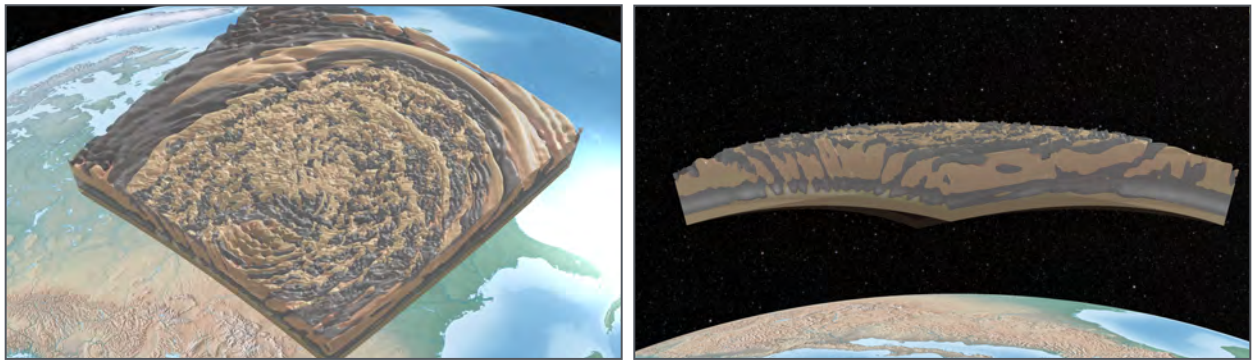
Figure 4.3. 3D renders of CO_2 isosurfaces of $\pm 11.4\%$ perturbations of the simulation data in two different views. Positive perturbation are shown in grayscale colormap and negative in pink. The height axis has been stretched by 10 times (scale of 10:1 vertical vs horizontal). Simulated data: Midwest thunderstorm 2016/07/08 5:15:12 UTC.
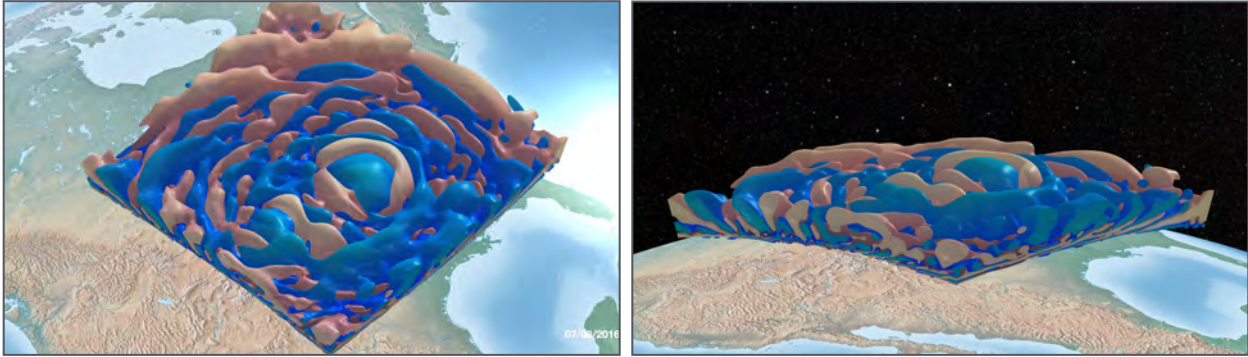
Figure 4.4. 3D renders of temperature isosurfaces of ± 10K perturbations of the simulation data in two different views. Positive perturbation are shown in blue colormap and negative in pink. No stretching has been applied (scales are true or 1:1 relative to each other). Simulated data: Midwest thunderstorm 2016/07/08 5:15:12 UTC.

4.2. Filtering of scales and line-of-sight intensity enhancements

To understand how measured wave parameters may change purely due to line-of-sight effects, we propose an analysis of the total spectral power (TSP) for unwarped images at the same location at different imager positions, thus changing the FOV of observations. Spectrum and periodogram analysis of airglow images has long been a useful tool for determining wave parameters (Hecht, Walterscheid et al. 1994, Garcia, Taylor et al. 1997, Coble, Papen et al. 1998, Sivjee 2005). The expectation is that as viewing angles become aligned with wavefronts there will be an increase in both intensity of the integration and sharpness of the spectral components. Thus, more filtering of scales leads to more distributed spectral power and less filtering leads to denser spectral peaks concentrating near certain wavenumbers. We first define the periodogram of an image, in a method similar to Jing, Kamalabadi et al. (2005): let $I(x, y)$ denote the unwarped $n \times n$ pixels image and $J(k, l)$ its windowed discrete Fourier transform, the windowed periodogram $S(k, l)$ is then defined as

$$S(k,l) = \frac{1}{n^2 f^2} \left| J(k,l) \right|^2 \tag{4.1}$$

and is a measure of the spectral density of the image with units of power/frequency. In the equation above k, l are the zonal and meridional wavenumber respectively, n is the number of data points in both dimensions, f a normalizing factor of the window $w(x,y)$ defined as:

$$f(x,y) = \frac{1}{n^2} \sum_{n_x} \sum_{n_y} w(x,y) \tag{4.2}$$

and $n_x = n_y = n$ are the number of data points in each dimension. The empirically chosen window is the Hanning window (Coble, Papen et al. 1998), defined as

$$w(n_i) = \frac{1}{2} \left[1 - \cos\left(2\pi \frac{n_i}{n} \right) \right], \quad 0 \leq n_i \leq n \tag{4.3}$$

The 2D implementation of this 1D window is just a revolution around the center of the image. The wavenumber vectors are defined as:

$$k_i = \frac{2\pi}{\Delta x} \left[\frac{n_i}{n} \right], \quad -\frac{n}{2} \leq n_i \leq \frac{n}{2} \tag{4.4}$$

$$l_i = \frac{2\pi}{\Delta y} \left[\frac{n_i}{n} \right], \quad -\frac{n}{2} \leq n_i \leq \frac{n}{2} \tag{4.5}$$

with units of cycles/km. The total spectral power is then the summation of the periodogram over all the wavenumbers:

$$P = \sum_{n_x} \sum_{n_y} S(k, l) \, \Delta k \, \Delta l \qquad (4.6)$$

The units of the total spectral power, in this case radiant power, are typically Watts (W) or decibel-Watts (dB) defined by the relation $dB = 10 \log_{10}(Power/W)$. We however will use units of $photons^2/km^2$ for spectral density (periodogram) and $photons^2$ as a proxy for total power to match the units of our IVER images. To perform this spectral analysis, a specific tool has been created to visualize and quantify the periodograms. Specifically, a peak-finding method has been incorporated to identify more prominent frequencies, up to a certain spectral energy threshold, from which wave parameters can be obtained. While the focus of this discussion is not the successful identification of waves and their characteristics, it is noteworthy to mention that such capability has been implemented and its total spectral power estimates will be used throughout this chapter, henceforth referred to as the "spectral analysis tools".

For this study we have chosen to measure the total spectral power of all the frequencies that are bounded by the interval ± 0.121 km^{-1}, which correspond to wavelengths larger than 8.26 km. This latter value is approximately twice the resolution of the original data, which in turn is also the chosen resolution for the interpolation grid for all unwarped images. We have chosen the dimensions of the discrete Fourier transform (DFT) to only allow for twice the wavelengths[6]; this satisfies the Nyquist-Shannon sampling theorem. Additionally, by doing so, we have a measure of the prominence of observable wavelengths and how it changes for different viewing geometries. We will compare images that are unwarped at the exact same coordinates, but imaged from different positions. Firstly, let us exemplify this process with 5 trial synthetic OH(3,1) imagers, placed at the coordinates given in **Table 4.1**. All of the

---

[6] The small discrepancy between 8.26 km and 8 km comes from the fact that we ensure the size of the DFT is odd by adding 1 more pixel if the original data has even dimensions. This is so that zero is exactly at the origin.

imagers are 512×512 pixels and 180° FOVs. A center imager has been chosen to align with the center of the data at (40.82°N, 93.57°W). Four other imagers are placed on the cardinal positions at 500 km from the center.

Imager location	Coordinates (lat, lon)	Meridional shift	Zonal shift	Tilt angle to reference
Center	40.82°N, 93.57°W	0 km	0 km	0°
North	45.33°N, 93.57°W	500 km	0 km	82.450°
South	36.32°N, 93.57°W	-500 km	0 km	82.452°
East	40.82°N, 87.65°W	0 km	500 km	82.440°
West	40.82°N, 99.50°W	0 km	-500 km	82.440°

Table 4.1. Location of test surface imagers from the center of the data. Distances are calculated as arc lengths over rhumb lines at surface height along azimuths: 0° (Northwards), 180° (Southwards), 90° (Eastwards), 270° (Westwards). The *tilt angle to reference* is the tilt (zenith) angle from the imager's location to the center coordinates.

The imager location allows for all five imagers to contain within view the same square area at the center of the map, that is, a 500×500 km square that is unwarped at the mean airglow height of 87 km and will be used for spectral analysis. The resulting synthetic images are shown unwarped and plotted on the map in **Figure 4.5**; the vertical integration of the data is included for reference. All images have a fixed and shared color scale. It should be mentioned that all map plots correspond to the loximuthal map projection and all distances are calculated over rhumb lines. The simulated IVER images as seen by the synthetic imagers are shown in **Figure 4.6**. As was stated before, the spectral analysis is performed on a square area around the center of the image, and these are shown in **Figure 4.7**. At first glance, it is evident from these images how the loss of angular resolution impacts the detail on the images. Purely from a resolution standpoint there is indeed loss of spectral power associated with the

undersampled data. However, all of the off-center imagers have roughly the same angular resolution (see **Table 4.1** for reference), yet they still exhibit important differences. While these may be subtle to the eye, they reveal the a priori expectation that wave-aligned lines-of-sight provide enhanced detail. As mentioned before, there are two of the three semi-concentrical waves clearly visible in this area and they are propagating North-Northeast within the image. This should result in sharper images from the South and West imagers, and the opposite for the North and East ones. We can asses this supposition by looking at the frequency distribution of their periodograms of **Figure 4.8**. First and foremost, the power values of the vertical or column integration are the smallest as they should be since it represents the shortest possible path of integration. Nevertheless, its spectral distribution is very similar to that of the central imager, albeit at a much lower spectral density. Next, the spectral analysis tools found that the highest TSP correspond to the South and West imagers as expected, while the North and East ones have the smallest values. Additionally, the narrowest distribution is found for the South imager, so much in fact that the spectral analysis tools where able to find a peak within its energy and frequency requirements (10% energy threshold and only wavelengths smaller than half the domain size); the tools present this information as a cross-hair with the computed orientation and proper wavelengths length. In this instance it found a wave with parameters: $\lambda_x = 159.98$ km, $\lambda_y = 214.08$ km with $\lambda = \sqrt{\lambda_x^2 + \lambda_y^2} = 128.15$ km, orientation angle of $\angle = 37.77°$ and power ratio of $P = 28.77\%$. With the aid of the cross-hair we can verify this wavelength to coincide with the peak-to-peak distance of the prominent perturbations at the center/top-right portion of the image.
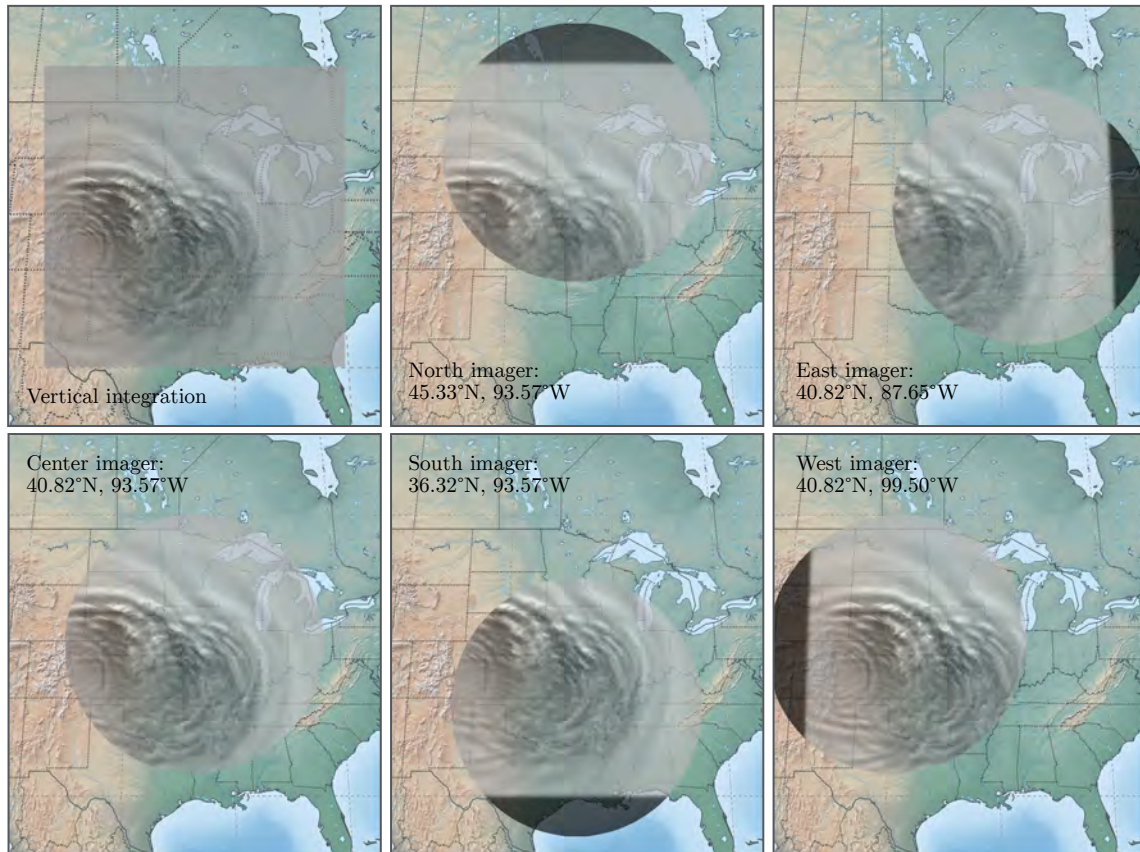
Figure 4.5. Five synthetic unwarped images of OH(3,1) IVER at 87 km from simulated ground imagers placed at five different locations looking straight up. Vertical integration of original data is included for reference. Center imager is at the center of the data at (40.83°N, 93.57°W). The other locations are 500 km away along parallel 93.57°W or meridian 40.83°N accordingly. Imagers are 512×512 pixels, 180° FOV. All images share color scale. Simulated data: Midwest thunderstorm 2016/07/08 5:15:12 UTC.
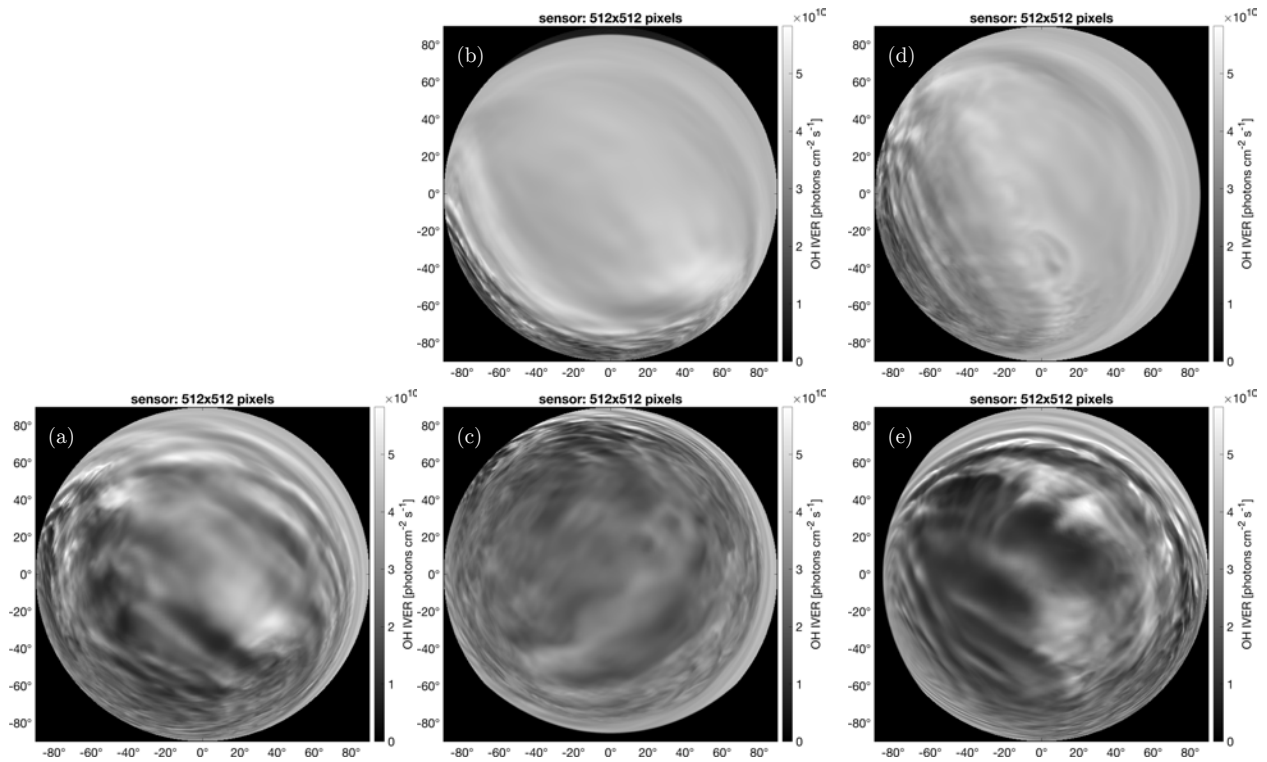
Figure 4.6. Five synthetic images of OH(3,1) IVER at 87 km from simulated ground imagers placed at five different locations looking straight up. Center imager (a) is at the center of the data at (40.83°N, 93.57°W). Locations are 500 km away along parallel 93.57°W or meridian 40.83°N accordingly, where: (b) is North, (c) is South, (d) is East and (e) is West. Imagers are 512×512 pixels, 180° FOV. Simulated data: Midwest thunderstorm 2016/07/08 5:15:12 UTC.
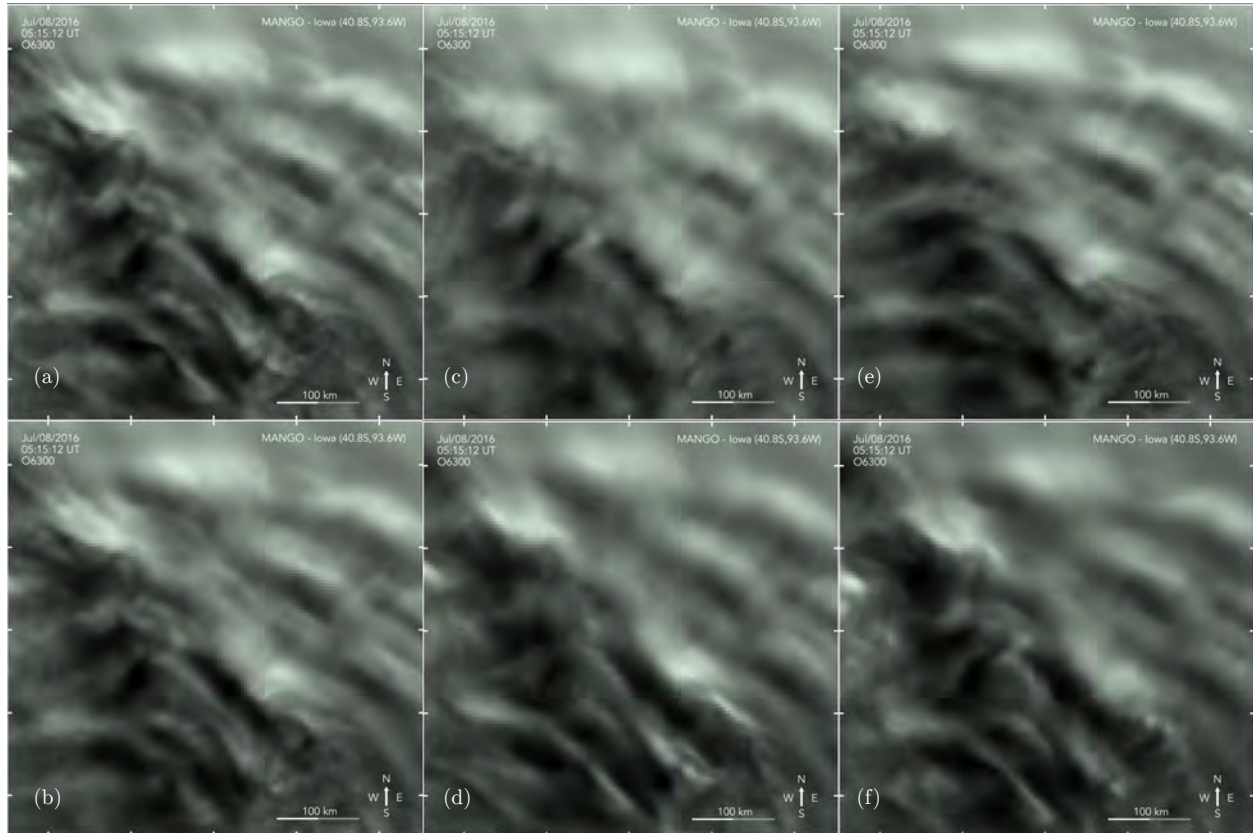
Figure 4.7. 500×500 km unwarped OH(3,1) IVER at 87 km detail images around center of data (40.83°N, 93.57°W) for 4 imagers and vertical integration. (a) vertical integration of original data; (b) center imager; (c) North imager, (d) South imager, (e) East imager, (f) West imager. All images have been unwarped at 4×4 km resolution. Imagers are 512×512 pixels,180° FOV and are pointed towards the center of data at mean airglow height. Simulated data: Midwest thunderstorm 2016/07/08 5:15:12 UTC.
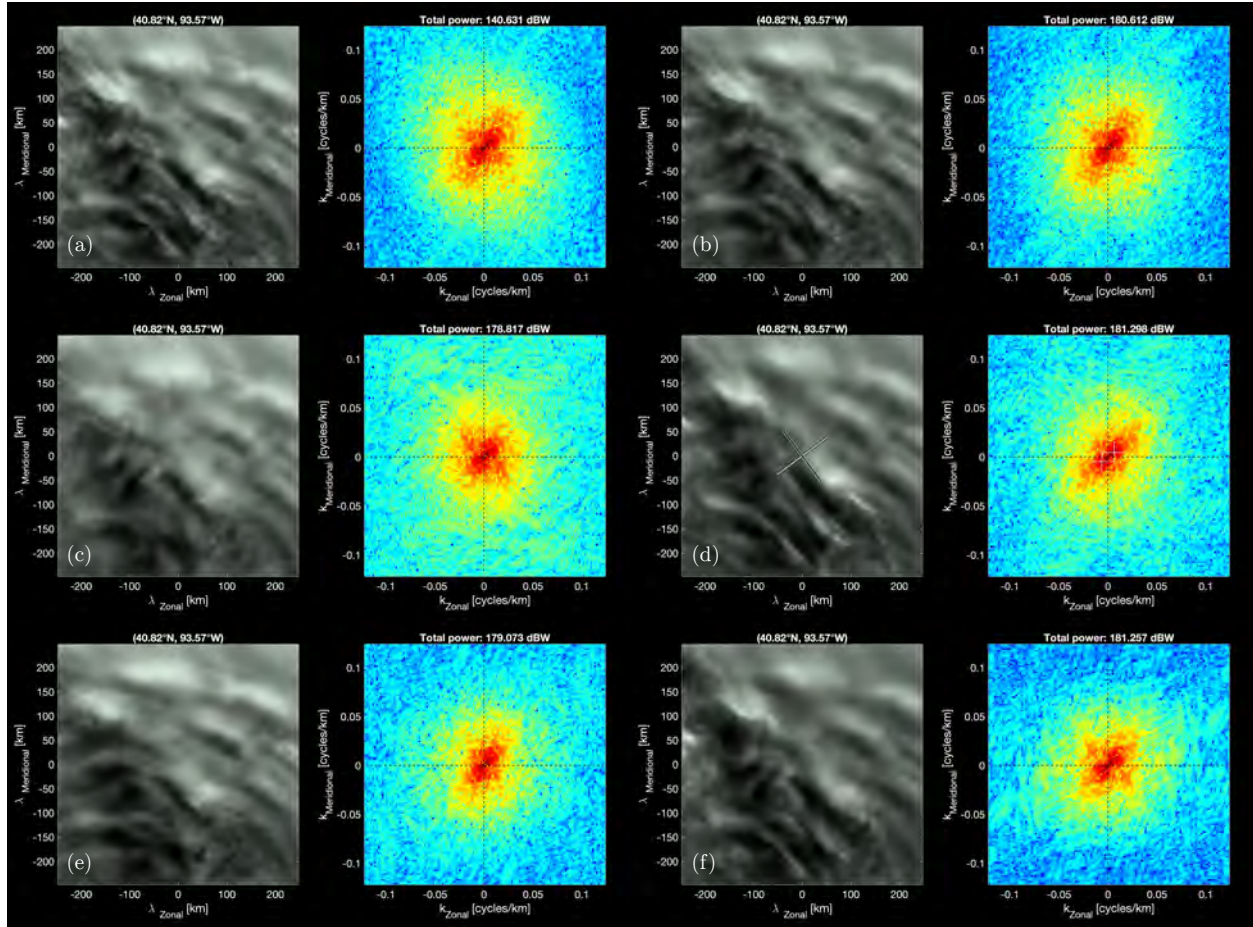
Figure 4.8. 500×500 km unwarped OH(3,1) IVER at 87 km detail images around center of data (40.83°N, 93.57°W) and their periodograms of frequencies bounded by ±0.121 km⁻¹ (±8.26⁻¹ km⁻¹). (a) vertical integration of original data; (b) center imager; (c) North imager, (d) South imager, (e) East imager, (f) West imager. All images have been unwarped at 4×4 km resolution. Imagers are 512×512 pixels, 180° FOV and are pointed towards the center of data at mean airglow height. Simulated data: Midwest thunderstorm 2016/07/08 5:15:12 UTC.

We now proceed to place the imagers on the same locations as before, but this time they will be pointing towards the center of the data at the OH(3,1) airglow height. It is worthwhile to validate the geometry of the code by plotting the interpolation coordinates as seen by the code itself. We show this in **Figure 4.9**. These 3D scatter plots show the data interpolation coordinates and imagers' line-of-sight coordinates both in ENU, where the location of the imager is the ENU origin. These types of visual validations are an integral part of the synthetic imaging code and represent the results of the line-of-sight-ellipsoid intersection algorithm of **Section 2.4**.
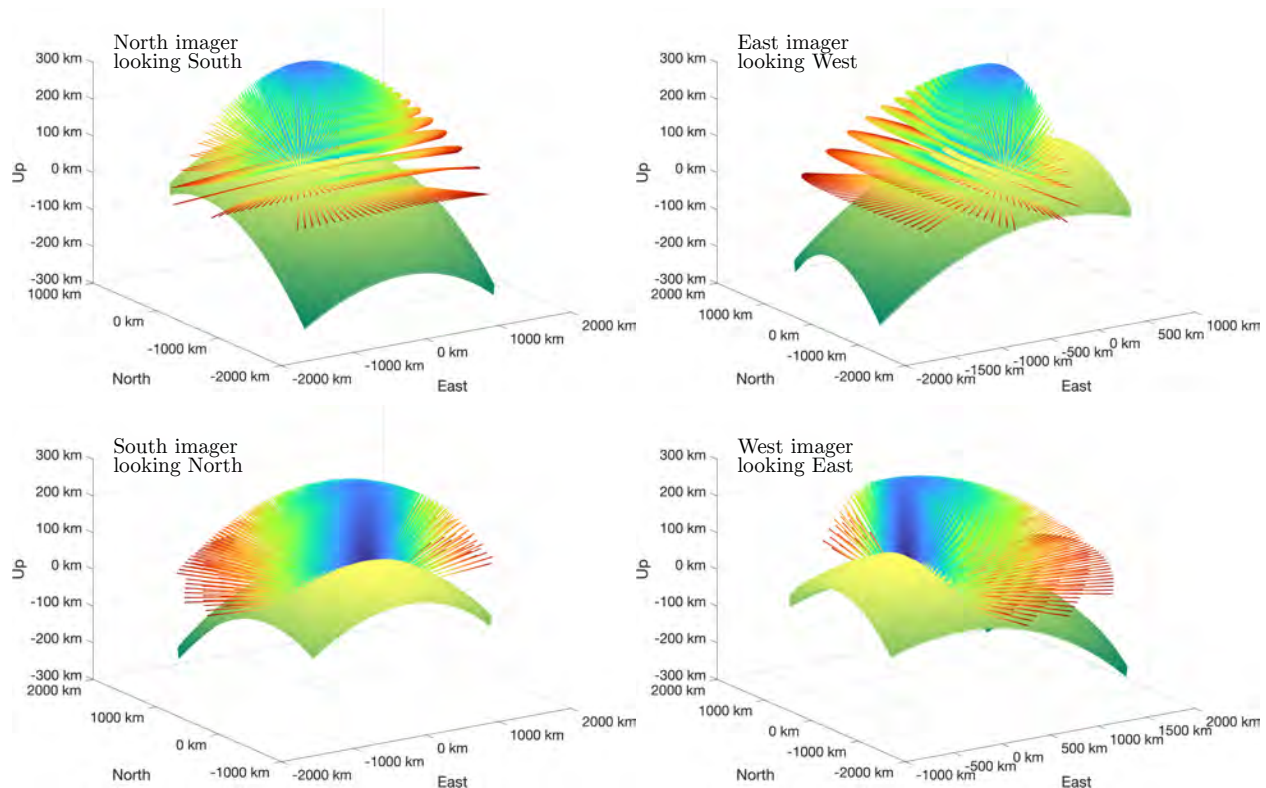
Figure 4.9. Scatter plots of ENU coordinates for interpolation of 4 imagers pointed towards the center of data. Green colormaps correspond to the input coordinates, color coded with height; turbo colormaps corresponds to query coordinates color coded to distance from origin. The imager is $32{\times}32$ pixels and the data is at full resolution of $4{\times}4{\times}1$ km ($x{\times}y{\times}z$). Line-of-sight coordinates beyond the horizon have been discarded.

The synthetic unwarped and map-projected images are shown in **Figure 4.10**. The original IVER images as seen from the imagers are shown in **Figure 4.11**. As before, we analyze an overlapping center area of 500×500 km around the center coordinates and perform spectral analysis on it. These areas are shown in **Figure 4.12** and their corresponding periodograms shown in **Figure 4.13**.
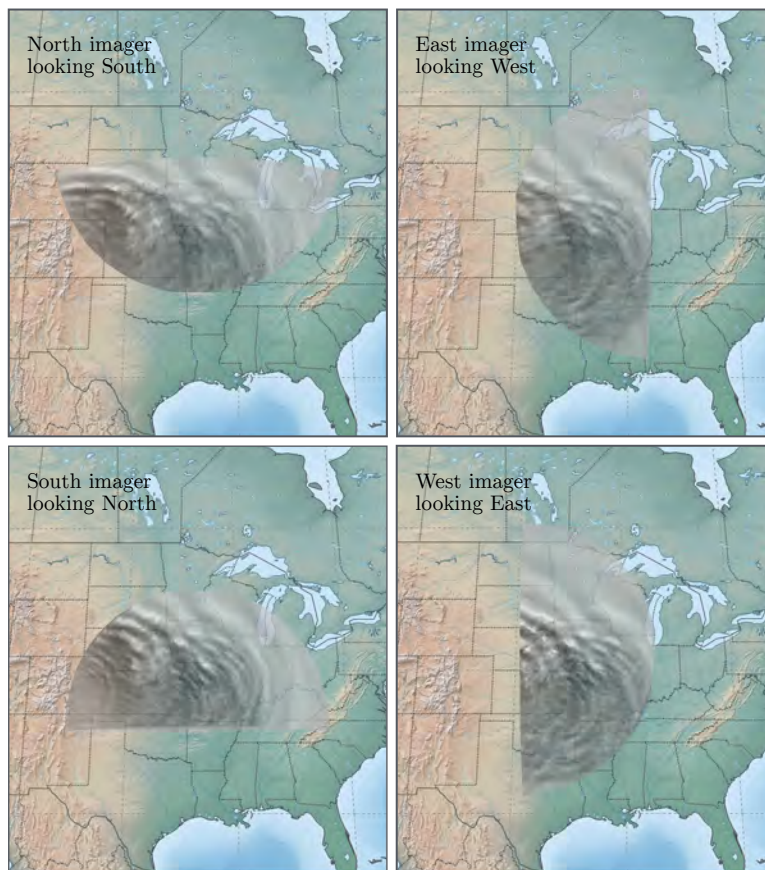
Figure 4.10. Four synthetic unwarped images of OH(3,1) IVER at 87 km from simulated ground imagers placed at four different locations with their zeniths aimed towards the center of the data (40.83°N, 93.57°W) at the mean airglow height. Locations are 500 km away along parallel 93.57°W or meridian 40.83°N accordingly. Imagers are 512×512 pixels, 180° FOV. All images share color scale. Simulated data: Midwest thunderstorm 2016/07/08 5:15:12 UTC.
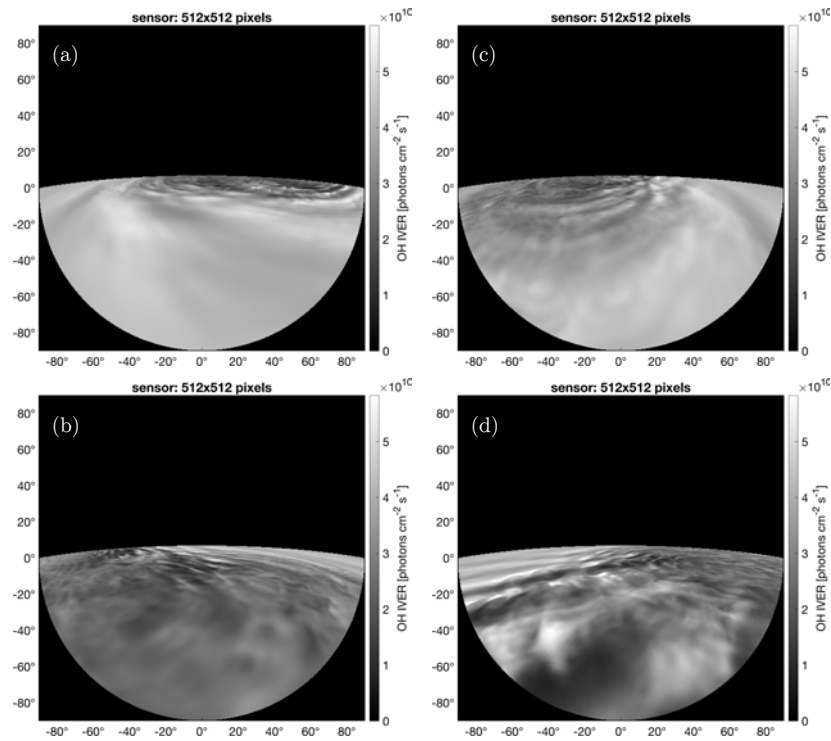
Figure 4.11. Four synthetic images of OH(3,1) IVER at 87 km from simulated ground imagers placed at four different locations with their zeniths aimed towards the center of the data (40.83°N, 93.57°W) at the mean airglow height. Locations are 500 km away along parallel 93.57°W or meridian 40.83°N accordingly, where: (a) is North, (b) is South, (c) is East and (d) is West. Imagers are 512×512 pixels, 180° FOV. Simulated data: Midwest thunderstorm 2016/07/08 5:15:12 UTC.
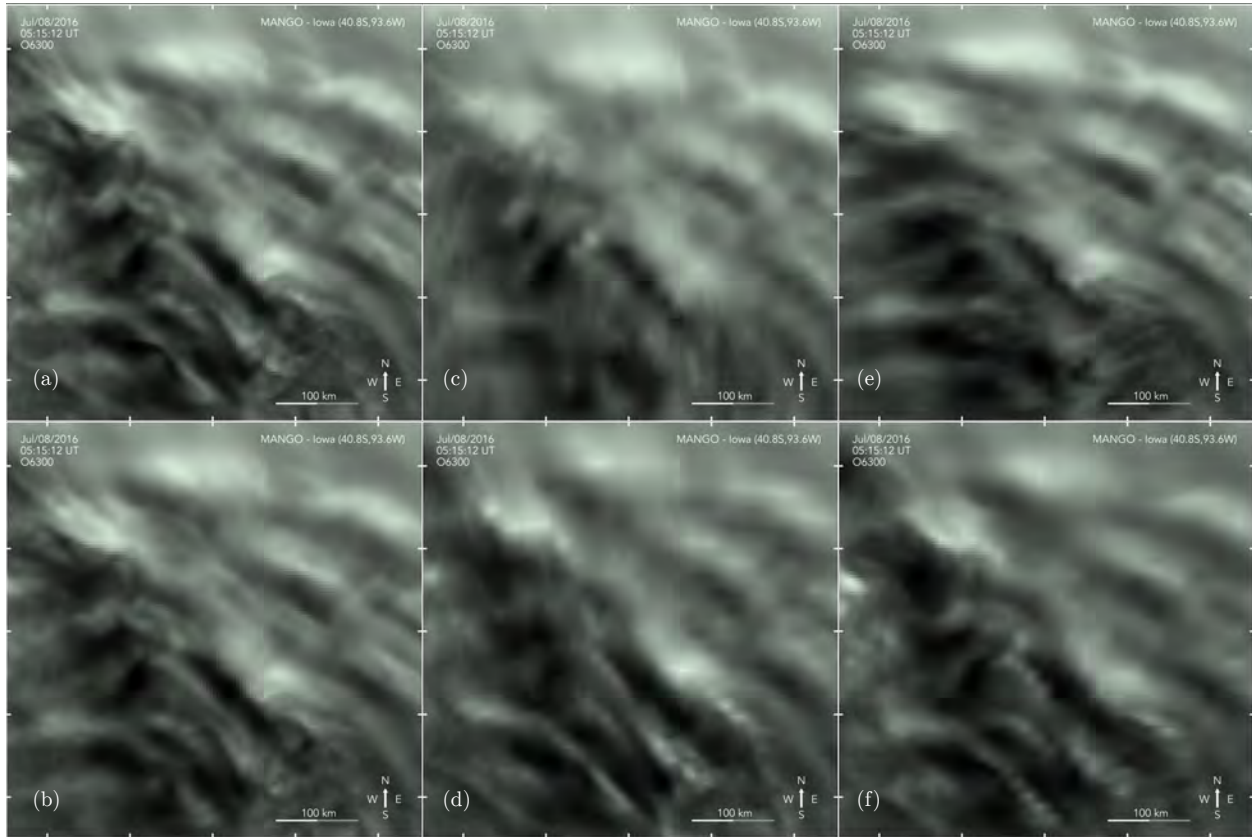
Figure 4.12. 500×500 km unwarped OH(3,1) IVER at 87 km detail images around center of data (40.83°N, 93.57°W) for 4 imagers and vertical integration. (a) vertical integration of original data; (b) center imager; (c) North imager, (d) South imager, (e) East imager, (f) West imager. All images have been unwarped at 4×4 km resolution. Imagers are 512×512 pixels,180° FOV and are pointed towards the center of data at mean airglow height. Simulated data: Midwest thunderstorm 2016/07/08 5:15:12 UTC.
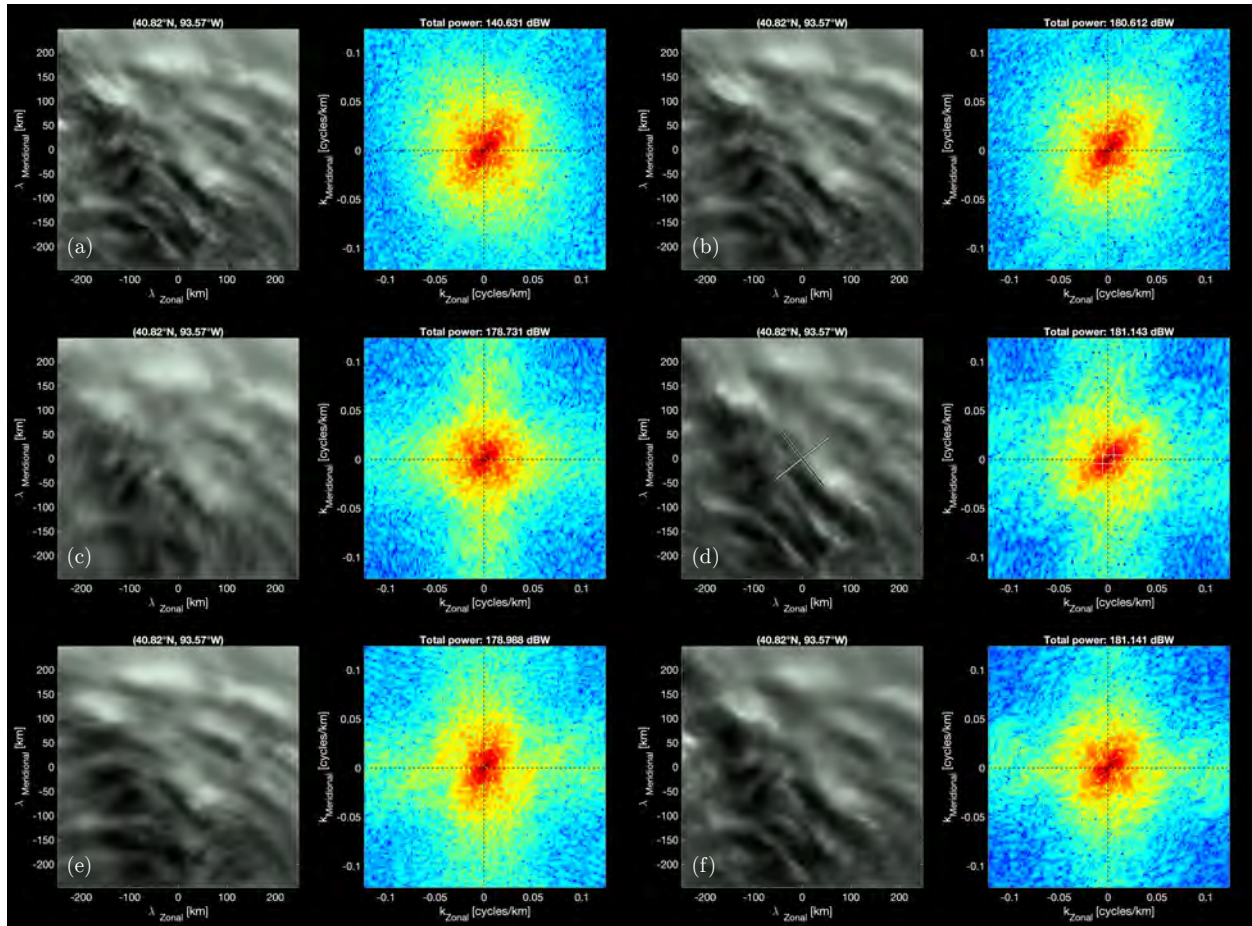
Figure 4.13. 500×500 km unwarped OH(3,1) IVER at 87 km detail images around center of data (40.83°N, 93.57°W) and their periodograms of frequencies bounded by ±0.121 km⁻¹ (±8.26⁻¹ km⁻¹). (a) vertical integration of original data; (b) center imager; (c) North imager, (d) South imager, (e) East imager, (f) West imager. All images have been unwarped at 4×4 km resolution. Imagers are 512×512 pixels,180° FOV and are pointed towards the center of data at mean airglow height. Simulated data: Midwest thunderstorm 2016/07/08 5:15:12 UTC.

The results of this trial are much more noticeable in the unwarped images themselves. We see that by pointing the imager off-zenith the spatial resolution is not improved, but in fact is reduced. While the angular resolution remains the same, the large horizontal distance between the imager and the center of the data results in less resolution at layer's height. This is particularly apparent for the North and East imagers, where the decreased spatial resolution compounds the filtering due to perpendicular imaging of the wavefronts. On the other hand the periodograms remain largely the same, but the total spectral power is lower, again, due to the diminished resolution. Another side-effect for the North and East imagers is the noticeable background brightness enhancements with respect to the others, which contributes to the perception of filtered scales. Another tell-tale sign, is the very even distribution of frequencies in the periodogram.

We will now detail the last study case, in which we now plot 50 imagers on two different "tracks" that are aligned and anti-aligned with the wavefronts. Then we proceed to plot the total spectral power and total intensity for each imager as a function of distance and tilt angle so that we can better understand the associated line-of-sight effects. The two tracks we will use and their design parameters are shown in **Table 4.2**, with a sketch both in **Figures 4.14 & 4.15**. As before, all imagers are 512×512 pixels and 180° FOV. The unwarped area is 500×500 km around the center coordinates.

Track parameters	SW2NE track	SE2NW track
no. of imagers	50	50
azimuth	34.3°	−55.7° (304.3°)
distance	1200 km	1200 km
start coordinates	36.36°N, 97.45°W	36.36°N, 97.45°W
end coordinates	45.11°N, 89.59°W	45.11°N, 89.59°W

Table 4.2. Design parameters of two tracks where simulated imagers are placed. All imagers have 512×512 pixel and 180° FOV resolution.
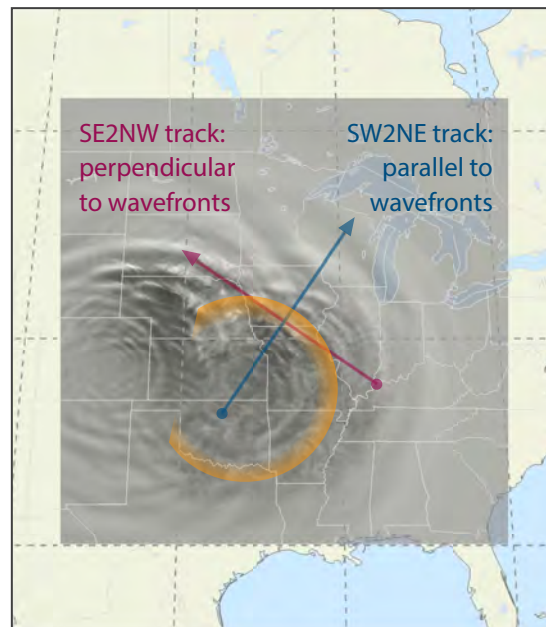
Figure 4.14. Two different perpendicular tracks with 50 locations where synthetic imagers are placed for a design study. Blue track is at 34.3° azimuth and red path is at −55.7° (304.3°) azimuth. Both cross at center of data at (40.83°N, 93.57°W). Blue path was chosen as it is largely parallel to the wavefronts of the concentric wave highlighted by the orange circle; red path is, therefore, perpendicular to the wavefronts. First imager position is located at center of the dot of each arrow at −600 km loximuthal distance from center; last imager is at the bottom of the arrowhead. Total traveled distance is 1200 km. Additionally, for this reason, distance intervals between each imager position are not uniform and are reduced for higher latitudes. Simulated data: OH(3,1) vertical IVER, Midwest thunderstorm 2016/07/08 5:15:12 UTC.
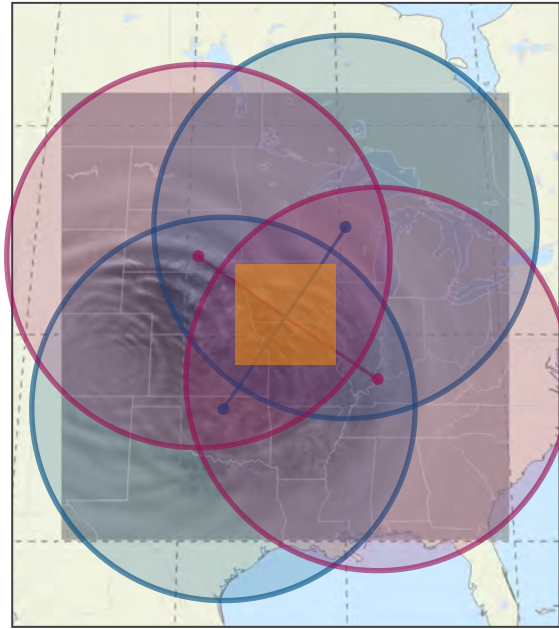
Figure 4.15. Four circles representing the 180° FOV of four imagers located at the beginning and the end of the two design tracks. Blue track is at 34.3° azimuth and red path is at –55.7° (304.3°) azimuth. Both cross at center of data at (40.83°N, 93.57°W). All four FOVs cover the sought area of 500×500 km in the middle, which is represented by the orange square. Simulated data: OH(3,1) vertical IVER, Midwest thunderstorm 2016/07/08 5:15:12 UTC.

As seen in **Figure 4.15**, all imagers encompass the center area. The Southwest-to-Northeast 34.3° track is codenamed SW2NE and the Southeast-to-Northwest –55.7° track is codenamed SE2NW. **Figure 4.14** highlights the most prominent circular wavefronts present in the image. However the other source to the East, although minor, creates noticeable superpositions especially at the North of the image. This does not influence the phase clarity greatly, but it is important to keep in mind that it is far from an idealized case. So each track will have some parallel and perpendicular influence. All of the track results are presented in **Figures 4.16-4.19**.
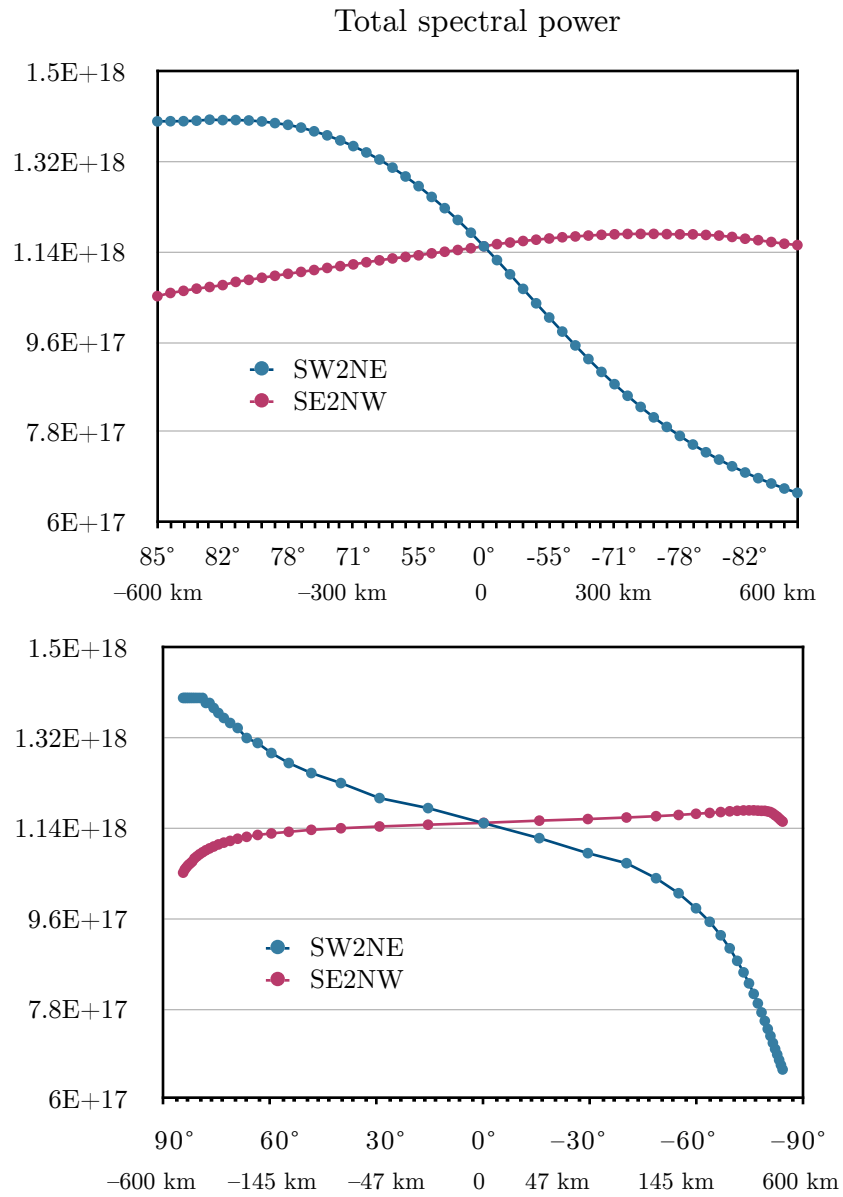
Figure 4.16. Total spectral power (TSP) of fifty 500×500 km (4×4 km resolution) unwarped images of OH(3,1) IVER centered at (40.83°N, 93.57°W). (top) x-axis is uniform distance in kilometers. (bottom) x-axis is uniform tilt angles. Each data point is the TSP for frequencies bounded by $\pm 8.26^{-1}$ km^{-1} in both axes. Simulated images from ground-based 512×512 pixel, 180° FOV. Tilt angle is measured between the imager's zenith and the unwarped images' center coordinates. Positive tilt angles correspond to imagers that are Southwest of the coordinates and negative when Northeast of them. Simulated data: Midwest thunderstorm 2016/07/08 5:15:12 UTC.

TSP change from 0° tilt (%)
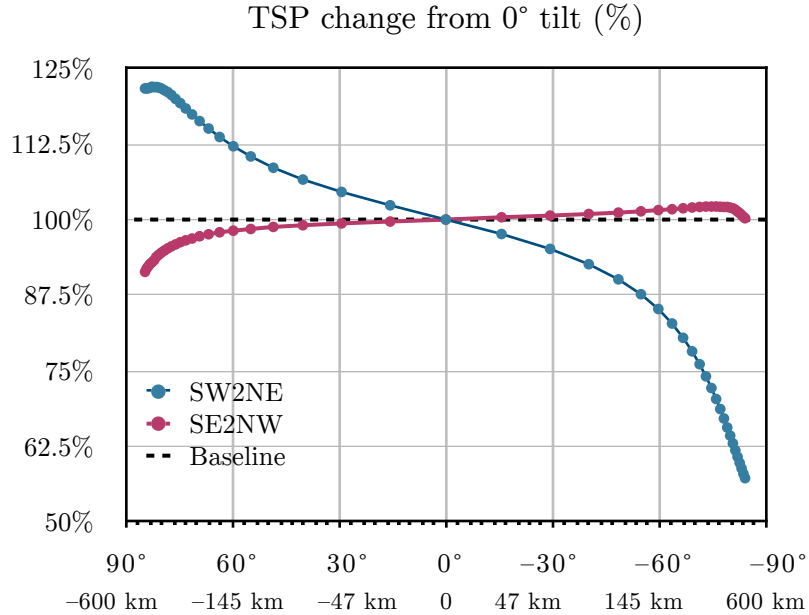
Figure 4.17. Total spectral power (TSP) change of fifty $500{\times}500$ km² ($4{\times}4$ km² resolution) unwarped images of OH(3,1) IVER from that of a ground-based imager located at 0° tilt from center of imaged data along two tracks: Southwest-to-Northeast track at 34.3° azimuth that is parallel to target wavefronts and Southeast-to-Northwest track at $-55.7°$ azimuth that is perpendicular to target wavefronts. 0° tilt has both imager and center of data aligned at (40.83°N, 93.57°W). Each data point is the TSP for frequencies bounded by $\pm 8.26^{-1}$ km^{-1} in both axes. Simulated images from ground-based $512{\times}512$ pixel, 180° FOV imagers. Simulated data: Midwest thunderstorm 2016/07/08 5:15:12 UTC.

From the total spectral power results we clearly see the difference between both tracks and wavefront alignments. The SW2NE track is wavefront-aligned for the first half and anti-aligned for the second half. The flatness of the wavefronts is responsible for the initial flat curve in the first 300 km. The subsequent sharp decline is also a consequence of it. On the other side, the SE2NW track becomes slowly wavefront-aligned as it images the portions of the concentric wave that are propagating towards the Northwest, as it remains largely unaffected by the other sources. According to

131

Figure 4.17, the wavefront alignment provides a 25% spectral enhancement, while the anti-alignment causes a dip of over 50% at the larger FOVs.
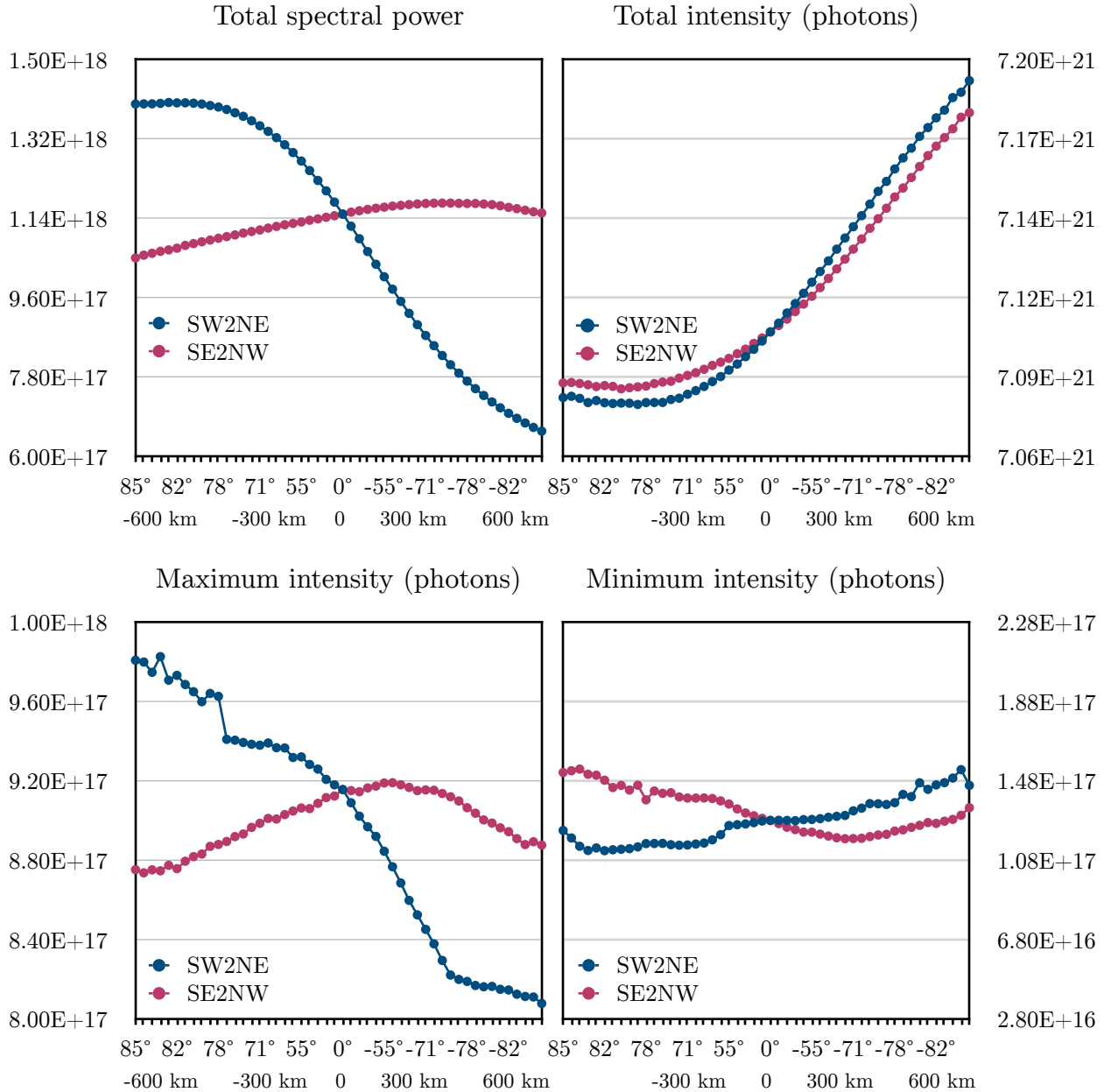
Figure 4.18. Total spectral power (TSP), total, max and min intensity (photons) of fifty 500×500 km (4×4 km resolution) unwarped images of OH(3,1) IVER centered at (40.83°N, 93.57°W) for two tracks. x-axis is uniform distance in kilometers. TSP frequencies bounded by $\pm 8.26^{-1}$ km^{-1} in both axes. Simulated images from ground-based 512×512 pixel, 180° FOV imagers. Tilt angle is measured between the imager's zenith and the unwarped images' center coordinates. Positive tilt angles correspond to imagers that are Southeast of the coordinates and negative when Northwest of them. Simulated data: Midwest thunderstorm 2016/07/08 5:15:12 UTC.

Figure 4.19. Total spectral power (TSP), total, max and min intensity (photons) of fifty 500×500 km (4×4 km resolution) unwarped images of OH(3,1) IVER centered at (40.83°N, 93.57°W) for two tracks. *x*-axis is uniform tilt angle. TSP frequencies bounded by ±8.26⁻¹ km⁻¹ in both axes. Simulated images from ground-based 512×512 pixel, 180° FOV imagers. Tilt angle is measured between the imager's zenith and the unwarped images' center coordinates. Positive tilt angles correspond to imagers that are Southeast of the coordinates and negative when Northwest of them. Simulated data: Midwest thunderstorm 2016/07/08 5:15:12 UTC.

The intensity results further dissect the differences in loss of resolution, spectral distribution and line-of-sight intensity enhancements. The first thing to note is that all of the plots follow opposite trends for each track, with the exception of the total intensity. This may seem like a surprising result at first. To explain this we must elaborate as to what the filtering of scales do in an ideal case. Recall **Chapter 1**, **Figures 1.8 & 1.9**, where we showed an ideal wave extended arbitrarily, then imaged with a synthetic imager. Let us now comment further on that ideal example. **Figures 4.20 & 4.21** show an ideal case of a nonlinear simulated wavefront, that has been replicated to further extend the domain.
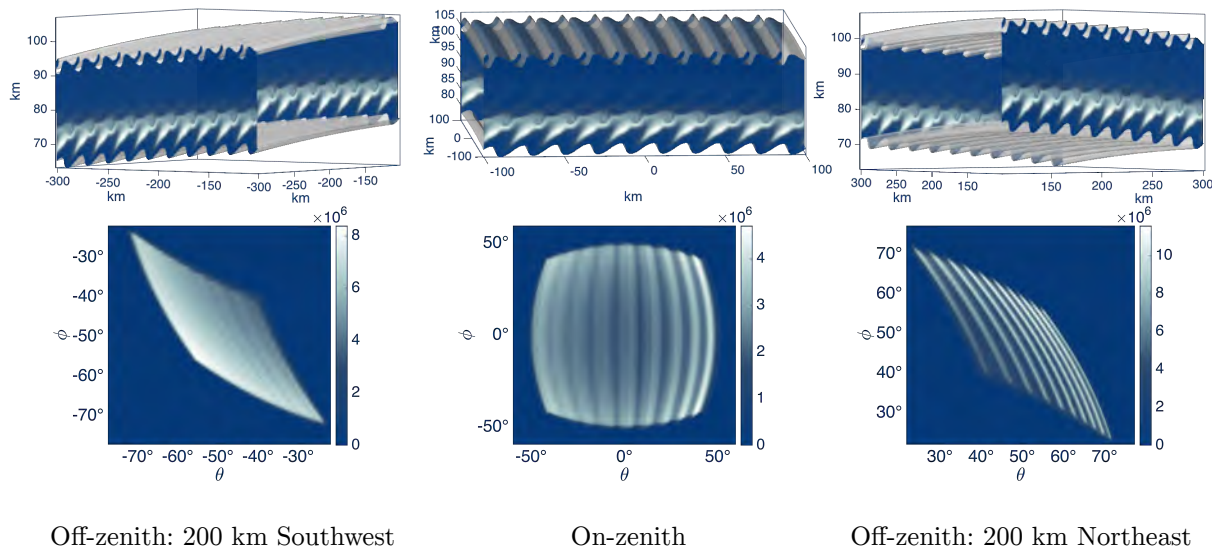
Off-zenith: 200 km Southwest   On-zenith   Off-zenith: 200 km Northeast

Figure 4.20. 3D visualizations of the OH(3,1) emission layer from an ideal simulation imaged from different locations. The input data are 125 m resolution blocks of $20\times10\times160$ km (x, y, z) that have been replicated along x and y to further extend the domain. (top) 3D slices of the wave structure. (bottom) LOS integration at the specified location: the data is displaced by ±200 km along x. (left) Oblique LOS leads to scale filtering. (center) Imaging over the zenith provides the most straightforward depiction of the wave. (right) Parallel LOS produces clear enhancements. The intensity units are (photons·cm^{-3}·s^{-1}).
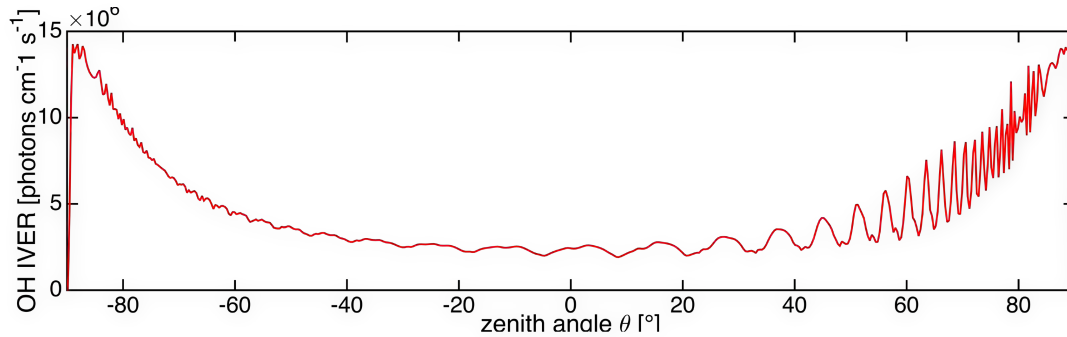
Figure 4.21. 1D plot of the structures shown in **Figure 4.20**. Using a slice of the 3D data, the domain is extended up to 2000 kilometers to further enhance the cancelation effect that happens when the LOS aligns (or not) with the wavefronts. Significant filtering happens for anti-alignment.

Shown in **Figure 4.20** are three identical blocks that are placed at different locations from the synthetic imager. Left block is placed at 200 km West, center block is aligned at zenith, and right block is placed at 200 km East. It is worth noting that these displacements fall within the trial tracks used above. The 3D slice plots at the top of **Figure 4.20** (these are actually caps to isosurfaces not shown) show the shape of the wavefronts, where it is easy to imagine and trace how significant of an impact line-of-sight alignment can have. This is greatly evident in the synthetic images. Furthermore, in **Figure 4.21** the blocks are replicated even farther, 2000 km exactly. This is approximately the diameter of the domain for a 180° FOV imager at 87 km; see **Figure 1.7**. We can deduce three things for the anti-alignment from these plots:

- the cancellation effect due to anti-alignment is more severe than the enhancement,

- the total intensity is actually increased for the anti-alignment due to less "gaps" being present, and

- wave spectral peak of interest is also reduced as is evident from the diminishing perturbations as the anti-alignment becomes predominant.

With these results in mind we can now explain the overall intensity enhancements present in the unwarped images of the first two trials. Furthermore we can also explain the opposite relationship between spectral power and rising total intensity of **Figures 4.18 & 4.19**. As the anti-alignment becomes larger, the spectral components are reduced, but the total intensity keeps rising. Similarly, the maximum intensity plot largely aligns with the shape of the TSP. This is due to the fact that sharper and clearer intensity peaks lead to narrower and more energetic frequency peaks, which contribute more to the TSP. The same can be said for the minimum intensity plot. These ones have a smaller intensity range than the maximum intensity, but this is due to the background intensity being integrated as well; a more even spread between min/max would be present if we were to remove the background integration. While all these conclusions are clear-cut for the SW2NE wavefront-aligned track, less is clear for the other one. Two situations of note arise: firstly, the maximum and minimum intensity plots peak right before the TSP does. This could imply that intensity peaks happen before optimal viewing angles. Secondly, while the TSP rises, increasing the spectral components of the image, the total intensity never goes down. So far we have suggested there is a relationship between enhanced spectral components and enhanced intensity for line-of-sight effects, but this last result suggests that they may be independently characterized. However, this may be simply due to the fact that the other gravity wave sources are, in fact, skewing the results significantly. The SE2NW track starts aligned to this source, and becomes anti-aligned about two-thirds of the way, which would coincide with the max/min intensity peak. This is a probable cause for the continued rise of the total intensity plot. The along-track slices in **Figures 4.22 & 4.23** provide a better insight into the shapes of the wavefronts and the paths of integration revealing that the wavefronts are highly vertical in the analyzed ± 500 km region for the SE2NW track.
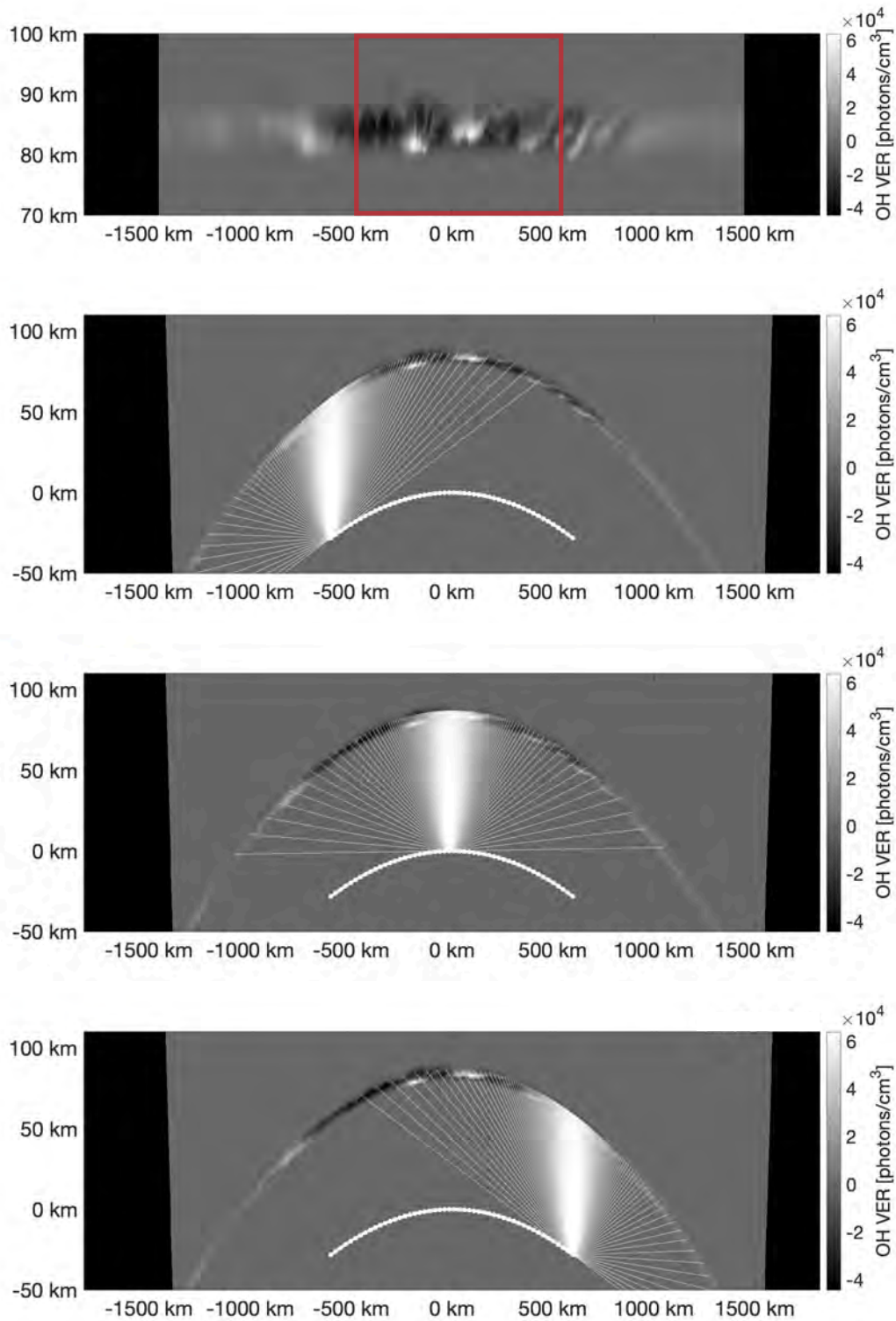
Figure 4.22. Slices along the SE2NW (–55.7°) track. (top) Cartesian slice of original MAGIC data (ratio 30:1 vertical:horizontal). (bottom 3) ENU slices and positions of the 50 surface imagers and 256 lines-of-sight of three of them.
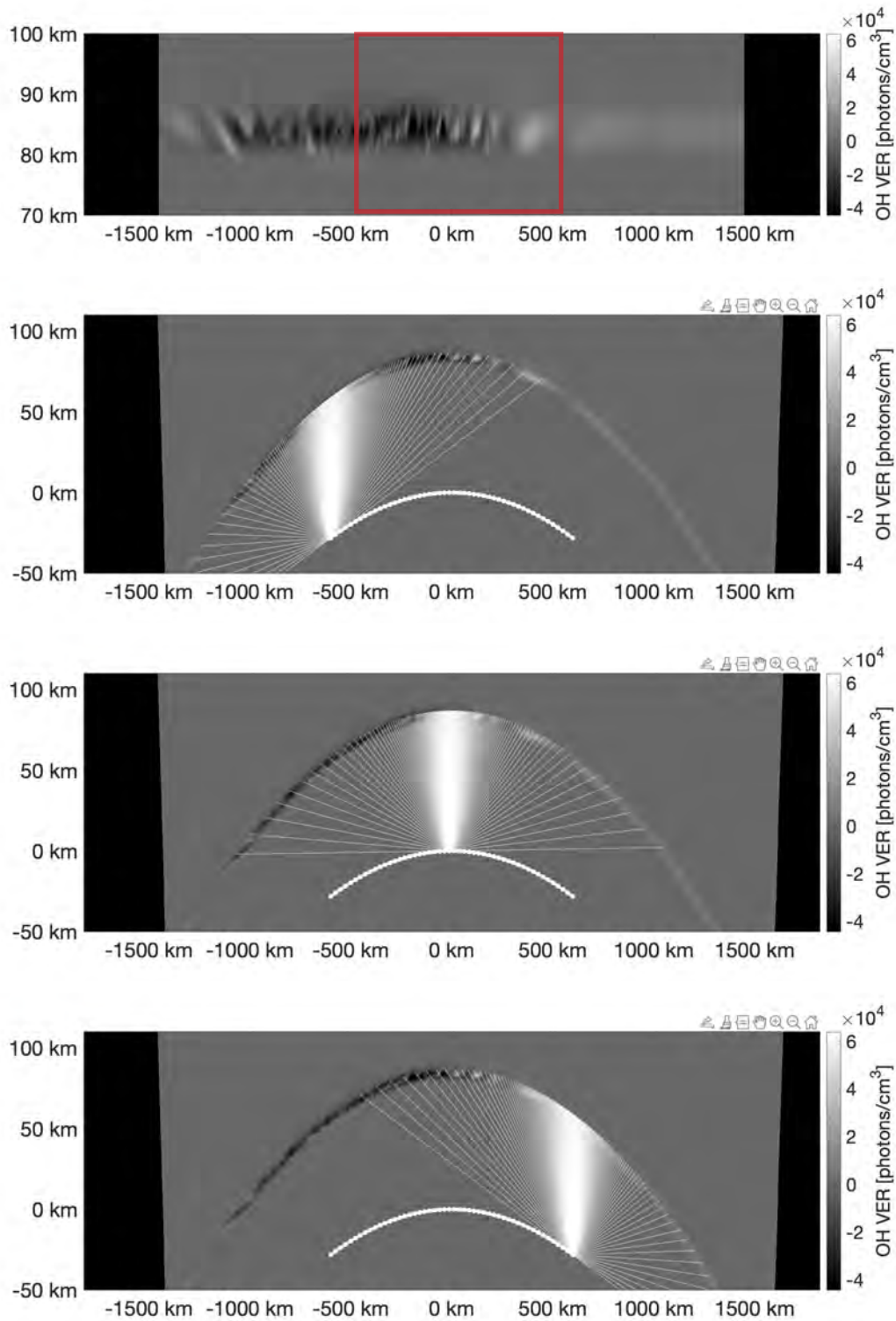
Figure 4.23. Slices along the SW2NE (34.3°) track. (top) Cartesian slice of original MAGIC data (ratio 30:1 vertical:horizontal). (bottom 3) ENU slices and positions of the 50 surface imagers and 256 lines-of-sight of three of them.

4.3. Line-of-sight effects for satellites and O(^{1}D)

So far, we have studied the line-of-sight effects present in the OH(3,1) airglow layer. One of the defining characteristics of the imager-airglow relationship for this layer is the fact that it is the lowest observable layer from ground-based imagers. For large vertical wavelengths AGWs, this distance between imager and layer becomes crucial. **Figure 4.24** shows imaged gravity waves from imagers at different layer distance.
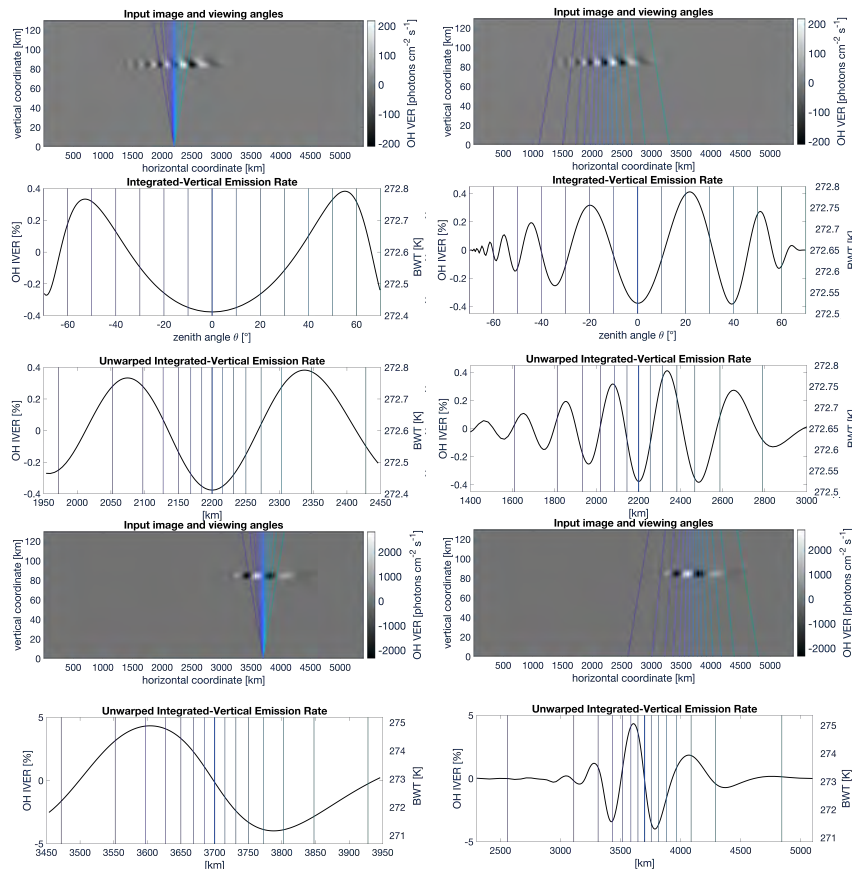
Figure 4.24. Line-of-sight integrations of a (left) ground- and a (right) satellite-based imager at 400 km height at two different times from the onset of a MAGIC OH(3,1) airglow response due to a tsunami. The results are presented as perturbations to the background mean. Due to the larger coverage of the satellite imager FOV at the airglow height, more wavelengths are observed and available for analysis.

We mentioned in the previous section that while the angular resolution of the imager does not change, the location of the intersection of the layer will ultimately determine the imaged spatial resolution of such layer. The extreme case of this would be limb-scans, where small angles may represent several hundreds of kilometers of horizontal layer integration. The satellite imaging in **Figure 4.24** has lower angular resolution because of its greater distance to the layer. This in turn minimizes its sensitivity to line-of-sight effects for large vertical wavelengths. There are cases when this is opposite, such as Rayleigh waves with large horizontal wavelengths that can be measured by GPS networks (Inchin 2020).

Beyond the OH(3,1) airglow simulation products from MAGIC discussed so far, we also have other observables available, namely CO_2 BWT, which was already shown at the beginning of this chapter, and $O(^1D)$ and $O(^1S)$, the redline and greenline airglow respectively, as GEMINI outputs. Both the redline and greenline were coded as part of this thesis as a supplemental capability for GEMINI. The necessary chemistry and reaction rates are based on the work of Witasse, Lilensten et al. (1999). While this chemistry model, in its current GEMINI implementation, needs further validation, some preliminary results are presented here. Specifically the redline is of interest given the existence of imagers and particularly the ones available as comparison to the data presented in the previous section. The CO_2 BWT data available is from the AIRS 4.3μ BWT, which was mentioned in **Chapter 1**, and is collected onboard the AQUA satellite at 725 km mean orbital height. The redline peaks in the F-region of the atmosphere at around 250 km and is observed by ground-imagers or satellites. Both of these observables, therefore, are less susceptible to line of sight effects at extreme FOVs. Effectively, only mild intensity enhancement due to the van Rhijn effect occur and are usually accounted for as part of the background removal. Nevertheless, we present the imaging capabilities for these observables.
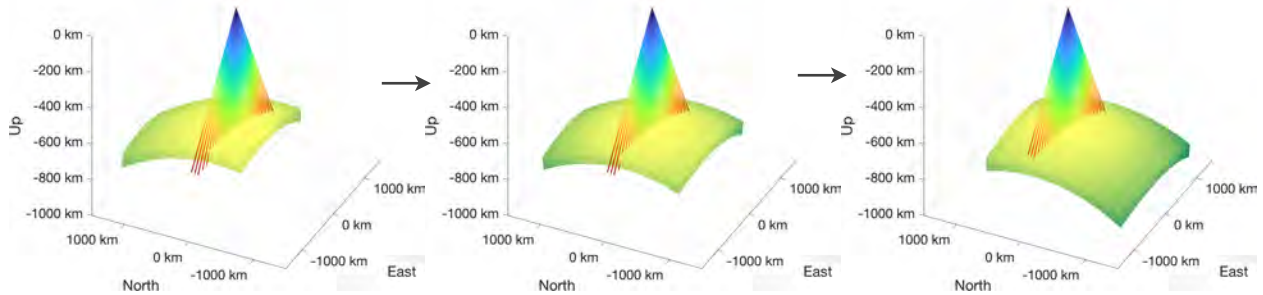
Figure 4.25. Scatter plots of ENU coordinates for interpolation of three cross-track slabs of lines-of-sight for a satellite at 725 km height as it moves Northwards looking through a CO_2 BWT layer that spans 0 to 100 km height from the surface of the Earth. Green colormap correspond to the input coordinates, color coded with height; turbo colormap corresponds to query coordinates color coded with radial distance from origin.

Figure 4.25 shows the scatter plots of the interpolation coordinates for validation for the AIRS synthetic images simulation (Aumann, Chahine et al. 2003). As usual, the interpolation coordinates are in ENU centered at the imager, so the layer appear to move with respect to the imager. The mean peak intensity for CO_2 BWT is around 37 km height, with the layer extending up 60 km height, which is at a sufficiently large distance from the imager so that line-of-sight effects are small. The synthetic images are shown in **Figure 4.26** for 3 satellite tracks, zonally shifted by ± 500 km. Note that the resolution along-track is limited by both the satellite's velocity of 7.5 km/s and the exposure cycle cadence of 2.67 s as it scans across track. We can readily appreciate the subtle peak enhancement that occurs for the center and right tracks, where the lines-of-sights are aligned with the Eastward propagating waves. There is also a slight resolution degradation for the left track and partially for the center track due to the anti-alignment of the fronts. While these effects will mostly be noticeable and measurable for clear AGWs events, these line-of-sight effects might explain why the

AIRS data looks so filtered at medium viewing angles, which correlate with perpendicular wavefront intersections; see **Figure 4.26**.

Figure 4.26. Simulated images of CO_2 BWT as seen by an imager on board a satellite with parameters: 725 km height, 7.5 km/s orbital velocity, 14.4° azimuth track, 2.67 s time between exposures, 512 cross-track pixels and 48.7° FOV. (left) track shifted by 500 km East. (center) original track through center of data. (right) track shifted by 500 km West.
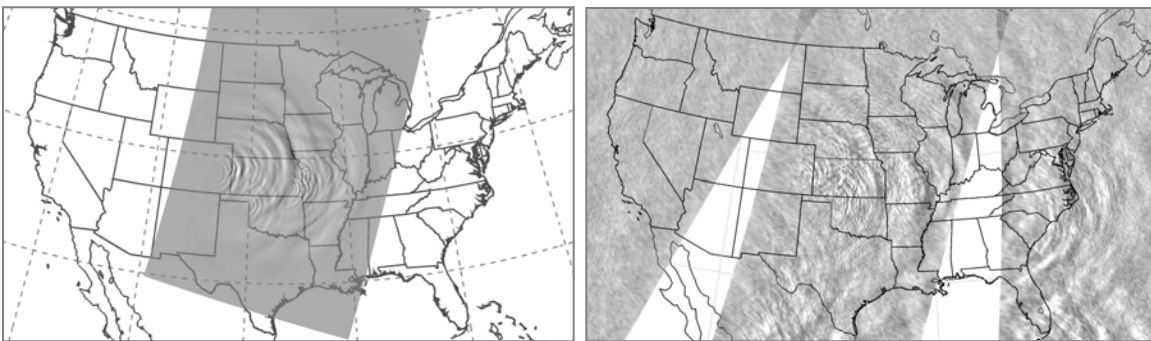
Figure 4.27. AIRS Comparison of simulated images of CO_2 BWT as seen imaged by an imager on board a satellite with parameters: 725 km height, 7.5 km/s orbital velocity, 14.4° azimuth track, 2.67 s time between exposures, 512 cross-track pixels and 48.7° FOV. The AIRS map projection was found to be the Albers Equal-Area Conic Projection with standard parallels at 29.5°, 49.5°, which is a standard map projection for the contiguous USA; our simulation results are plotted accordingly to resemble that of the AIRS data. Simulated data: Midwest thunderstorm 2016/07/08 5:15:12 UTC.

Let us look now at the GEMINI O(^{1}D) simulation results. The scatter plot of interpolation coordinates is shown in **Figure 4.28**. Since GEMINI domain includes the entire magnetic field lines, we trim it at 600 km height and ignore the opposite hemisphere. We first show the electron density in **Figure 4.29**, which is a good tracer for the dynamics across the entire height domain. We also include a height gauge, as it may become useful to readily estimate height with accurate scaling. Here on display are large electron perturbations and suggesting a large background interaction. The O(^{1}D) 630.0 nm airglow perturbations are shown in **Figure 4.30**. With a FWHM of 60 km, this layer is much deeper than the mesospheric airglow, and it presents opportunities for significant intensity enhancements for large vertical wavefronts at small FOVs. For the location of the synthetic imagers we have chosen the site location of MANGO imagers, although currently only data from one is available; refer to **Table 4.3**. These coordinates are well distributed along the cardinal points from the center of our data, so they provide a natural choice. Finally the synthetic imagers are presented in **Figures 4.31 & 4.32**.

Comparisons with MANGO O(^{1}D) imager data for two different simulation times have been performed and shown side-by-side in **Figures 4.33 & 4.34**. Simulated MANGO images are made following the procedure they use for own data processing: a time-difference image with two 4-minute exposure integrations 1 minute apart. It is found that there is an important disagreement with the simulated data. This simulation currently assumes the perturbation depend primarily on the electron density disturbances, where the neutrals are obtained from the MSIS model. This realization leads to belief that perturbations in the neutral densities play a bigger role in the chemistry of the O(1D) emission. This will be addressed with additional tests that includes natural outputs from GEMINI, which is not a typical data product yet.
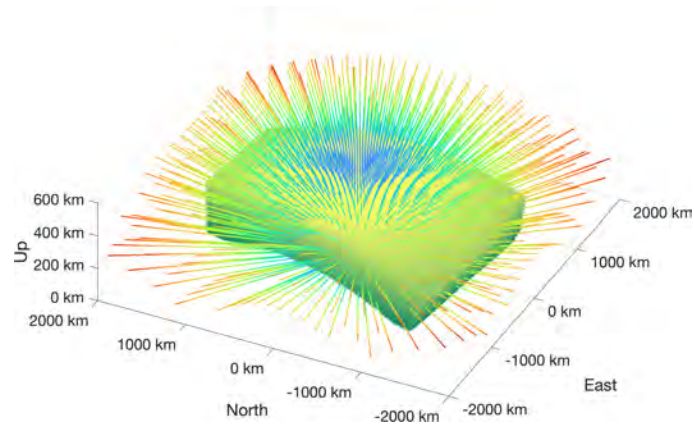
Figure 4.28. Scatter plots of ENU coordinates for interpolation of GEMINI domain and a ground based imager. Green colormap corresponds to the input coordinates, color coded with height; turbo colormap corresponds to query coordinates color coded with radial distance from origin.
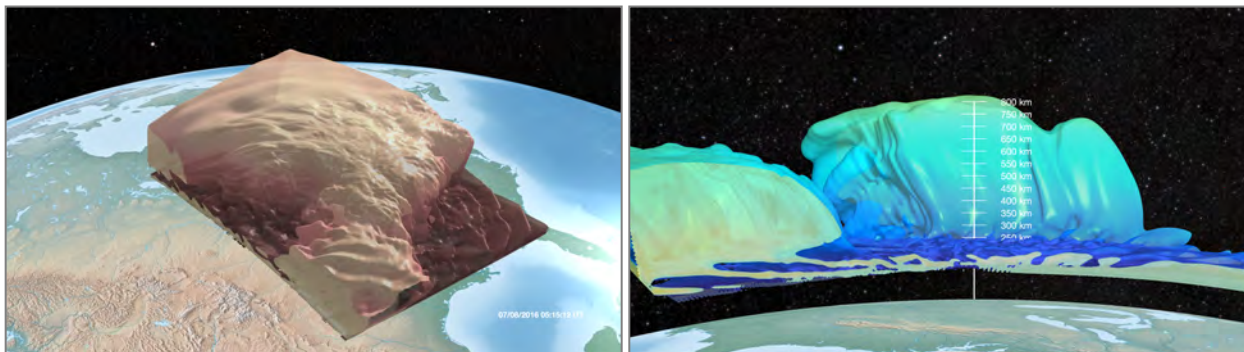
Figure 4.29. 3D renders of isosurfaces of ± 500 electrons/cm³ perturbations of the simulation data in two different views. Positive perturbation are shown in blue/green colormap and negative in pink. A height gauge is included in the side view. (Scale of 1:1 vertical vs horizontal). Simulated data: Midwest thunderstorm 2016/07/08 5:15:12 UTC.
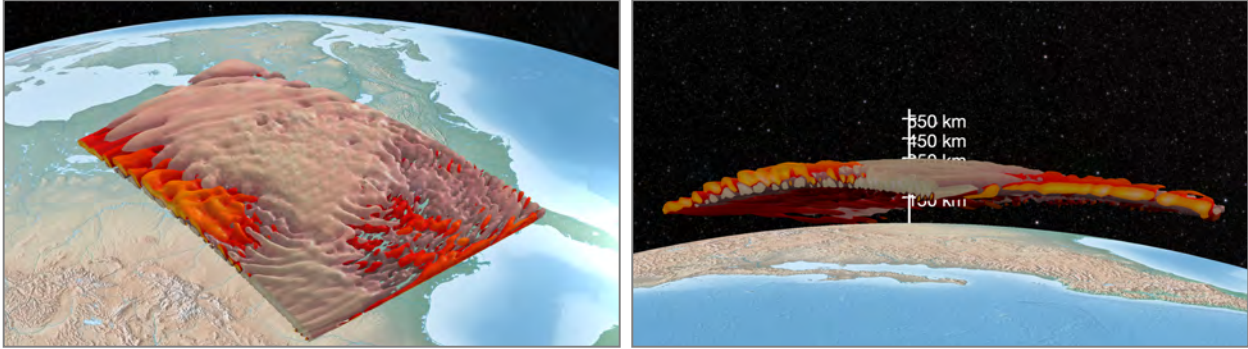
Figure 4.30. 3D renders of O(^{1}D) isosurfaces of ± 200 photons/cm³ perturbations of the simulation data in two different views. Positive perturbation are shown in red colormap and negative in pink. (Scale of 10:1 vertical vs horizontal). Simulated data: Midwest thunderstorm 2016/07/08 5:15:12 UTC.

MANGO imager station	Coordinates (lat, lon, h)
Ely, IA	41.89°N, 92.00°W, 255 m
Madison, KS	38.12°N, 96.10°W, 333 m
French Camp, MS	33.29°N, 89.39°W, 148 m
Pisgah, NC	35.20°N, 82.87°W, 921 m

Table 4.3. Location of synthetic imager that matches MANGO redline imagers stations. *Source: https://github.com/mangonetwork/mangopy/; heights retrieved from Google Earth.*
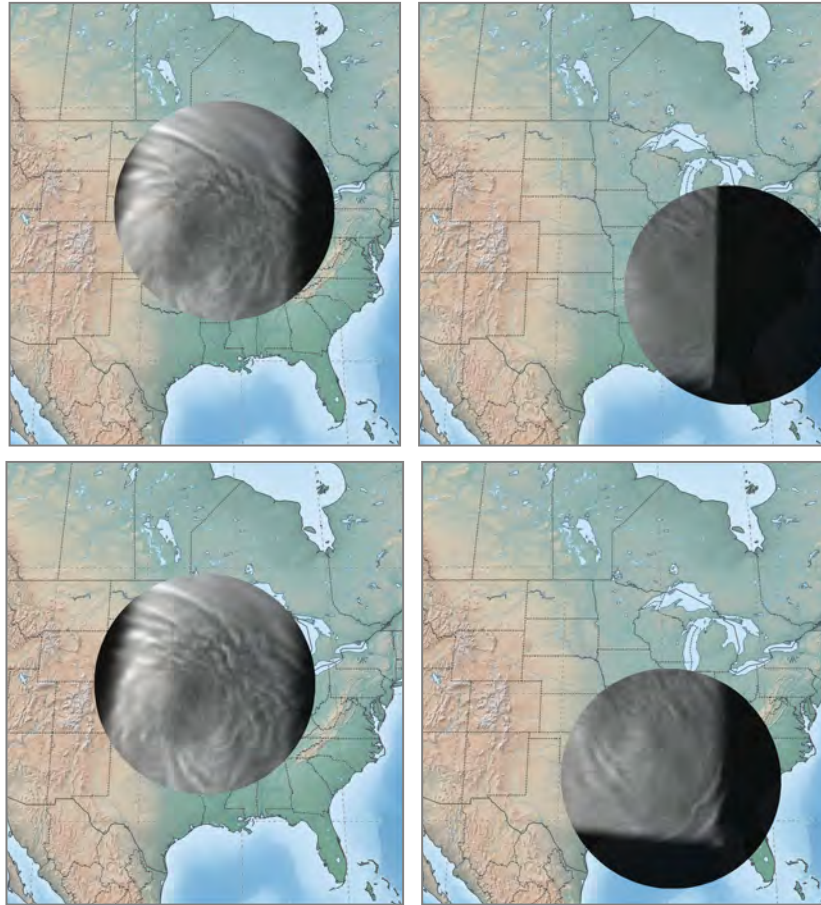
Figure 4.31. Unwarped synthetic O(^{1}D) 630.0 nm airglow imagers at MANGO locations. From left to right and top to bottom: Ely, Pisgah, French Camp and Madison All images share color scale from 0 to 16×10^7 photons/cm^2. Simulated data: Midwest thunderstorm 2016/07/08 5:15:12 UTC.
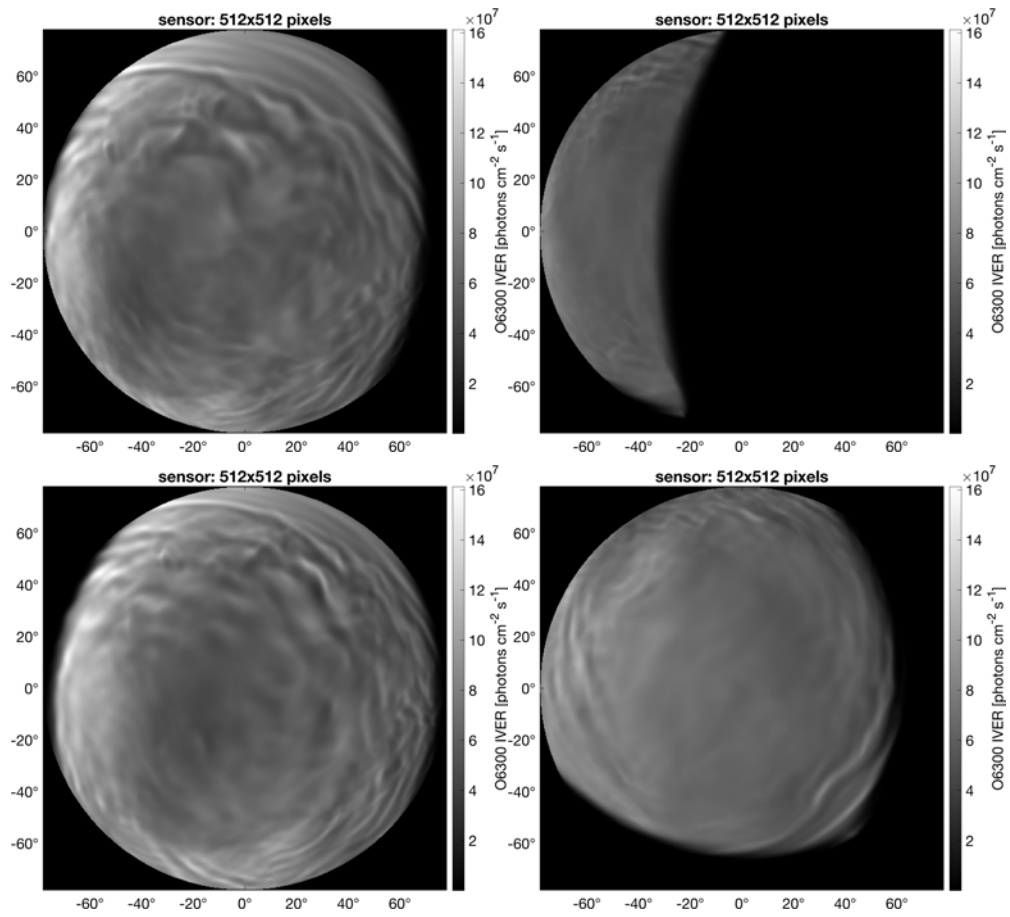
Figure 4.32. Synthetic IVER images of O(^{1}D) 630.0 nm as seen by the imagers at MANGO locations. Simulated data: Midwest thunderstorm 2016/07/08 5:15:12 UTC.
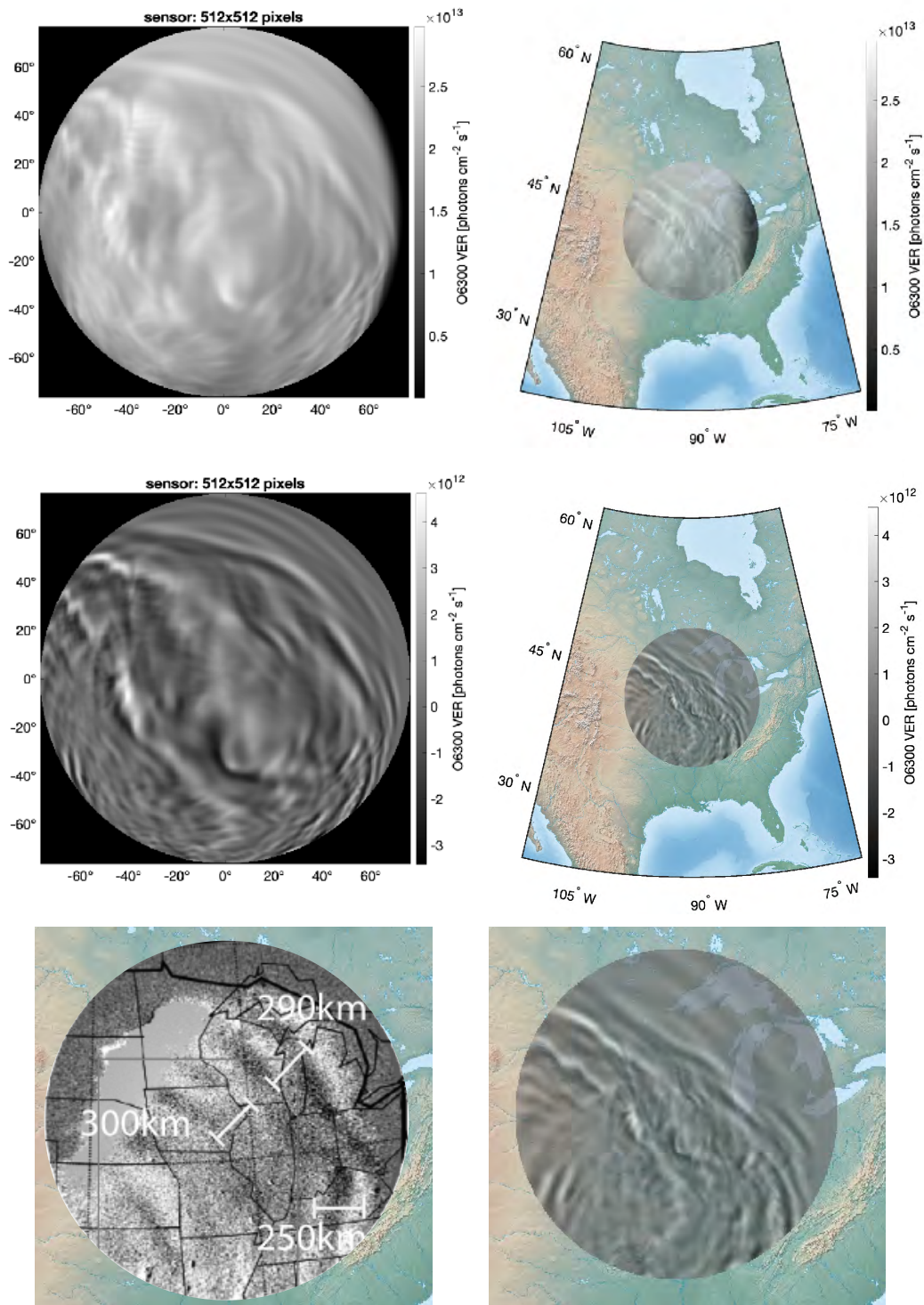
Figure 4.33. O(^{1}D) synthetic images at 250 km heigh at MANGO's Ely, IA location. (top) 1-minute exposure image at 4:15:12 UT. (middle) Time-difference simulated image with 2 4-minutes exposures, 1 minute apart centered on 4:15:12 UT. (bottom) MANGO data comparison. Simulated data: Midwest thunderstorm 2016/07/08 4:15:12 UTC.
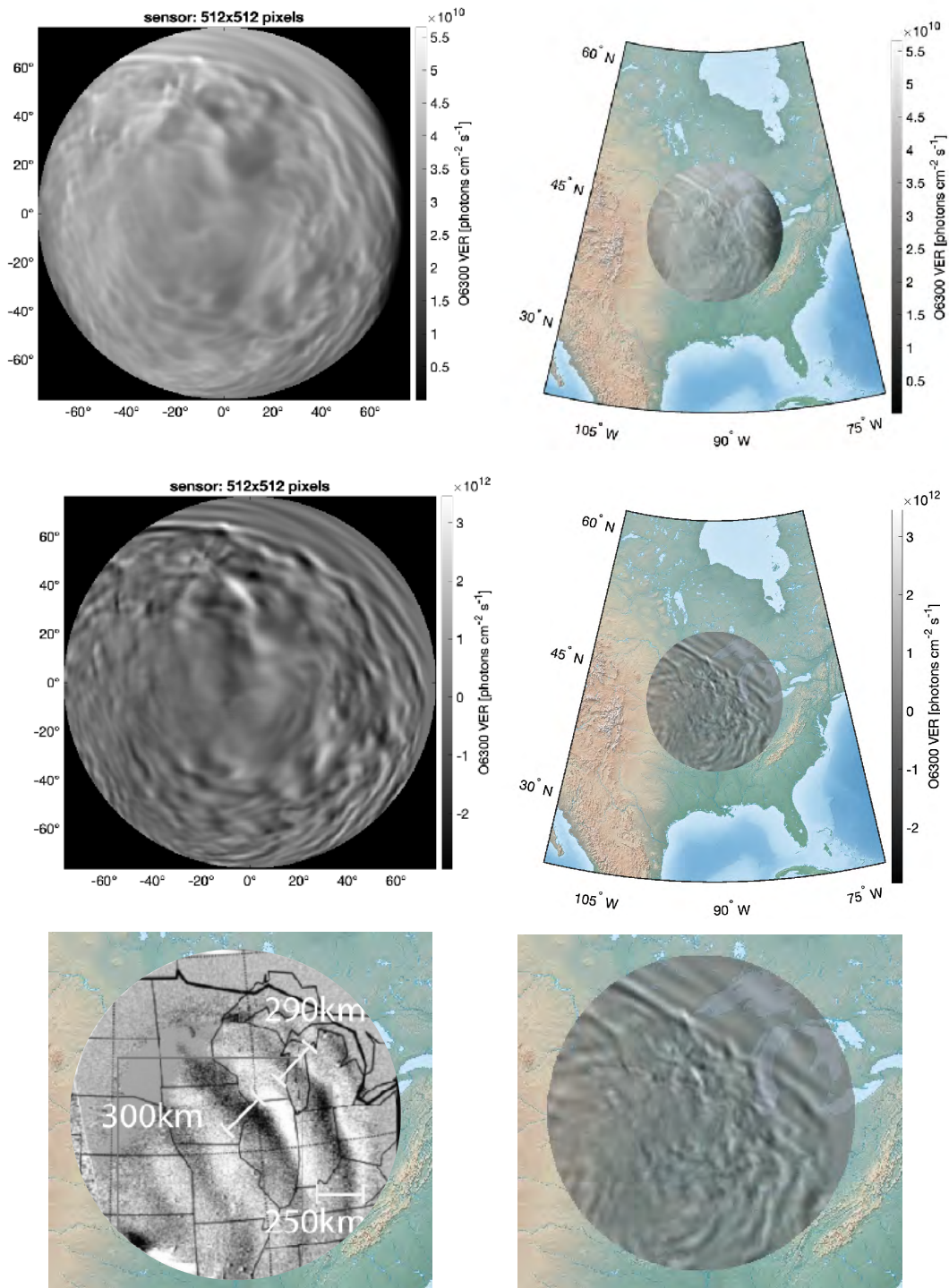
Figure 4.33. O(^{1}D) synthetic images at 250 km heigh at MANGO's Ely, IA location. (top) 1-minute exposure image at 5:15:12 UT. (middle) Time-difference simulated image with 2 4-minutes exposures, 1 minute apart centered on 5:15:12 UT. (bottom) MANGO data comparison. Simulated data: Midwest thunderstorm 2016/07/08 5:15:12 UTC.¶

Chapter 5

Conclusions and future work

Whether it is ground-based or space-borne imaging of horizontal structures of the atmospheric layers or limb-scan views from satellites for 2D height measurements, a full description of the observed phenomena is incomplete from images alone. For this reason multi-layer and multi-instrument observations have become necessary, and it goes hand-in-hand with the need for modeling. As these models become more accurate, so must our simulated observables. The basis for this thesis are the observable products from the MAGIC-GEMINI models, including airglow volume emission rates, temperature and electron density. The capability of the models to simulate large domain gravity wave phenomena, and effects on the ionosphere, gives rise to the opportunity to study how real instruments would measure such data. Of particular interest is the measurement of airglow intensity, due to the widespread availability of all-sky airglow imager data and its usefulness for determining horizontal features for gravity waves.

5.1. On the creation of synthetic instruments

This thesis has focused on creating a meticulous geometric description of the airglow-observer coordinate mappings, first, based on purely trigonometric relations using a spherical Earth. Then an ellipsoidal model was introduced, where the trigonometric relations were replaced by a ray-tracing algorithm which effectively

determines the intersection between an observer's line-of-sight with an ellipsoid. Both methods were thoroughly described in **Sections 2.1-2.5**. The second method circumvents the limitations of the trigonometric relations, allowing for a free placement of the observer anywhere in 3D space, while also admitting any viewing angle. The intersection points are a result of the quadratic solution of the system of equations for the line-of-sight-ellipsoid mappings, and the type of solution determines whether the intersection exists or not, there are two or one intersection points and whether the observer is within the ellipsoid or outside. This contains all the necessary information for an instantaneous representation of positions in 3D space that can then be used for simulating measurements. It can also be extended to future model datasets provided from a variety of coordinate systems.

Along with the geometric descriptions, a framework has been developed to create synthetic imaging instruments with different configurations, whether they are single-line instruments such as GPS receivers or spectrometer/radiometer such as AIRS, to sensors with grids of imaging units such as CCD panels in all-sky imagers. The algorithm allows for specification of number of imaging units (pixels), and a simplified optics system with parameters of FOV and a lens function. It is also possible to specify the orientation, zenith angle and geographic coordinates of these synthetic sensors. These design variables determine the angular resolution, zenith and North alignment, as well as location on the globe. Once the instrument parameters have been specified, the ray-tracing solution is used for 3D scattered interpolation and to create the 3D coordinates for the line-of-sight-ellipsoid/airglow system. This description, along with appropriate examples is described in **Sections 2.6-2.9**. As part of the coordinate validation process, a 3D scatter plot is used for a visual validation of these mappings, which includes the proper warping of MAGIC data to conform with geographic coordinates; see **Figures 2.7, 4.9 & 4.23** for reference.

5.2. On the implications of map projections

The mapping transformations are determined for a reference ellipsoid of choice. In this case we have used the World Geodetic System of 1984 (WGS84). This ellipsoid describes both the shape of the Earth and of the airglow layer. It is possible, for example, to choose a geoid for the specification for the airglow layer height such as the Earth Gravitational Model of 1996 (EGM96)[7]. The use of these ellipsoids have the added benefit of providing higher accuracy in map projection distortions, for which we have dedicated **Section 3.3**. There are two important conclusions from this:

- map projections introduce errors in right-angles, distances and areas and can skew horizontal wave parameters with varying severity depending on the projection of choice and location within it, and

- unwarping of MAGIC data suffers the same distortions introduced by map projections, which can be compounded when plotting it on a map.

For these reason, we evaluated different map projections and discussed their merits and limitations. On the subject of projection of atmospheric data one important consideration was made, and that is the importance for a separate description of zonal and meridional components. This deciding factor rises naturally due to the fact that winds are effectively described by these components, predominantly driven by differences in zonal heating and the rotation of the Earth. With this in mind, we tested the map projections that align zonal, meridional directions directly to the x and y axes, namely cylindrical map projections and the loximuthal projection. The biggest problem with these is the large scaling error that occurs at high latitudes. For this reason, the loximuthal projection, a compromise pseudo-cylindrical map projection, was chosen. Also, in agreement with the conclusions of **Section 2.5**, loxodromes, or rhumb lines, provide the accurate distance measurements for calculating arc distances in viewing

---

[7] For displaying model data, the choice of geopontential height would be incompatible with the gravity values used for either MAGIC or GEMINI, which are based on gravity values dependent only on height and not geographic location

geometries, which follows from the fact that such geometries are determined by their fixed azimuth. In summary, the benefits of the loximuthal map projection are:

- *y*-axis is aligned South-North and *x*-axis is aligned West-East,

- angle, scaling and area distortions are low around the origin of the projection,

- all distortions can be accounted and corrected for when determining horizontal parameters, and

- all lines crossing through the origin are loxodromes which directly conform to the observer-airglow geometry.

Interestingly enough, this map projection is not widely used in our field. In fact, it is my opinion that map projections are rarely a conscious design choice for representing data. This could be for several reasons, including the scale of the mapped data, the lack of need to characterize the errors associated with the distortions and perhaps more commonly, the absence of subsequent analyses on the projected data. As an example refer to **Figures 3.28 & 3.29** where it was discussed what projection needs arise from the purpose of the displayed data. If one does not need to appropriately represent area, then perhaps the choice of map projection may not be an important one. However, if subsequent analyses are needed from such data, then the type of projection may become more significant, especially as the scales represented in the data become distorted as they get larger and further away from the projection's origin. This is the case for many imagers, including all-sky airglow imagers. It was briefly mentioned in **Section 4.3** that MANGO post-processing calculates distances over great circles, which is the method we suggest not to do in **Section 2.5**. Moreover, it might be relevant to put this information front and foremost, since it leads to measurable error; otherwise, the data analyst will assume risks the data analyst to assume distances are geographically accurate. Other systems, such as satellite position algorithms, may use GPS for geolocating their data products; in this case, the map projection error does not compound with the geolocating

of data. In fact, for very precise mapping, such as city roads and local terrain, highly precise coordinate reference systems (CRS) are used. These combine a coordinate system such as ellipsoidal (lat, lon) or Cartesian (x, y), a horizontal datum such as WGS84 and a map projection, all of these chosen to most accurately represent the particular region of the world. For this purpose there exists the EPSG Geodetic Parameter Dataset or EPSG codes (https://epsg.org), which is a public registry of codes with very specific uses and locations, such as cities, countries, continents or any geographic area of interest. The framework we have developed here allows for the use of these EPSG codes as input for the mapping projections. However, the scales of the phenomena we wish to study, namely atmospheric gravity waves do not warrant highly precise geolocating. Moreover, MAGIC-GEMINI is not yet a georeferenced model, so any error introduced due to projections on the synthetic data is only representative of the projection itself. This is a perfect example of why the choice of map projections might be often overlooked as a fundamental part of data portrayal and visualization.

5.3. On the characterization of line-of-sight effects

A method using power spectrum analysis was devised for characterizing the filtering of scales in all-sky airglow imagery. It was found that the frequency content of unwarped images varies for different viewing geometries when oblique lines-of-sight align or anti-align with the wavefronts. The periodogram features sharper peaks for parallel viewing and larger frequency spread for perpendicular views. With the aid of an idealized case of replicated nonlinear wave this simple filtering mechanism was explained. For quantifying the scale-filtering effect the total power spectrum (TSP) was chosen as the characterizing variable. This scalar quantity represents the prominence of the frequency content available, in our case, of spatial frequencies for wavelengths over 8.26 km. The higher spectral power the more discernible the fluctuations or sinusoidal

features of the images. By fixing the unwarped images to the same geographical area, we were able to vary the position of the imager and determine TSP in terms of the tilt angle, for both wavefront-aligned and anti-aligned imaging. It was found that aligned imaging provided up to 25% increase in the spectral power at around 86° viewing angle, while the anti-alignment dipped down to 50% at the same viewing angle. When we placed the imagers on a track perpendicular to the wavefronts, the change was minimal, peaking at 102% and dipping at 91%. The study was designed at around a very specific semi-concentric wave, which was observed to be mostly Eastward and is in line with the original work by Heale, Snively et al. (2019). The wavefront-aligned track leverages such wave, while the anti-aligned track, having less influence to this main gravity wave, seems to be influenced more by the other sources, leading to less conclusive results regarding the shape of its TSP profile. In addition, total, maximum and minimum intensity plots were also provided. It was found that for the wavefront-aligned track the total intensity increases as the viewing angles become anti-aligned. This was explained by using the ideal wave case, and is due to shape of the wavefronts, where perpendicular imaging has no gaps.

5.4. Products and publications

The structure of this thesis reflects the intended publications, first, a detailed technical description of the imager-airglow intersection algorithm, and a secondly, the spectral analysis studies for line-of-sight effects based on the Midwestern thunderstorm case, as well as detailed reconstructions of multi-layered synthetic data as may be observed from instruments on ground or in space. While these two publications are in preparation, the tools developed here have contributed to one published paper and one that is currently in revision. The first paper is titled "Mesopause airglow disturbances driven by nonlinear infrasonic acoustic waves generated by large earthquakes" by Inchin,

Snively, et al. (2020). This paper details the tsunamigenic AGWs from MAGIC that were used in the discussion of **Chapter 3**. In this work mesopause airglow perturbations are driven by infrasonic acoustic waves after the 2011 M9.1 Tohoku-Oki earthquake and subsequent tsunami off the coast of Japan. MAGIC was used to simulate the airglow observables and synthetic images were created to characterize the atmospheric response to the earthquake, which in turn, can be used to describe the earthquake itself. Given the widespread availability of imagers in Japan, as well as the fact that the region is located between 4 tectonic plates, it is of great value to evaluate the imaging capabilities of the mesospheric airglow as an early warning system, as proposed by the authors. The results that were included in the publication are presented in **Figure 5.1**. These synthetic images represent the first of their kind; no real imager has yet captured acoustic wave signatures as such in the mesospheric airglow above an earthquake leading to a tsunami. The results of this study show very large perturbations and, as the manuscript suggests, it should be possible to image acoustic wave signatures in as little as 6 minutes from the onset of the earthquake. A numerical test of this hypothesis is made possible by the synthetic imaging framework developed in this thesis.

A second coauthored publication is currently in revision (minor, and due for resubmission by the time of defense). The title of this work is "Simulation of infrasonic acoustic wave imprints on airglow layers during the 2016 M7.8 Kaikoura earthquake" bye Inchin, Aguilar Guerrero et al. (2022). This work aligns well with the objectives of the analysis of **Chapter 4**. By applying a similar philosophy of scale-filtering and line-of-sight enhancements, this work attempts to establish parameters for enabling successful imaging of yet-to-be seen infrasonic acoustic waves (IAWs) in the mesosphere. This particular type of gravity waves require faster and higher resolution imagers, and the authors test for different exposure times by integrating several IVER unwarped images. This is a standard procedure used to improve signal-to-noise ratio for all-sky imagers, one that we can replicate. For fast transient IAWs the exposure time will lead to an

effective scale filtering, or blurring; see details in the text, that note of which IAWs features are retained which each longer exposure time. The results presented as they are in the manuscript are shown in **Figure 5.2**. Next presented are different synthetic images for imagers that have been pointed with different tilt angles. In this case the line-of-sight effects are visible, including some minor scale filtering and significant intensity enhancements. Since these two effects inform over the shape of the wavefronts, targeted images like this provide some insights into the 3D morphology of the wave. This work is another proof-of-concept and further showcases the potential for more studies like this.
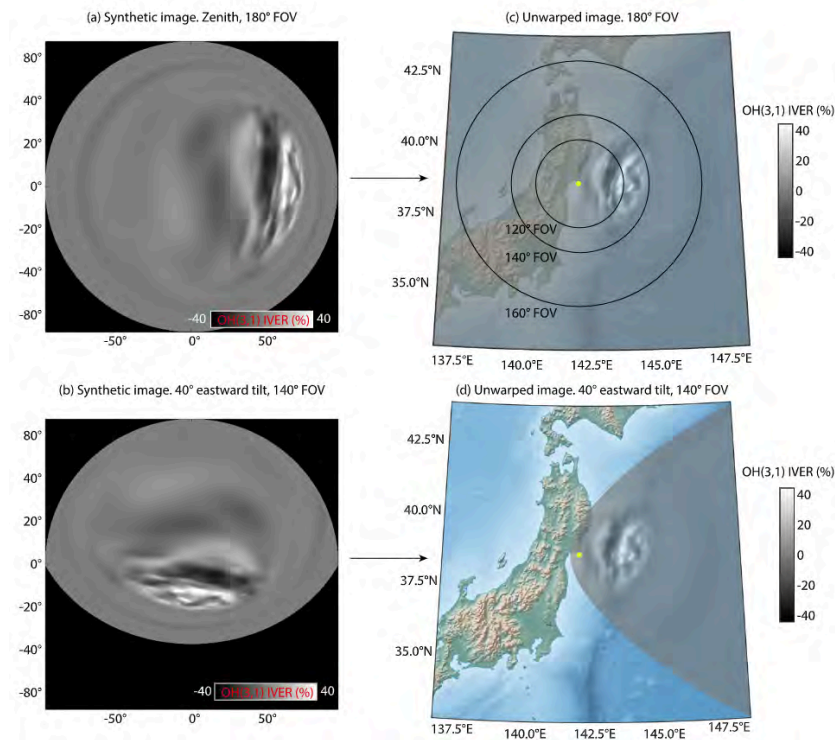
Figure 5.1. Synthetic images of OH(3,1) integrated volume emission rates (IVER) for (a) a zenith pointing wide field (180°) imager and (b) an eastward pointing imager with 40° tilt angle of 140° FOV. (c,d) Synthetic images unwarped on a geographic map and shown on an oversaturated scale for better visibility of weaker features. Black circles in plot (c) show observable regions for imagers with 120°, 140°, and 160° FOVs, whereas a wide field imager covers the whole region. The yellow point in plots (c) and (d) represents the position of the imager. *Sourced from Inchin, Snively, et al. (2020).*
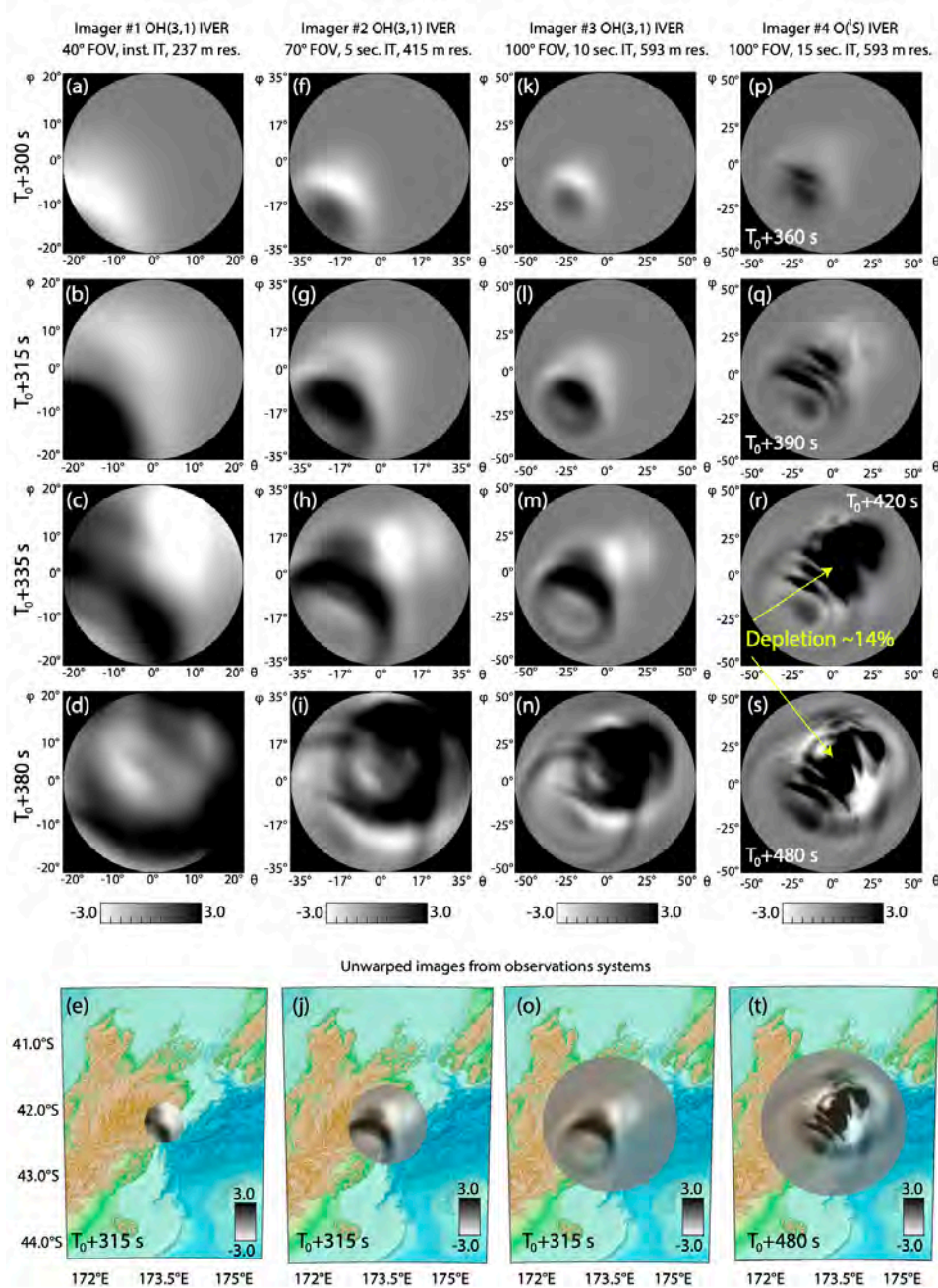
Figure 5.2. Synthetic images of IVER for the observation systems presented in Table 2 and their unwarped representations on a geographic map. The images are shown on an oversaturated scale for visibility of weaker features. An opacity is added to the unwarped images to visualize the underlying topography. Time epochs of snapshots for O(1S) IVER are specified separately. *Sourced from (Inchin, Aguilar Guerrero et al. 2022).*
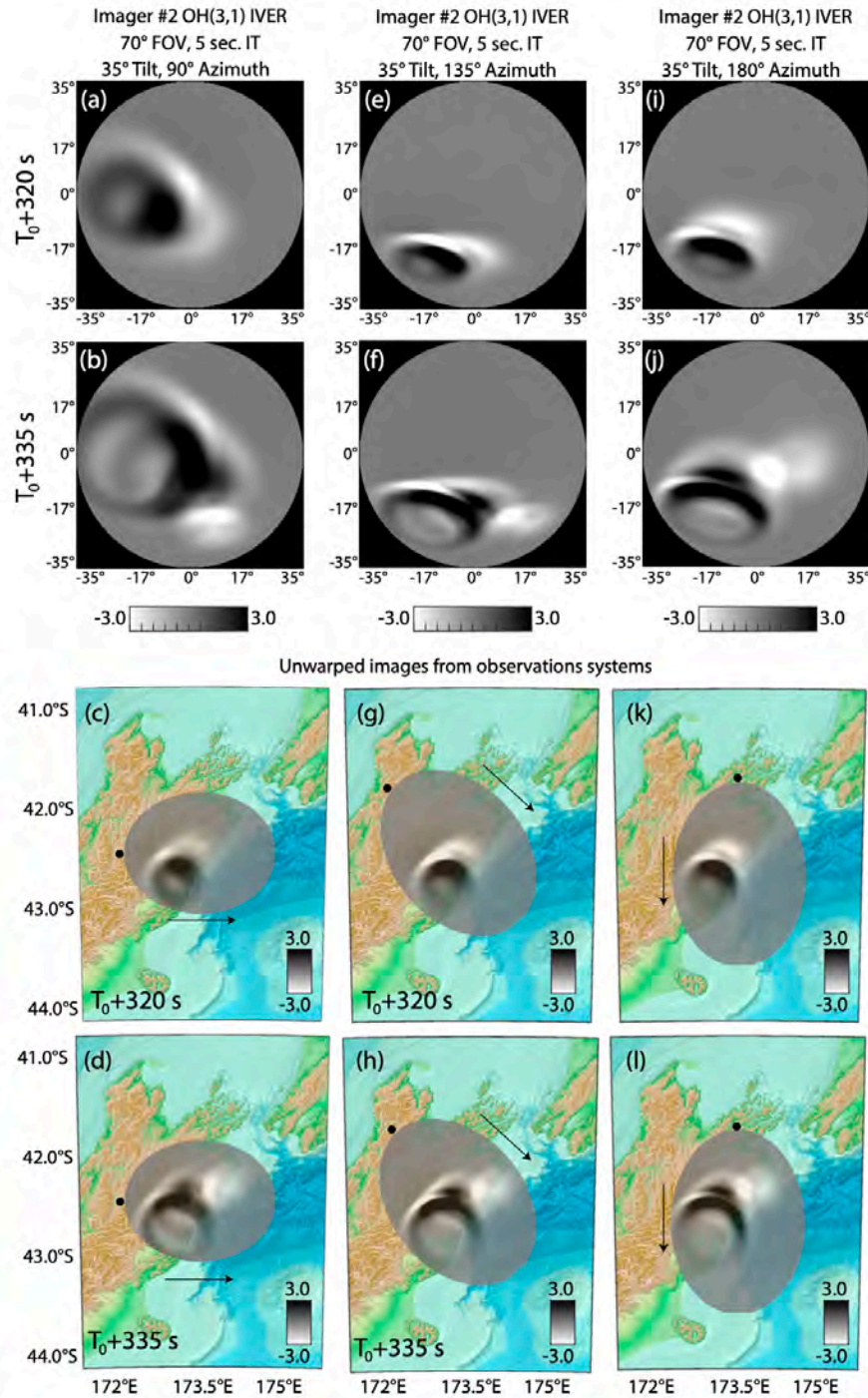
Figure 5.3. Synthetic images of integrated volume emission rates (IVER) captured with observation systems 2 with different azimuth angles and location of the imager and its unwarped representations on a geographic map. Black dots depict the position of imagers and arrows: directions of pointing. *Sourced from (Inchin, Aguilar Guerrero et al. 2022).*

It should be mentioned that the software suite created for this thesis, part of which has supported the two publications discussed above, will be made available in an online repository (GitHub) following software documentation. This includes the imager-airglow algorithm, which creates an imaging sensor and performs the ray-tracing solution, the map projection and the 3D visualization tools. All code has been created to run within the latest version of MATLAB© by MathWorks   (release 2021b as of this writing). However, the fundamental methods and geometries applied can be readily adapted for use in other environments pending software development.

5.5. Future work

The bulk of this thesis reports development of the tools necessary for freedom in the design of synthetic imaging instrumentation for atmospheric phenomena, in a detailed MATLAB prototype. The scientific applications greatly depend on the modeling work done with MAGIC-GEMINI and is motivated by the present and future availability of data products and future versions of the code that may include more-flexible capabilities and more-realistic geometries. With this in mind, we now have the capability for effortlessly providing imager data for airglow measurements. Additionally, it was not discussed in this thesis, but all techniques may be applied equally to path integrations for Global Navigation Satellite System (GNSS) Total Electron Content (TEC). These are modeled single-LOS instruments, whose geometry is specified by the receiver and satellite locations. In **Figure 5.4** we present a detail from Inchin, Snively et al. (2021) where the airglow-imager framework is used in this 1D form through a 2D domain. In this case the airglow layer description is a proxy for the thin-shell representing of the ionosphere, where the electron density is unwarped at the so-called IPP position, chosen as 300 km for this specific study. In general, analysis for the

GEMINI domain-specific products is still to come, enabled by the latest efforts in coupling multi-scale simulations from MAGIC.

In addition to GPS studies, future research is needed to unequivocally demonstrate cases for which the detection of fast acoustic and acoustic-gravity waves, such as later detected in TEC, is possible in the mesospheric airglow layers. Preliminary work on this has been performed and the results of the Tohoku-Oki case study are promising. This particular scenario has the caveat that such massive earthquakes are not very common, and less likely to be captured on airglow imagers. This leads to another area of opportunity for future studies, which is simulation of satellite data. While we have shown here results from the simulation of AIRS, there are several other satellites with imaging products that we are well poised to simulate. This includes a future addition to the framework for limb scans. This will require to adequately discern the appropriate solutions to the line-of-sight-ellipsoid system of equations, to allow for both quadratic solutions.
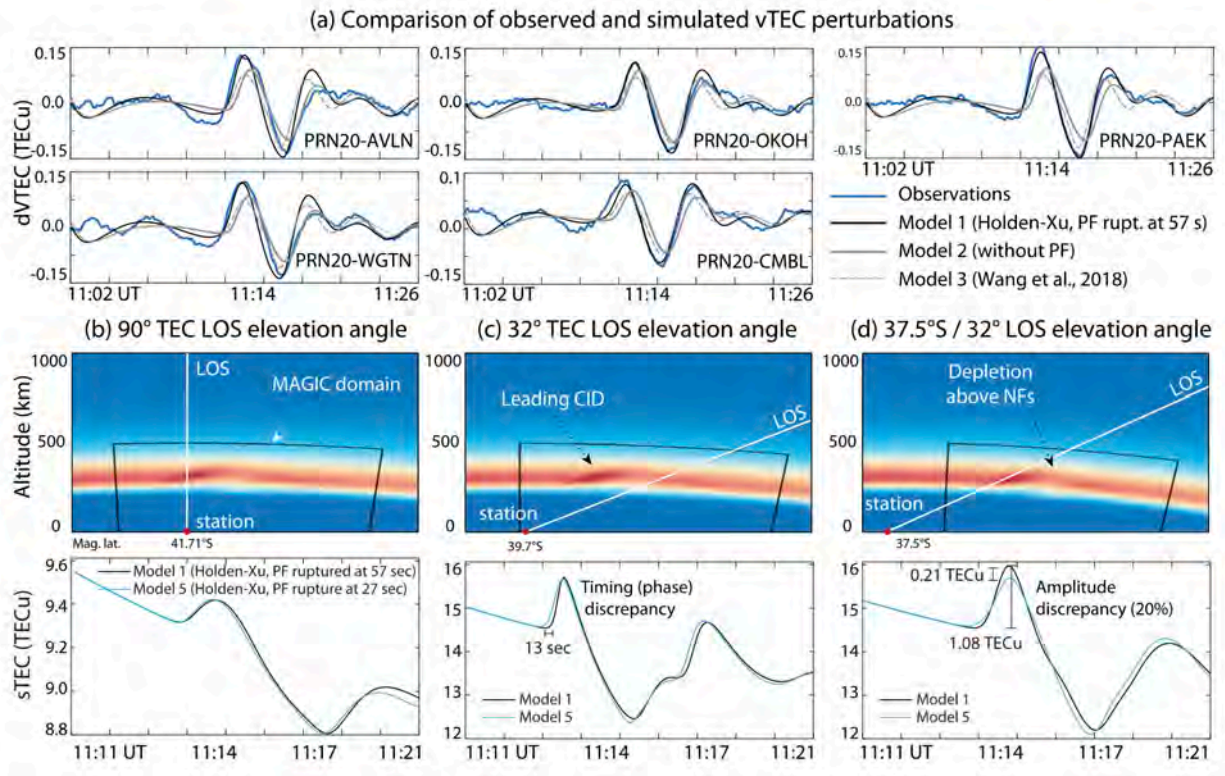
Figure 5.4. Detail from (Inchin, Snively et al. 2021), in which the GPS capabilities of our framework are being used to compare simulated vertical-total-electron-content (vTEC).

As a final note, it is worth mentioning that additional products have been created related to 3D visualization tools. This include the capability of producing augmented reality (AR) models of our volumetric data sets and was featured in AGU 2021 conference (Guerrero, Heale et al. 2020). This capability offers outreach opportunities that can be easily distributed online and accessible for mobile users. This process requires integration of the MATLAB 3D visualization outputs described in **Chapter 3** into Blender, an open-source 3D modeling software. This is then converted into a AR model via Apple's own ARKit or Adobe's Aero software, which is compatible with non-Apple users; see **Figures 5.5 & 5.6** for two examples. The most exciting part of this technology is that is constantly being developed and is poised to grow larger in the

coming years. The scientific and education applications are numerous and we are trying to leverage this momentum by extending our framework capabilities with meaningful AR applications.

Figure 5.5. An AR model of the O(^{1}S) redline airglow from the Tohoku-Oki simulation. These are mobile screenshots of the model placed on a living room table.
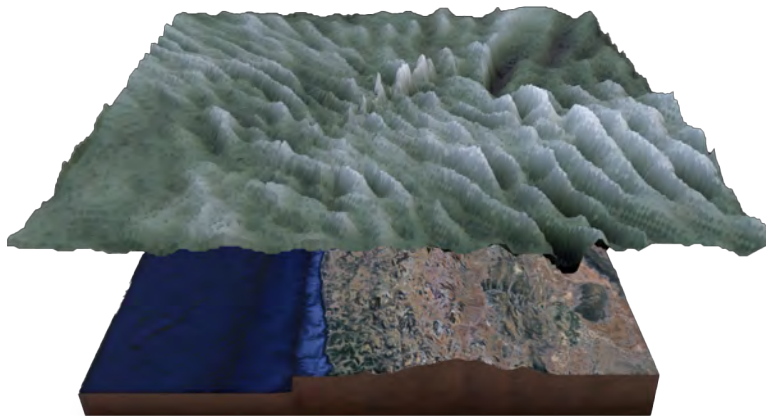
Figure 5.6. 3D AR model of airglow imager data with mountain waves over to Ande mountains in Chile.

As a final thought, we have shown the importance of multi-layer, multi-sensor and even multi-visualization for comprehensive studies of atmospheric phenomena. The ultimate goal is to simultaneously analyze data, modeled quantities, modeled observables from synthetic instruments and meaningful 3D visualizations. The data has to unambiguously measure the observed phenomena, the model results have to accurately portray such phenomena, the synthetic observables have to accurately replicate the data observations and the visualizations have to be informative. When all of these variables are in accordance, or not, we gain knowledge, and with it we can improve every aspect of the process. Existing data can be reprocessed with new understanding, the models can be revamped to accommodate for more-appropriate assumptions, higher resolutions, or new capabilities, the synthetic observables can better represent the stochastic nature of the real data, and visualizations can be replotted to better convey the author's point of view. At the end of the process, new instruments, models and tools will eventually emerge where the quality and footprint of the work produced is ever more accurate, ever more engaging and ever more impactful.

Appendix

3D Earth-referenced coordinate mappings

A.1. Observer-ellipsoid Coordinate Systems.

The coordinate system in which we define our geometry is an Earth-Centered-Earth-Fixed (ECEF) which is defined as the Cartesian coordinate system where the center of the Earth is the origin, positive x, y and z axes are towards the Prime Meridian, 90° East and North Pole respectively. The Earth is modeled as an oblate ellipsoid defined by its principal semi-major axis a (equator) and its flattening f; the polar semi-axes b is then obtained from the flattening given its definition $f = (a - b)\big/a$. The satellite position is denoted by the ECEF Cartesian coordinates x, y and z. The satellite's orientation is defined by the unitary pointing vector whose directions are given in its local tangent plane system namely North-East-Down (NED) or East-North-Up (ENU). These local Cartesian coordinates are relative to the location of the satellite to the surface of an ellipsoid, therefore their origin is determined by their geodetic latitude ϕ[8], geodetic longitude λ and ellipsoidal height h and this is the geodetic coordinate system. Alternatively, the satellite's orientation may be given in local azimuth-tilt or azimuth-elevation coordinates where azimuth is the angle on the plane tangent to the ellipsoid and is clockwise from North and tilt/elevation is the angle from the local vertical or from the tangent plane respectively; the local vertical is the line that intersects the satellite's position with the center of the Earth and it can be defined

---

[8] The term *geodetic* is preferred over geographic to avoid confusion with the *geocentric* latitude.

positive when it's radially outward (satellite's zenith) or defined positive when it's radially inward (satellite's nadir). The azimuth-tilt and azimuth-elevation systems are in fact a local spherical coordinate system with unitary spherical radius.

A.2. 3D Coordinate Mappings

The intersection equation presented in **Section 2.4** requires that all the coordinate representations be in ECEF. Given the different systems we use to describe the satellite-ellipsoid geometry we need different mappings to and from ECEF:

II. Geodetic to ECEF,

III. ECEF to geodetic,

IV. ENU/NED to ECEF,

V. ECEF to ENU/NED,

VI. local spherical to ENU/NED, and

VII.ENU/NED to local spherical.

A.2.1. Geodetic to ECEF $\phi, \lambda, h \rightarrow x, y, z$

This is a straightforward mapping that follows from geometrical geodesy:

$$x = (N + h) \cos \phi \cos \lambda \tag{A.1}$$

$$y = (N + h) \cos \phi \sin \lambda \tag{A.2}$$

$$z = \left((b/a)^2 N + h \right) \sin \phi \tag{A.3}$$

where $N(\phi)$ is the east-west or prime vertical radius:

$$N(\phi) = \frac{a}{\sqrt{a^2 \cos^2 \phi + b^2 \sin^2 \phi}} \tag{A.4}$$

which is the distance from the ellipsoid's surface along its normal to the intersection with the z-axis of the ECEF system[9].
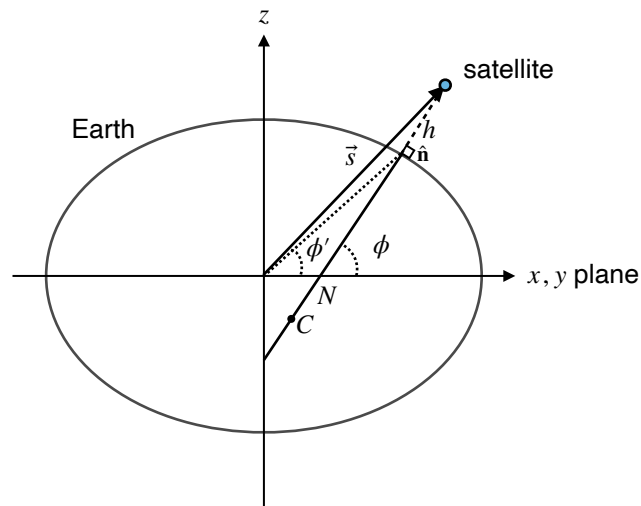
Figure A.1. Geodetic to ECEF mapping. The satellite position vector is $\vec{s}$, the prime vertical radius $N(\phi)$ that intersects the z-axis lies along the normal to the ellipsoid surface. The geodetic coordinates are given by the ellipsoidal height h, the latitude ϕ and the longitude λ (not shown here, lies on the x, y plane). The geocentric latitude ϕ' is different from the geodetic latitude ϕ, while the geocentric and geodetic longitudes are equivalent. C represents the center of curvature of the spheroid corresponding to the foot of h, tip of N.

---

[9] For derivations see Bomford, G, (1962). Geodesy. 2nd Ed. Oxford University Press and Smart, W. M. Spherical astronomy. Cambridge University Press (1944).

A.2.2. ECEF to geodetic: $x, y, z \rightarrow \phi, \lambda, h$

This mapping is usually obtained iteratively, however closed-form solutions are possible with a slight compromise in accuracy. The problem can be setup by combining **Equations (A.**1**) & (A.**2**)** to obtain an equation for h and ϕ:

$$\rho = \sqrt{x^2 + y^2} = (N + h) \cos \phi$$
$$h = \frac{\rho}{\cos \phi} - N \tag{A.5}$$

Another equation for h and ϕ can be obtained by using $f = (b - a)/a$, expanding equation (3) and dividing by ρ:

$$z = (N + h - e^2 N) \sin \phi$$
$$\frac{z}{\rho} = \left(1 - e^2 \frac{N}{N + h}\right) \tan \phi \tag{A.6}$$

where $e^2 = (a^2 - b^2)/a^2$ is the square of the first eccentricity. **Equations (A.**5**) & (A.**6**)** can be solved iteratively by taking an initial guess $h = 0$. The longitude is readily obtained by

$$\lambda = \operatorname{atan2}(y, x) \tag{A.7}$$

where atan2() is the full-circle inverse tangent function. In practice, a more efficient fixed-point iterative formula is used. Developed by Bowring in 1976[10,11], this will be the method of choice for calculations involving satellites. Bowring used the concept of center

---

[10] Bowring, B. R. (2013). "Transformation from Spatial to Geographical Coordinates." <u>Survey Review</u> **23**(181): 323-327.

[11] See implementation at Wolf, P. R., B. A. Dewitt and B. E. Wilkinson (2014). Coordinate Transformations. <u>Elements of Photogrammetry with Applications in GIS</u>. New York, McGraw-Hill Education.

of curvature of the spheroid C with coordinates $\left(e^2 a \cos^3 \beta, -e'^2 b \sin^3 \beta\right)$ where β is its parametric latitude and $e'^2 = e^2 / \left(1 - e^2\right)$ is the square of the second eccentricity (see **Figure A.1**). The iterative formulae are then:

$$\beta_0 = \text{atan2}\left(z, \left(1 - f\right)\rho\right) \tag{A.8}$$

$$\phi_i = \text{atan2}\left(z + e'^2 b \sin^3 \beta, \rho - a e^2 \cos^3 \beta\right) \tag{A.9}$$

The updated value of β is then computed from

$$\beta_{i+1} = \text{atan2}\left(\left(1 - f\right) \sin \phi_i, \cos_i \phi\right) \tag{A.10}$$

which in turns updates the latitude ϕ_{i+1} which can be used to obtain the height h from equation (A.5). To avoid the problems with the division by $\cos \phi$ for large latitudes, the height can be rewritten as a linear combination of $\cos^2 \phi$ and $\sin^2 \phi$ using **Equations** (**A.5**) & (**A.6**) and the fact that $\cos^2 \phi + \sin^2 \phi = 1$:

$$h = \frac{\rho}{\cos \phi} - N; \quad h = \frac{z}{\sin \phi} - N\left(1 - e^2\right) \tag{(A.5) \& (A.6)}$$

$$h = h\left(\cos^2 \phi + \sin^2 \phi\right)$$

$$h = \left(\frac{\rho}{\cos \phi} - N\right) \cos^2 \phi + \left(\frac{z}{\sin \phi} - N\left(1 - e^2\right)\right) \sin^2 \phi$$

$$h = \rho \cos \phi + z \sin \phi + N\left(e^2 \sin^2 \phi - 1\right) \tag{A.11}$$

The first iteration of this method already has micrometrical accuracy for calculations on the Earth's surface and converges to sub-millimeter accuracy for extraterrestrial calculations.

A.2.3. ENU/NED to ECEF

This mapping starts with right-handed local tangent coordinates, whether East-North-Up or North-East-Down, translates them to the origin and applies a rotation to the ECEF coordinates. The location of the local tangent plane is given in geodetic coordinates ϕ_0, λ_0, h_0 and it is necessary to obtain the equivalent ECEF position applying a geodetic to ECEF transformation: $\phi_0, \lambda_0, h_0 \rightarrow x_0, y_0, z_0$. Local tangent coordinates are usually notated with primes, x', y' and z', to distinguish them from ECEF, however for clarity the triplets E, N, U or N, E, D will be used for East-North-Up and North-East-Down respectively as defined in Figure A.2; the two systems are equivalent if East and North are swapped and Up or Down is negated. Each coordinate triplet defines a vector that points from (x_0, y_0, z_0) to (x, y, z). A simple representation of this mapping is obtained using a rotation matrix with an added translation operation:

$$\vec{r}_{\text{ECEF}} = R\vec{r}_{\text{ENU/NED}} + \vec{r}_0$$
$$[x, y, z]^T = [u, v, w]^T + [x_0, y_0, z_0]^T$$

(A.12)

where $\vec{p} = R\vec{r}_{\text{NED/ENU}} = u\hat{\mathbf{x}} + v\hat{\mathbf{y}} + w\hat{\mathbf{z}}$ is the direction vector of the local tangent coordinates rotated to ECEF and $\hat{\mathbf{p}} = \vec{p}/\|\vec{p}\|$ is the corresponding unitary direction vector. The expanded version of **Equation** (**A**.12) for each coordinate system is:

$$\begin{bmatrix} x \\ y \\ z \end{bmatrix} = \begin{bmatrix} -\sin\lambda_0 & -\sin\phi_0\cos\lambda_0 & \cos\phi_0\cos\lambda_0 \\ \cos\lambda_0 & -\sin\phi_0\sin\lambda_0 & \cos\phi_0\sin\lambda_0 \\ 0 & \cos\phi_0 & \sin\phi_0 \end{bmatrix} \begin{bmatrix} E \\ N \\ U \end{bmatrix} + \begin{bmatrix} x_0 \\ y_0 \\ z_0 \end{bmatrix}$$

(A.13)

$$\begin{bmatrix} x \\ y \\ z \end{bmatrix} = \begin{bmatrix} -\sin\phi_0\cos\lambda_0 & -\sin\lambda_0 & -\cos\phi_0\cos\lambda_0 \\ -\sin\phi_0\sin\lambda_0 & \cos\lambda_0 & -\cos\phi_0\sin\lambda_0 \\ \cos\phi_0 & 0 & -\sin\phi_0 \end{bmatrix} \begin{bmatrix} N \\ E \\ D \end{bmatrix} + \begin{bmatrix} x_0 \\ y_0 \\ z_0 \end{bmatrix}$$

(A.14)

The rotation matrix can be understood as the projection of the local tangent coordinates that have been translated to the ECEF's origin and projected onto the Cartesian x, y and z axes. Using the ENU system as an example, **Figure A.2** shows the projections of a point denoted by coordinates (E, N, U) onto the ECEF axes x, y and z; the resulting vector has Cartesian components $u\hat{\mathbf{x}}$, $v\hat{\mathbf{y}}$, $w\hat{\mathbf{z}}$ and it is the vector that results from the multiplication of the local tangent coordinates by the rotation matrix.
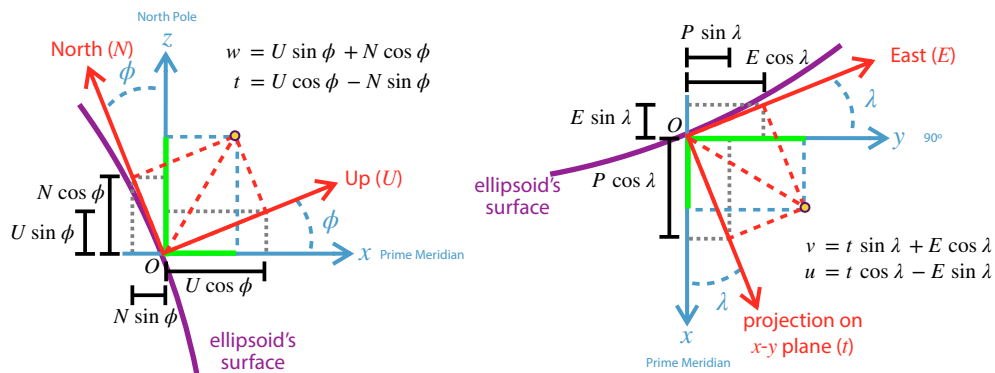
Figure A.2. Projection of the ENU coordinate system onto the ECEF coordinate system. In this figure the ECEF's origin has been translated to align with the ENU's at the local tangent plane. The green segments are the sought projections and their lengths correspond to the values of t, u, v and w.

The matrix operations from **Equations** (**A**.13) & (**A**.14) yield the final results for the NED/ENU to ECEF mapping:

$$
\begin{aligned}
x &= \left(U\cos\phi_0 - N\sin\phi_0\right)\cos\lambda_0 - E\sin\lambda_0 + x_0 \\
y &= \left(U\cos\phi_0 - N\sin\phi_0\right)\sin\lambda_0 + E\cos\lambda_0 + y_0 \\
z &= U\sin\phi_0 + N\cos\phi_0 + z_0
\end{aligned}
\tag{A.15}
$$

$$
\begin{aligned}
x &= \left(-D\cos\phi_0 - N\sin\phi_0\right)\cos\lambda_0 - E\sin\lambda_0 + x_0 \\
y &= \left(-D\cos\phi_0 - N\sin\phi_0\right)\sin\lambda_0 + E\cos\lambda_0 + y_0 \\
z &= -D\sin\phi_0 + N\cos\phi_0 + z_0
\end{aligned}
\tag{A.16}
$$

Equations A.15 **& A**.16 can be verified with **Figure 4.3**. Given the equivalence of ENU and NED, using the substitution $U = -D$ in **Equation** (**A**.16) yields the exact same equation as (A.15).

A.2.4. ECEF to ENU/NED

This mapping is the inverse transformation from the previous section. Recalling that the inverse of the rotation matrix is its transpose, the corresponding inverse mapping equation is:

$$
\begin{aligned}
\vec{r}_{\text{NED/ENU}} &= R^T \left(\vec{r}_{\text{ECEF}} - \vec{r}_0 \right) \\
[u, v, w]^T &= [x, y, z]^T - [x_0, y_0, z_0]^T
\end{aligned}
\tag{A.17}
$$

The matrix equations are:

$$
\begin{bmatrix} E \\ N \\ U \end{bmatrix} = \begin{bmatrix} -\sin \lambda_0 & \cos \lambda_0 & 0 \\ -\sin \phi_0 \cos \lambda_0 & -\sin \phi_0 \sin \lambda_0 & \cos \phi_0 \\ \cos \phi_0 \cos \lambda_0 & \cos \phi_0 \sin \lambda_0 & \sin \phi_0 \end{bmatrix} \begin{bmatrix} x - x_0 \\ y - y_0 \\ z - z_0 \end{bmatrix}
\tag{A.18}
$$

$$
\begin{bmatrix} N \\ E \\ D \end{bmatrix} = \begin{bmatrix} -\sin \phi_0 \cos \lambda_0 & -\sin \phi_0 \sin \lambda_0 & \cos \phi_0 \\ -\sin \lambda_0 & \cos \lambda_0 & 0 \\ -\cos \phi_0 \cos \lambda_0 & -\cos \phi_0 \sin \lambda_0 & -\sin \phi_0 \end{bmatrix} \begin{bmatrix} x - x_0 \\ y - y_0 \\ z - z_0 \end{bmatrix}
\tag{A.19}
$$

The final mapping equations are:

$$E = -(x - x_0)\sin\lambda_0 + (y - y_0)\cos\lambda_0$$
$$N = -\left((x - x_0)\cos\lambda_0 + (y - y_0)\sin\lambda_0\right)\sin\phi_0 + (z - z_0)\cos\lambda_0 \qquad \text{(A.20)}$$
$$U = \left((x - x_0)\cos\lambda_0 + (y - y_0)\sin\lambda_0\right)\cos\phi_0 + (z - z_0)\sin\phi_0$$

$$N = -\left((x - x_0)\cos\lambda_0 + (y - y_0)\sin\lambda_0\right)\sin\phi_0 + (z - z_0)\cos\lambda_0$$
$$E = -(x - x_0)\sin\lambda_0 + (y - y_0)\cos\lambda_0 \qquad \text{(A.21)}$$
$$D = -\left((x - x_0)\cos\lambda_0 + (y - y_0)\sin\lambda_0\right)\cos\phi_0 - (z - z_0)\sin\phi_0$$

A.2.5. Local Spherical to ENU/NED

This is a standard mapping from local spherical coordinates with coordinates azimuth, elevation and slant range (az, el, s) to the local tangent coordinates which is a Cartesian system. Local means they share the same origin on the tangent plane of the ellipsoid which is determined by the geodetic coordinates, ϕ_0, λ_0 and h_0. The azimuth is measured clockwise from North, the elevation is the angle from the local tangent plane and the slant range is the distance from the local origin. The mapping equations are:

$$E = s\cos az \sin el$$
$$N = s\cos az \cos el \qquad \text{(A.22)}$$
$$U = s\sin el$$

$$N = s\cos az \cos el$$
$$E = s\cos az \sin el \qquad \text{(A.23)}$$
$$D = -s\sin el$$

A.2.6. ENU/NED to local spherical

This is the inverse mapping of the previous section. The equations are:

$$az = \text{mod}\left(\text{atan2}\left(E, N\right),\ 360°\right)$$
$$el = \text{atan2}\left(U, \sqrt{E^2 + N^2}\right) \tag{A.24}$$
$$s = \sqrt{E^2 + N^2 + U^2}$$

$$az = \text{mod}\left(\text{atan2}\left(N, E\right),\ 360°\right)$$
$$el = \text{atan2}\left(-D, \sqrt{N^2 + E^2}\right) \tag{A.25}$$
$$s = \sqrt{N^2 + E^2 + D^2}$$

where $\text{mod}\left(\right)$ is the modulo operation or remainder after division.¶

Bibliography

Akiya, Y., A. Saito, T. Sakanoi, Y. Hozumi, A. Yamazaki, Y. Otsuka, M. Nishioka and T. Tsugawa (2014). "First spaceborne observation of the entire concentric airglow structure caused by tropospheric disturbance." Geophysical Research Letters **41**(19): 6943-6948.

Artru, J., V. Ducic, H. Kanamori, P. Lognonné and M. Murakami (2005). "Ionospheric detection of gravity waves induced by tsunamis." Geophysical Journal International **160**(3): 840-848.

Aumann, H. H., M. T. Chahine, C. Gautier, M. D. Goldberg, E. Kalnay, L. M. McMillin, H. Revercomb, P. W. Rosenkranz, W. L. Smith, D. H. Staelin, L. L. Strow and J. Susskind (2003). "AIRS/AMSU/HSB on the aqua mission: design, science objectives, data products, and processing systems." IEEE Transactions on Geoscience and Remote Sensing **41**(2): 253-264.

Azeem, I., J. Yue, L. Hoffmann, S. D. Miller, W. C. Straka and G. Crowley (2015). "Multisensor profiling of a concentric gravity wave event propagating from the troposphere to the ionosphere." Geophysical Research Letters **42**(19): 7874-7880.

Berger, M. J., D. L. George, R. J. LeVeque and K. T. Mandli (2011). "The GeoClaw software for depth-averaged flows with adaptive refinement." Advances in Water Resources **34**(9): 1195-1206.

Bowring, B. R. (2013). "Transformation from Spatial to Geographical Coordinates." Survey Review **23**(181): 323-327.

Chisham, G., M. Lester, S. E. Milan, M. P. Freeman, W. A. Bristow, A. Grocott, K. A. McWilliams, J. M. Ruohoniemi, T. K. Yeoman, P. L. Dyson, R. A. Greenwald, T. Kikuchi, M. Pinnock, J. P. S. Rash, N. Sato, G. J. Sofko, J. P. Villain and A. D. M. Walker (2007). "A decade of the Super Dual Auroral Radar Network (SuperDARN):

scientific achievements, new techniques and future directions." Surveys in Geophysics **28**(1): 33-109.

Chun, H.-Y. and Y.-H. Kim (2008). "Secondary waves generated by breaking of convective gravity waves in the mesosphere and their influence in the wave momentum flux." Journal of Geophysical Research **113**(D23).

Coble, M., G. C. Papen and C. S. Gardner (1998). "Computing two-dimensional unambiguous horizontal wavenumber spectra from OH airglow images." IEEE Transactions on Geoscience and Remote Sensing **36**(2): 368-382.

Donn, W. L. and E. S. Posmentier (1964). "Ground-coupled air waves from the Great Alaskan Earthquake." Journal of Geophysical Research **69**(24): 5357-5361.

Drob, D. P., J. T. Emmert, G. Crowley, J. M. Picone, G. G. Shepherd, W. Skinner, P. Hays, R. J. Niciejewski, M. Larsen, C. Y. She, J. W. Meriwether, G. Hernandez, M. J. Jarvis, D. P. Sipler, C. A. Tepley, M. S. O'Brien, J. R. Bowman, Q. Wu, Y. Murayama, S. Kawamura, I. M. Reid and R. A. Vincent (2008). "An empirical model of the Earth's horizontal wind fields: HWM07." Journal of Geophysical Research: Space Physics **113**(A12): n/a-n/a.

Eastes, R. W., W. E. McClintock, A. G. Burns, D. N. Anderson, L. Andersson, M. Codrescu, J. T. Correira, R. E. Daniell, S. L. England, J. S. Evans, J. Harvey, A. Krywonos, J. D. Lumpe, A. D. Richmond, D. W. Rusch, O. Siegmund, S. C. Solomon, D. J. Strickland, T. N. Woods, A. Aksnes, S. A. Budzien, K. F. Dymond, F. G. Eparvier, C. R. Martinis and J. Oberheide (2017). "The Global-Scale Observations of the Limb and Disk (GOLD) Mission." Space Science Reviews **212**(1-2): 383-408.

Englert, C. R., J. M. Harlander, C. M. Brown, K. D. Marr, I. J. Miller, J. E. Stump, J. Hancock, J. Q. Peterson, J. Kumler, W. H. Morrow, T. A. Mooney, S. Ellis, S. B. Mende, S. E. Harris, M. H. Stevens, J. J. Makela, B. J. Harding and T. J. Immel (2017).

"Michelson Interferometer for Global High-resolution Thermospheric Imaging (MIGHTI): Instrument Design and Calibration." <u>Space Sci Rev</u> **212**(1-2): 553-584.

Francis, S. H. (1975). "Global propagation of atmospheric gravity waves: A review." <u>Journal of Atmospheric and Terrestrial Physics</u> **37**(6-7): 1011-1054.

Fritts, D. C. and M. J. Alexander (2003). "Gravity wave dynamics and effects in the middle atmosphere." <u>Reviews of Geophysics</u> **41**(1).

Fritts, D. C., R. B. Smith, M. J. Taylor, J. D. Doyle, S. D. Eckermann, A. Dörnbrack, M. Rapp, B. P. Williams, P. D. Pautet, K. Bossert, N. R. Criddle, C. A. Reynolds, P. A. Reinecke, M. Uddstrom, M. J. Revell, R. Turner, B. Kaifler, J. S. Wagner, T. Mixa, C. G. Kruse, A. D. Nugent, C. D. Watson, S. Gisinger, S. M. Smith, R. S. Lieberman, B. Laughman, J. J. Moore, W. O. Brown, J. A. Haggerty, A. Rockwell, G. J. Stossmeister, S. F. Williams, G. Hernandez, D. J. Murphy, A. R. Klekociuk, I. M. Reid and J. Ma (2016). "The Deep Propagating Gravity Wave Experiment (DEEPWAVE): An Airborne and Ground-Based Exploration of Gravity Wave Propagation and Effects from Their Sources throughout the Lower and Middle Atmosphere." <u>Bulletin of the American Meteorological Society</u> **97**(3): 425-453.

Fritts, D. C., S. B. Vosper, B. P. Williams, K. Bossert, J. M. C. Plane, M. J. Taylor, P. D. Pautet, S. D. Eckermann, C. G. Kruse, R. B. Smith, A. Dörnbrack, M. Rapp, T. Mixa, I. M. Reid and D. J. Murphy (2018). "Large-Amplitude Mountain Waves in the Mesosphere Accompanying Weak Cross-Mountain Flow During DEEPWAVE Research Flight RF22." <u>Journal of Geophysical Research: Atmospheres</u> **123**(18).

Fritts, D. C., L. Wang, G. Baumgarten, A. D. Miller, M. A. Geller, G. Jones, M. Limon, D. Chapman, J. Didier, C. B. Kjellstrand, D. Araujo, S. Hillbrand, A. Korotkov, G. Tucker and J. Vinokurov (2017). "High-resolution observations and modeling of turbulence sources, structures, and intensities in the upper mesosphere." <u>Journal of Atmospheric and Solar-Terrestrial Physics</u> **162**: 57-78.

Garcia, F. J., M. J. Taylor and M. C. Kelley (1997). "Two-dimensional spectral analysis of mesospheric airglow image data." <u>Appl Opt</u> **36**(29): 7374-7385.

Garcia, O. E. and H. L. Pécseli (2013). "Models for electrostatic drift waves with density variations along magnetic field lines." <u>Geophysical Research Letters</u> **40**(21): 5565-5569.

Ghodpage, R., A. Taori, P. Tukaram, S. Gurubaran and A. Sharma (2015). "On the vertical wavelength estimates using the Krassovsky parameters of OH airglow monitoring." <u>Current science</u> **108**.

Gille, J. C., J. J. Barnett, J. G. Whitney, M. A. Dials, D. Woodard, W. P. Rudolf, A. Lambert and W. Mankin (2003). The High-Resolution Dynamics Limb Sounder (HIRDLS) experiment on AURA. <u>Proc. SPIE 5152, Infrared Spaceborne Remote Sensing XI</u>. M. Strojnik. San Diego, CA, SPIE.

Goldberg, D. M. and J. R. Gott (2006). "Flexion and Skewness in Map Projections of the Earth." <u>arXiv</u>.

Guerrero, J. A., C. J. Heale, P. Inchin, J. B. Snively, M. D. Zettergren, A. Liu, F. Vargas, G. R. Swenson and A. D. Mangognia (2020). From simulated data to AR: 3D visualization techniques for meaningful representation of atmospheric gravity wave data and AR applications. AGU Fall Meeting 2020, AGU.

Hart, V. P., T. E. Doyle, M. J. Taylor, B. L. Carruth, P.-D. Pautet and Y. Zhao (2012). "Three-dimensional tomographic reconstruction of mesospheric airglow structures using two-station ground-based image measurements." <u>Applied Optics</u> **51**(7): 963-974.

Heale, C. J., J. B. Snively, A. N. Bhatt, L. Hoffmann, C. C. Stephan and E. A. Kendall (2019). "Multilayer Observations and Modeling of Thunderstorm-Generated Gravity Waves Over the Midwestern United States." <u>Geophysical Research Letters</u> **46**(23): 14164-14174.

Heale, C. J., J. B. Snively and M. P. Hickey (2014). "Numerical simulation of the long-range propagation of gravity wave packets at high latitudes." Journal of Geophysical Research: Atmospheres **119**(19): 11,116-111,134.

Hecht, J. H., R. L. Walterscheid and M. N. Ross (1994). "First measurements of the two-dimensional horizontal wave number spectrum from CCD images of the nightglow." Journal of Geophysical Research **99**(A6).

Hickey, M. P., G. Schubert and R. L. Walterscheid (2009). "Propagation of tsunami-driven gravity waves into the thermosphere and ionosphere." Journal of Geophysical Research: Space Physics **114**(A8): n/a-n/a.

Hines, C. O. (1960). "Internal Atmospheric Gravity Waves at Ionospheric Heights." Canadian Journal of Physics **38**(11): 1441-1481.

Hoffmann, L. and M. J. Alexander (2010). "Occurrence frequency of convective gravity waves during the North American thunderstorm season." Journal of Geophysical Research **115**(D20).

Holton, J. R., P. H. Haynes, M. E. McIntyre, A. R. Douglass, R. B. Rood and L. Pfister (1995). "Stratosphere-troposphere exchange." Reviews of Geophysics **33**(4).

Inchin, P. A. (2020). Atmospheric and Ionospheric Responses to Acoustic and Gravity Waves Driven by Earthquakes and Tsunamis Waves Driven by Earthquakes and Tsunamis. Doctor of Phylosophy in Engineering Physics.

Inchin, P. A., J. Aguilar Guerrero, J. Snively and Y. Kaneko (2022). Simulation of infrasonic acoustic wave imprints on airglow layers during the 2016 M7.8 Kaikoura earthquake. M. s. t. J. o. G. R.-S. Physics.

Inchin, P. A., C. J. Heale, J. B. Snively and M. D. Zettergren (2020). "The Dynamics of Nonlinear Atmospheric Acoustic-Gravity Waves Generated by Tsunamis Over Realistic Bathymetry." Journal of Geophysical Research: Space Physics **125**(12).

Inchin, P. A., J. B. Snively, Y. Kaneko, M. D. Zettergren and A. Komjathy (2021). "Inferring the Evolution of a Large Earthquake From Its Acoustic Impacts on the Ionosphere." AGU Advances **2**(2).

Inchin, P. A., J. B. Snively, A. Williamson, D. Melgar, J. Aguilar Guerrero and M. D. Zettergren (2020). "Mesopause Airglow Disturbances Driven by Nonlinear Infrasonic Acoustic Waves Generated by Large Earthquakes." Journal of Geophysical Research: Space Physics **125**(6).

Jing, T., F. Kamalabadi, S. J. Franke, A. Z. Liu and G. R. Swenson (2005). "Estimation of gravity wave momentum flux with spectroscopic imaging." IEEE Transactions on Geoscience and Remote Sensing **43**(1): 103-109.

Karney, F. F. C. (2021, 06-22-2021). "Rhumb lines, GeographicLib, Version 1.52." Retrieved 11-23-2021, 2021, from https://geographiclib.sourceforge.io/html/rhumb.html#rhumbform.

Kekesi, A. (2020). "TEMPEST-D : RaInCube Sees Typhoon Trami.pdf." NASA Scientific Visualization Studio Retrieved July 9th 2021, 2021, from https://svs.gsfc.nasa.gov/4859.

Kekesi, A. and L. Perkins. (2010). "Hurricane Katrina 3D Stereoscopic Viewfinder Image." Retrieved July 9th 2021, 2020, from https://svs.gsfc.nasa.gov/3745.

Kendall, E. A. and A. Bhatt (2017). MANGO Imager Network Observations of Geomagnetic Storm Impact on Midlatitude 630 nm Airglow Emissions. AGU Fall Meeting 2017. New Orleans.

Komatitsch, D. and J. Tromp (2002). "Spectral-element simulations of global seismic wave propagation-I. Validation." Geophysical Journal International **149**(2): 390-412.

Krassovsky, V. I. and M. V. Shagaev (1977). "On the nature of internal gravitational waves observed from hydroxyl emission." Planetary and Space Science **25**(2): 200-201.

Lehmann, A., C. Federrath and M. Wardle (2016). "SHOCKFIND - an algorithm to identify magnetohydrodynamic shock waves in turbulent clouds." <u>Monthly Notices of the Royal Astronomical Society</u> **463**(1): 1026-1039.

Liu, A. Z. and G. R. Swenson (2003). "A modeling study of O2and OH airglow perturbations induced by atmospheric gravity waves." <u>Journal of Geophysical Research</u> **108**(D4).

Liu, X., J. Xu, J. Yue, S. L. Vadas and E. Becker (2019). "Orographic Primary and Secondary Gravity Waves in the Middle Atmosphere From 16-Year SABER Observations." <u>Geophysical Research Letters</u> **46**(8): 4512-4522.

Macklin, M. and M. Müller (2013). "Position based fluids." <u>ACM Transactions on Graphics</u> **32**(4): 1-12.

Makela, J. J., P. Lognonné, H. Hébert, T. Gehrels, L. Rolland, S. Allgeyer, A. Kherani, G. Occhipinti, E. Astafyeva, P. Coïsson, A. Loevenbruck, E. Clévédé, M. C. Kelley and J. Lamouroux (2011). "Imaging and modeling the ionospheric airglow response over Hawaii to the tsunami generated by the Tohoku earthquake of 11 March 2011." <u>Geophysical Research Letters</u> **38**(24): n/a-n/a.

Mende, S. B., H. U. Frey, K. Rider, C. Chou, S. E. Harris, O. H. W. Siegmund, S. L. England, C. Wilkins, W. Craig, T. J. Immel, P. Turin, N. Darling, J. Loicq, P. Blain, E. Syrstad, B. Thompson, R. Burt, J. Champagne, P. Sevilla and S. Ellis (2017). "The Far Ultra-Violet imager on the ICON mission." <u>Space Sci Rev</u> **212**: 655-696.

Nakashima, Y., K. Heki, A. Takeo, M. N. Cahyadi, A. Aditiya and K. Yoshizawa (2016). "Atmospheric resonant oscillations by the 2014 eruption of the Kelud volcano, Indonesia, observed with the ionospheric total electron contents and seismic signals." <u>Earth and Planetary Science Letters</u> **434**: 112-116.

Nielsen, E. and K. Schlegel (1985). "Coherent radar Doppler measurements and their relationship to the ionospheric electron drift velocity." Journal of Geophysical Research **90**(A4).

Pautet, D. and G. Moreels (2002). "Ground-based satellite-type images of the upper-atmosphere emissive layer." Applied Optics **41**(5): 823-831.

Pautet, P. D., M. J. Taylor, W. R. Pendleton, Y. Zhao, T. Yuan, R. Esplin and D. McLain (2014). "Advanced mesospheric temperature mapper for high-latitude airglow studies." Appl Opt **53**(26): 5934-5943.

Peltier, W. R. and C. O. Hines (1976). "On the possible detection of tsunamis by a monitoring of the ionosphere." Journal of Geophysical Research **81**(12): 1995-2000.

Perwitasari, S., T. Sakanoi, A. Yamazaki, Y. Otsuka, Y. Hozumi, Y. Akiya, A. Saito, K. Shiokawa and S. Kawamura (2015). "Coordinated airglow observations between IMAP/VISI and a ground-based all-sky imager on concentric gravity wave in the mesopause." Journal of Geophysical Research: Space Physics **120**(11): 9706-9721.

Pilger, C., C. Schmidt, F. Streicher, S. Wüst and M. Bittner (2013). "Airglow observations of orographic, volcanic and meteorological infrasound signatures." Journal of Atmospheric and Solar-Terrestrial Physics **104**: 55-66.

Richter, J. H., F. Sassi and R. R. Garcia (2010). "Toward a Physically Based Gravity Wave Source Parameterization in a General Circulation Model." Journal of the Atmospheric Sciences **67**(1): 136-156.

Roach, F. E. and A. B. Meinel (1955). "The Height of the Nightglow by the Van Rhijn Method." The Astrophysical Journal **122**.

Roach, F. E. and A. B. Meinel (1955). "The Height of the Nightglow by the Van Rhijn Method." The Astrophysical Journal.

Russell III, J. M., M. G. Mlynczak and L. L. Gordley (1994). Overview of the Sounding of the Atmosphere Using Broadband Emission Radiometry (SABER) experiment for the Thermosphere-Ionsphere-Mesosphere Energetics and Dynamics (TIMED) mission. Optical Spectroscopic Techniques and Instrumentation for Atmospheric and Space Research. San Diego, CA, SPIE.

Russell III, J. M., M. G. Mlynczak and L. L. Gordley (1994). Overview of the Sounding of the Atmosphere Using Broadband Emission Radiometry (SABER) experiment for the Thermosphere-Ionsphere-Mesosphere Energetics and Dynamics (TIMED) mission. Proc. SPIE 2266, Optical Spectroscopic Techniques and Instrumentation for Atmospheric and Space Research. San Diego, CA, SPIE.

Sakanoi, T., Y. Akiya, A. Yamazaki, Y. Otsuka, A. Saito and I. Yoshikawa (2011). "Imaging Observation of the Earth's Mesosphere, Thermosphere and Ionosphere by VISI of ISS-IMAP on the International Space Station." IEEJ Transactions on Fundamentals and Materials **131**(12): 983-988.

Sassi, F., J. H. Richter and R. R. Garcia (2010). "Toward a Physically Based Gravity Wave Source Parameterization in a General Circulation Model." Journal of the Atmospheric Sciences **67**(1): 136-156.

Sharov, A. S. and N. A. Lipaeva (1973). Stellar component of the nightglow. Soviet Astronomy. **17:** 107-114.

Shiokawa, K. (2003). "Statistical study of nighttime medium-scale traveling ionospheric disturbances using midlatitude airglow images." Journal of Geophysical Research **108**(A1).

Shirah, G. (2018). "Inside Hurricane Maria in 360°." NASA Scientific Visualization Studio Retrieved July 9th 2021, 2020, from https://svs.gsfc.nasa.gov/4685.

Shirah, G. (2021). "Three years of SAGE III:ISS Stratospheric Aerosol Data.pdf." NASA Scientific Visualization Studio Retrieved July 9th 2021, 2021, from https:// svs.gsfc.nasa.gov/4861.

Sirk, M. M., E. J. Korpela, Y. Ishikawa, J. Edelstein, E. H. Wishnow, C. Smith, J. McCauley, J. B. McPhate, J. Curtis, T. Curtis, S. R. Gibson, S. Jelinsky, J. A. Lynn, M. Marckwordt, N. Miller, M. Raffanti, W. Van Shourt, A. W. Stephan and T. J. Immel (2017). "Design and Performance of the ICON EUV Spectrograph." Space Sci Rev **212**: 631-643.

Sivjee, G. G. (2005). "Observations of elevated power near the Brunt-Väisälä frequency." Journal of Geophysical Research **110**(A6).

Snively, J. B. (2013). "Mesospheric hydroxyl airglow signatures of acoustic and gravity waves generated by transient tropospheric forcing." Geophysical Research Letters **40**(17): 4533-4537.

Snively, J. B., V. P. Pasko and M. J. Taylor (2010). "OH and OI airglow layer modulation by ducted short-period gravity waves: Effects of trapping altitude." Journal of Geophysical Research: Space Physics **115**(A11): n/a-n/a.

Song, I.-S., H.-Y. Chun and T. P. Lane (2003). "Generation Mechanisms of Convectively Forced Internal Gravity Waves and Their Propagation to the Stratosphere." Journal of the Atmospheric Sciences **60**(16): 1960-1980.

Stephan, C. and M. J. Alexander (2015). "Realistic simulations of atmospheric gravity waves over the continental U.S. using precipitation radar data." Journal of Advances in Modeling Earth Systems **7**(2): 823-835.

Swenson, G. R., M. J. Taylor, P. J. Espy, C. Gardner and X. Tac (1995). "ALOHA-93 measurements of intrinsic AGW characteristics using airborne airglow imager and groundbased Na wind/temperature lidar." Geophysical Research Letters **22**(20): 2841-2844.

Taylor, M. J., S. D. Eckermann, J. M. Forbes, H. Liu, J. B. Snively, Y. Zhao, P. D. Pautet and W. R. Pendleton (2018). The Atmospheric Waves Experiment (AWE) on the International Space Station. 42nd COSPAR Scientific Assembly. Pasadena, CA.

Taylor, M. J., J. M. Forbes, D. C. Fritts, S. D. Eckermann, J. B. Snively, H. Liu, D. Janches, E. A. Syrstad, R. W. Esplin, P. D. Pautet, Y. Zhao and W. R. Pendleton (2019). Developing the NASA Atmospheric Waves Experiment (AWE). AGU Fall Meeting 2019.

Taylor, M. J. and M. A. Hapgood (1982). "Analysis of airglow image data." Annales de Geophysique **38**(6): 805-813.

Vadas, S. L. and E. Becker (2018). "Numerical Modeling of the Excitation, Propagation, and Dissipation of Primary and Secondary Gravity Waves during Wintertime at McMurdo Station in the Antarctic." Journal of Geophysical Research: Atmospheres **123**(17): 9326-9369.

Vadas, S. L. and D. C. Fritts (2004). "Thermospheric responses to gravity waves arising from mesoscale convective complexes." Journal of Atmospheric and Solar-Terrestrial Physics **66**(6-9): 781-804.

Vadas, S. L., D. C. Fritts and M. J. Alexander (2003). "Mechanism for the Generation of Secondary Waves in Wave Breaking Regions." Journal of the Atmospheric Sciences **60**(1): 194-214.

Wedi, N. P., I. Polichtchouk, P. Dueben, V. G. Anantharaj, P. Bauer, S. Boussetta, P. Browne, W. Deconinck, W. Gaudin, I. Hadade, S. Hatfield, O. Iffrig, P. Lopez, P. Maciel, A. Mueller, S. Saarinen, I. Sandu, T. Quintino and F. Vitart (2020). "A Baseline for Global Weather and Climate Simulations at 1 km Resolution." Journal of Advances in Modeling Earth Systems **12**(11).

Witasse, O., J. Lilensten, C. Lathuillère and P. L. Blelly (1999). "Modeling the OI 630.0 and 557.7 nm thermospheric dayglow during EISCAT-WINDII coordinated measurements." Journal of Geophysical Research: Space Physics **104**(A11): 24639-24655.

Wolf, P. R., B. A. Dewitt and B. E. Wilkinson (2014). Coordinate Transformations. Elements of Photogrammetry with Applications in GIS. New York, McGraw-Hill Education.

Wright, C. J., N. P. Hindley, M. J. Alexander, L. A. Holt and L. Hoffmann (2021). "Using vertical phase differences to better resolve 3D gravity wave structure." Atmospheric Measurement Techniques **14**(9): 5873-5886.

Wright, C. J., N. P. Hindley, L. Hoffmann, M. J. Alexander and N. J. Mitchell (2017). "Exploring gravity wave characteristics in 3-D using a novel S-transform technique: AIRS/Aqua measurements over the Southern Andes and Drake Passage." Atmospheric Chemistry and Physics **17**(13): 8553-8575.

Yiğit, E. and A. S. Medvedev (2015). "Internal wave coupling processes in Earth's atmosphere." Advances in Space Research **55**(4): 983-1003.

Yu, Y. and M. P. Hickey (2017). "Ionospheric Gravity Waves Driven by Oceanic Gravity Waves in Resonance: A Modeling Study in Search of Their Spectra." Geophysical Research Letters **44**(18): 9183-9191.

Yue, J., S. L. Vadas, C.-Y. She, T. Nakamura, S. C. Reising, H.-L. Liu, P. Stamus, D. A. Krueger, W. Lyons and T. Li (2009). "Concentric gravity waves in the mesosphere generated by deep convective plumes in the lower atmosphere near Fort Collins, Colorado." Journal of Geophysical Research **114**(D6).

Zettergren, M. and J. Semeter (2012). "Ionospheric plasma transport and loss in auroral downward current regions." Journal of Geophysical Research: Space Physics **117**(A6): n/a-n/a.

Zettergren, M. D. and J. B. Snively (2015). "Ionospheric response to infrasonic-acoustic waves generated by natural hazard events." <u>Journal of Geophysical Research: Space Physics</u> **120**(9): 8002-8024.

Zhao, Y., M. J. Taylor and X. Chu (2005). "Comparison of simultaneous Na lidar and mesospheric nightglow temperature measurements and the effects of tides on the emission layer heights." <u>Journal of Geophysical Research</u> **110**(D9).

Zhou, T., A. A. Scaife, K. Sato, P. Preusse, E. Manzini, A. Hertzog, M. Ern, J. Bacmeister, P. T. Love, M. J. Alexander and M. A. Geller (2013). "A Comparison between Gravity Wave Momentum Fluxes in Observations and Climate Models." <u>Journal of Climate</u> **26**(17): 6383-6405.

Zhou, X., J. R. Holton and G. L. Mullendore (2002). "Forcing of secondary waves by breaking of gravity waves in the mesosphere." <u>Journal of Geophysical Research</u> **107**(D7).